UNIVERSITÀ
DEGLI STUDI
DI PADOVA

Head Office: Università degli Studi di Padova
Department of Physics and Astronomy

Ph.D. COURSE IN PHYSICS
SERIES: XXX

Nb thick films
in 6 GHz superconducting resonant cavities

Thesis written under the financial contribution of Fondazione Cariparo

Work supported by the INFN V group experiment ISIDE and performed
under the CERN-INFN-FTSC Agreement N. KE2722/BE/FCC

Coordinator: Prof. Gianguido Dall'Agata
Supervisor: Prof. Vincenzo Palmieri

Ph.D. student : Cristian Pira

Abstract

A key challenge for the next accelerators is the cost reduction. Bulk niobium cavities performances are closer to their theoretical limits and an alternative technology is mandatory. Niobium thin film copper cavities are the most explored solution, but the Q-slope characteristic of these resonators limits the applications where high accelerating fields are requested.

In this work an original approach is adopted in order to enhance the performances of sputtered cavities, exploring the possibility to sputter 70 micron thick films to straighten up the Q-slope in Niobium sputtered copper cavities. The engineering of Nb thick films deposition on 6 GHz copper cavities, necessary to minimize the stress on niobium thick films and avoid film peeling from the substrate, is reported. Thick films show RRR values over 60.

Different strategies have been used for stress reduction: deposition at high temperature of 550 °C, deposition at the zero stress pressure point (5·10^{-2} mbar), and the development of a multilayer deposition procedure. Rf tests at 4,2 K and 1,8 K on 6 GHz resonant cavities are the tool used to evaluate the influence of the critical deposition parameters on the cavity performances. Two different venting procedures have been tested: a standard one, and a high temperature one, in which pure nitrogen is inserted in the vacuum chamber immediately after the end of the sputtering process. Thick films open the possibility to post treatments on sputtered cavities: the effect of buffer chemical polishing and heat treatments at different temperature have been investigated.

The Rf tests on 6 GHz cavities show the fundamental role played by the surface preparation and the possibility to enhance the maximum accelerating field minimizing the film stress. Above all, for the first time, the possibility to obtain flat curve of Q-factor versus accelerating field in sputtered cavities with thick films it is demonstrated.

Acknowledgements

It may seem trivial, but this is the truth. This work was possible only thanks to the help and friendship of many colleagues and friends that I had the luck to meet during my professional carrier and life. I would like to acknowledge their contributions here.

First, I want to thank prof. Palmieri, for more than ten years in which I have been trying to learn as much as possible from him (I hope he will come back to lab soon). Thanks to the SRF research group: Giovanni, Daniel and Filippo. The results of this thesis are the fruit of a team work. Thanks to Fabrizio and Eduard for the chemistry on cavities. Thanks to Alex for his ability to satisfy any mechanical request. Many many thanks to Silvia for the tough revision work. Thanks to Oscar for his help with SEM characterization and continuous support. Thanks to Giorgio for his precious advices. Thanks to Hanna and Sara for sharing their experience on thick films. Thanks to Alessandro and Luca for the support with the cryogenics. Thanks to Rossano and Flavio to move the helium dewar around all LNL. Thanks to all my friends at LNL, for making the workdays more enjoyable. A big thank to Tom Powers who spent two weeks with us in Legnaro to teach how to properly perform a rf test and how to read English children books. Thanks to my parents, that always helped and sustained me in any decision of my life. And finally thanks to my loves: Nadia, Rebecca and Agata. Nothing is more important than you!

Contents

Abstract iii

Acknowledgements v

Contents vii

Introduction 1

Scientific context 1

Thick films: a new approach to solve the Q-slope problem 1

1 SRF Fundamentals 3

1.1 Normal conductors and their limitation in RF 3

1.1.1 DC behavior: the Drude model 3

1.1.2 RF Behaviour: skin effect and anomalous skin effect 4

1.2 Superconductivity 5

1.2.1 SC Introduction: perfect conductivity and Meissner effect 5

1.2.2 Key parameters in BCS 6

1.3 Resonant Cavity Fundamentals 10

1.3.1 Basic principle and key parameters in Resonant Cavities 10

1.3.2 Q_0 VS E_{acc} curve and principal limitations in SRF cavities 12

1.4 Niobium on Copper Cavities 14

1.4.1 Niobium 14

1.4.2 Niobium Bulk Cavities 15

1.4.3 Motivations for Niobium on Copper Cavities 15

1.4.4 Principal limitation in Niobium Copper Cavities: the Q-slope 17

1.4.5 A new cause for the Q-slope: the Nb/Cu interface 19

2 Sputtering generalities and state of the art on Nb/Cu cavities 21

2.1 Introduction 21

2.2 Physics of sputtering process 21
2.3 Plasma generation 22
2.3.1 The gas ionization: Townsend discharge 22
2.3.2 The sputtering regime: the abnormal glow discharge 24
2.4 Film growth 25
2.5 Stress on sputtered coating 27
2.6 Sputtering Configurations and state of the art in Nb/Cu deposition for SRF 30
2.6.1 DC Diode Bias Sputtering 30
2.6.2 DC Magnetron Sputtering 32
2.6.3 High Power Impulse Magnetron Sputtering 34
2.6.4 Nb films via (non sputtering) energetic condensation technique 36
2.6.5 Nb/Cu clad cavities, an alternative to PVD deposition 37
3 The thick film way 39
3.1 State of the art on sputtering thick films 39
3.2 Motivations for SRF thick films 41
4 Cavity surface preparation 45
4.1 Introduction to copper surface treatments 45
4.2 Fabbrication of 6 GHz copper cavities by spinning 46
4.3 Mechanical polishing 48
4.4 Degreasing in ultrasonic bath 49
4.5 Electropolishing 49
4.5.1 LNL software for EP 52
4.5.2 LNL apparatus and procedure for EP 53
4.6 Chemical polishing: SUBU5 53
4.7 High pressure rinsing 55
5 RF test on 6 GHz cavities 57
5.1 6 GHz cavities approach 57
5.2 Fundamental equations for rf test 58
5.3 6 GHz rf test apparatus 61
5.4 System Calibration 63
5.4.1 Forward and reflected power calibration 63
5.4.2 Transmitted power calibration (pickup calibration) 64
5.4.3 Internal cables calibration 64

5.5 Cavity measurement procedure 65

5.6 Cavity measurement software 66

5.7 Cryogenic apparatus and cavity stand 67

5.8 Cavity and stand preparation for the rf test 70

5.9 Upgrade of the kapton sealing system 71

6 Nb films characterization methods 73

6.1 Superconductive properties: RRR, T_c and ΔT_c 73

6.2 Profilometer 74

6.3 Optical inspection 75

6.4 XRD 76

6.5 SEM 78

7 Deposition system and procedure 79

7.1 Vacuum system 79

7.2 The cathode 81

7.3 Coating parameters 82

7.3.1 Nomenclature 83

7.3.2 Magnetic field and current 84

7.3.3 Temperature 86

7.3.4 Pressure 86

7.3.5 Deposition rate 87

7.3.6 Venting modes 89

7.3.7 Multilayer mode 90

7.4 Post treatments 92

7.4.1 BCP 92

7.4.2 Heat treatments 93

8 Results and discussion 95

8.1 Planar sample test 95

8.1.1 Superconductive properties 95

8.1.2 XRD 96

8.1.3 SEM and EDS 97

8.2 Cavity rf test 98

8.3 Results discussion 129

8.3.1 Flat Q and Q slope on thick film cavities 129

8.3.2 Role of pressure ... 130
8.3.3 Role of venting ... 131
8.3.4 Role of multilayer deposition ... 132
8.3.5 Role of BCP ... 134
8.3.6 Role of thermal treatments ... 134
9 Conclusions ... 137
9.1 Future developments ... 138
Bibliography ... 139
List of figures ... 144
List of tables ... 147
List of abbreviations ... 149

Introduction

Scientific context

Particle accelerators are fundamental tools in nuclear and high-energy Physics and the development of more efficient superconducting radio frequency cavities is a key challenge for the next accelerators.

Bulk niobium has been the standard choice for SRF cavities for several decades and Hasaan Padamsee, one of the most important contributors of the SRF community, recently has referred to this time as the golden age for the Superconducting Radio Frequency (SRF) particle accelerators [1]. After 50 years of advancement, several limits on SRF cavities performance have been exceeded, and the Nb bulk cavities reach accelerating fields close to 50 MV/m, not far from the theoretical limit.

However, cost reduction must be a necessary issue for the future linacs, as for example International Linear Collider (ILC), in which the demand of thousands of cavities, makes the cavity production cost a factor that is not negligible, especially in economic crisis period as the one we are living today.

A solution already exists and was developed in the 1980s at CERN by Cris Benvenuti [2]. The solution consists in the deposition by magnetron sputtering (or other PVD techniques) of several microns of niobium onto a copper cavity. The Nb/Cu thin films cavities were installed with success at LEP and LHC at CERN [3] [4], ALPI at LNL-INFN [5] and this is the technology choice for the ISOLDE upgrade at CERN [6]. Nb films show clear advantage compared to bulk Nb for defined accelerator parameter sets, in particular for low frequency cavities or for operation at 4.2 K. However, the large Q-slope that affects these cavities, limit their use in high field accelerators.

Since the early 1990s researchers of many laboratories tried to understand and solve the Q-slope problem in thin films cavities, but until now, it remains an unsolved problem.

Thick films: a new approach to solve the Q-slope problem

In this work, a totally new approach is attempted to solve the Q-slope problem. We have explored the possibility of growing thick films of the order of tens of microns and we have tested how the SRF performances are affected. The idea comes from the assumption that the Q-slope certainly is caused by the film deposition and is not an intrinsic problem of the Niobium-Copper system [7]. The experimental evidence of the Niobium-clad Copper Cavities shows the possibility

for Nb-Cu to have a flat Q-factor and accelerating fields up to 40 MV/m [8]. Niobium-clad cavities differ from sputtered cavities for at least three factors: Nb microstructure, Nb-Cu interface and Nb thickness. The first two are intrinsically distinctive of clad Nb/Cu technology, but if the thickness plays the main role in the Q-slope issue, with magnetron sputtering we can increase the thickness and try to increase the SRF performances of the cavity modulating this parameter. It remains to explain how a high thickness of the Niobium could affect cavity RF performances.

Two principal reasons can describe the influence of thick films on SRF. The first one concern the reported fact that RRR (purity index of the material) increases with thickness [9]. The second one involves the thermal boundary resistance at Nb/Cu interface, a model recently proposed by Vaglio and Palmieri [10]. In the hypothesis of this model, the Q-slope is related to local enhancement of the thermal boundary resistance at the Nb/Cu interface, due to poor thermal contact between film and substrate. The thermal defects at the interface locally increase the boundary resistance. In the case of thin film, the heat flow, produced by the rf power, pass through the thermal defect because the heat flow will be transmitted unidimensionally from the film to the Cu substrate [7]. In thick films, instead, the heat flow path occurs three-dimensionally, and the heat flux can easily bypass the thermal defect at the interface.

The subject of this dissertation is the engineering of Nb thick films deposition onto 6 GHz cavities to demonstrate the possibility of flat Q in Nb/Cu sputtered cavities.

This dissertation is organized as follows:

- chapter 1 introduces the basics of superconductivity and resonant cavities;
- chapter 2 introduces the sputtering techniques and the state of the art for superconducting Nb/Cu technologies;
- chapter 3 describes the theoretical reasons for thick film approach;
- chapter 4 describes the cavity surface preparation;
- chapter 5 describes the rf test apparatus and procedure used to characterize the cavities;
- chapter 6 describes the characterization techniques used for the preliminary samples;
- chapter 7 describes the deposition system used and the procedure applied in the sputtering deposition;
- chapter 8 contains the results of this work and a critical discussion on that;
- chapter 9 summarizes the important results of this work and a roadmap for future work.

1 SRF Fundamentals

In this chapter a brief introduction on Superconducting Resonant Cavities is presented. In the first paragraph the limitation of normal conductors in RF applications is remarked. The second paragraph introduces superconductivity, while in the third one, basic principles and key parameters of resonant cavities are showed. At the end, advantages and limits of Nb/Cu cavities compared to bulk Nb cavities are highlighted.

1.1 Normal conductors and their limitation in RF

The anomalous skin effect is one of the main limitations of normal conductors in particle accelerator cavities. Because of it, increasing in metal purity and working at low temperature does not reduce the surface resistivity and the consequent current losses. To reduce R_S below the mΩ range for RF application we need superconductivity!

1.1.1 DC behavior: the Drude model

The Drude model provides an understanding of what conductivity is. The steady state solution is useful for RF application, where the RF period is much longer than the scattering time [11]. The model adapts the kinetic theory of gases to the conduction electrons in metals. In this model, the conduction electrons when traveling through a perfect crystal lattice, suffer no scattering. However, electrons do get scattered when they suffer frequent collisions with lattice imperfections, such as missing atoms, interstitial atoms and chemical impurities [12]. Another important source of scattering are phonons, but if the temperature is low enough, the number of thermally excited phonons is rather small compared to the number of impurities, so that impurity scattering is dominant. Between collisions, electron moves freely for a mean free time τ, called the relaxation time or scattering time. Probability of scattering within time interval dt is dt/τ.

From the Drude model we can obtain the following equation, called Ohm's law, for the conductivity in a metal:

$$j = \sigma E \qquad \textbf{Equation 1.1}$$

where σ is the DC electrical conductivity given by:

$$\sigma = \frac{ne^2\tau}{m}$$ **Equation 1.2**

Typically $\tau = 10^{-14}$ s from observed resistivity [12].

1.1.2 RF Behavior: skin effect and anomalous skin effect

For accelerator applications, the rate of oscillation of the Electro Magnetic field is in the order of radio frequency (RF) range (3 kHz-300 GHz). Combining the Drude Model and the Maxwell equations, it is possible to demonstrate that the RF electric field penetrates into normal conductor to a skin depth δ:

$$\delta = \sqrt{\frac{2}{\mu_0 \mu \sigma \omega}}$$ **Equation 1.3**

Qualitatively speaking, the surface currents in the skin of the metal, shield the bulk of metal from the electric field. Note that the skin depth decreases with increasing frequency. The surface impedance is defined as:

$$Z = \frac{|E_0|}{\int_0^\infty J(z)dz} = \frac{E_0}{H_0} = R_s + iX_s$$ **Equation 1.4**

The impedance has an imaginary part because the surface field is not in phase with the total current in the conductor, due to the rate of change of magnetic flux in the conductor. The real part, R_s gives the RF resistance, and the imaginary part, X_s gives the reactance. The RF surface resistance is thus:

$$R_s = X_s = \frac{1}{\sigma\delta} = \sqrt{\frac{\mu_0 \mu \omega}{2\sigma}}$$ **Equation 1.5**

At low temperature the σ(T) increases and δ decreases. The skin depth can become less than the mean free path of electrons and only the electrons that are traveling almost parallel to the surface (see Figure 1.1) participate to the conduction.

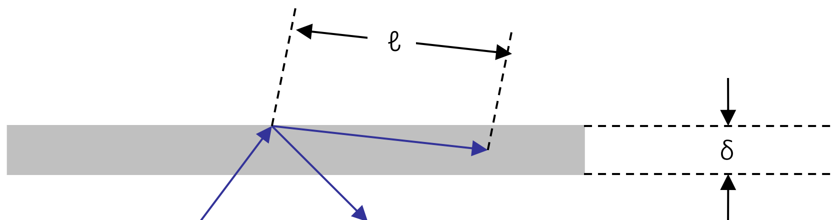

Figure 1.1 Only the electrons that are traveling almost parallel to the surface participate to the conduction.

Equation 1.1 is not valid anymore and it is necessary to introduce a new relationship where J is related to E over a volume of the size of the mean free path (ℓ). In that case, called anomalous skin effect, the effective conductivity is given by:

$$\sigma_{eff} = \frac{\sigma}{\ell} \qquad \textbf{Equation 1.6}$$

Contrary to the DC case, higher purity (longer ℓ) does not increase the conductivity. The implications are significant. When a copper cavity is cooled to low temperature, even if the dc conductivity increases by a factor 100, the largest improvement in surface resistance one can expect is only a factor of 6. From an economic point of view, this meager improvement is not enough to pay for the refrigeration cost [12].

1.2 Superconductivity

An ideal particle accelerator should provide high accelerating electric fields (E_{acc}) at minimum power consumption in a radio-frequency (RF) resonator cavity structure. Accelerating field, in existing particle accelerators, are typical in the order of $10–10^2$ MV/m. The limitation is mainly due to the cavity material parameters, so, increasing the energies of accelerated particles inevitably requires increasing the number (up to tens of thousands) of cavities. The necessity to reduce the power consumption in big machines brought about the idea of using superconducting RF resonating (SRF) cavities, proposed more than 50 years ago [13] [14].

1.2.1 SC Introduction: perfect conductivity and Meissner effect

Superconductivity was discovered in 1911 by H. Kamerlingh Onnes in Leiden [15], just 3 years after he had first liquefied helium, which gave him the refrigeration technique required to reach temperatures of a few Kelvin degrees [16]. What Kamerlingh Onnes observed, was that the electrical resistance of various metals such as mercury, lead, and tin disappeared completely in a small temperature range at a critical temperature T_c, which is characteristic of each material. In the pure metals of the periodic table, T_c would typically be below 10 K. As years went by, most, but not all, metals were found to be superconductors. Famous examples of non superconductors, paradoxically, were the best metals like gold, silver and copper. Soon, also a great variety of metallic alloys were found to possess the superconducting property. The complete disappearance of resistance is most sensitively demonstrated by experiments with persistent currents in superconducting rings [17]. Once set up, such currents have been observed to flow without measurable decrease for a year. Using nuclear resonance to detect any minimum reduction in the field produced by the circulating current, a characteristic decay time higher than 10^5 years has been established [16]. Perfect conductivity is the first traditional hallmark of superconductivity.

The second aspect of superconductors, discovered in 1933, came just as unexpectedly as the sudden loss of electrical resistivity in 1911 [18]. A piece of metal was first held in the normal state above Tc, while its entire body was permeated by an externally applied magnetic field from the solenoid in which it was located. The resulting magnetic field inside the sample was then very nearly the same as outside. The sample was then cooled through the critical temperature T_c. On passing

T_c, it was recorded that the magnetic field inside was suddenly and completely expelled. Hence, by lowering the temperature by just a small fraction of a degree, the material changed its magnetic character completely, from weakly paramagnetic above T_c, to a state of complete screening, with no magnetic field in the body below T_c, i.e. perfect diamagnetism. This must have been caused by the sudden creation of an opposing field, which exactly cancelled the applied field inside. This remarkable behavior, never observed before, is referred to as the Meissner effect [19].

For decades, a fundamental understanding of this phenomenon eluded the many scientists who were working in the field. Then, in the 1950s and 1960s, a remarkably complete and satisfactory theoretical picture of the classic superconductors emerged. Three principal theories describes the superconductors behavior:

- London Theory, based on Maxwell´s equations; phenomenological theory that can describe zero resistance and the Meissner effect [20].
- Ginzburg Landau Theory can describe non-local effects [21].
- Bardeen Cooper Schrieffer Theory (BCS Theory), the first microscopic theory of superconductivity, published 46 years after the discovery of superconductivity [22] [23].

The behavior of a superconductor immersed in a RF electro-magnetic field, instead, can be easily described by the Two Fluid Model of Gorther and Casimir.

1.2.2 Key parameters in BCS

This thesis is not supposed to present an exhaustive theoretical treatment of superconductivity, but just show and briefly explain the key parameters that play a role in the SRF.

1.2.2.1 Cooper pairs

In 1957 Bardeen, Cooper and Schrieffer published a theory of superconductivity in which an attractive interaction between electrons, forming “Cooper pairs” exists. This interaction occurs through the exchange of a lattice phonon. Size of a cooper pair is large compared to the lattice constant and is related to the coherence length ξ.

As a results of this interaction, a bound state with energy lower than $2E_F$ (Bose- Einstein condensation below T_c) exists. This bound state of the two electrons is energetically favorable. As the overall spin of these two paired electrons is zero, many of these pairs can co-exist coherently, just like other bosons. Within the BCS theory the energy gap can be calculated:

$$\Delta(0) = 1.764 k_B T_C \qquad \textbf{Equation 1.7}$$

For Nb Δ (0) = 1.55 meV [24]. The number of Cooper pairs is temperature dependent and only at T=0 K all conduction electrons are condensed into Cooper pairs. The superconducting electrons co-exist with their normalconducting counterparts. The number of normalconducting electrons, n_n is given by the Boltzmann factor:

$$n_n(T \to 0) \approx n_s(0) e^{\frac{\mu - \Delta(T)}{K_B T}} \qquad \textbf{Equation 1.8}$$

1.2.2.2 BCS coherence length and penetration depth

Coherence length ξ_0 can be defined as the interaction distance between electrons forming a Cooper pair. Pippard [25] introduced the concept of a coherence length while studying the nonlocal generalization of London's equation.

$$\xi_0 = \frac{\hbar v_f}{\pi \Delta(0)} \qquad \textbf{Equation 1.9}$$

where ħ is the Plank constant and v_f is the Fermi velocity. Typical values for the coherence length in niobium are around 39 nm [24].

Penetration depth, $\lambda(T)$ is the decay length of magnetic field in the superconductor. In the BCS theory it is temperature dependent and is related to the London penetration depth at 0 K, when all the electrons are condensed into Cooper pairs. London introduced this parameter to explain the Meissner effect [20]. He derived an exponential decay of the external magnetic field B_0 into the superconductor, along the x direction, normal to the surface:

$$B(x) = B_0 e^{-\frac{x}{\lambda_L}} \qquad \textbf{Equation 1.10}$$

where the London penetration depth is:

$$\lambda_L = \sqrt{\frac{m}{\mu_0 n_S e^2}} \qquad \textbf{Equation 1.11}$$

BCS introduces a different temperature dependence, but in physical terms it has the same meaning:

$$\lambda(T) = \frac{\lambda_L(0)}{\sqrt{1-\left(\frac{T}{T_C}\right)^4}} \qquad \textbf{Equation 1.12}$$

Typical values for the decay length in niobium are around 36 nm [24]. Adding impurities to a superconductor reduces the normal electrons mean free path, so that the electrodynamic response changes from "clean" ($\ell >> \xi$) to the "dirty" limit ($\ell << \xi$). Changes in the characteristic lengths of the SC can be approximated as:

$$\lambda(l,T) = \lambda(T)\sqrt{1+\frac{\xi_0}{\ell}} \qquad \textbf{Equation 1.13}$$

1.2.2.3 Surface resistance of superconductors

Superconducting currents are transported by Cooper pairs, formed by two electrons, that flow without friction (DC supercurrents are lossless). As said before, for temperature above 0 K, not all electrons form Cooper pairs. In RF fields, the time-dependent magnetic field in the penetration depth induces an electric field.

Because Cooper pairs have a finite inertia (mass=$2m_e$) they can not completely shield normal conducting electrons from this E-field. Normal electrons see this field, move and dissipate. There are several ways to derive a theoretical formula for the surface resistance in superconductors. The easiest is probably with the two fluid model, which qualitatively gives the same results of the treatment within BCS theory. Quantitatively they can differ by an order of magnitude.

Numerous experiments have shown that $R_s(T)$ can be described by the following semi empirical relation [12]:

$$R_s = \left(\frac{Af^2}{T}\right) exp\left(-\frac{\Delta}{k_B T}\right) + R_i \qquad \textbf{Equation 1.14}$$

The factor A depends on material parameters, like coherence length, electron mean free path, Fermi velocity and penetration depth. For niobium the factor A is about $9\text{x}10^{-5}$ ΩK/(GHz)^2. The appearance of a finite R_i is not predicted by the BCS theory, since it gives $R_s(T)\rightarrow 0$ at $T \rightarrow 0$.

1.2.2.4 Residual resistance

In the literature R_i was attributed to many causes. The principals are listed below [14].

- Dissipation caused by trapped vortices oscillating under the rf field [26];
- Lossy oxides or metallic hydrides on the Nb surface [12]. Hydrogen in the Nb cavities is usually absorbed during the standard buffer chemical polishing or electropolishing or machining, which dissolves or damages the passivating layer of dielectric pentoxide, Nb_2O_5, on the Nb surface.
- Grain boundaries. Experimental evidences of the contribution of grain boundaries to R_i have been inconclusive. In some papers the residual surface resistance of small grain Nb films was attributed to grain boundaries. In other works, on the contrary, it was shown that under proper heat treatment of sputtered Nb films, R_i can be reduced down to the level of ∼1−10nΩ, comparable to Ri of high-performance polycrystalline Nb cavities, and no significant dependence of R_i on the grain size was observed [14].
- Generation of hypersound or localized surface electronic states.
- Interface losses, surface roughness and absorption of noble gases on the Nb surface [27].

1.2.2.5 Type I and type II superconductors

When an external dc magnetic field H_{ext} is turned on, supercurrents flow in the penetration depth to cancel out the field in the interior. In a superconductor material, a thermodynamic critical field H_c exists, above which all the flux enters in the superconductor. The Ginzburg–Landau (GL) parameter, $\kappa_{GL} = \lambda/\xi$, defines two kinds of superconductors: type I superconductors with $\kappa_{GL} < 1/\sqrt{2}$ and type-II superconductors with $\kappa_{GL} > 1/\sqrt{2}$.

Type I-superconductors remain in the Meissner state until the critical field H_c is reached which forces the material into the normal state.

Type II-superconductors have three phases: the Meissner, mixed and normal states. They are characterized by two critical fields:

- The lower critical field H_{c1} at which the material passes from a complete Meissner state to the mixed state.

- The upper critical field H_{c2} above which the material becomes fully normal.

The mixed state (called also vortex state) is characterized by a partial penetration of magnetic flux in a complicated microscopic structure of thin normal conducting filaments, called vortexed, surrounded by superconductive regions. A current crossing the superconductor will act on vortex with a Lorentz force, causing its moving and consequently dissipative forces an heat generation.

Clean Nb is a marginal type-II superconductor with $\lambda \approx \xi \approx 40$ nm. At zero temperature, $H_{c1}^{Nb} = 170$ mT, $H_{c2}^{Nb} = 240$ mT.

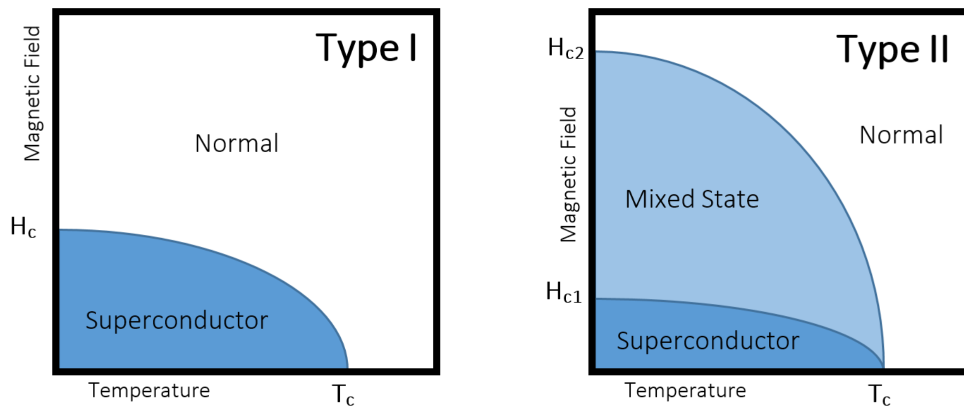

Figure 1.2 Different behavior of type I and type II superconductors in a magnetic field

1.2.2.6 Superheating field

Penetration and oscillation of vortices under the rf field give rise to strong dissipation, However, the Meissner state can remain metastable at higher fields, $H > H_{c1}$ up to the superheating field H_{sh} at which the Bean–Livingston surface barrier for penetration of vortices disappears and the Meissner state becomes unstable. Thus, H_{sh} is the maximum magnetic field at which a type-II superconductor can remain in a true non dissipative state, not altered by dissipative motion of vortices.[14]

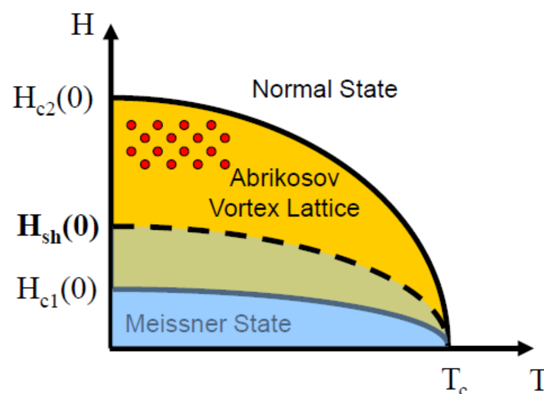

Figure 1.3 the Meissner state can remain metastable at higher fields, $H > H_{c1}$ up to the superheating field H_{sh}

1.3 Resonant Cavity Fundamentals

A key component of the modern particle accelerator is the device that imparts energy to the charged particles. This is an electromagnetic cavity. The ultimate purpose of an electromagnetic cavity resonating at a microwave frequency is just this: to provide longitudinal acceleration to a beam of charged particles.

1.3.1 Basic principle and key parameters in Resonant Cavities

In the picture below, the beam acceleration process on a pill box cavity is schematized.

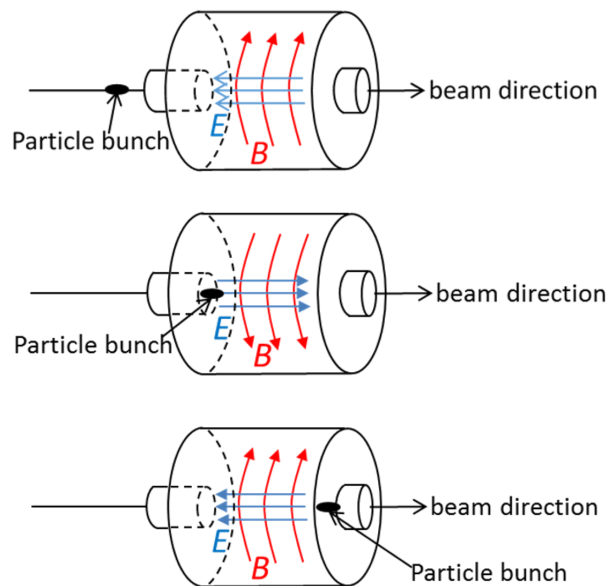

Figure 1.4 Electric and magnetic electric fields in a pill box cavity during the acceleration process, schematized in three phases [11].

The reason why superconducting material is very attractive for the accelerating cavities, is very easy to understand, qualitatively, just looking at that picture. The alternating electric field used to accelerate particles causes an alternating magnetic field. The cavity confines the electromagnetic fields by surface shielding currents that create losses (heating). The losses at the cavities wall can be reduced by using superconducting materials instead of normal conductor materials.

There are three major classes of superconducting accelerating structures: high, medium, and low- β (here β =v/c, where v is the speed of the accelerated particle and c is the speed of light). The high- β structure, based on the TM010 resonant cavity, is for acceleration of electrons, positrons, or high-energy protons with β ~1. The cavity gap length (cell length in the elliptical cavities) is usually βλ/2, where λ is the wavelength corresponding to the frequency choice for the accelerating structure. A typical high-β accelerating structure consists of a chain of coupled cells operating in the TM010 mode, where the phase of the instantaneous electric field in adjacent cells is shifted by π to preserve acceleration as a charged particle traverses each cell in half an rf period. Single-cell cavities are generally used for SRF R&D, but also find accelerator applications [28]. In Figure 1.5 the structure of an elliptical high-β resonant cavity like the ones used in this work is schematized.

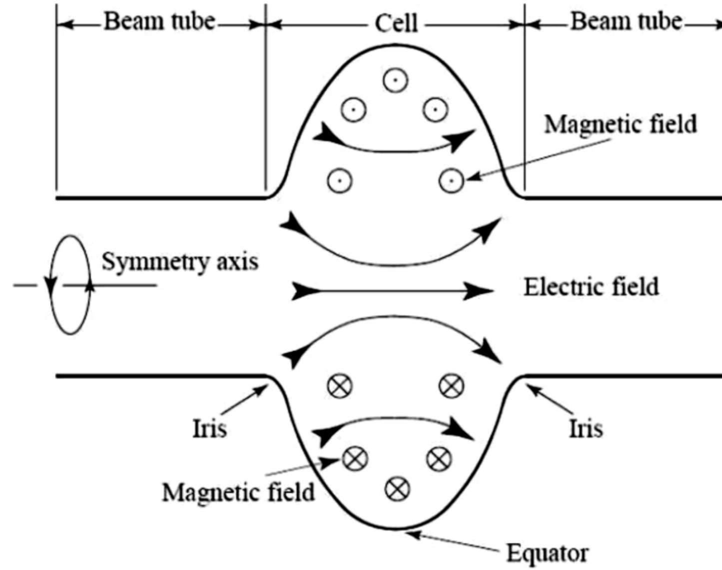

Figure 1.5 Elliptical cavity description [29].

The beam enters and exits the structure from the beam tubes. Input coupler devices attached to ports on the beam tubes bring rf power into the cavity to establish the field and deliver beam power; higher order mode couplers extract and damp the higher order modes (HOMs) excited by the beam, and smaller ports carry pick-up probes to sample the cavity field for regulation and monitoring.

1.3.1.1 Key parameters in Resonant Cavities

To evaluate the resonant cavities performance we measure the Quality Factor Q_0 as a function of the cavity accelerating field level. The accelerating field is defined as following:

$$E_{acc} = \frac{V_{acc}}{d} \qquad \textbf{Equation 1.15}$$

where V_{acc} is the accelerating voltage to which a particle with charge e is subjected while traversing the cavity and d is the cell dimension of the resonant cavity. The Quality Factor Q_0 is related to the power dissipation and is defined as:

$$Q_0 = \frac{\omega_0 U}{P_d} \qquad \textbf{Equation 1.16}$$

where U is the stored energy and P_d is the power dissipated in the cavity walls. The Q_0 is roughly 2π times the number of rf cycles it takes to dissipate the energy stored in the cavity. Since the time averaged energy in the electric field equals that in the magnetic field, the total energy in the cavity is given by:

$$U = \frac{1}{2}\mu_0 \int_V |H|^2 \, dv = \frac{1}{2}\varepsilon_0 \int_V |E|^2 \, dv \qquad \textbf{Equation 1.17}$$

where the integration is taken over the volume of the cavity. The dissipated power can be expressed as follows:

$$P_d = \frac{1}{2} R_s \int_S |H|^2 \, ds \qquad \textbf{Equation 1.18}$$

where the integration is taken over the interior cavity surface, assuming the surface resistance (R_s) constant in the cavity surface. Q_0 can now be rewritten as:

$$Q_0 = \frac{\omega_0 \mu_0 \int_V |H|^2 dv}{R_s \int_S |H|^2 ds} \qquad \textbf{Equation 1.19}$$

Q_0 is frequently written as:

$$Q_0 = \frac{G}{R_s} \qquad \textbf{Equation 1.20}$$

where G is called **geometry constant**. The shunt impedance is another import quantity used to characterize the losses in a cavity and is defined as follows:

$$R_A = \frac{V_{acc}^2}{R_s} \qquad \textbf{Equation 1.21}$$

1.3.2 Q_0 VS E_{acc} curve and principal limitations in SRF cavities

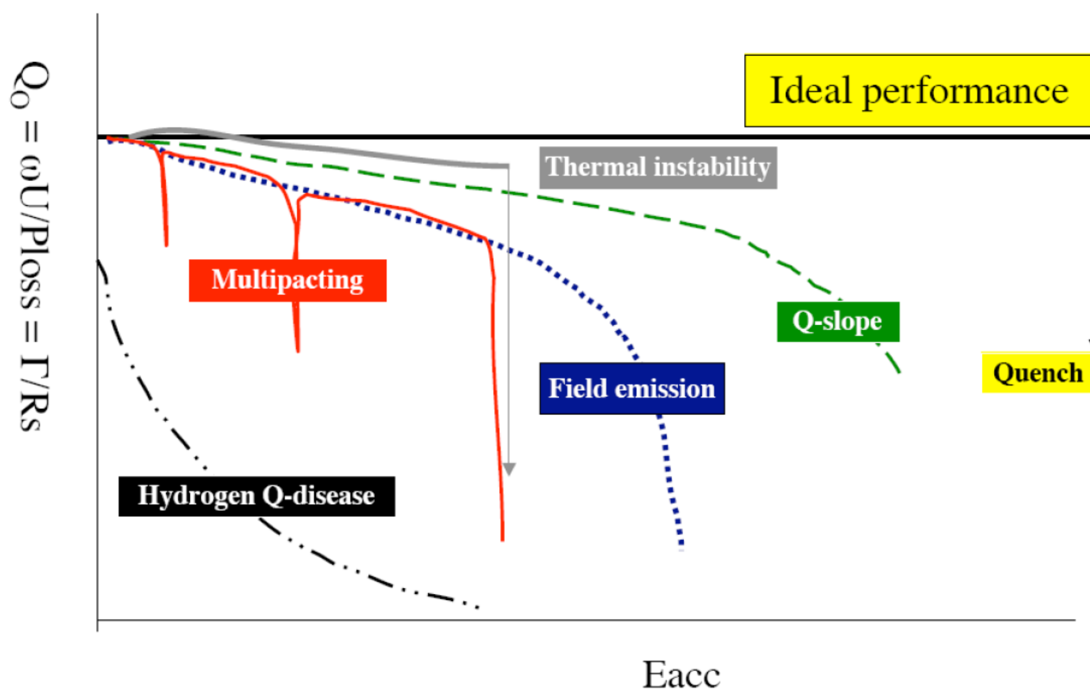

Figure 1.6 Principal limitation in a superconducting resonant cavity [1]

The above picture shows as a Q_0 VS E_{acc} curve for SRF resonant cavities looks like. In the ideal case, le line is almost horizontal, but in the real case, different causes limit the accelerating gradient and move out the curve from ideality.

1.3.2.1 Q-slope

The observed Q of a niobium cavity is not flat, but shows several interesting features with increasing field. In the low-field region the Q increases [30], a surprising effect, named the "low-field Q-slope." Mild baking (100–120 °C for 48 h) generally enhances the low-field Q-slope. At medium fields the gradual Q fall is called the "medium-field Q-slope" [30] and is a common feature of all niobium cavities. The medium-field Q-slope is generally attributed to a combination of surface heating and nonlinear BCS resistance. Baking generally (but not always) decreases the medium-field Q-slope. Medium Q-slope is higher in Nb/Cu resonant cavities than in bulk cavities. Finally, there is a strong Q-drop at the highest field. Eventually superconductivity quenches either due to a thermal instability initiated by local heating at a defect, or a phase transition at the local rf critical magnetic field.

1.3.2.2 Thermal Breakdown

The prevailing model of thermal breakdown (quench) states that heating originates at submillimeter-size regions of high rf loss, called defects. When the temperature of the good superconductor just outside the defect exceeds the superconducting transition temperature, T_c, rf losses increase considerably, as a growing region becomes normal conducting leading to rapid loss of stored energy called "quench."[28]

1.3.2.3 Multipacting

In rf resonant cavities, stray electrons can hit the cavity surface, creating secondary electrons. The secondary electrons, which in turn, can be accelerated by rf fields, absorb the rf energy and hit the wall surface to create more secondary electrons. When these secondary electrons happen to hit the same area, the absorbed rf energy heats the surface, thus creating a local hot spot. This not only limits the accelerating gradient, but also creates more rf surface loss, even leading to a possible thermal quench. By adjusting the resonant cavity shape, the multipacting can be reduced but it can not be completely eliminated.

1.3.2.4 Field emission

Another important phenomenon limiting the E_{acc} from reaching its maximum, is field emission. When the accelerating gradient exceeds 10 to 20 MV /m [12], field emission can appear and in this case the Q_0 of a niobium cavity starts to fall exponentially. In the presence of a high surface electric field, RF power is lost to electrons that tunnel out of the cavity wall at very localized points. The emitted electrons are accelerated by the electromagnetic fields and, upon impact, heat the cavity wall and produce X-rays. Field emission scales exponentially with the electric field and, like the multipacting phenomenon, it absorbs a huge amount of rf power. Microparticle contaminants are the dominant emission sources [12]. Increased vigilance in cleanliness during final surface

preparation and assembly procedures is important to keep particulate contamination and associated emission under control [28].

1.3.2.5 Hydrogen Q-disease

If the cooling-down speed is slow, the precipitation of the dissolved hydrogen occurs around 100 K and this increases the surface resistance of a niobium cavity. This phenomenon is called "hydrogen Q-disease" and it was well studied around 15 years ago [31].

1.4 Niobium on Copper Cavities

RF cavities are made either of normal conducting materials (most commonly water-cooled copper operating near room temperature), or of superconducting materials (most commonly niobium operating at cryogenic temperatures cooled by liquid helium). As already seen before, superconducting materials have the advantage of having much smaller surface resistance R_s, reducing the RF dissipation in the walls of the cavity by a factor of approximately 10^6 compared to similar normal conducting cavities. This allows SRF cavities to operate at high fields in continuous wave mode (meaning that the RF power is continuously applied with a 100% duty factor) in a stable manner whereas similar copper cavities would overheat and melt if operating CW at these fields [12]. The standard material for SRF cavities is niobium, either in bulk form, or as film on a copper substrate.

1.4.1 Niobium

Table 1.1 Physical and superconducting parameters for niobium

Parameter	Symbol	Value	Unit
Crystalline lattice	-	b.c.c.	-
Reticular parameter	a	3,3033	-
Electrical resistivity (300K)	ρ_n	14,9	(μΩ cm)
Thermal conductivity (300K)	Λ	53,7	(W m^{-1} K^{-1})
Density	D	8570	(kg m^{-3})
Melting Point	T_m	2741	(K)
Critical temperature	T_c	9,23	(K)
Critical field	H_c	0,2	(T)
Lower critical field	H_{c1}	0,18	(T)
Upper critical field	H_{c2}	0,28	(T)
London Penetration Gap	λ_L	40	(nm)
Coherence Length	ξ	35	(nm)
Energy Gap	Δ	1,5	(meV)

For the past five decades, bulk niobium (Nb) has been the material of choice for superconducting rf (SRF) applications such as accelerating cavities for particle accelerators. The primary reason is that Nb has the highest critical temperature (T_c = 9.23 K) and the highest lower

magnetic field H_{c1} of all the pure metals. In addition, it is relatively simple to use in terms of fabrication. Many compounds (including the new high-T_c ceramic materials) have shown higher critical temperatures than Nb. However, at present, none of these materials can match Nb in terms of its performance with increasing RF fields or its ease of use for accelerator applications [32].

1.4.1.1 The Residual Resistivity Ratio (RRR)

For Niobium, a common indicator of the level of purity is the residual resistance ratio, RRR, also called triple-R. The main interstitially dissolved impurities, oxygen, nitrogen, hydrogen and carbon (O, N, H, C), act as scattering centers for unpaired electrons and reduce the *RRR*. [33] Oxygen is dominant due to its high affinity to Nb.

The *RRR* is defined as the ratio:

$$RRR = \frac{\rho(300K)}{\rho(4.2K)} \qquad \textbf{Equation 1.22}$$

where $\rho(300\ K)$ and $\rho(4.2\ K)$ are the resistivity of Nb at room and liquid helium temperatures, respectively, at standard atmospheric pressure. The superconducting behavior of Nb has to be taken into account for *RRR* determination. In this particular case, the low temperature resistivity is defined as the normal-state value extrapolated at 4.2 K, but this value does not differ much from the 10 K value.

For bulk Nb cavities normally RRR>300, instead Nb sputtered thin films generally have low values of RRR. For example LHC cavities have RRR around 10 [34].

1.4.2 Niobium Bulk Cavities

The RF performance of bulk Nb cavities has continuously improved over the years and it is approaching the intrinsic limit of the material ($H \sim H_c$ = 200 mT). SRF researchers have been developing preparation methods for niobium cavities that avoid many non fundamental limitation mechanisms. The principal methods developed are: high pressure rinsing (HPR) with purified water to clean surfaces and prevent field emission, electropolishing for extremely smooth surfaces, 120°C baking to avoid high field Q-slope (HFQS), and nitrogen doping to increase Q_0.

However, Nb bulk cavities remain very expensive and the use of substrates with higher thermal conductivity could also lead to substantial cost reduction in cryomodules.

1.4.3 Motivations for Niobium on Copper Cavities

The rf dissipation results in a thin layer (∼100 nm) determined by the London penetration depth λ, over which a low-frequency magnetic field penetrates in a superconductor (for the cavity-grade niobium, λ ≈ 40 nm at 2K). The materials and superconducting properties of this thin layer (much thinner than the 2–3-mm-thick cavity wall) at the inner cavity surface controls the SRF performance. These reasons pushed Cris Benvenuti at CERN in the 1980s to develop the Nb/Cu technology [2], where just several microns of Nb are grown on the internal surface of a copper resonant cavity. Superconducting Nb/Cu cavities produced by the sputtering technology have been successfully exploited at CERN with LEP-II II (352 MHz, 4 K) [3] and LHC (400 MHz, 4 K) [4]. This

technology is also employed in several other present and future accelerator facilities, such as ALPI (INFN-LNL) [5] and HIE-ISOLDE (CERN) [6].

Nb films show clear advantage compared to bulk Nb for defined accelerator parameter sets, in particular for low frequency cavities or for operation at 4.2 K. The BCS surface resistance for thin films is lower than for bulk Nb, due to a normal state electrical resistivity close to the theoretical optimum (see Figure 1.7). The principal advantages of Nb/Cu cavities are listed below.

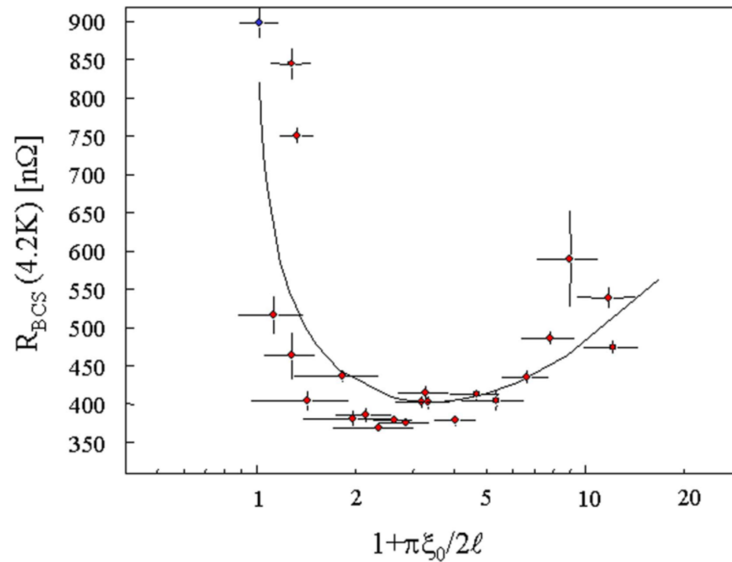

Figure 1.7 The BCS surface resistance at 1.5 GHz as a function of Nb purity. The abscissa is equal to 1 in the limit of electron mean free path $\ell\rightarrow\infty$ [27]

Thermal stability

High purity bulk Nb has a typical heat conductance of about 75 W m^{-1} at 4.2 K, while Cu heat conductance is as high as 300–2000 W m^{-1}. Thus, the amount of heat generated by a defect inside a superconducting cavity (typically 10 mW for a 40 mT rf magnetic field in the area of a 50 µm size defect) can be more easily conducted to the helium bath in the case of a Cu cavity substrate. A thermal breakdown model for defects in a resonant cavity [15] allows simulations which accurately illustrate the effect of the defect size and the Nb purity level (represented by RRR, residual resistivity ratio). The large thermal conductivity of Cu helps the thin film cavity to be more resistant to multipacting and field emission.

Low cost

The cost of Cu material is only about 10% of the cost of bulk Nb. This is especially advantageous for accelerators operating at low frequencies since the dimensions of the cavities are inversely proportional to their operating frequency. The cavity manufacturing cost associated with Cu can also be substantially lower than with bulk Nb. Decoupling the SRF surface (Nb film) from its substrate can also open the way to significant simplifications in cryomodule design, thus affecting the building cost.

Insensitivity to Earth magnetic field trapping.

One source of residual resistance in the Nb surface is trapped magnetic flux. Nb films have shown an unexpected advantage, in which their surface resistance is almost insensitive to the Earth's magnetic field, eliminating the need of complex cavity magnetic shielding [7, 16]. The effect of the Earth's magnetic field is 100 nW Gs−1 of external magnetic field for bulk Nb, and only 1 nW Gs−1 for Nb films.

Freedom from undissolved inclusions.

Due to the manufacturing process (pressing, rolling and melting, etc.), the Nb sheet or the Cu sheet usually present micro-inclusions, typically elements such as steel, nickel and some oxide compounds. Though not necessarily a cause of decrease of the metal sheet RRR, they can be distributed deep inside the material and can be uncovered with etching. Such inclusions occur during the cooling process by precipitation of some compound dissolved in the molten Nb and present in amounts exceeding the solubility. Although these inclusions content can be well controlled, the resulting added process steps do increase the cost for raw bulk material as well as the cost for extra processing during cavity manufacturing. Additionally, inclusions are very easily introduced into bulk Nb from machining tools [17]. In general, vacuum deposition of thin film is known to produce excellent surface quality in many applications.

1.4.4 Principal limitation in Niobium Copper Cavities: the Q-slope

The Nb on Cu cavities, despite the advantages over the Nb bulk cavities, have limited use in particle accelerators, because thin film cavities present a severe Q decay problem, with the Q quasi-exponentially decreasing as a function of the RF injected power, at T below 2K. This Q-degradation caused by the increased external RF field actually exists in both bulk Nb and in thin film cavities but for the latter, it limits the cavity operation to relatively low field. Figure 1.8 schematically shows this fact. In bulk niobium cavities the Q-factor is almost constant versus field, whereas for niobium sputtered film cavities, the Q-value is higher than a bulk cavities at low field, but it rapidly decays versus the accelerating field. In Figure 1.9 real data on the best 1.5 GHz thin film cavities are reported. The cavity shows indeed a very high Q-factor, but still a significant Q-slope and at high accelerating fields all the curves converge at the same Q values.

During these decades, several models and theories have been proposed in order to explain the Q-slope (or Q-drop) mechanism, but the reason underlying the strong decay of the Q-factor versus the accelerating field in thin film cavities is still unknown. We can only say with confidence that it is enclose in the residual term of the surface resistance, since the BCS component of the surface resistance reduces exponentially with temperature and, below 2 K, the residual term is dominant.

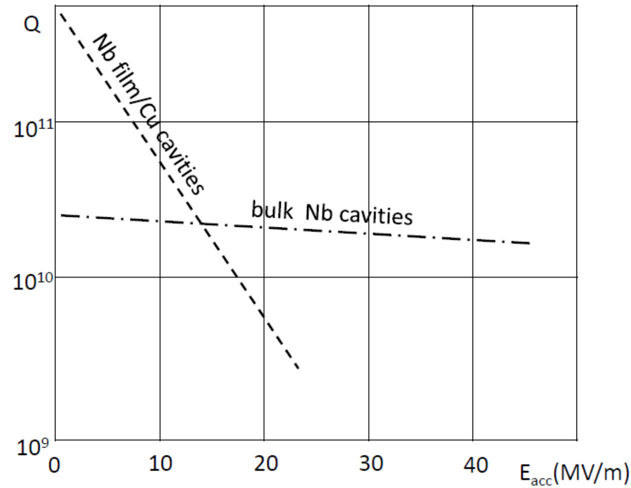

Figure 1.8 Q-factor versus the accelerating field for Nb film sputtered cavities compared to bulk niobium cavities. Typical behavior is schematically reported for 1.3 - 1.5 GHz CERN cavities at low temperatures (1.7-1.8K).

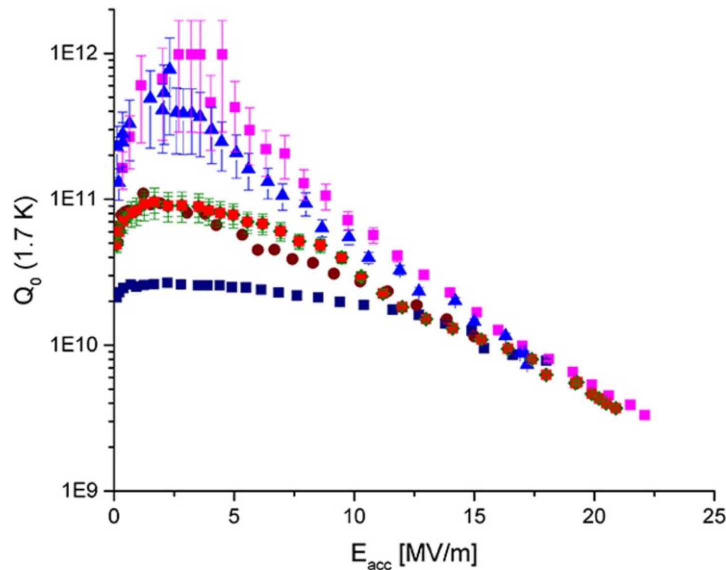

Figure 1.9 Best RF performance at 1.7 K for several 1.5 GHz Nb/Cu cavities sputtered coated with Kr at CERN [22]. The symbols correspond to individual Nb films.

The main actors accused of being the cause of Q-drop, are:

Roughness.

Thin films typically replicate the morphology of the substrate they are deposited on. Thus, the roughness of the substrate has a strong influence on the roughness of the film [32]. Studies were performed with different substrate roughness (hydroformed, spun and electroplated Cu cavities), showing that the smoother substrates led to lower residual losses. A further improvement of the residual losses was achieved by adopting electropolishing which yields a smoother surface finish [18] [23].

Impurities

A certain number of impurities can be found in Nb sputtered films, mainly due to the deposition process and the affinity of Nb for O and H. These impurities can be present as scattering centers and thus induce RF losses. A deep study on the amount of gas imbedded in the Nb growing films was done at CERN in the past [35].

Inter-grain losses

Another potential source of RF losses is inter-grain losses, a basic effect for fine-grained superconductors. However, larger grain sizes do not seem to have any effect in decreasing the Q-slope [32].

1.4.5 A new cause for the Q-slope: the Nb/Cu interface (and the thermal boundary resistance model)

In summary, though the whole mechanism described before to justify the Q-slope is possibly at work in real cavities, there has been no strong experimental evidence that really convinced the superconducting accelerating cavity community in favor of a specific one as the main actor. At the same time, all experimental attempts to reduce the Q-slope in thin film cavities by improving the film quality essentially failed.

A recent paper [10] considers the hypothesis that the Q-slope is related to local enhancement of the thermal boundary resistance at the Nb/Cu interface, due to poor thermal contact between film and substrate. The authors shows how bad Nb/Cu adhesion due to voids, or other mechanisms as powder inclusions, can create thermal defects, locally increasing up to high values the interface thermal boundary resistance. Due to the small film thickness the heat is not efficiently dissipated at the defect location, locally producing a temperature increase (at high incident power, the local temperature can overcome the critical temperature T_c).

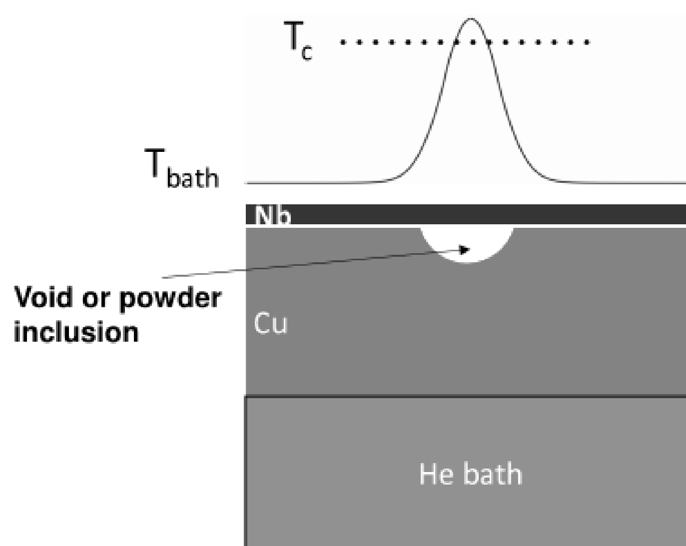

Figure 1.10 Model for an isolated thermal defect at the Nb/Cu interface, and relative local temperature profile [36].

Summarizing, the presence of a large interface thermal resistance $R_{Nb/Cu}$ locally affects the value of the surface resistance R_s through the thermal feedback mechanism. The model assumes that the thermal resistance is only due to the interface thermal resistance $R_{Nb/Cu}$ and obtains a function for the Nb surface resistance R_s that depends on T_0 (the helium bath temperature), E_{acc} and $R_{Nb/Cu}$. The measured cavity quality factor Q is then related to the average value of R_s as follows:

$$\overline{R_s(T_0, E_{acc})} = \int_0^\infty R_s(T_0, E_{acc}, R_{Nb/Cu})\, f(R_{Nb/Cu}) dR_{Nb/Cu} \qquad \text{Equation 1.23}$$

From the rf test curve we know Q (E_{acc}) and remembering the relation of page 12, we can calculate $R_s(T_0, E_{acc})$:

$$Q_0 = \frac{G}{R_s(T_0, E_{acc})} \qquad \text{Equation 1.24}$$

For the interface thermal resistance two more relations can be written:

$$\overline{R_{Nb/Cu}} = \int_0^\infty R_{Nb/Cu}\, f(R_{Nb/Cu}) dR_{Nb/Cu} \qquad \text{Equation 1.25}$$

Where $\overline{R_{Nb/Cu}}$ is the average value of the interface thermal resistance, and of course:

$$\int_0^\infty f(R_{Nb/Cu})\, dR_{Nb/Cu} = 1 \qquad \text{Equation 1.26}$$

With well known inverse problem methods it is possible to extract $f(R_{Nb/Cu})$. The results showed that f is well described by a power law dependence of the form:

$$f(R_{Nb/Cu}) = \alpha R_{Nb/Cu}^{-\beta} \qquad \text{Equation 1.27}$$

The fractional area of the detached surface, can be defined as:

$$I_d = \int_0^\infty f(R_{Nb/Cu})\, dR_{Nb/Cu} \qquad \text{Equation 1.28}$$

$R^{min}_{Nb/Cu}$ is the minimum “measured” value of $R_{Nb/Cu}$, corresponding to the maximum measured value of the accelerating field E_{acc}. Below this value the $R_{Nb/Cu}$ behavior is unknown. The values of I_d reported were of the order of 10^{-3} - 10^{-4}. This showed how it is sufficient to assume that a very small fraction of the overall cavity surface presents adherence problems to explain the quite large Q-slope observed in thin film cavities. At CERN [37], measurement of the inner cavity surface temperature does not show any increment due to RF power. The estimated very low values of the interface thermal boundary resistance $R_{Nb/Cu}$ are in agreement with the experimental results.

2 Sputtering generalities and state of the art on Nb/Cu cavities

In this chapter the general concepts relating to sputtering are treated with a focus on magnetron sputtering, the deposition technique used in this work for the niobium film growth on 6 GHz copper cavities. The state of the art on the niobium copper deposition technique for accelerator cavities is also shown and discussed.

2.1 Introduction

Sputtering is a mature, widely used deposition technology for thin films deposition, part of the main class of PVD processes. PVD, acronym of Physical vapor deposition, often just called thin film processes, are atomistic deposition processes in which material is vaporized from a solid or liquid source in the form of atoms or molecules and transported in the form of a vapor through a vacuum or low pressure gaseous (or plasma) environment to the substrate, where it condenses [38]. Typically, sputtering technique is used to grow films with thicknesses in the range of a few nanometers to several micrometers; however, it can also be used to form multilayer coatings and very thick deposits as in this work.

W.R Grove was the first to study what came to be known as “sputtering” in 1852, although others had probably previously noted the effect while studying glow discharges [39]. The first reported film coating by sputtering was by Wright in 1877 and in 1904 Edison patented a sputter deposition process for depositing gold on wax photograph cylinders [38]. However sputter deposition was not widely used in industry until the 1970s, when commercially viable device solutions became available [40]. In late 1980s, Cris Benvenuti applied the sputtering deposition onto the SRF cavities for LEP-II particle accelerator at CERN and today the sputtering remain the principal technique for the production of Nb/Cu cavities.

2.2 Physics of sputtering process

André Anders wrote this simple definition about sputtering: “it is the process of removing surface atoms from a target by particle (usually ion) bombardment. The liberated surface atoms

can move to a surface to be coated, the substrate, and may condense there, thereby contributing to form a solid (thin) film or (thick) coating" [40]. Physical sputtering is a non-thermal vaporization process where surface atoms are ejected from the target by momentum transfer from the gaseous ions, accelerated from a plasma [38]. A schematic illustration of the process is visible in Figure 2.1.

The ion energy is more than about 30 eV, the sputtered atoms leave the target surface with relatively high energies (~10 eV) compared to evaporation atoms (~0.1 eV).

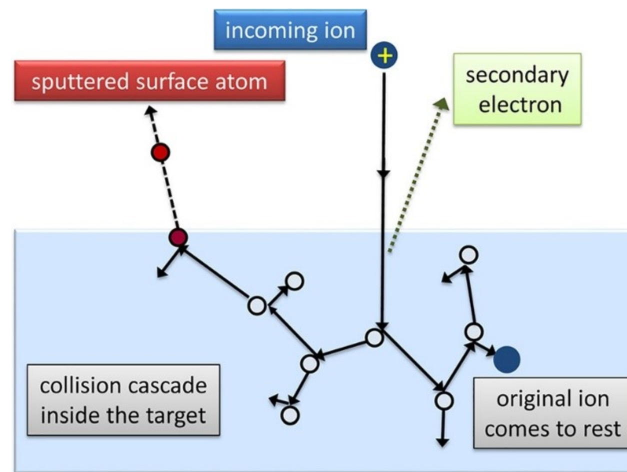

Figure 2.1 Schematic illustration of the sputtering process: A collision cascade is triggered inside the target, caused by an energetic ion, knocking off one or more surface atoms. Besides surface atoms, secondary electrons may also be emitted [40].

2.3 Plasma generation

The plasma in the sputtering process is generated by the application of a sufficiently high DC voltage between metal electrodes immersed in a low-pressure gas in order to ionize the neutral gas atoms (usually argon or krypton). In this paragraph the ionization process will be described, as well as the principal discharge regime, and the Paschen curves will be introduced.

2.3.1 The gas ionization: Townsend discharge

The process starts when a stray electron is accelerated toward the anode by the applied electric field. After gaining sufficient energy, the electron impacts with a neutral gas atom extracting a second electron and converting the neutral gas atom into a positively charged ion (A^+). The ionization process can be summarized with the following equation:

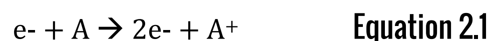

$$e^- + A \rightarrow 2e^- + A^+$$ **Equation 2.1**

Note that mass and charge conservation are respected. The two electrons are now accelerated and bombard two additional neutral gas atoms, generating more ions and electrons in an avalanche process. Meanwhile, the electric field drives ions in the opposite direction where they collide with the cathode. The collision generates, at the same time, a lot of processes (see Figure 2.1) including

sputtering of the target atoms and secondary electrons that participate to the charge multiplication process. A sufficiently large avalanche current ultimately causes the gas to breakdown.

In order for breakdown to occur, the distance *(d)* between electrodes must be large enough to allow electrons to reach the necessary energy for an ionization cascade. Townsend equation describes mathematically the ionization process [41]:

$$i = i_0 \frac{e^{\alpha d}}{[1-\gamma_e(e^{\alpha d}-1)]} \qquad \textbf{Equation 2.2}$$

Where i_0 is the initial current; α represents the probability per unit length of ionization occurring during an electron-gas atom collision and is called Townsend ionization coefficient; γ_e is the Townsend secondary-electron emission coefficient and is defined as the number of secondary electrons emitted at the cathode per incident ion.

For practical purpose it is very useful to know the *breakdown voltage*, the voltage value between the two electrodes at which the breakdown process occurs. Relating the mean free path to the ionization probability α, the critical breakdown voltage can be calculated with a bit of algebra, and expressed in terms of a product of pressure and interelectrode spacing. The result, known as *Paschen's Law*, is expressed by:

$$V_B = \frac{APd}{ln(Pd)+B} \qquad \textbf{Equation 2.3}$$

where *A* and *B* are constants. The Paschen curve, a plot of V vs P·d, is shown in Figure 2.2 for different gases, including Argon, the one used for this work.

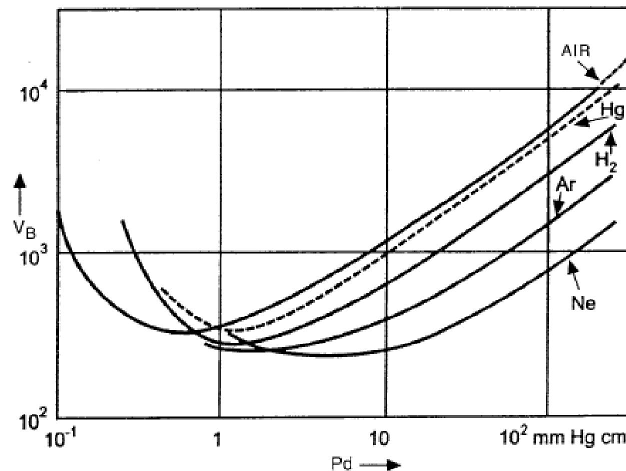

Figure 2.2 Paschen curve for a number of gases.(CIT A. Von Engel, Ionized Gases, Oxford university press 1965)

Typical sputtering configuration presents fixed distance between the electrodes. It is easy to note, looking the Paschen curve, that there is a minimum in voltage to sustain the discharge. The reason is easy to understand: at low values of pressure, there are few gas atoms for the electron-gas collisions and the secondary electron yield is too low to sustain ionization in the discharge. On

the other hand, at high pressures, there are frequent collisions, and electrons mean free path is too short to acquire sufficient energy and the gas ionization is quenched. Similar consideration can be done for the cathode-anode distance *d.* Therefore at either extreme of the Paschen curve, ion generation rates are low and high voltages are required to sustain the discharge. In between, at typically a few hundred to a thousand volts, the discharge is self-sustaining.

2.3.2 The sputtering regime: the abnormal glow discharge

Figure 2.3 represent the progress of a glow discharge in a low- pressure gas using a high-impedance DC power supply. In the regime just considered, the Townsend discharge, a very small current initially flows due to the small number of ions generated in the system. With charge multiplication, the current increases rapidly, but the voltage remains constant. Eventually, when electrons produce a number of ions large enough to regenerate the same number of initial electrons, the discharge becomes self-sustaining. At this point the voltage drops accompanied by a sharp rise in current and *normal glow* occurs. Initially, ion bombardment of the cathode is not uniform but concentrated near the cathode edges or at other surface irregularities. As more power is applied, the bombardment increasingly spreads over the entire surface until a nearly uniform current density is achieved [41]. A further increase in power results in both higher voltage and cathode current-density levels. The *abnormal discharge* regime has now been entered and this is the operative domain for sputtering and other discharge processes such as plasma etching. Further increasing the current, the cathode does not dissipate the heat anymore. Now thermionic emission of electrons exceeds that of secondary-electron emissions and low-voltage arcs propagate.

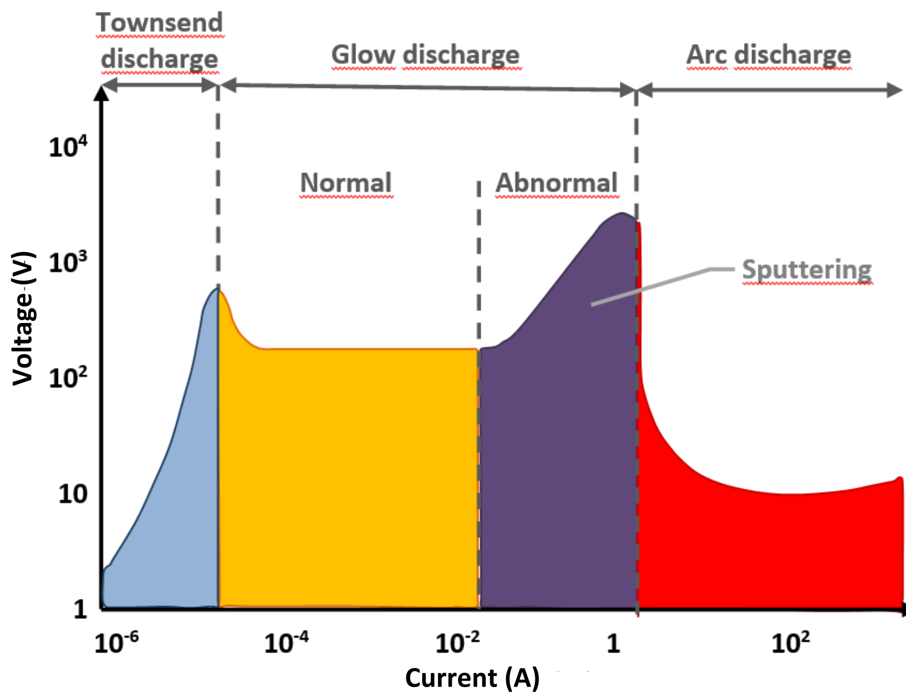

Figure 2.3 Characteristic I-V curve of an electrical discharge in vacuum.

2.4 Film growth

The film growth, as well as the nucleation mode, determines many film properties such as film density, surface area, surface morphology, and grain size. Important aspects of film growth are:

- surface roughness;
- surface temperature [42];
- adatom surface mobility;
- geometrical shadowing effects (angle-of-incidence effects) [43];
- reaction and mass transport during deposition, such as segregation effects and void agglomeration;

Surface morphologies may vary from very smooth (e.g. glass surface) to very rough. Generally, as the film grows, the surface roughness increases, because some features or crystallographic planes grow faster than others [38]. Atomically deposited films generally exhibit a unique growth morphology, that look like logs or plates aligned and piled together, and called a columnar morphology. This morphology develops due to geometrical effects and it is found whether the material is crystalline or amorphous. Generally, the columns are not single crystal grains but amorphous or polycrystalline. Energy of the adatom on the surface can modify the film structure from columnar morphology to a more dense morphology or with larger grains. The film morphology can be described by a structure zone model (SZD), introduced in 1969 by Movchan and Demchishin [44] for very thick films growth by evaporation, where only the effect of the homologous temperature T_h was took into account.

$$T_h = \frac{T}{T_m} \qquad \textbf{Equation 2.4}$$

Where T_m is the material melting point. The concept of an SZD evolved over the years as PVD technology expanded from evaporation to sputtering first, and later to ion beam assisted deposition, HIPIMS, etc. To describe better the SZD for the magnetron sputtering technique, Thornton introduces also the dependence on pressure. This SZD has become a classic and is reproduced in many textbooks on PVD.

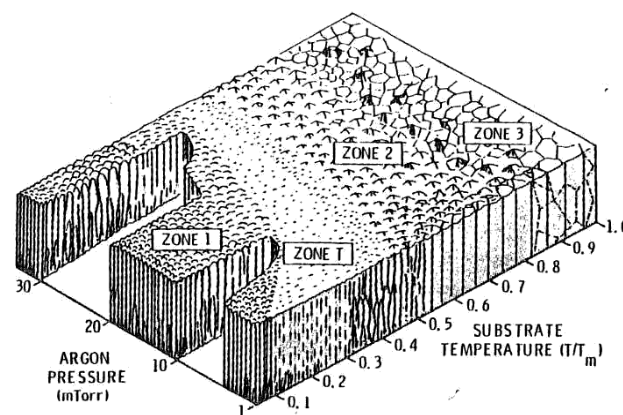

Figure 2.4 Structure zone diagram (SZD) proposed by Thornton. Substrate temperature and process pressure influence the film morphology [42].

Temperature influences the adatom mobility. Increasing T_h bulk diffusion and recrystallization are possible and change drastically the film structure. The sputtering pressure influences the kinetic effects of particle impingement on film growth [8]. At low pressure, the collision between sputtered particles and gas atoms are almost quenched. Sputtered atoms have typically several eV of kinetic energy, which is enough for the adatom rearrangement process on the surface. On the other side, at high pressure, the sputtered atoms suffer collisions with the process gas before arriving at the growth surface, and their distribution function is shifted to much lower energies [10]. In Figure 2.4 the original Thornton SZD is reported.

In 2010 [45], in order to develop an SZD that is as universal as feasible, Anders proposed to extend and modify the Thornton SZD by maintaining the number of process axes but generalizing their meaning. The changes are the following:

- the linear T_h axis is replaced with a generalized temperature, T^*, which includes the homologous temperature plus a temperature shift caused by the *potential* energy of particles arriving on the surface;
- the linear pressure axis is replaced with a logarithmic axis for a normalized energy, E^*, describing displacement and heating effects caused by the *kinetic* energy of bombarding particles;
- the unlabeled *z*-axis is replaced with a net film thickness, t^*, which will allow us to maintain the familiar qualitative illustration of film structure while indicating thickness reduction by densification and sputtering; it also include i.e. ion etching as “negative thickness”.

The SZD proposed by Anders is visible in Figure 2.5.

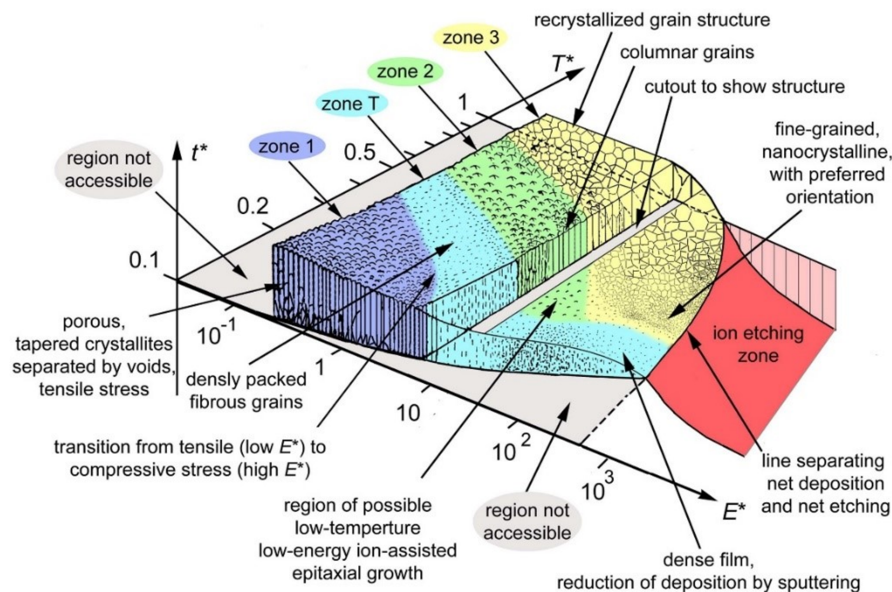

Figure 2.5 Structure zone diagram (SZD) proposed by Anders in 2010 [45].

In both SZD four different film structures can be identified:

ZONE 1: characterized by a fine-grained structure of textured and fibrous grains, pointing in the direction of the arriving vapor flux. The morphology is caused by the low mobility of the adatoms that produce a continued nucleation of grain.

ZONE T: a dense fibrous structure with a smooth, highly reflective surface. Diffusion is "remarkable" but grain boundary diffusion is strongly limited. Ionic bombardment of the growing film can move the morphology from zone 1 to zone T.

ZONE 2: surface diffusion sets in, leading to uniform columnar grains.

ZONE 3: dense films with large grains, drive by bulk diffusion and recrystallization.

2.5 Stress on sputtered coating

Virtually all vacuum-deposited coatings are in a state of stress. The total stress is composed of a thermal stress and an intrinsic stress. The thermal stress is due to the difference in the thermal expansion coefficients of the coating and the substrate materials. The intrinsic stress is due to the accumulating effect of the crystallographic defects produced during the growth of the film.

In high melting point materials, like niobium, intrinsic stresses tend to dominate over thermal stresses [42]. Stress cracking and film peeling are commonly observed.

Thermal stress is well explained by Figure 2.6. When a thin film is deposited on a high temperature substrate, the subsequent cooling to room temperature produce a different change in volume between film and substrate, proportional to the difference between the thermal expansion coefficients of the two materials. This is the origin of thermal stress.

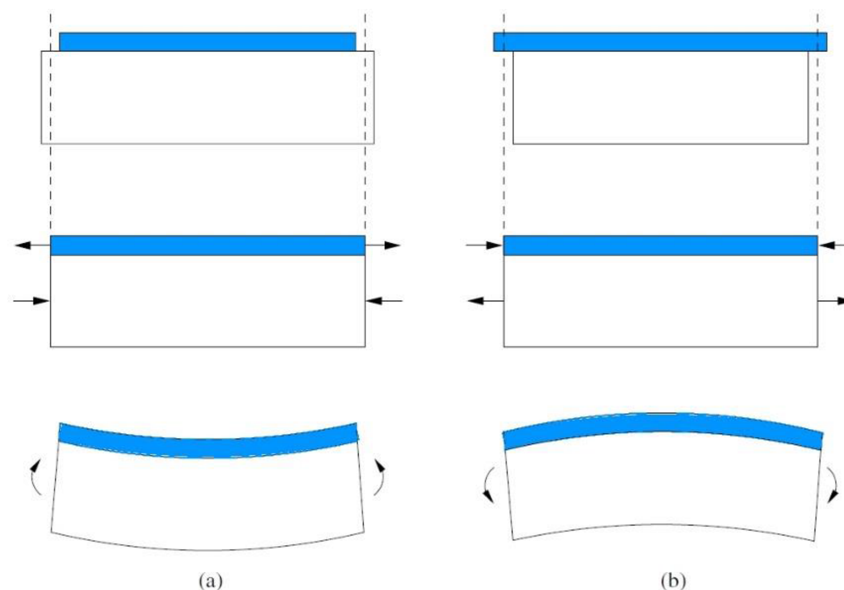

Figure 2.6Tensile (a) and compressive (b) thermal stress in thin film [46].

The intrinsic stress reflects the internal structure of a material during its deposition. Its understanding is less evident than the thermal stress. In most cases, intrinsic stress is non-uniform through the depth and is therefore responsible of stress gradient. We have already seen (paragraph 2.4), how the microstructure of deposited films, and therefore the intrinsic stress, is strongly dependent on deposition conditions. Dislocations and grain boundaries are the most common defects in thin films.

At low T_h, the intrinsic stress dominates over the thermal stress, but when we enter in the zone 2 of Thornton SZD (approximately when T_h exceeds 0.25-0.3) the recovery process reduces the

intrinsic stress and the thermal stress dominates. Thermal stress have a linear dependence with T_h [42].

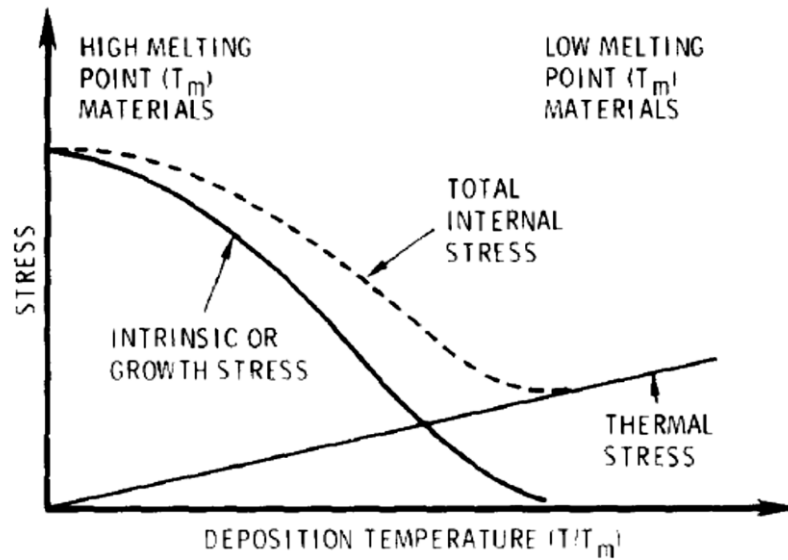

Figure 2.7 Schematic representation of thermal and intrinsic stress contribution [42].

Although the connection between film growth, stress, and microstructure is not yet fully understood, the growth of polycrystalline films can be classified into a sequence of stages, summarized by Barna and Adamik (Barna & Adamimik, 1998). In this paper, they established that the growth of the films has the following evolution: nucleation, island growth, coalescence of islands, formation of polycrystalline islands and channels, development of continuous structure, and thickness growth. This sequence can be summarized in three principal stages and we can define a general trend in film stress behavior during the growth as shown in Figure 2.8 [47].

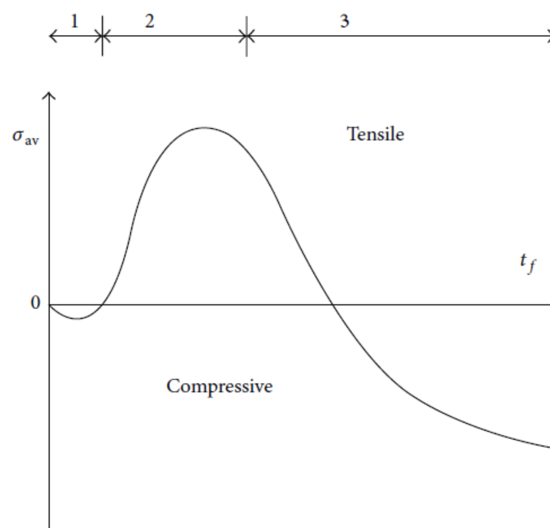

Figure 2.8 Typical evolution of average film stress σ as a function of film thickness t_f during the deposition procedure. The curve describes the three stages of film growth (compressive, tensile, and compressive stress) for vapor deposited polycrystalline films at deposition temperature [47].

In stage 1, the material deposited forms discrete clusters or islands on the substrate surface. These islands are usually subjected to compressive stress, which is attributed to the action of surface and/or interface stress that reduces the lattice spacing compared with a bulk crystal of the same material. In stage 2, island growth leads to island-to-island contact and the formation of grain boundaries, which is the cause of tensile stress that arises in the film. In stage 3, the growth stress in polycrystalline materials decreases, which often leads to compressive film stress. A possible explanation for this experimentally observed change from tensile to compressive stresses with increasing film thickness is the migration of surface atoms into the grain boundaries.

In Figure 2.9 the stress-pressure dependence for sputtering depositions is shown. Increasing the pressure, the film stress changes from a compressive to a tensile one. The gas pressure, in which the stress value is zero, is called critical pressure. Critical pressure increases with the atomic mass of the coating material. At low pressure, the arriving atoms have high kinetic energy and the film growth in these conditions has a dense microstructure, resulting in a compressive stress. At relatively high pressure, the frequency of the gas phase collision increases, reducing kinetic energy of sputtered atoms. The film exhibits an open porous microstructure and the interatomic attractive forces produce tensile stress. Similar considerations, on stress influence, can be done about the distance target-substrate.

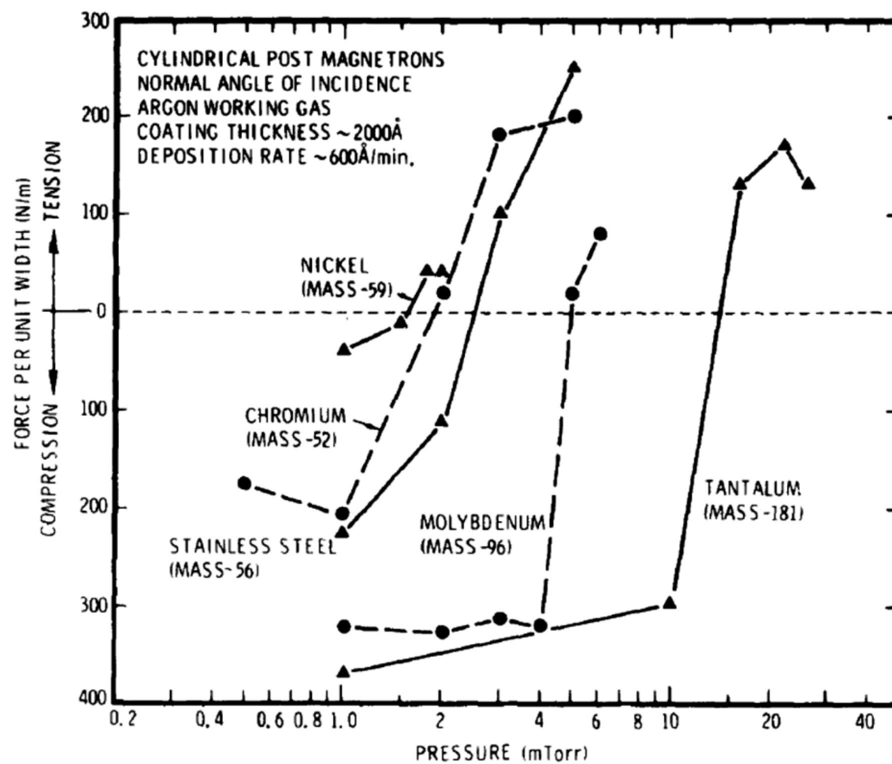

Figure 2.9 Force per unit width produced at coating-substrate interface by internal stress in coatings deposited at various argon pressures using cylindrical post magnetrons.

2.6 Sputtering Configurations and state of the art in Nb/Cu deposition for SRF

Several sputtering configurations have been developed during the years. Here it is not reported a full description of all the different possible configurations in sputtering deposition, but only a brief review of the principal ones used by the SRF community for Nb deposition on copper resonant particle accelerator is presented.

2.6.1 DC Diode Bias Sputtering

Dc diode is the basic configuration in sputtering process. The cathode electrode is the sputtering target and typically the substrate is placed on the anode, which is often at ground potential.[20] The applied potential drop (several thousand volts dc) appears across a region very near the cathode and the plasma-generation region is close to the cathode surface. In argon, the gas pressure must be greater than about 10^{-2} mbar, but under 10^{-1} mbar, the atoms sputtered from the target is scattered back to the electrode and sputter deposition is very slow.

The mean energy of the bombarding species is often less than 1⁄3 of the applied potential. The dc diode configuration is used to sputter deposit simple, electrically conductive materials, although the process is rather slow and expensive compared to magnetron sputtering. An advantage of a dc diode sputtering configuration is that a plasma can be established uniformly over a large area. The target surface does not need to be planar but can be shaped so to be conformal to a substrate surface, as in the quarter wave resonator (QWR) sputtering configuration.

Bias voltage

A negative bias voltage can be applied on the substrate in order to control the flux and energy of depositing charged species. With target voltages of -1000 to -3000 V, bias voltages of -50 to -300 V are typically used.

The bias voltage on substrate can be utilized in all sputtering configurations and has been effective in modifying a broad range of properties in the growing films. The bias voltage can be used to:

- improve film adhesion (with the re-sputtering of no-well attached atoms on substrate surface);
- increase film density (and change the electrical and thermal properties of the coating);
- change the film hardness and residual stress (either increase or decrease);
- alter the morphology (e.g., columnar film microstructure replaced by a compacted, fine-grained structure).

2.6.1.1 Sputtering of the QWR resonator of ALPI linac

The Nb/Cu sputtering on QWR resonator of ALPI linac in the 1990s [48] and HIE-ISOLDE [49] for heavy ions was done with this configuration, because the complicated cavity structure makes the application of the magnetron sputtering configuration difficult. For the sake of completeness some depositions for HIE Isolde were done also in the magnetron sputtering configuration at CERN and at LNL-INFN [6].

The configuration adopted at the LNL for ALPI linac is visible in Figure 2.10 a. The intention of the authors was to develop the simplest sputtering configuration possible in order to easily transfer the technology to non-specialists or other laboratories who could install high performance resonators into accelerators without necessarily developing material science know-how or plasma coating engineering [50]. They developed a sputtering target consisting of a simple Niobium cylinder of 2 mm thickness, with the right diameter to obtain an equal sputtering rate on both the central shaft and the surrounding cylinder. For the deposition of the top-plate, there is no ring or special piece, and the target comes to an abrupt end at the top rim. No supplementary cathodes were used for the sputtering of the beam-ports and top-plate. The cavity was negative biased and the ground reference was provided by an additional electrode, positioned near the cavity bottom. The principal sputtering parameters used were the following [5]: argon pressure of 0,2 mbar, bias voltage of 120 V, substrate temperature between 300 and 500 °C, for 8 runs of sputtering that gives a total of 4 hour of process. The final Nb film thickness was 2-3 µm. This configuration brought ALPI to the outstanding result of an accelerating field of more than 6 MVm^{-1} in 1993. 52 quarter wave Nb/Cu resonators [32] are now installed.

More recently, the new HIE-ISOLDE accelerator at CERN requires the production of 32 superconducting quarter-wave cavities in order to increase the energy of the rare isotope beam delivered to the experiments [49]. In view of the success of the ALPI accelerator, dc bias diode sputtering has been chosen to prepare these cavities. The configuration is very similar to the one adopted at LNL-INFN, except for the ground reference. In the HIE-ISOLDE configuration two grids (one internal and one external to the cathode) have been used. In Figure 2.10 the two configurations are visible.

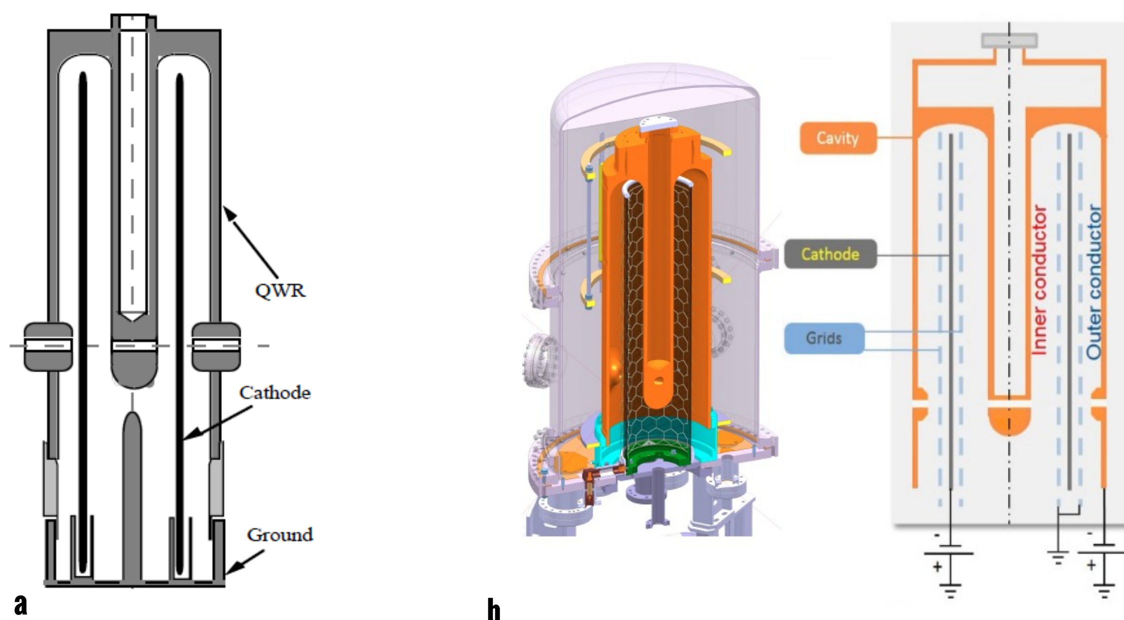

Figure 2.10 Diode Bias Sputtering configuration for the ALPI QWR (a) [5] and HIE Isolde (b) [51].

2.6.2 DC Magnetron Sputtering

As the name suggests, the magnetron uses a magnet to effectively trap and utilize energetic electrons for ionization processes at low pressure. The magnetron discharge is a magnetically enhanced glow discharge [40].

The magnetic field is used to increase the electron path in the space in front of the target. In a magnetron source, two forces act on the electrons: the electric field acceleration and the Lorentz force. The result is a spiral motion of the electrons around the magnetic field line with a proper gyration radius directly correlated with the magnetic field intensity:

$$r_{g,e} = \frac{m_e u_{e\perp}}{eB} \qquad \textbf{Equation 2.5}$$

Where $u_{e\perp}$ is the electron velocity component perpendicular to the magnetic field vector B, e is the elementary charge, and m_e is the electron mass.

The magnetic field in magnetron sputtering may be formed using permanent magnets, electromagnets or a combination of the two. The magnets may be internal to the target, such as in the planar magnetron, or can be external to the target.

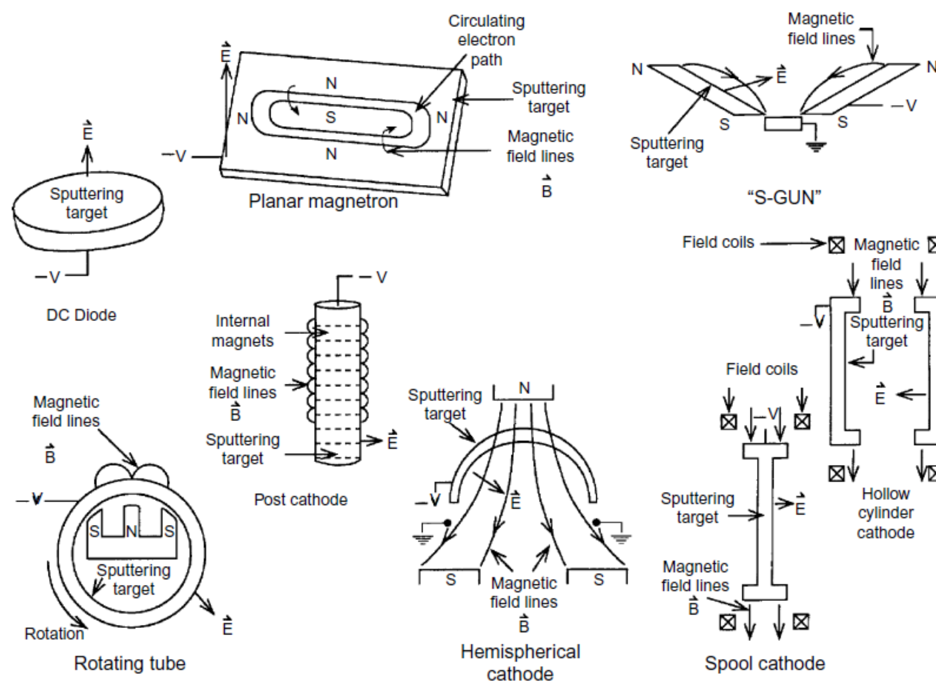

Figure 2.11 Sputtering target configuration [39].

The principal advantage of the magnetron configuration over the diode configuration are:

- one to two orders of magnitude more current for the same applied voltage;
- higher deposition rate;
- reduced operating pressure: from typically 10^{-2} mbar or higher for the diode to typically 10^{-3} mbar or even lower.

One disadvantage of the planar magnetron configuration is that the plasma is not uniform over the target surface. This fact has two fundamental consequences:

- the deposition rate is not uniform, but dependent on the position of the substrate with respect to the target;
- target utilization is non-uniform, sometimes with only 10–30% of the target material being used before the target is recycled. A great deal of effort has been put forth to improve utilization of the target material.

During the years several magnetron sputtering configurations were developed. A sketch of the most common are reported in Figure 2.11.

2.6.2.1 Elliptical Nb/Cu cavities: the CERN LEP-II and LHC experience and R&D on 1.5 GHz Nb/Cu MS cavities

CERN has developed for first the sputtering of Nb onto Cu for SRF resonant cavities and successfully implemented this technology in LEP-II [2] [3] and LHC accelerators [4]. Cylindrical magnetron sputtering was the configuration chosen for the preparation of the 288 cavities (4-cells, 352 MHz) of LEP-II. In the following years CERN continued the R&D on Nb magnetron sputtering in order to understand the superconducting properties of Nb thin films and pushing the performances of the sputtered cavities. Sputtered cavities achieved gradients up around 25 MV/m [35], but the Q-slope remained the principal issue of these cavities and is not ever solved (see paragraph 1.4.4). The same technology was applied for the LHC coatings, adding the experience learned over the years. The LHC cavity specifications at 4.2 K was $Q = 2 \cdot 10^9$ at $E_{acc} = 5.5$ MV/m [32].

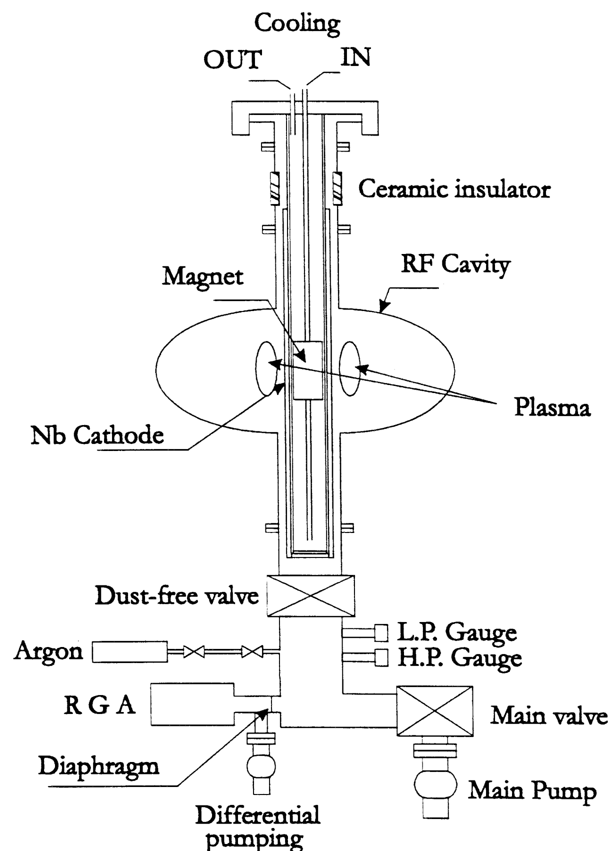

Figure 2.12 Schematic drawing of the CERN elliptical single cell resonator coating system [27].

In Figure 2.12 the sputtering system configuration used for the R&D on 1.5 GHz cavities is reported. In this cylindrical configuration, the resonant cavity is used as vacuum chamber. The niobium cathode (RRR300) is a cylindrical tube 48 mm in diameter. The magnetic field of about 100 G is produced by a permanent magnet, located inside the cathode and free to move along the cathode length. The magnetic confinement produces an increase of the ionization efficiency by approximately two orders of magnitude. Cavities are usually coated at 150 °C, a compromise between lower temperatures causing a deterioration of the film purity and higher temperatures causing the copper substrate to become softer. For the central cell 15 minutes are necessary for an average film thickness of 1.5 µm. Typical RRR values are included between 15 and 30, depending on the gas process (Ar, Kr or Xe).

2.6.3 High Power Impulse Magnetron Sputtering

High power impulse magnetron sputtering is also known under other names, such as High Power Pulsed Magnetron Sputtering (HPPMS). In recent years, most workers in the field use the acronym HIPIMS or HiPIMS. Whatever the name used to call it, HiPIMS is an alternative magnetron sputtering configuration, which is gaining more and more attention both in academic world and in the industry. The reason is that with HiPIMS sputtered atoms are ionized (in MS sputtered atoms are generally neutral) and can be driven by the substrate bias and magnetic field (the neutral atoms of MS can not). Ionized sputtered flux in HiPIMS is used to a controlled ion bombardment of the growing film, by the acceleration of the sputtered material across the plasma sheath, created by a negative bias applied to the substrate.

Some basic concepts of HiPIMS can be traced back to the 1970s (e.g., self-sputtering [52]), but, conventionally, the paternity of the HiPIMS technique is acknowledged at a paper by Kouznetsov and co-workers [53]. In this paper a conventional planar magnetron was used to demonstrate a high degree of ionization of the target material (copper in this case) by supplying very high current pulses [40].

In HiPIMS, high power is applied to the magnetron target in unipolar pulses at a low duty cycle and low repetition frequency while keeping the average power about two orders of magnitude lower than the peak power. This high discharge power leads to the generation of a very high density plasma and thus a high ionization fraction of sputtered atoms. Thus, for the sputtered material, the ion flux is larger than the neutral flux and HiPIMS can be referred to as ionized physical vapor deposition [54]. The high peak power, which can reach and exceed 1 MW in larger systems, implies that the duty cycle of pulsing should be low to allow the target to cool [40].

HiPIMS plasma and the resulting films present the following advantages: [55]:

- high level of ionization;
- high energy ions, tunable with bias voltages;
- possibility to control the film structure;
- phase-tailoring leading to improved performance;
- allows lower temperature process;
- proven improved coverage of complex-shaped surfaces (even for high aspect ratio objects and rough substrate surfaces);
- enhanced adhesion to substrate;

- film smoothness;
- film densification.

2.6.3.1 HIPIMS development for Nb/Cu cavities.

The HIPIMS process for SRF purpose has been extensively studied at LBNL in the group of Andre Anders [56], but today there are several important research groups working on HIPIMS: CERN [57], Jefferson Lab [58], STFC [59], each one with its own original configuration.

At LBNL various experiments have been carried out to explore the plasma physics and characteristics of the HIPIMS process [60], [61], especially applied to Nb. The possibility of "gasless" self-sputtering has been demonstrated, but only with high sputter yield materials like copper [62]. In the case of Nb, the sputter yield is not sufficient to produce enough "Nb gas" [56]. The configuration chosen for elliptical cavities coating is the one in Figure 2.13. Using two magnetrons, one can employ the dual magnetron concept where one target serves as the cathode, and the other as the anode. The polarity of the targets is alternated at a frequency typical for HIPIMS, such a 100 Hz. As a result, the cavity does not participate in the discharge process and can be biased at will, using another, independent power supply.

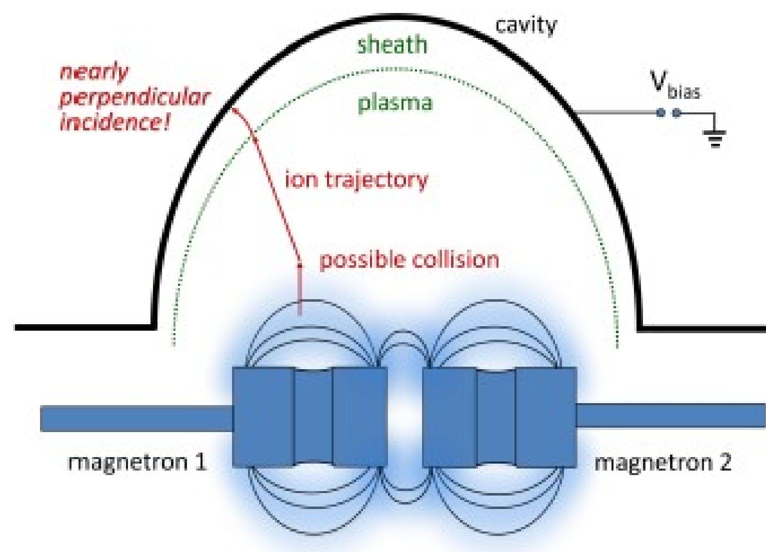

Figure 2.13 schematic of the LBNL dual magnetron HIPIMS deposition system for 1.3 GHz cavities coating [56].

Unfortunately, no cavity has been coated at LBNL, and the Nb film on planar samples shows T_c less than 9 K. At CERN, on the other hand, with a completely different configuration, promising results have been achieved. Last coatings on 1.3 GHZ cavities, show a mitigated Q-slope compared to the DC-MS. The interpretation of these results is very complicated, because the substrate preparation plays a fundamental role and influence the performance of a cavity more than the superconductive film itself [51] [63]. The copper surface preparation is an important issue in this work, too.

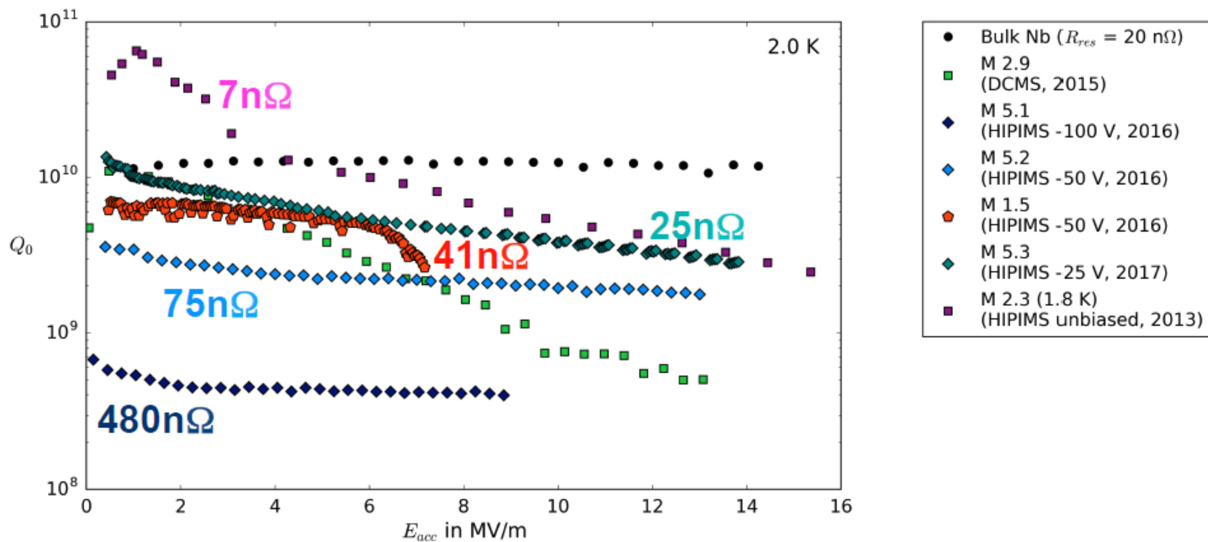

Figure 2.14 HIPIMS results at CERN. Different BIAS voltage was applied [51].

2.6.4 Nb films via (non sputtering) energetic condensation technique

HiPIMS, in order of time, was the last energetic condensation process explored for SRF Nb on Cu coatings. Energetic condensation means a deposition process where a significant fraction of the condensing species has hyper-thermal and low energies (10 eV and greater) [32]. It is characterized by a number of surface and sub-surface processes that are activated or enabled by the energy of the ions arriving at the surface [32], [45]. As implicitly mentioned before, an energetic condensation requires a flux of ions arriving on the surface of the growing film. Two principal techniques (in addition to HiPIMS) were developed for SRF films: ECR and cathodic arc deposition.

2.6.4.1 Cathodic Arc Deposition at INFN Rome2 and Alameda Applied Science

Vacuum arc deposition has been fully described in details in many text books, like [64]. In this deposition technique an electric arc is established over the cathode surface by a suitable trigger (high voltage or laser pulse). The main characteristic of the vacuum arc deposition is the possibility of a gasless self sputtering, with a plasma of fully ionized atoms of the target material. The typical Nb ions kinetic energy can be higher than 100 eV and are multiply charged (the mean ionization for Nb is +3) so the average kinetic energy of the Nb atoms reaching the substrate can reach up to 350 eV for a −80 V [32]. The technique provides a high coating rate and very dense film. A strong disadvantage is however the formation of macro-particles.

The cathodic arc deposition was implemented, few years ago, at INFN Rome2 [65]. The Nb/Cu samples have shown good quality Nb with RRR values ranging from 20 to 60 and very good substrate adhesion, however, the good result on small samples was not reproduced on cavities [66].

A similar technique, but named coaxial energetic deposition (CEDTM), is now at the development stage, at Alameda Applied Sciences [67].

2.6.4.2 ECR at Jefferson Lab

Electron Cyclotron Resonance (ECR) was developed and extensively studied at Jefferson Lab on the Larry Philips group [68]. First neutral atoms of Nb are evaporated with an electron beam gun. The Nb vapor is introduced in the ECR chamber, where a perpendicular magnetic (874 G) and RF electrical fields (2.45 GHz) are applied. The residual electrons are accelerated to their cyclotron resonance and ionize the neutral Nb vapor. The generated plasma consists of ions almost only singly charged. The ions are accelerated towards the substrate by applying a bias voltage. The main advantages of this technique are the production of a high flux of singly charged ions with controllable kinetic energy in ultra-high vacuum environment and the absence of macro-particles (main drawback of cathodic arc depositions). ECR Nb deposition has been studied on a variety of substrates, from highly crystalline to very rough polycrystalline and amorphous surfaces, from Cu to insulators, at various temperatures and bias voltages [55], achieving RRR values similar to bulk Nb values (up to 700). The limit of this technique is the complicated set up, difficult to adapt in a complex geometry as that of resonant cavities.

2.6.5 Nb/Cu clad cavities, an alternative to PVD deposition

International collaborations between KEK, INFN, DESY and Jefferson Lab [8] [69] [70] [71] [72], developed an alternative technique to PVD deposition, for the production of Nb/Cu cavities. The idea was to use clad materials, in which thin niobium material (maybe 0.5 - 1 mm thick) is bonded with thicker copper material (2 - 5 mm thick). The cavity will be fabricated from sheet material (spinning), or tube material (spinning, hydro-forming), therefore electron beam welding is eliminated, and at the same time a rather small amount of niobium material is used compared with bulk niobium. Nb/Cu clad cavity is close to the niobium film coated cavity by PVD, but keeping the niobium bulk property is definitely different [69].

The advantages of this option can be easily pointed out [71].

- cost effective: allows saving a lot of Nb. A rough estimate shows that the NbCu clad cavities of TESLA shape will be 30% cheaper than standard bulk Nb cavities. This can be essential for large projects like ILC;
- the bonded Nb layer has still microstructure and properties of bulk Nb (the competing sputtered niobium layers do not have such advantages);
- the well developed treatment of the bulk Nb such as buffered chemical polishing (BCP), EP, annealing at 800 °C, bake out at 150 °C, high pressure water rinsing (HPR), high power processing (HPP) can be applied (excluding only post purification at 1400 °C);
- high thermal conductivity of Cu improves thermal stabilization;
- stiffening against Lorentz-force detuning and microphonics can be easily done by increasing the thickness of the Cu layer.

Several Nb/Cu clad cavities were built by spinning technique and hydroforming. RF performances of the best Nb/Cu clad cavities are comparable to the best bulk niobium cavities, as it is visible in Figure 2.15.

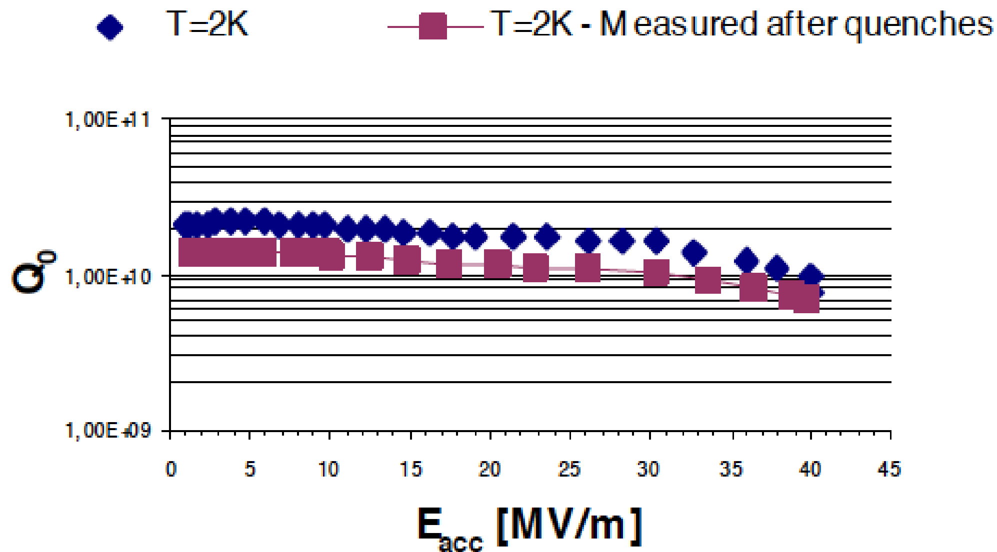

Figure 2.15 The best result achieved in a single-cell NbCu clad cavity produced at DESY from explosively bonded tube. Preparation and RF tests done at Jefferson Lab: 180 lm BCP, annealing at 800 °C, baking at 140 °C for 30 h, HPR. [72]

At first sight the idea to fabricate SC cavities from a bimetallic composite material is very attractive. However there are also some drawbacks in this technique, caused by differences in physical properties of the two metals. The main problem areas are listed below [72]:

- the difference in the thermal expansion coefficient between Cu and Nb (more than by factor of two) will produce stress in the interface during cooling or annealing and in the worst case can destroy the bonding;
- the diffusion of the gases or impurities from the Cu into Nb can cause a deterioration of the niobium material properties important for cavity performance;
- insufficient bonding can cause enhanced thermal resistance at the interface;
- the softening annealing represents a problem because of the big difference in the melting temperature of Nb and Cu.
- the generation of thermo-electric currents, during cool down or quenches, reduces the quality factor of the cavity.

This last point remains an open issue and limits the interest of SRF community on Nb/Cu clad cavities.

3 The thick film way

In this chapter the motivations behind the exploration of thick films for SRF applications are described. Criticality on thick film deposition by magnetron sputtering and state of the art on sputtering thick films are also illustrated.

3.1 State of the art on sputtering thick films

There are several widely used thick coating preparation methods, for example electroplating, thermal plasma spraying, Sol–Gel technique, chemical vapor deposition (CVD), etc. These techniques have good process stability and in many cases low costs, and they have been adapted for industrial production [73]. Nevertheless, some of the above mentioned techniques, such as electroplating, are not suitable for niobium deposition, while for other techniques the coatings can exhibit low density, poor adhesion, and poor superconductive properties. Magnetron sputtering, as illustrated in the previous chapter, can overcome many of the above listed disadvantages for the different coating techniques. However, sputtering films are normally used in a thickness range of under 5 µm. At elevated coating thicknesses, the coatings tend to form cracks or to delaminate because of the accumulated high residual stresses as the total coating thickness increases [74]. Also an inhomogeneous film structure can be observed in many cases, and, furthermore, the preparation of thicker films by PVD is a very time-consuming operation [75]. For these reasons, on literature not many papers are present and they are mainly referred to arc cathodic deposition instead of sputtering. The principal applications of thick films are in the wear protection, but are only applied in very special cases, for example, on high performance piston rings [76].

In principle, it is not difficult to produce a thick coating by PVD. The amount of the deposited material is directly correlate to the length of the deposition time. That means: the longer the deposition time, the more material deposited. However, in Figure 3.1 you can see clear differences when you compare the surface of a 1 µm thick CrN coating with a 30 µm thick coating [75]. In the case of the 1 µm film particles, defects up to a size of 10 µm are visible (Figure 3.1a). It is the normal size range of particles coming from the arc source. These kinds of defects do not disturb, remarkably, the coating performance for typical applications. In the case of a 30 µm film (Figure 3.1b) defects up to a size of 100 µm are visible. Macro particles in arc sources are not so big. The cross section of a SiO_2 film (Figure 3.1c) shows the problem in principle: an initial small defect is increasingly growing during the subsequent deposition process. The consequence is a porous film

structure of thicker films. The film structure can be slightly influenced by adjusting the process conditions during deposition. However, such coatings are very porous [75].

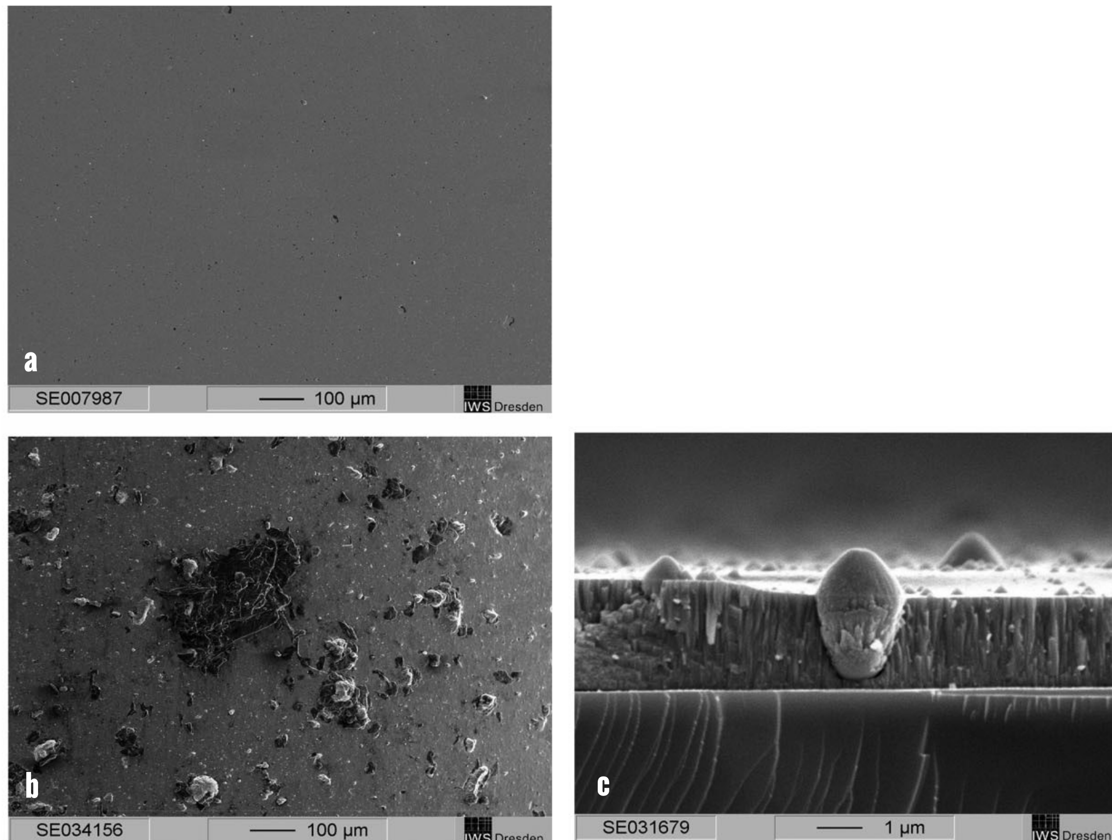

Figure 3.1 Defect growth during deposition: (a) Surface of a 1 µm thick CrN-film/arc deposition, (b) surface of a 30 µm thick CrN-film/arc deposition, (c) 2 µm thick SiO_2-film/evaporation [75].

There are two different approaches to avoid a defect growth: preventing the initial defect or preventing the growth of existing defects.

The first approach is very difficult, but heating the substrate helps to reduce the defect formation (see paragraph 2.5). In the second approach, multilayer structure is the more used. The idea implies that defects grow if the same material is deposited subsequently. If the coating material is changed, an interface is defined and a new crystalline structure can start to grow. The precondition is that the new material cannot grow in the same structure (or orientation) as the defect [75].

In some cases the multilayer deposition of different material is not possible, because the request is a thick film of a single specific element. This is the case of the superconductive niobium thick films, objective of this work. An analogous problem was already addressed at LNL for the developing of a solid target of ^{99}Mo for the radionuclides production [77]. The solutions adopted to reduce film stress are also in this case high substrate temperature (500 °C) and a multilayer deposition of the same material, operated turning on and off the DC power supply in order to have a pause time in which a sort of self annealing of the growing film occurs.

An ingenious solution was patented in 2011 [78] and 2013 [79] for manufacturing a highly efficient flexible thin metal film-laminated strip (Figure 3.2). The method consists in forming a first thin film having residual compressive stress on a board by magnetron sputtering, then forming a

second thin film having tensile residual stress on the first thin film by magnetron sputtering, and then depositing the thick film by repeating the forming of the first and second thin films for more than one time, so that the overall residual stress is controlled within a predetermined range. According to this method, a thick film of same or different materials can be formed, while the overall stress of the thick film is controlled within an acceptable range.

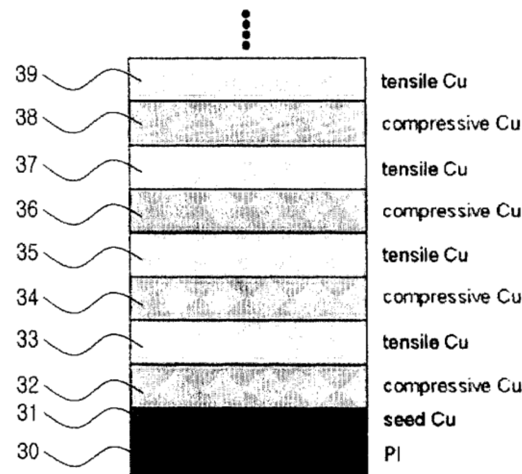

Figure 3.2 Stress-free thick film composed by a multilayer of alternative compressive and tensile Cu thin single layers [80].

3.2 Motivations for SRF thick films

All attempts to solve the Q-slope problem, made in the past, failed in their own way. The main part of the works were based on the idea that Q-slope cause is correlated to the low RRR value of thin films compared to Nb bulk material. At CERN, the R&D experience on 1,5 GHz has demonstrated that increasing the RRR it is possible to enhance the Q_0 value. However, Q-slope was never reduced [35]. Recently, energetic condensation techniques (paragraphs 2.6.3 and 2.6.4) have opened new possibilities. At JLab, with ECR coatings, RRR values up to 700 (higher than standard bulk Nb values) have been measured [55]. ECR Nb films on planar samples also show a surface resistance similar to bulk Nb [34], but an evaluation of the RF performance on a resonant cavity has never been done. Moreover, HIPIMS on 1.3 GHZ cavities at CERN indicate a mitigated Q-slope compared to the DC-MS [51]. From the point of view of the thermal boundary resistance model (paragraph 1.4.5 and [10]), HIPIMS results can be explained by the fact that the conformal coating, characteristic of the technique, improves the interface contact.

The approach of this work to Q-slope problem, is completely different from what has been done so far. The idea comes from the assumption that the Q-slope are certainly caused by the film deposition and is not an intrinsic problem of the Niobium-Copper system [7]. The experimental evidence of the Niobium-clad Copper Cavities (paragraph 2.6.5) shows the possibility for Nb-Cu to have a flat Q-factor and reach accelerating fields up to 40 MV/m [8]. Niobium-clad cavities differ from sputtered cavities for at least three factor: Nb microstructure, Nb-Cu interface and Nb thickness.

The microstructure of sputtered Nb demonstrates the possibility to enhance the Q value at low accelerating fields. Moreover, the enhancement in rf performances by N or Ti doping in bulk Nb

cavities, by many authors, is due to the change in mean free path on the bulk material, with a situation similar to the one of sputtered films [81]. These reasons push to look elsewhere for Q-slope responsible. The Nb/Cu interface, today, is the principal candidate in Q-slope explanation and the clad Nb-Cu interface, actually, could be better than Nb-Cu interface in sputtering cavities, but is very hard to believe that there is not any point of no-contact at the interface of clad copper cavities. To explain the absence of Q-slope in clad copper cavities remains only high thickness. Nevertheless, how to explain that high thickness of the Niobium could affect cavity RF performances?

Two possible explanations have been identified. The first one concerns the possibility that increasing the thickness, the sputtered film becomes more similar to bulk niobium. In magnetron sputtering depositions it was reported that RRR increases with thickness [9], as it is visible in Figure 3.3. A similar trend was reported also for diode sputtering [82]. This behavior cannot be ascribed to surface scattering effect related to the finite film thickness, nor to substrate-film interface stress or, obviously, to randomly distributed impurities. The only possible explanation of the reported behavior is related to the increase of the average grain dimension with thickness [82] [9] [73]. In the grain-growth model described in ref. [83], the average grain dimension turns out to be a function of the growth direction *z* in the film, according to the law:

$$D(z) = az^{0,4} \quad \textbf{Equation 3.1}$$

where *a* depends on the film and substrate nature, on the sputtering parameters, and on the presence of impurities and *z* is the film thickness [82].

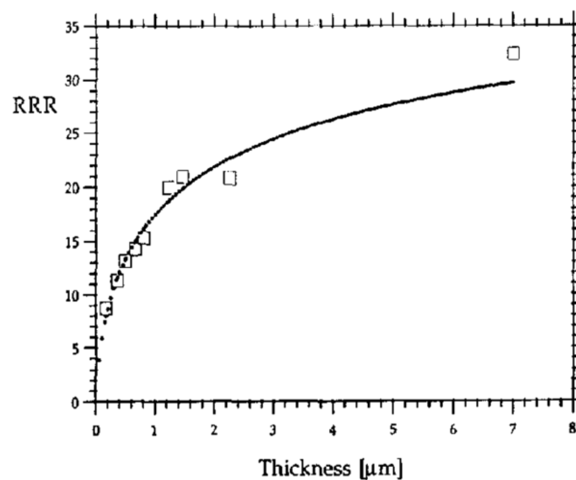

Figure 3.3 Variation of RRR as a function of the Nb film thickness. The dotted line represents the best fit to the experimental values [9]

The second possible explanation involves, instead, the many times here cited thermal boundary resistance at Nb/Cu interface model proposed recently by Vaglio and Palmieri [10]. In the hypothesis of this model, the Q-slope is related to local enhancement of the thermal boundary resistance at the Nb/Cu interface, due to poor thermal contact between film and substrate. The

thermal defects at the interface locally increase the boundary resistance. In the case of thin film, the heat flow, produced by the rf power, passes through the thermal defect since it will be transmitted unidimensionally [7] from the film to the Cu substrate (Figure 3.4). In thick films, instead, the heat flow path occurs three-dimensionally, and the heat flux can easily bypasses the thermal defect at the interface (Figure 3.5). It is worth noting, that thermal defect at the interface is the opposite case of the defect on the surface [84]. In that specific case, thin films are more efficient than thick films and bulk niobium as well.

Figure 3.4 The heat flow in thin film will be transmitted only unidimensionally and cannot by-pass the thermal defect.

Figure 3.5 The heat flow in thick film could be transmitted more tridimensionally and can easily shunt the defect at the interface

This work wants to prove whether the theoretical considerations on thick films are really valid and may open up a new field of research in Nb/Cu cavities. The subject of this dissertation is the engineering of Nb thick films deposition onto 6 GHz cavities to demonstrate the possibility of flat Q in Nb/Cu sputtered cavities. Different deposition parameters and sputtering solutions are investigated; the details on that are reported on chapter 7.

4 Cavity surface preparation

In this chapter all the surface treatments done during this work on the copper surface of the 6 GHz cavities before the coating process, are described. For the chemical and electrochemical polishing of the cavities for this project, a protocol developed and optimized along the years at LNL for the 6 GHz cavities has been used. The cavity production by spinning process, instead, has been optimized in order to increase the initial quality of the internal surface, especially in the cell position. My role in the surface preparation was to supervise the various steps of this fundamental phase in the cavity coating procedure.

4.1 Introduction to copper surface treatments

The importance of cavity preparation for bulk niobium has been already mentioned in 1.4.2. The developments on Niobium bulk cavities surface treatments move the accelerating field from few MV/m to over 40 MV/m [1]. The surface damaged layer, due to cavity fabrication methods (sheet rolling and cell stamping or hydro- forming or spinning), has been established to be 100–200 µm deep [85] [86] [28] so that a bulk chemistry to remove this amount of material is necessary. An other important aspect is the final roughness. Saito, in 2003 [86], deduced the relationship between the surface roughness and the field enhancement. He found that in order to get high gradient E_{acc} > 30 MV/m, the surface roughness should be smoother than 2 µm. Similar considerations can be done for Nb/Cu cavities, because the morphology, and the roughness of the cavity copper surface is replicated by the Nb growing film. On copper cavities, the research on surface preparation is not pushed as far as for niobium cavities, since copper, unlike niobium, is a well known and used material in many research fields, and because it is more difficult to correlate SRF properties of Niobium to substrate preparation. By the way, this last point remains an important issue to explore for the SRF community. Our research group at LNL is currently involved in the international ARIES project [87], where one of the task is just to understand the role of copper substrate preparation.

Looking at the surface preparation of Nb/Cu QWR at LNL-INFN and CERN, respectively for ALPI linac [5] and HIE-ISOLDE, we can see a very similar procedure, except for the adding of the electropolishing (EP) process in the ALPI QWR preparation. In the ISOLDE QWR whole the surface material is removed by chemical polishing with a solution called SUBU5. In INFN preparation, SUBU5 is used only for a final polishing in order to reduce the surface roughness.

In this work we have adopted, and optimized for 6 GHz elliptical cavities, the ALPI procedure. The 6 GHz cavities used on this work have been realized by spinning process (see next paragraph). We can summarize the coating of a Nb/Cu cavity in a protocol with 10 principal steps. Step from 2 to 7 refers to the surface preparation and they are described in the following paragraphs, starting from the spinning fabrication process, responsible for the initial condition of the cavity surface. The 6 GHz coating protocol used in this work is the following:

1. fabrication of the copper cavity by spinning (only for new cavity)
2. lapping of the flanges
3. stripping from the previous coating (if the cavity has already been used)
4. degreasing with soap in ultrasonic bath
5. 1+1 hour electropolishing
6. 5 minutes chemical etching SUBU5
7. 3 minutes passivation
8. High Pressure Water Rinsing (HPWR) at 100 bar
9. Coating keeping the cavity at 600 °C for baking
10. HPWR at 100 bar
11. rf test

4.2 Fabbrication of 6 GHz copper cavities by spinning

In this work all the copper substrates are 6 GHz resonant cavities made by spinning technique in private company, with the knowledge developed since 1990s, and under the supervision of SRF research group of LNL.

The spinning technique first appear among the SRF community during the conference of 1993 at CEBAF [50], presented by Palmieri. He showed the possibility to spun a copper and niobium monocell, complete with cut-off tubes, starting from planar blanks. Today, the technique is mature, and it has been demonstrated the feasibility to produce a nine cell cavity, and compete with hydroforming in the seamless production of elliptical resonant cavities [88]. For his cheapness, spinning technique today is largely used by the SRF community for the production of R&D cavities, both in niobium and copper.

The spinning fabrication technique and performance of the spun cavities is described in details in ref. [89]. The procedure to obtain a spun copper mono-cell from blank is mainly divided in four steps:

1. a circular disk of 400 mm diameter and 3 mm thickness is first preformed onto a frustum shaped mandrel;
2. the first half-cell is formed and a cylindrical shape is given to the remaining part of the piece, by means of a second pre-mandrel;
3. spinning the obtained object onto a collapsible mandrel that has exactly the same shape of the cavity interior, up to when the roller overcomes the equator and fixes the piece to spin onto the mandrel;
4. inserting a further frustum-shaped collapsible mandrel in order to guide the material when spinning the second half-cell.

Both collapsible mandrels are then removed. The presence of an internal mandrel ensures the high respect of tolerances on internal dimensions, and as a consequence of the resonance frequency. Generally most part of the working time is spent in order to set-up the machine. The whole forming operation for a monocell takes less than 10 minutes, a time absolutely competitive in comparison with the standard half-cell drawing, edge trimming, positioning into the EB-Chamber, vacuum pumping and welding. The dismounting operation of the mandrel takes a few minutes.

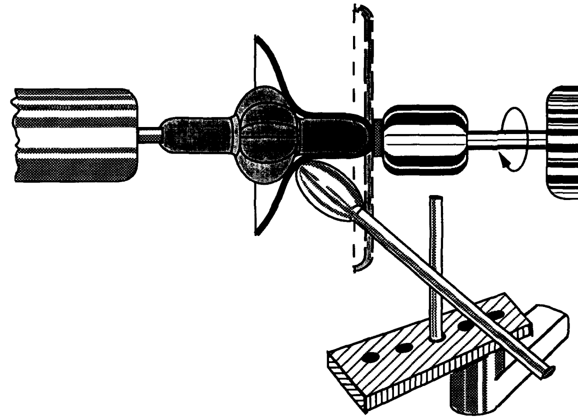

Figure 4.1 Schematic representation of a spinning process for an elliptical single cell cavity from a single sheet of copper or niobium [50].

Spun cavities present a damaged internal surface and micro cracks. The problem arising from the crack presence is twofold: on one hand rf currents are obstructed in their path, on the other hand, the crack becomes a receptacle of contamination from chemical polishing residuals, water, dust, and so on. To fight this problem a mechanical grinding and a successively electropolishing is applied.

As we will see in the results part of this thesis, the initial substrate probably plays a fundamental role in the final performance of the cavities. For that reason, a new kind of mold for 6 GHz cavities has been developed in order to reduce micro cracks and increase the internal surface quality. This advancement in the spinning procedure is under patenting procedure.

In order to have mirror like flanges and avoid leaks during the rf test, a lapping of the flanges with 4 different grades abrasive paper. The process has been done at LNL.

Figure 4.2 Lapping of the flanges (a). The flange surface appearance after the lapping process (b).

4.3 Mechanical polishing

The first essential surface treatment applied to the cavity in order to remove micro cracks and obtain a smoother surface is a mechanical brushing of the surface. On Niobium bulk cavities the mechanical polishing is done by centrifugal barrel polishing (CBP), called also tumbling. At KEK, the cavity is partially filled with liquid soap and plastic chips embedded with ceramic abrasive powder. The cavity rotates in a horizontal orientation at 100 rpm. The chips press onto the cavity inside surface and remove several microns, reducing the roughness to 1-2 µm [28].

In this work, the mechanical polishing of 6GHz copper monocell cavities is done by mechanical grinding with Scotch Brite™ cross shaped rotating tools. Two abrasive sizes are used, first the big one and then the small one. The abrasives showed in Figure 4.3a can be inserted easily inside the cell of a monocell cavity and they are great for creating a uniform surface finishing or blending surface imperfections. In this way both the iris and the equator are mechanically finished.

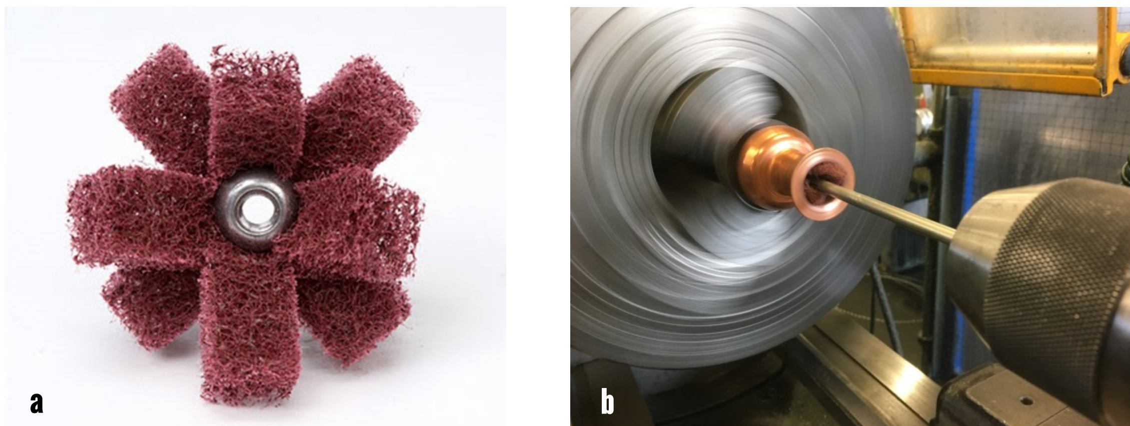

Figure 4.3 a) Scotch Brite™ cross shaped abrasive. b) Mechanical grinding of the 6 GHz monocell. The cavity is rotating while the operator press with the cross shaped abrasive tool on the internal cavity surface.

In the figures below, we can see how the internal surface of the copper cavity was before and after the mechanical polishing. Unfortunately, grinding is not able to completely remove all the scratches (Figure 4.5) and further surface treatments are necessary for a smoother surface.

The grinding polishing of a cavity requires about 30 minutes.

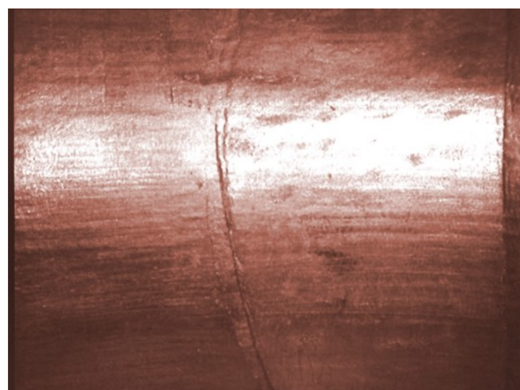

Figure 4.4 Internal surface of the 6 GHz cavities (cell zone) as appear after the spinning production process.

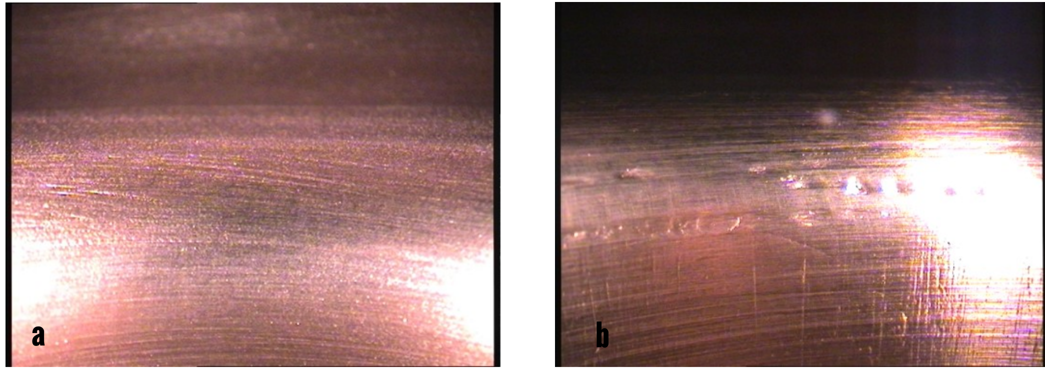

Figure 4.5 Internal surface of the 6 GHz cavities (cell zone) as appear after the mechanical polishing treatment. In b the fact that mechanical polishing is not able to remove all the micro cracks produced during the spinning cavity production is visible.

4.4 Degreasing in ultrasonic bath

During the spinning process, oil or grease are used to increase the tribological properties of the copper. The surface must be polished before the chemical treatments. The degreasing process is done with an ultrasonic cleaning process.

In ultrasonic cleaning, high frequency sound waves are applied to a liquid cleaning solution. These sound waves generate zones of high and low pressure throughout the liquid. In the zones of negative pressure, the boiling point decreases and microscopic vacuum bubbles are formed. As the sound waves move, this same zone becomes one of positive pressure, thereby causing the bubbles to implode. This is called cavitation and is the basis for ultrasonic cleaning. Cavitation exerts enormous pressures (approximately 700 bar) and temperatures (approximately 1000 °C on a microscopic scale). These pressures and temperatures loose contaminants and perform the actual scrubbing of the ultrasonic cleaning process [90].

In this work, ultrasonic cleaning is used for the degreasing before the electrochemical polishing and for all the rinsing in deionized water among the different polishing processes.

Typical parameters used for degreasing are the following:

- Solution: NGL 1740 (commercial surfactant solution)
- Temperature: 40 °C
- process time ≈ 1 hour

For rinsing, all the parameters remain the same except for the solution; deionized water is used instead of NGL 1740.

4.5 Electropolishing

After mechanical polishing, some scratches remain on the surface (paragraph 4.3), but it is not the only problem due to grinding. It is well known, indeed, that mechanical polishing produces an altered microstructure of the outermost layer. Turley and Samuels [91] propose the microstructure in Figure 4.6 for an OFHC Copper surface abraded by P1200 grade silicon carbide abrasive paper, a

mechanical polishing similar to the one adopted in this work. In the case of Niobium sputter-coated Copper cavities, it is clear that an altered Copper superficial layer at the interface between Cu and Nb should be removed since it could influence thermal boundary. In fact, it is well known that dislocations induced by plastic deformations can decrease the thermal conductivity even of an order of magnitude. Even from the point of view of contamination trapped on the Copper surface, this altered layer should be removed. Indeed, foreign inclusions such as Al, Ca, Mg, coming from the abrasive media were found on mechanical polished surface, even after deionized water rinsing, [92].

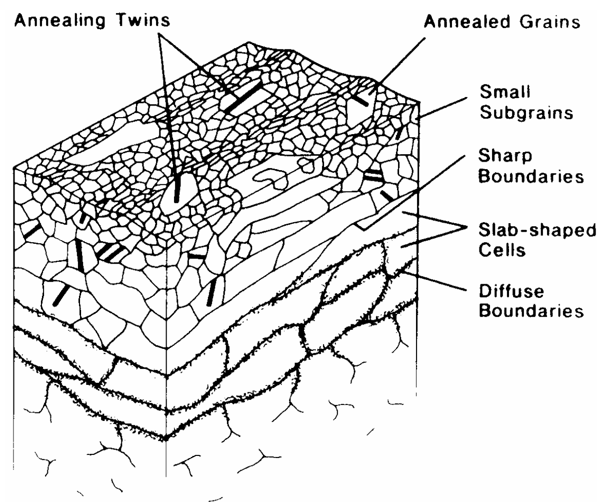

Figure 4.6 Schematic sketch of the structure observed for an abraded OFHC Copper surface [92].

The technique adopted in this work to remove the altered copper layer is electropolishing. In the electrolytic cell the anode (+) is the copper cavity and the cathode (–) is made from pure copper. The electrolyte is a mixture of phosphoric acid and butanol in a volume ratio of 2 : 3.

In a review of the copper electropolishing mechanism [92] several hypotheses were analyzed to explain the mechanism of electropolishing of Copper in phosphoric acid solutions. All of them concern with the existence of a thin bluish viscous layer of electrolyte forming in proximity of the anode, where oxidation reaction and copper dissolution occur. In a simple one, the thickness of such a film influences the erosion rate. On the protrusions, the film is thinner than the surrounding valleys. Hence, protrusions dissolve more rapidly than valleys. Another hypothesis starts from a simple geometrical consideration: the electric field has higher intensity at corners edges and protuberances than at wells, cavities and craters. Surface levelling occurs as a result of greater dissolution probability of peaks.

One of the key parameters characterizing the EP process is the current (I) – voltage (V) characteristic curve [28]. Figure 4.7 shows the ideal and typical the I–V characteristics for EP [92]. Depending on the voltage applied, it is possible to obtain pitting, polishing, or gas evolution. For voltages less than V_b, the surface preserves its mechanically worked appearance and shows some signs of pitting. This region is not recommended for EP. Just above V_b, there occur fluctuations in both voltage and current and a simultaneous drop in current density. Between V_b and V_c, a current plateau appears, usually attributed to diffusion-limited phenomena. Over the plateau, the current

density remains constant even though the voltage increases. A polishing effect is observed between V_b and V_c, but the best results are obtained near point V_c. The first bubbles of gaseous oxygen appear on the anode at V_c. At higher voltages, evolution of oxygen accompanies the dissolution of metal, and pitting may occur due to oxygen bubbles trapped on the anode surface. The current density is inversely proportional to viscosity of the layer. Moderate agitation of the electrolyte reduces the thickness of the viscous layer so the current density increases, and the voltage drops. Vigorous agitation reduces the thickness to a few tenths of a millimeter and voltage drops even more. However intense stirring gives a rougher surface finishing rather than polished [28]. Other important parameters are the electrolyte temperature, the acid concentration and the solution viscosity.

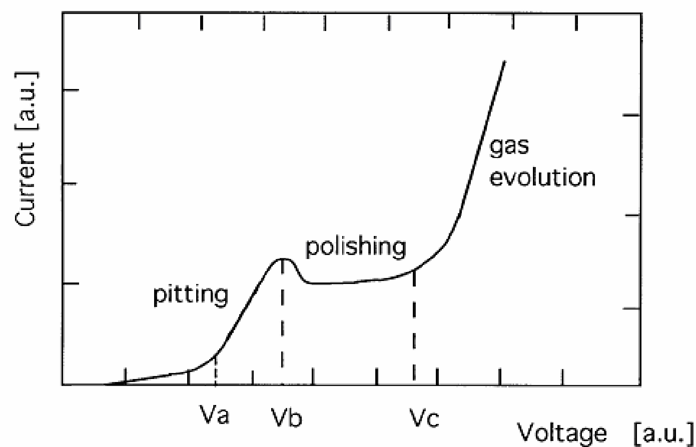

Figure 4.7 Current density vs. voltage for Copper electropolishing in phosphoric acid [92].

The I-V characteristic evolves with time [93], as we see in Figure 4.8. The reason for this is twofold. The leveling action decreases the roughness, but also the surface area decreases. Moreover in the hypotheses of an anodic passivating oxide film, the longer is the process, the more stable is the film and the weaker is the etching.

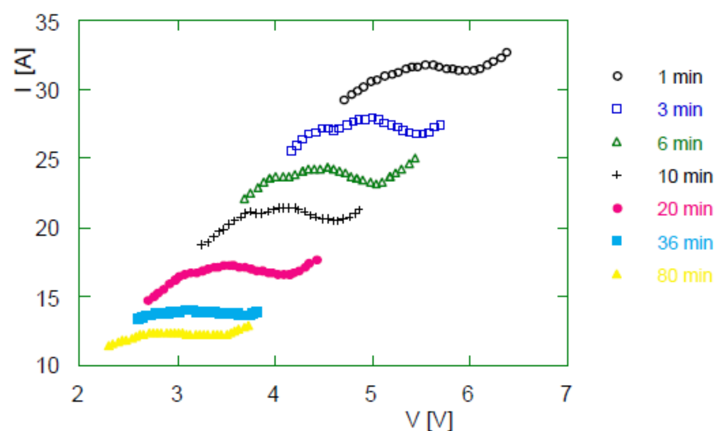

Figure 4.8 *Time evolution of the I-V characteristic plateau* [93].

4.5.1 LNL software for EP

At LNL a method for controlling the electropolishing process has been developed [93]. The method consists in computer monitoring the I-V characteristic. The process is driven in voltage. An automatic program displays the numeric derivative of I versus V. The working point is chosen as the minimum of such derivative, i.e. the minimum of bath differential conductance that corresponds to the point of maximum resistance of the viscous layer. In Figure 4.9 it is showed the differential conductance compared to the ratio I-V together with the I-V characteristic are shown. By locking the minimum of the differential conductance, we see that the plateau moves to very low values of Copper dissolution rate (Figure 4.8). Hence, the removal of large thicknesses cannot be obtained by simply increasing the process time. It is possible, from time to time, to reset the process and inject high currents in order to destroy the viscous layer. Then the process can be restarted. All this procedure is automatized in the program. The program is written in Labview and in this work has been interfaced with a Power System Supply HP 6032 (0-60V, 0-50A, 1000W).

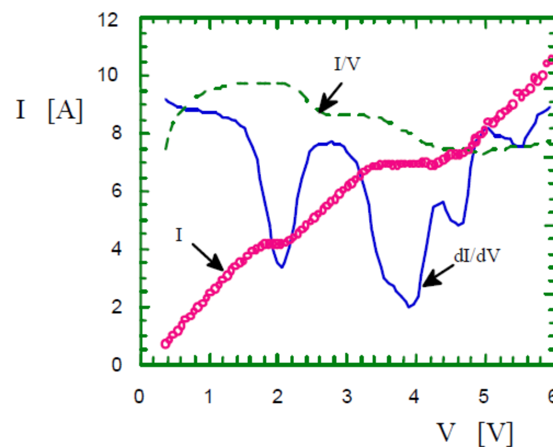

Figure 4.9 Figure 4: I-V characteristic for a standard electropolishing process (circles); The differential conductivity dI/dV (continuous line) and the ratio I/V (shaded line) are displayed versus voltage [93].

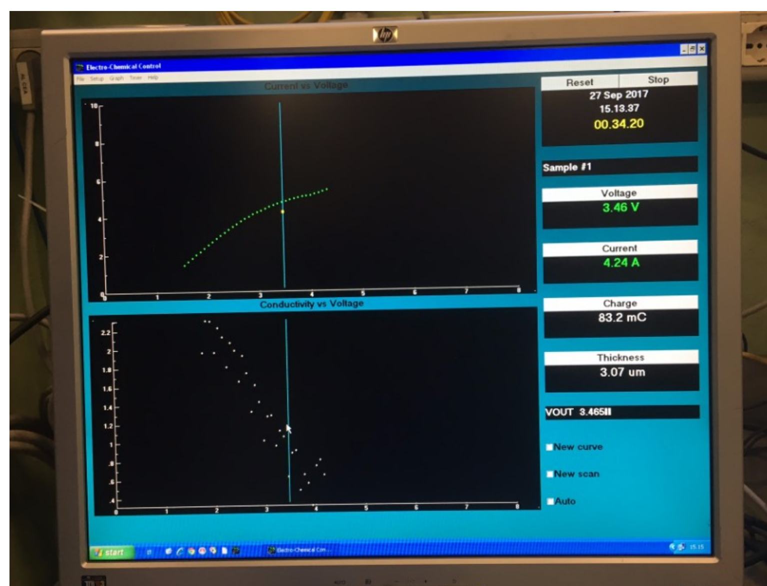

Figure 4.10 EP software used at LNL.

4.5.2 LNL apparatus and procedure for EP

At LNL, for the EP of 6 GHz copper cavities, a totally PVDF (a chemical inert polymer) made implant is used. The implant uses a PVDF pump to recirculate the solution into the cavity, which is placed in a vertical position. The solution used in this work, that is a standard in copper cavities EP [93], is composed by a Phosphoric acid (85%) and Buthanol (99%) mixture, in the ratio 3:2. The cathode is OFHC copper with a purity of 99.9%, in order to prevent contamination of the bath. With this configuration, only the low part of the cell is perfectly treated. In the upper part, the bubbles created by the motion of the solution, limit the polishing action of the EP. To obtain a uniform polished surface the process is divided in two parts. In the first part the cavity is fixed in one position, in the second part the cavity is fixed rotated of 180°.

Standard parameters used for the EP of 6 GHz cavities are the following:

- Solution: Phosphoric acid (85%) : Buthanol (99%), ratio 3:2
- Cathode material: OFHC copper
- Temperature: Room Temperature
- Agitation: flux of recirculating solution
- process time ≈ 2 hours (1 + 1)
- internal surface erosion ≈ 140 µm (70 µm + 70 µm)

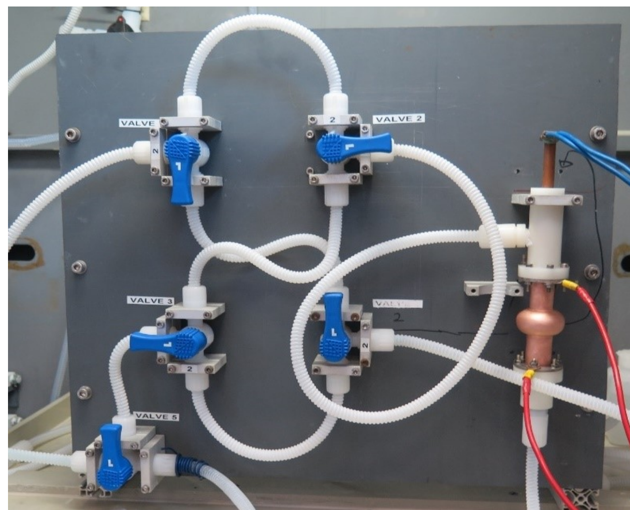

Figure 4.11 In this picture the mini-chemical system set up for 6 GHz cavities EP is visible. In particular, a copper cavity installed in vertical position and equipped with special PVDF flanges for EP can be seen on the right. The acid flux is directed from the bottom to the top of the cavity in order to quickly evacuate the hydrogen produced during the process. The 3-way valves are useful to invert the flux direction.

4.6 Chemical polishing: SUBU5

After the electropolishing, the copper substrate is chemically polished in order to obtain a smoother surface . Chemical polishing is easier and cheaper than electropolishing, and, mostly, it is not affected by geometry, since no electric field is needed: the dissolution process is driven only by chemical reactions. The polishing agent is SUBU5, a solution developed for LEP2 at CERN [2] [94] [95]. SUBU5 is a mixture of sulfamic acid (5g/l), hydrogen peroxide 32% (50ml/l), n-butanol 99%

(50ml/l) and ammonium citrate (1g/l) and the working temperature is around 72°C. After SUBU the cavity is passivated 3 minute with an aqueous solution 20g/l of sulfamic acid and then rinsed in deionized water. It is very important to carry out the passivation task as faster as possible, in order to prevent oxidation.

There are not so many works on SUBU polishing mechanism. The role of each component of the solution is reported in an internal CERN report [96]. Sulfamic acid, at 70 °C, in the presence of an oxidant (H_2O_2), form with the copper a copper sulfamate. Oxygen peroxide generates active oxygen and dissolves the copper. Ammonium citrate is a moderator of the reaction, it limits the pitting process on the surface. N-butanol limits the bubble production.

Standard parameters used for the chemical polishing of 6 GHz cavities are the following:

- Solution: sulfamic acid (5g/l), hydrogen peroxide 32% (50ml/l), n-butanol 99% (50ml/l), ammonium citrate (1g/l)
- Temperature: 72 ± 2 °C
- Agitation: with magnetic stirrer
- process time = 5 minutes
- internal surface erosion ≈ 5 µm

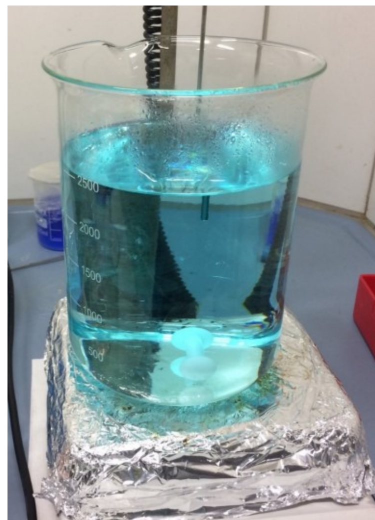

Figure 4.12 The SUBU 6 GHz cavities configuration. A 3 l becker, with a magnetic stirrer for the agitation, placed on a heater. Temperature is controlled and stabilized with a thermometer connected to the heater.

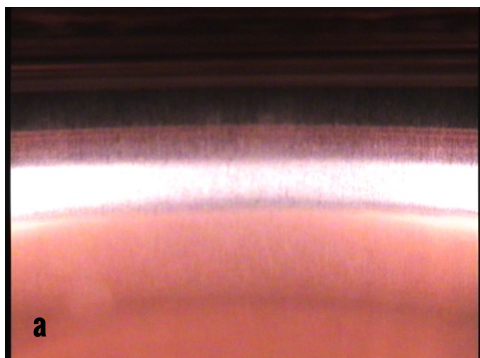

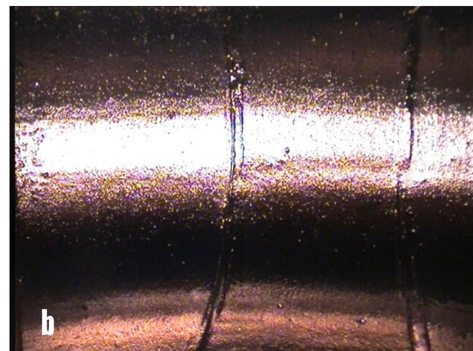

Figure 4.13 After all the polishing process, the internal cavity surface looks very glossy (a). Nerveless, in some cavities (b), the scratches caused by the spinning die are very deep and remain also after the EP and SUBU process.

4.7 High pressure rinsing

The High Pressure Water Rinsing (HPR) is commonly used as a final step to remove dust particles from the cavity surface. This is extremely important before the deposition, in order to avoid holes in the deposited film. But HPR is used also after the deposition and more in general before mounting the cavity in the cryomodule or in a cryostat for the RF test. Paragraph 1.3.2 shows that microparticle contamination has been identified to be the leading cause of field emission. High pressure rinsing with ultrapure water is a powerful tool to remove microparticles and therefore reduces field emission [97].

HPR configuration for the 6 GHZ cavities is very simple (Figure 4.14). We use a commercial water jet to clean a cavity from the two beam ports. The process time is approximately 10 minutes. Water Pressure is 100 bar.

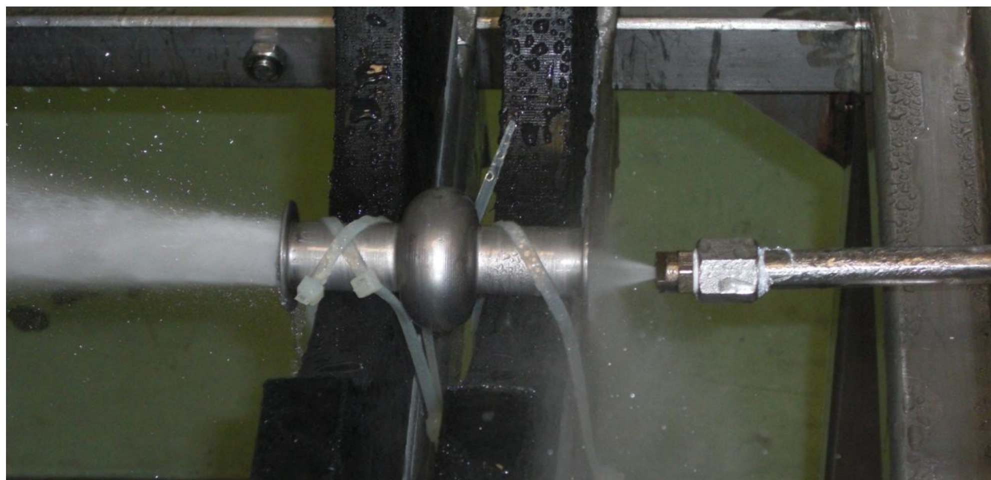

Figure 4.14 High Pressure Rinsing (HPR) of a 6 GHz cavity at LNL. On the right the water jet used is visible.

5 RF test on 6 GHz cavities

The advantages of the 6 GHz approach is described at the beginning of this chapter. Then, after a summary of the rf measurement theory, the rf system is described in detail. The 6 GHz RF apparatus and software were developed in the past at LNL. During this work, no upgrade to the RF part was done, but a development on the 6 GHz stand flanges was carried out in order to prevent superfluid leaks. The RF tests have been performed directly by myself with the help of the colleagues of the SRF team of LNL. Paragraphs 5.2 and 5.3 are based on [98] [99] [29] [100] written by Stark, Lanza, De Ambrosis and Rossi, who developed and built the 6 GHz RF test apparatus.

5.1 6 GHz cavities approach

In the field of SRF it is very expensive to use real cavities for the R&D, because the surface preparation, the coating and mainly the RF test, require several weeks for each cavity due to dimension. For example, it is very difficult to obtain a statistics on a new coating procedure, when working with real cavities. Currently, several approaches exist for the rf characterization of superconductive samples to overcome the problem [101] [102] [82]. This kind of characterization is a useful diagnostic tool to accurately investigate local properties of superconducting materials. However, a common limitation of these systems often consists in the difficulty of scaling the obtained results to the real resonator [103], since they are always indirect measures. At LNL we use a different approach, presented in 1997 during the SRF workshop [103]. The idea is to use real but small cavities, with a frequency of 6 GHz. Reducing the cavity dimension, all the steps (cavity production, surface preparation, coating and RF test) will become faster and cheaper. On the other hand, with 6 GHz cavities, we can obtain a direct measure of the Q at increasing accelerating field. Today, this approach is adopted also from other laboratories, in some cases with an intermediate dimension of 3 GHz.

6 GHz cavities are 93 mm long and have a 45 mm diameter cell (Figure 4.1). They are produced through the spinning technology (paragraph 4.2) and because of that, the material mechanical stress is considerable and the imprints caused by the internal collapsible mandrel must be removed. These cavities are extremely light and easy to handle: they can be quickly mounted on a suitable stand and they can be measured directly by immersion in a liquid helium dewar or, as in the case of this work, in a 6 GHz cryostat, where 3 cavities at once can be measured.

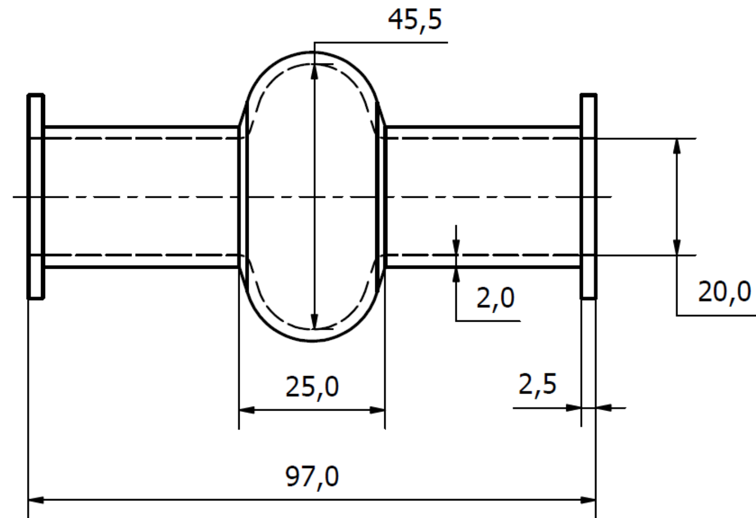

Figure 5.1 Principal dimension of a 6 GHz elliptical resonant cavity (expressed in mm).

5.2 Fundamental equations for rf test

The basic rf properties such as maximum accelerating gradient, field emission onset, and quality factor Q_0 as a function of gradient, can be determined with a rf test on cold cavity (4,2 K and 1,8 K). Rf tests are done inside the cryostat where the cavity is held vertically. Ideally, these tests are done at or near critical coupling (reflected power from the cavity equal or close to zero). In addition, setting the fundamental power coupler at or near critical coupling reduces the rf power requirement to a value close to that required for cavity wall losses, reducing the systematic errors. The critical variable for calculating the rf parameters of a superconducting cavity is the shunt impedance, which relates the stored energy to the effective accelerating gradient. Along with it, cavity geometry is the parameter necessary for calculating peak electric field, and peak magnetic field for any given mode. In our case they are determined using the electromagnetic simulation tool called Superfish and all important parameters determined for 6 GHz cavities, and the standard 1.5 and 1.3 GHz cavities, are collected in Table 5.1.

Table 5.1 Important parameters when calculating the cavity excitation curve [29].

Parameter		Tesla-type cavity		
		6 GHz	1,5 GHz	1,3 GHz
$2\pi\omega_0$	frequency (Hz)	$3{,}77 \cdot 10^{10}$	$9{,}425 \cdot 10^{9}$	$8{,}168 \cdot 10^{9}$
r/q	Geometric shunt impedance (Ω/m)	82,7	82,7	82,7
L	Electrical length (m)	0,025	0,1	0,1154
G	Geometry factor	287	287	287

When a cavity mode oscillates with a resonance frequency ω_0, a stored energy U, and rf losses on the cavity walls P_d, the quality factor can be defined as we already saw in chapter 1:

$$Q_0 = \frac{\omega_0 U}{P_d} \qquad \text{Equation 5.1}$$

Theoretically, a direct measure of Q_0 is possible in the frequency domain, where it can also be expressed as:

$$Q_0 = \frac{\omega_0}{\Delta\omega_0}$$ **Equation 5.2**

where $\Delta\omega_0$ is the 3-dB band width. Unfortunately, the direct measurement of the 3-dB band width of a superconducting cavity is practically impossible, because it can attain very small values if compared with the center frequency: some Hz or fractions of Hz out of thousands of Megahertz. Any commercially available network or spectrum analyzer with these resolution does not exist at the moment.

Rf power is injected in the cavity via an input cable and an input antenna (coupler) from a power amplifier driven by a signal generator which is locked exactly onto the resonance frequency of the cavity mode. The transmitted power is extracted from the cavity by the output antenna (pickup probe). All antennas are connected to calibrated power meters and it is possible to calculate the total power lost P_L with the following power balance:

$$P_{\mathrm{L}} = P_{\mathrm{d}} + P_{\mathrm{cpl}} + P_{\mathrm{pk}}$$ **Equation 5.3**

where P_d is the power dissipated in the cavity walls, P_{cpl} is the power emitted from the fundamental power coupler and P_{pk} is the power transmitted out via pick up antenna. This equation is valid for a cavity with no driving term that has a stored energy U. In this condition the so called "Q loaded" is introduced to take into account the resonant circuit behavior when it is coupled with an external line:

$$Q_{\mathrm{L}} = \frac{\omega_0 U}{P_{\mathrm{L}}}$$ **Equation 5.4**

The quality factor, for each dissipated power, could be written as:

$$Q_0 = \frac{\omega_0 U}{P_d}$$ **Equation 5.5**

$$Q_{\mathrm{cpl}} = \frac{\omega_0 U}{P_{cpl}}$$ **Equation 5.6**

$$Q_{\mathrm{pk}} = \frac{\omega_0 U}{P_{pk}}$$ **Equation 5.7**

the Q values are proportional to the number of cycles the system needs to dissipate all the energy on the considered transmission line. It is important to control if the dissipated power in the couplers is higher or lower than the power dissipated on the cavity walls. It follows that:

$$\frac{1}{Q_L} = \frac{1}{Q_0} + \frac{1}{Q_{cpl}} + \frac{1}{Q_{pkl}}$$ **Equation 5.8**

the external coupling factor β for the two lines is defined, respectively:

$$\beta_{\mathrm{cpl}} = \frac{Q_0}{Q_{cpl}}$$ **Equation 5.9**

$$\beta_{\mathrm{pk}} = \frac{Q_0}{Q_{pk}}$$ **Equation 5.10**

As explained later, the transmission antenna should be sized in order to avoid perturbation of the cavity operation. This condition is reached when $\beta_{pkl} << 1$; in this way the antenna picks up the bare minimum energy requested for the measurement. Moreover, its position respect to the coupler antenna is far enough to avoid the signal transmission without resonance inside the cavity (no cross-talking). On the other side, to be able to transfer all the input power to the cavity, the coupler should satisfy the condition $\beta_{cpl} = 1$ (critical coupling). That condition assures a perfect match of the system and the cavity electrical impedances (coupling). In fact, when $\beta_{cpl} = 1$ the input power equals the power dissipated in the cavity plus the small amount of power that goes out of the pickup port:

$$P_{\mathrm{d}} = P_{\mathrm{i}} - P_{\mathrm{ref}}$$ **Equation 5.11**

where P_i is the incident power, P_{ref} is the reflected power and we are assuming $P_{pk} << P_d$. Impedance matching is essential, otherwise a mismatch causes power to be reflected back to the source from the boundary between the high impedance and the low impedance. The reflection could create a standing wave, which leads to further power waste. As described in the following sections, the impedance matching device is the antenna tuner. This is a particular case on a RF test configuration, where the system allows us to achieve critical coupling prior to doing a decay measurement. In RF systems with a fixed input antenna or in the operating case, where cavities are used to accelerate beam, β is not equal to 1 and the determination of the stored energy becomes more complex (a detailed mathematic treatment of this general case is done in [104]). Our particular case simplifies the math and allows us to make several assumptions, which are described below. When switching off the power supply, the cavity enters into a state of free decay, loosing energy due to dissipation on the cavity walls and the power flowing through the input and the output antennas. During a free decay, the power lost corresponds to the variation with time of the stored energy, thus:

$$\frac{\mathrm{dU}}{\mathrm{dt}} = -P_L = -\frac{\omega_0 U}{Q_L} = -P_d - P_{pk}$$ **Equation 5.12**

the solution (assuming that Q_L is independent from U) is an exponential decay, with

$$\mathrm{U} = \mathrm{U}(0)\mathrm{e}^{-t/\tau}$$ **Equation 5.13**

and

$$\tau = \frac{Q_L}{\varpi_0}$$ **Equation 5.14**

The decay time constant τ is experimentally measured and it is used to calculate a value for the loaded-Q, Q_L. Then Q_L, P_i, P_{ref} , P_{pk} are used to calculate Q_0. In fact, when the cavity is critically coupled:

$$Q_0 = (1 + \beta_{cpl} + \beta_{pk})Q_L = 2Q_L = 2\varpi_0\tau \qquad \textbf{Equation 5.15}$$

$$Q_{pk} = \frac{2\varpi_0\tau(P_i - P_{ref})}{P_{pk}} \qquad \textbf{Equation 5.16}$$

In summary, measuring P_i, P_{ref} , P_{pk} and τ are sufficient to derive Q_L and Q_{pk}.

The next step is increasing the power P_{cpl} in order to raise the stored energy value U. Q_{pk} is a constant that is strictly dependent on the probe/cavity geometry. Equation 5.15 is not valid anymore, but, using Q_{pk}, the Q_0 and E values, can be calculated from the measured values of P_i, P_{ref}, P_{pk}.

$$Q_0 = \frac{Q_{pk}P_{pk}}{P_i - P_{ref} - P_{pk}} \qquad \textbf{Equation 5.17}$$

The gradient may then be calculated as:

$$\mathrm{E} = \sqrt{Q_{pk}P_{pk}\frac{r/Q}{L}} \qquad \textbf{Equation 5.18}$$

5.3 6 GHz rf test apparatus

At LNL, for the Q measurement and rf processing of superconducting resonators, a computer-controlled system was developed, capable to test different resonators in a wide range of frequencies (from 100 MHz of Alpi QWR to 6 GHz of elliptical test cavities of this work) [105]. The first, computer based, measuring system, developed at LNL in 1994 for superconducting cavity testing, covered two frequency bands around 160 and 1300/1500 MHz. Later, the 6 GHz band was added for a small scale cavity characterization. The software developed for the cavity measurement was continuously upgraded until 2013 when a new calibration procedure and the possibility of a multiple rf tests on 6 GHz were implemented [105].

The software, mainly developed by Sergey Stark, is the same for all the resonators and the procedures are similar. Also, most of the expensive parts of the equipment can be shared, the only things that differ are the elements that have got a small frequency range. A block diagram of the measurement apparatus is shown in Figure 5.2.

The computer is interfaced with the signal generator (Agilent N5181A), the three power meters (Agilent E4417A), the DC amplifier (EG&G 5113) and the frequency counter (Agilent 53131A). A dedicated computer board allows the acquisition of analog and digital inputs and the setting of digital and analog outputs. The rf generator signal is divided into three paths (Figure 5.2). One goes through the programmable phase shifter to feed the mixer local oscillator (LO) input. Once the cavity frequency is determined, the loop phase is adjusted, such that the pickup signal (i.e. stored

energy) is maximized. A second line goes to the frequency counter. The third is routed to the power amplifier (the choice of which depends on the cavity frequency), via a PIN diode switch and a variable attenuator. The output of the amplifier is used to drive the fundamental coupler of the cavity.

Depending on the coupling factors Q_L and Q_0, the cavity reacts a mismatch in the circuit and reflects back to the amplifier part of the incident power. The bi-directional coupler (Narda, model 3024A) allows one to monitor the forward and reflected power with two different power meters (Agilent E4417A). Prior to turning the rf power off, both types of power meters provide the average power readings. When the incident power is turned off, the power meter also provides a wave from record which is post processed in order to determine the decay time, τ, of the system. After amplification (or attenuation) a portion of the signal is routed to the rf power meter for measurement. The level of this signal is proportional to the amount of energy stored in the cavity. The amplification/attenuation is accomplished by using a computer-controlled switch (PIN diode switch/Attenuator combination) and a low noise amplifier with 30dB gain. The signal is then split into two paths. One is routed to a limiting amplifier before going to the RF mixer input, the second is connected directly to the pickup power meter (Agilent E4417A).

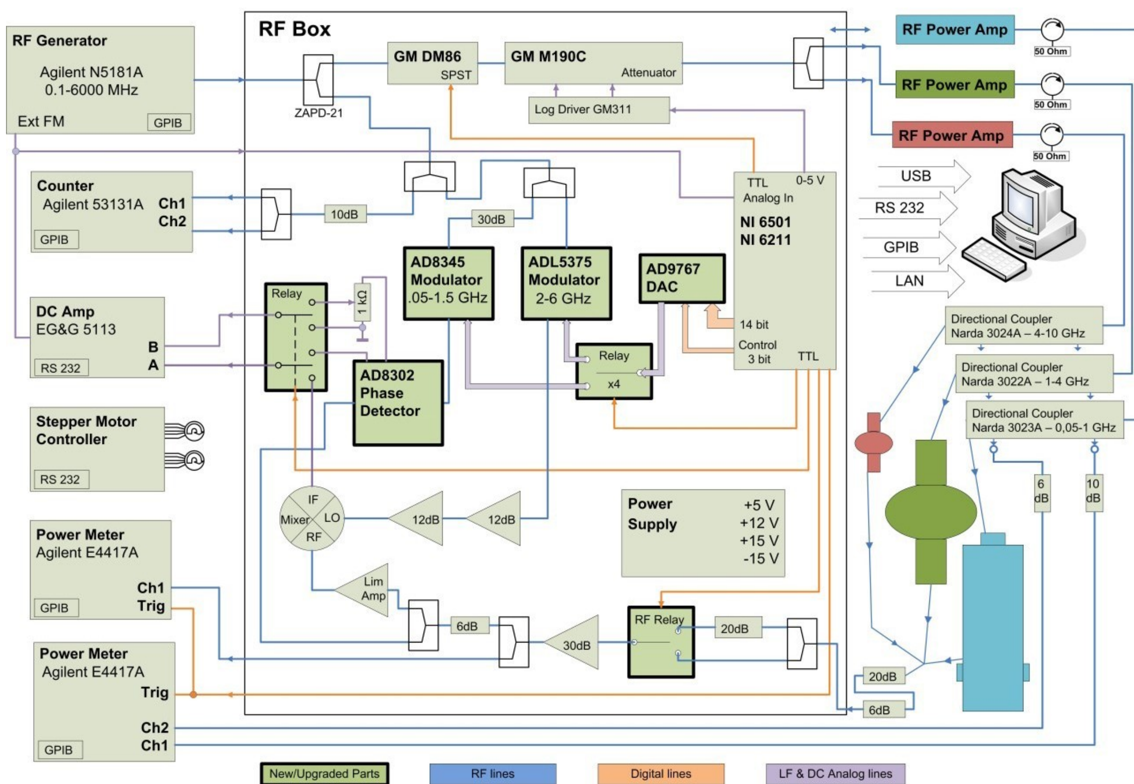

Figure 5.2 Measuring System layout [105].

The first operation is finding the value of ω_0 using the computer program developed for the tests. The operator looks at the input-output phase difference $\Delta\Phi$ versus frequency, which is swept by the generator. The signal proportional to $\Delta\Phi$ is used as a feedback to correct the delivered frequency. When the phase shift is properly adjusted the system will track variations in the cavity frequency. The mixer output is a dc signal proportional to the phase difference between P_{pk} and P_i.

The limiting amplifier (cavity output line) and the phase shifter (cavity input line) correct the initial value and keep the difference of phase at minimum. Thus, the working point of the sweep generator is controlled by the output of the mixer to close the loop. Finally, the frequency is measured with a Frequency Counter. A DC amplifier with programmable gain closes the frequency loop.

There are two antennas on the resonator: coupler and pickup. The "*coupler*" is the forward rf power antenna feeding the cavity and the "*pickup*" is the transmitted rf power antenna, which allows collecting a small signal proportional to the electromagnetic field inside the cavity. With the pickup signal we can follow the resonator energy change. The coupler antenna positioned inside the cavity is adjustable. The coupler antenna is welded on a CF16 flange mounted on a bellow that is connected to a linear feedthrough moved by a step motor. The step motor is directly controlled by the rf software. By changing the coupler location we can modify the *coupling conditions* and consequently the transferred power and the resonator Q_L (and the related bandwidth). We can distinguish three different cases: if the resonator is seen as a perfect matched load by the source, the coupling is *critical*, if the cavity impedance exceeds the feeding line one we speak about *under-coupling*, if the cavity impedance is lower than the feeding line one we have an *over-coupling*. In critical coupling conditions, if we start feeding the cavity with constant power at its resonance frequency, the energy in the resonator rises until it reaches an equilibrium value where all the power transferred to the cavity is used to balance the losses. In a critical coupling condition, Q_{cpl} has to be approximately equal to the cavity quality factor ($Q_{cpl} \approx Q_0$).

The pick-up antenna should collect a signal sufficient to drive the rf control loop, but small enough to reduce the measurement errors. A Q_{pk} between 10 and 100 times higher than the cavity Q is a good compromise.

5.4 System Calibration

Before starting the RF test it is very important to do a complete calibration of the system. At the end of paragraph 5.2, we saw that the calculation of Q_0 and E, is based on the measure of forward, reflected and transmitted power levels at the cavity ports. This power levels are very low in the case of superconducting cavities and it is extremely important to minimize the error in the measure. To this end, it is important to properly measure and compensate all the intervening circuit elements. The calibration of the entire RF circuit is used for this scope and it is done before every RF test. The power sensor heads are calibrated with the standard procedure described by the manufacturer (Agilent). The cable calibration in LNL system is semi-automated and the RF software does the calculations (see [105]). The cables calibration procedure is explicated below.

5.4.1 Forward and reflected power calibration

Step 1 and step 2 are used for the forward and the reflected calibration. During the first step, forward and reflected power values are measured at the directional coupler sampling ports. A short, placed at the end of the forward cable, guarantees a full reflection. The second step gives the forward and reflected power measured at directional coupler in case of full transmission, when the forward cable is connected to a third power head through a calibrated 10dB attenuator. At this point, both forward and reflected overall attenuations are calculated.

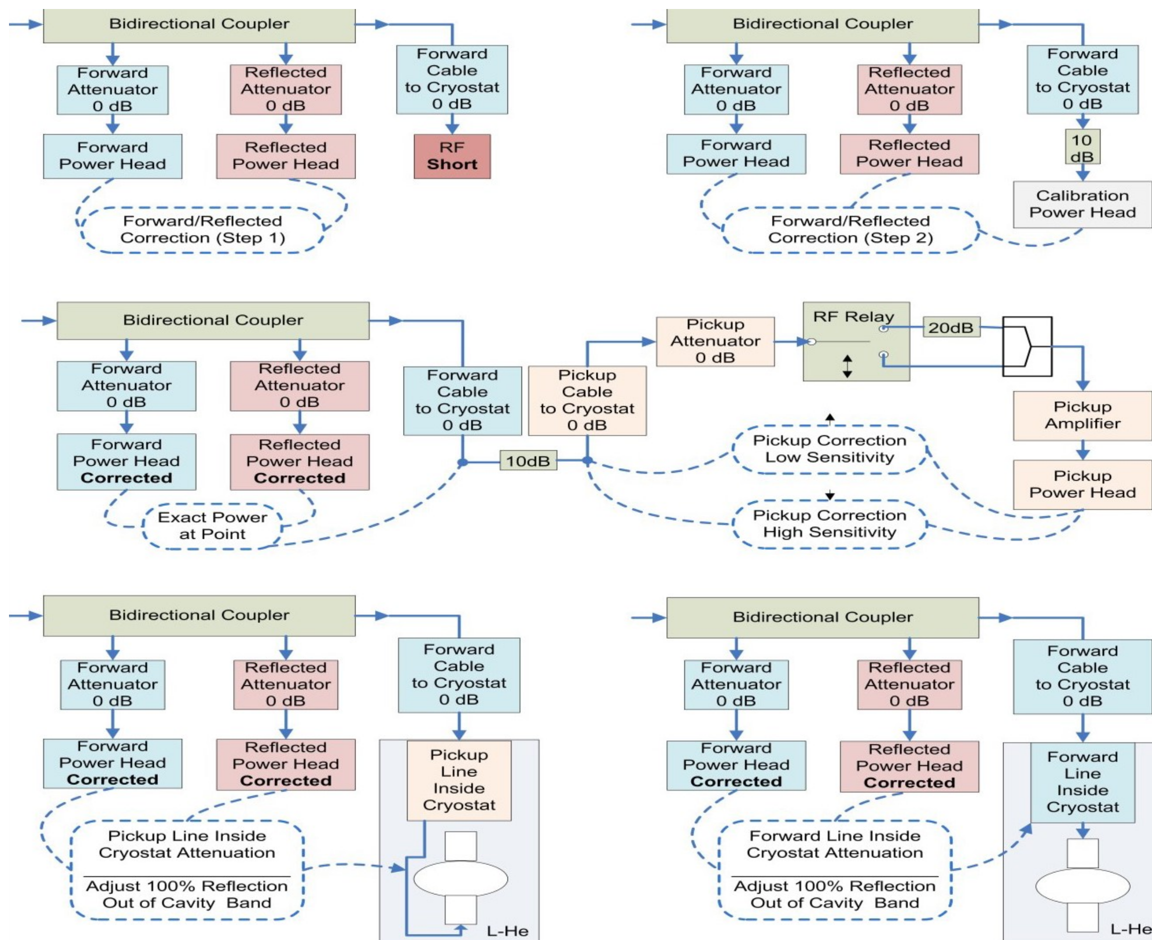

Figure 5.3 Five steps of the calibration procedure [105].

5.4.2 Transmitted power calibration (pickup calibration)

This is done simply connecting the forward cable, already calibrated to the transmitted cable one: the circuit is closed without connecting the cavity. Along the pickup line a sensitivity PIN diode switch is inserted (see Figure 5.2): a 20 dB attenuator can be placed in or not, depending on the power level measured by power meter. The transmitted power calibration (BD attenuation) starting point can be selected: it has to guarantee that the calibration range (5 dBm) includes the sensitivity switching. We need to know the transmitted circuit gain/attenuation with and without the attenuator. At the end of the procedure, the rf control system returns two values: the high sensitivity correction and the low sensitivity one (20 dB attenuator placed in).

5.4.3 Internal cables calibration

Input and output ports (on the top plate of the cryostat) are connected to the cavity antennas through two cables (see Figure 5.2): they are referred to as "*internal*" because they have to be closed in the cryostat with the cavity. The forward cable has to be attached to the fundamental coupler port on the top plate of the cryostat. If the rf generator frequency is set to be out of the cavity bandwidth, the forward power is completely reflected by the cavity. In this situation the losses in the internal cable affects the readings observed on the forward and reflected power meters. The internal cable attenuation can be evaluated looking at the reflected power percentage.

It is necessary to adjust the correction (in dB units) writing it on the dedicated software window. The cable attenuation is correct when the reflected power percentage rises to 100%. In this way, we iteratively determine the losses for internal forward (coupler) cable. Then the forward cable has to be connected to the pickup port on the top plate of the cryostat and the same procedure described above is performed to determine the attenuation of the transmitted (pickup) cable.

5.5 Cavity measurement procedure

Once the superconducting state of the material is reached, the cavity is ready for the rf test. The rf test consists in the measuring of the quality factor of the cavity Q_0, at increasing accelerating field E_{acc}. Q_0 and E_{acc} are determined from a direct measurement of incident, reflected and transmitted power (respectively P_i, P_r and P_t), from the decay time τ, and from the resonance frequency of the cavity ω_0.

In order to search for the cavity resonance frequency, the input-output phase difference as a function of frequency is observed. This value, which is used as a feedback signal to correct the frequency delivered by the generator, shows a visible variation around the resonance frequency. Searching of the resonance frequency is done at low power (1 W) with two 10dB attenuators connected at the power amplifier input. Using such a low power it is possible to work locally without the risk of x-ray production. Sometimes, the frequency searching has been performed using a network analyzer, since in the superconducting state the cavity band will be of a few Hertz and it is very hard to find.

After each sweep, the above mentioned phase difference is displayed on the computer as a function of frequency. The resonance frequency corresponds to a sharp variation which looks like a discontinuity. Now the cavity can be locked and it is desirable to work as close as possible to the critical coupling, where the reflected power is zero. By adjusting the location of the input antenna and the loop phase, one is able to minimize the reflected power and maximize the cavity gradient. Desired values of reflected power are under 2%. When the critical coupling is set, the decay time measurement is performed. The relevant cavity parameters are calculated and are saved automatically. After that, the two attenuators may be removed from the amplifier, the laboratory is evacuated and all measurements are executed remotely. This is done to avoid ionizing radiation hazards.

To record the Q_0-E_{acc} curve using the INFN rf test software, the procedure can be resumed in these 7 steps:

1. turn on the amplifier;
2. turn on rf on the control panel;
3. search and lock the cavity, according to the above given procedure;
4. perform a Q_0 (decay) measurement, and save the set up file;
5. click on the "Q(E)" button: the curve begins to be displayed on the control panel;
6. gradually increase the power, wait that the point become stable, and save the point;
7. repeat step 6 until maximum E_{acc} is reached or a cavity quench appears.

The rf test is done at 4,2 K and at 1,8 K. At 4,2 K the R_{BCS} contribution is dominant, while at 1,8 K the residual term of surface resistance becomes dominant.

During the cooling down from 4,2 K to 1,8 K the cavity band continues to shrink and it is better to leave it locked in the phase lock loop.

5.6 Cavity measurement software

The control program allows to:

- calibrate the rf lines;
- find the resonance frequency;
- set the loop phase;
- lock the generator to the resonator frequency;
- adjust suitable coupling conditions and the forward power level;
- measure the levels of pick-up, forward and reflected power signals;
- measure the decay time;
- compute the Q_0 and plot it as a function of the accelerating field E_{acc}, allowing both a fast data analysis and recording .

All these procedures are started from the program panel (figure 5.8): the main control panel is designed to give complete manual control of the measurement, indicating all the crucial system parameters in real time. The automatic procedures are activated by the buttons and after completing the process, the system returns to the manual mode. It is possible to stop the automatic procedure and to operate the devices manually, resuming the automatic process later, if required. The control panel is composed of numeric controls and indicators, indicator bars, several scroll bars and a custom menu. Starting from the right part of the screen (Figure 5.4):

- the power indicator ("Forward") gives the power delivered to the cavity. The value expressed in Watts is obtained using the calibration factors. In the boxes below the power indicators, the violet value expressed in dB, indicates the power read directly from the respective power head.
- The "Pickup" indicator shows the power level transmitted by the resonator. It is possible to change the sensitivity of the pickup power head between "High" and "Low" or leave it in an automatic mode.
- The "Reflected" power indicator: this is the ratio, in percent, of the reflected power divided by the forward power. It can be expressed in "Power" or "Voltage" percentage. It is crucial to minimize this signal in order to improve the measure accuracy.
- The "Resonator" box, placed under the "Reflected" indicator, displays the actual loop frequency.
- Just below there is the generator frequency setting ("Reference"). It is also the sweep center frequency of the graph placed on the left and it can be adjusted by the operator.
- The "Offset" appears as number and position of the cursor in the indicator bar. It is the phase error signal coming out from the DC amplifier.
- The "Phase" provides a user control of the loop phase setting.
- The "Power" knob is in logarithmic scale and it allows one to increase or decrease the power from the amplifier.
- The "Follow" box sets the generator frequency to the resonance frequency of the cavity.
- The "Lock" box closes the loop (see section 5.2).

- On the graph box placed on the left the frequency is spanned by the sweep. The frequency range could be selected with the scroll bar of the "Span" buttons, and, accordingly, the step width (the sweep is actually a discrete sequence in the frequency domain, with a given step).
- The "Scan" modality shows the pickup signal intensity versus frequency on the graph box.
- The "Pulse" modality switches on the pulse power for the cavity conditioning. "Period" and "Width" of the pulse can be changed.
- The "Q(E)" button changes the graph box to display the Q versus E curve. Each point of the curve can be registered in a file with the "Save" button.
- The "Decay" button starts the decay time calculations.
- The CW button goes back to the normal procedure and it is used to exit the "Decay" and "Q(E)" modality.

Another simple, but important software, has been developed for the coupler motion. A stepping motor lift up and bring down a tube connected to the lamellar bellow of the antenna. The stepping motor could be controlled acting on the "Speed", the number of "Steps" and the movement direction (up or down). This software allows to complete an rf measurement remotely, controlling all instruments and measurement parameters. The software is programmed to display several warnings in case of problems occurring during the test.

Figure 5.4 LNL rf software main panel

5.7 Cryogenic apparatus and cavity stand

During the rf test, the cavity has to be cooled at cryogenic temperatures in order to reach the superconducting state. The transition temperature for Nb is 9,2K.The cavity is pumped at pressure below 10^{-7} mbar in order to limit gas ionization effects. This cryostat has been designed for operating at 4.2K and 1.8K with 3 cavities at once. It is composed by 4 coaxial vessels in order to minimize the helium dissipation. From the outside to the inside we have got: the first vessel in vacuum, the second vessel connected to the liquid nitrogen tank placed outside the laboratory, the

third vessel, in vacuum as well, to insulate the fourth vessel. The latter, internal one, is filled in with liquid helium, where the three 6 GHz cavities are housed.

At the top, thermal insulation is improved by several copper screens cooled with the recovery helium cold gas, pumping it through a pipe thermally anchored to them. The pumping is performed by the centralized Helium pumping system through the valve C visible in Figure 5.5. The internal vessel is filled in with helium from an external 500 l helium dewar. The transfer takes almost 3 hours. The cryostat is capable to contain 50l of helium, but, taking into account the dissipations of the transfer process, about 150 l of liquid helium are necessary to fill in the tank.

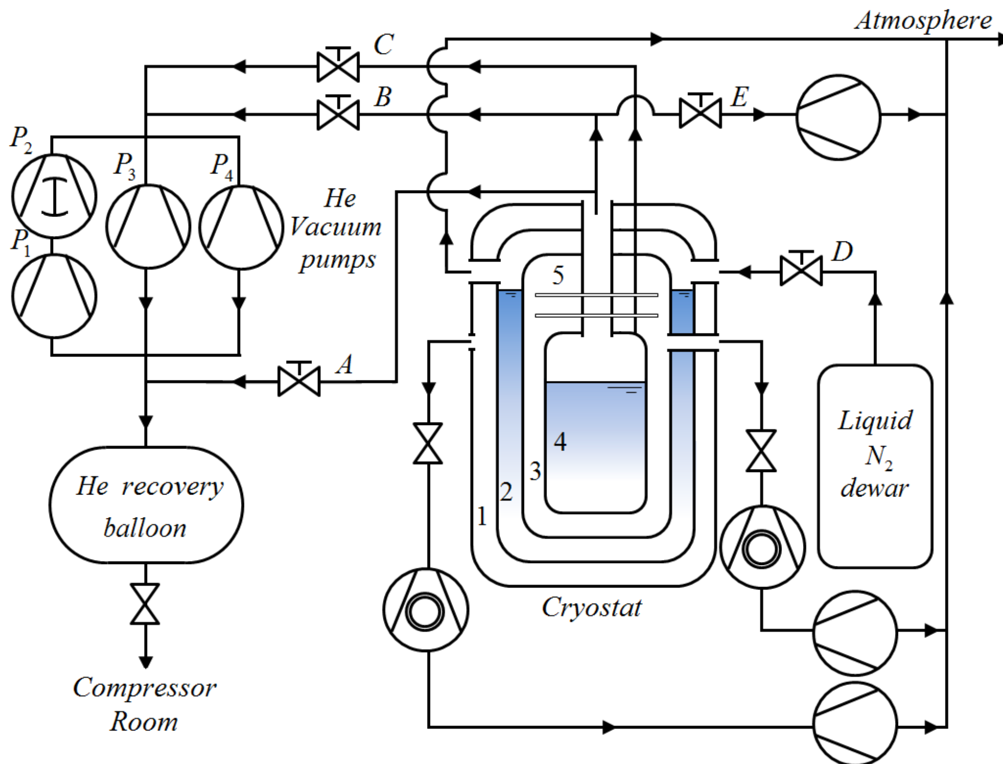

Figure 5.5 Simplified scheme of the INFN-LNL 6 GHz cryostat and the pumping system [106].

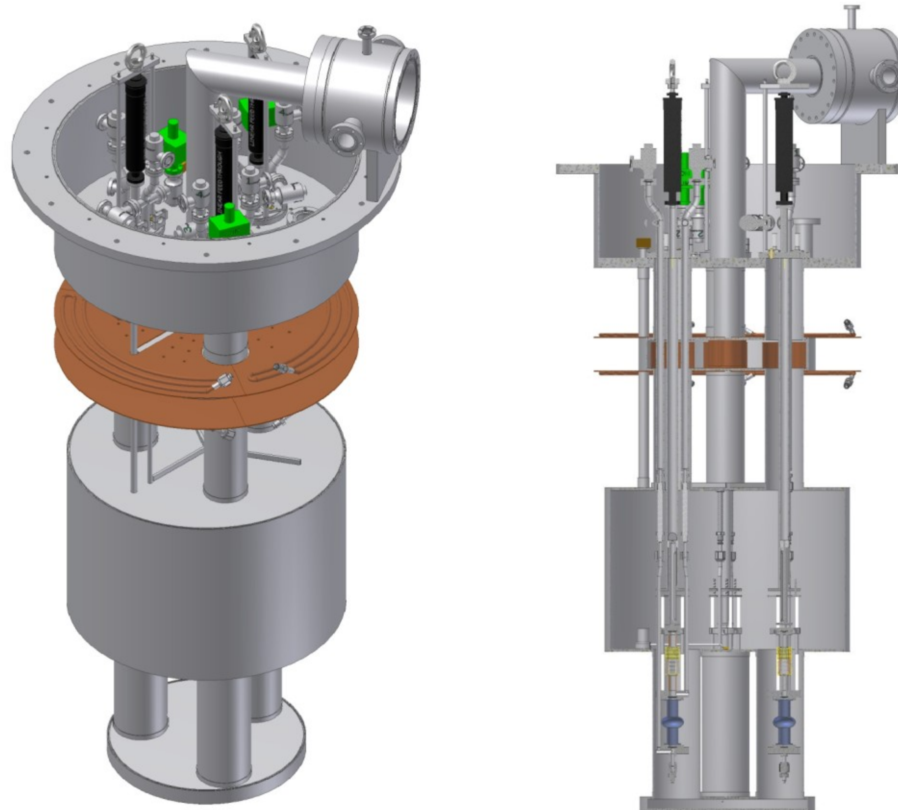

Figure 5.6 Helium tank (A) and helium tank cross section (B). In the figures the 3 cavity stands, and the low temperature screens are visible [107].

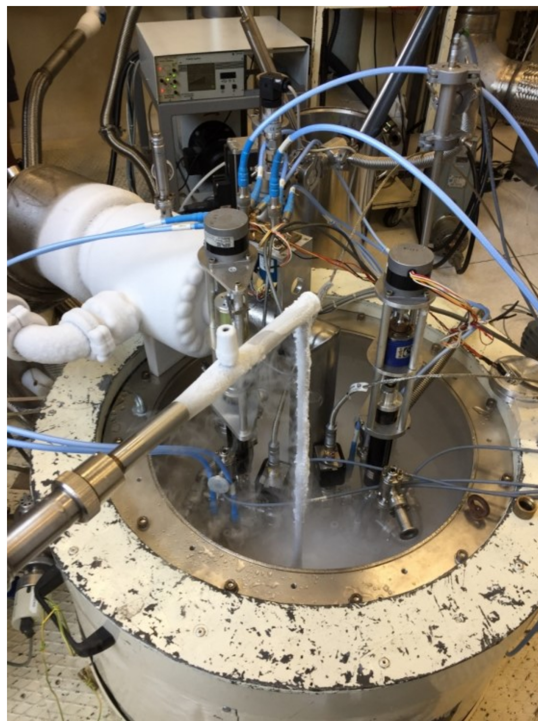

Figure 5.7 6 GHz cryostat, with two stands mounted, during a helium transfer.

The cavity is tested at 4.2K and then at 1.8K, the actual operational temperature of the TESLA-type superconducting accelerating cavities, where the superconducting properties are enhanced. During the measurements the cavity is completely immersed in the liquid Helium bath, and sustained with a special stand for the RF vertical test. The bath temperature decrement is simply obtained by reducing the vapor pressure in equilibrium with the liquid. This is achieved by pumping above the Helium bath through the valve B, with a series of vacuum pumps (P_1, P_2, P_3 and P_4 in Figure 5.5). Obviously, every pump has its pressure range of operation and is selected from a centralized controlled system inside the lab. The pumping operation, on the other hand, implies a huge additional consumption of liquid, but becomes indispensable to fully characterize the cavity performances. When the temperature reaches the lambda point at 2,17 K (following the coexistence line in Figure 5.8), i.e. the triple point where He I normal fluid, He II superfluid and vapor He coexist, the superfluid transition takes place. By further pumping above the Helium bath, the superfluid concentration becomes higher as the temperature decreases, and the superconducting properties are enhanced due to the lower temperature and the better thermal exchange efficiency of the cavity with the bath.

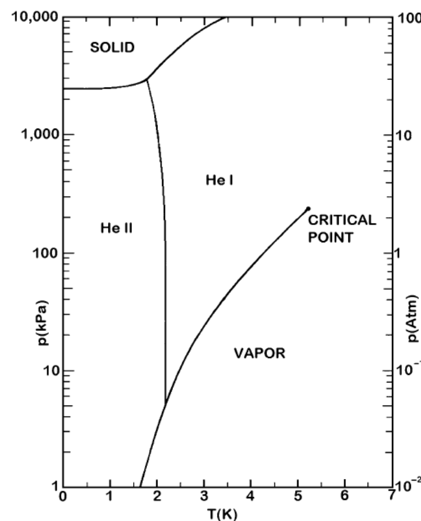

Figure 5.8 Phase diagram of Helium. At the temperature of the lambda point 2,168 K we are at the triple point where He I (normal fluid), He II superfluid and gaseous He coexist.

5.8 Cavity and stand preparation for the rf test

The cavity must be prepared and mounted on the the vertical rf test stand. In order to minimize the possibility of field emission during the measurement, a good grade of cleanness is mandatory. Therefore, just before the cavity assembling on the RF stand, a ultrapure water high pressure rinse (HPR) with a pressure of 100 mbar is done, in order to eliminate particles from the cavity inner surface. The particles on the cavity surface are in fact a big issue, because they enhance the probability of field emission as we have already seen in 1.3.2.4. The cavity mounting is therefore performed inside a clean-room with a controlled environment. After the cavity is mounted on the RF stand, it is connected to the vacuum pumping line to be evacuated. The pressure generally achieved is about 10^{-7} mbar before starting the RF test. A leak test on the stand is done at this point,

and, if passed, the stand is inserted into the cryostat. The system is now ready for the helium transfer and the consequential rf test.

5.9 Upgrade of the kapton sealing system

The cavity is produced by spinning (see paragraph 4.2) without any welding and does not have the standard CF flanges to seal it on the rf stand. It is therefore used a different sealing method, with Kapton® gaskets and vacuum grease (Apiezon®), adopted at LNL for 6 GHz since 2012 [107] [106]. This kind of sealing system is absolutely unconventional, and was not completely tested before this project. During several RF test in the first year of this work, a leak appeared at the helium lambda point. In technical slang, these kinds of leaks are called superleaks, and are very complicated to find and fix. After a deep analysis we have understood that the cause of superleak is the kapton sealing. This because the long time spent at 550 °C, during the deposition process, imperceptibly bends the cavity copper flanges. The problem has been solved with a new design of the flange, substituting the 4 flange pieces with the new flange of Figure 5.9. This new design allows a uniform press on the whole cavity copper flange. To obtain a plane surface, the flange is first machined in one piece, then cut in two pieces, remounted after the mechanical processing and re-machined again. With this new flange design the superleak is now very rare.

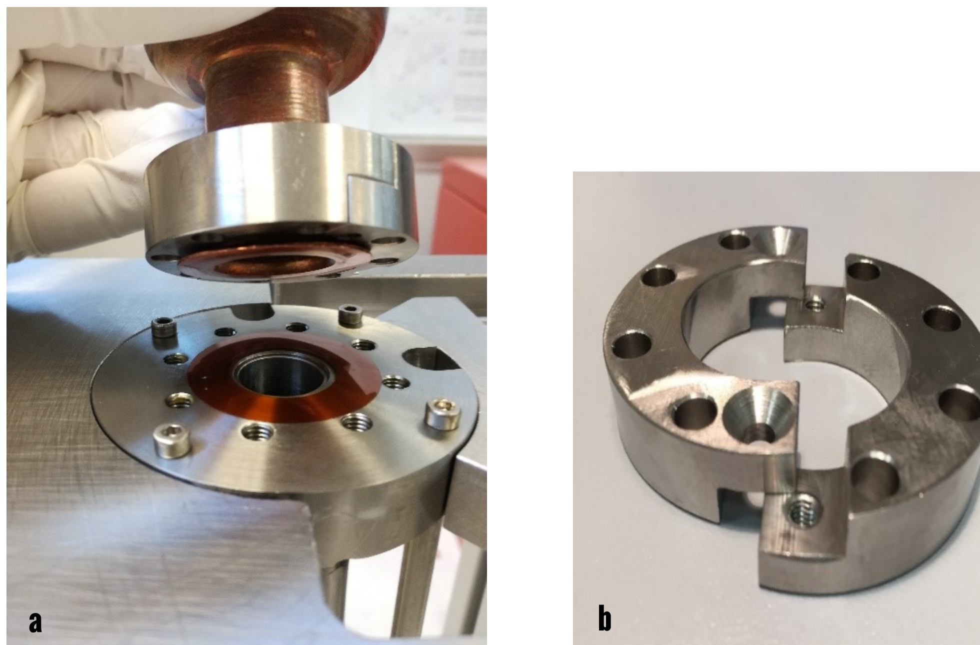

Figure 5.9 New flange design for the stand flange. This composed by two pieces, machined together. The flange is inserted in the cavity cut off and then mounted before sealing the cavity flange with kapton gasket.

6 Nb films characterization methods

This chapter provides an overview of the different methods that were used to analyze the film microstructure and morphology of Nb films deposited on quartz samples. This characterization was preliminary to 6 GHz cavity coating. In this work, I directly used all the described instrumentation.

6.1 Superconductive properties: RRR, T_c and ΔT_c

The Residual Resistivity Ratio *RRR* (see 1.4.1.1), and the transition temperature T_c of sputtered films on insulating quartz, was measured with the four point method to eliminate the effect of possible contact resistance at the contact point between niobium films and the tips of the measuring device. A Visual Basic program, developed in the past at LNL, is able to acquire the resistance curve from 300 K to the transition temperature. A DC current of 5mA is injected into the sample and the resulting voltage is measured. The same method is used to reading the temperature. A DC current of 10mA is injected in the thermometer and the resistance is measured. The exact temperature values are obtained from a calibration curve.

The holder that contains the four points probe with the sample and the thermometer are visible in Figure 6.1. The measure is carried out inserting the sample holder stand into a liquid helium tank, at a certain distance from the liquid level. The temperature is varied slowly (in order to ensure the system thermalization) moving the sample holder closer to the liquid level. Each series of measurements took from one to six hours, depending on the cooling and heating speed.

The low temperature resistance of the sample is determined at 10K and the RRR calculated with the following formula:

$$\mathrm{RRR} = \frac{R(300\,K)}{R\,(10\,K)} \qquad \textbf{Equation 6.1}$$

The transition temperature $T_c \pm \Delta T_c$ is calculated from the resistance curve with the following formula:

$$T_C = \frac{T_{90\%}+T_{10\%}}{2} \qquad \Delta T_C = T_{90\%} - T_{10\%} \qquad \textbf{Equation 6.2}$$

where $T_{(90\%)}$ and $T_{(10\%)}$ are respectively the temperatures corresponding to the 90% and 10% of the resistance before the transition. ΔT_c is the error on the critical temperature estimation.

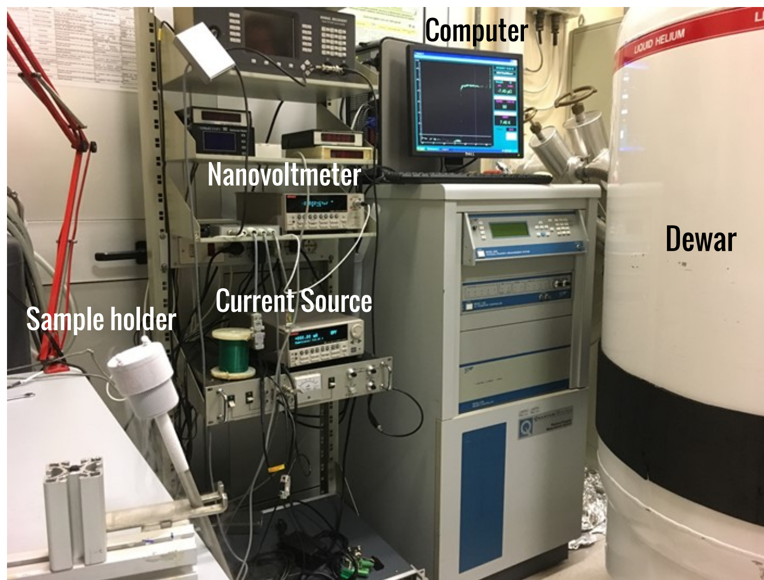

Figure 6.1 Picture of all the instrumentation used for RRR and T_C characterization

6.2 Profilometer

For the measurement of Nb film thickness, a profilometer Veeco Dektak 8 (Figure 6.2), available at LNL, was used. The Dektak 8 takes measurements electromechanically, by moving a diamond stylus over the sample. The stylus is moved, according to a user-programmed scan length, speed and stylus force. The stylus is mechanically coupled to the core of a Linear Variable Differential Transformer (LVDT). As the scan drive moves the stage and sample, the stylus rides over the sample surface. Surface variations cause the stylus to be translated vertically. Electrical signals corresponding to stylus movement are produced as the core position of the LVDT changes. The LVDT produces an analog signal proportional to the position change, which, in turn, is conditioned and converted to a digital format through a high precision, integrating analog-to-digital converter [108].

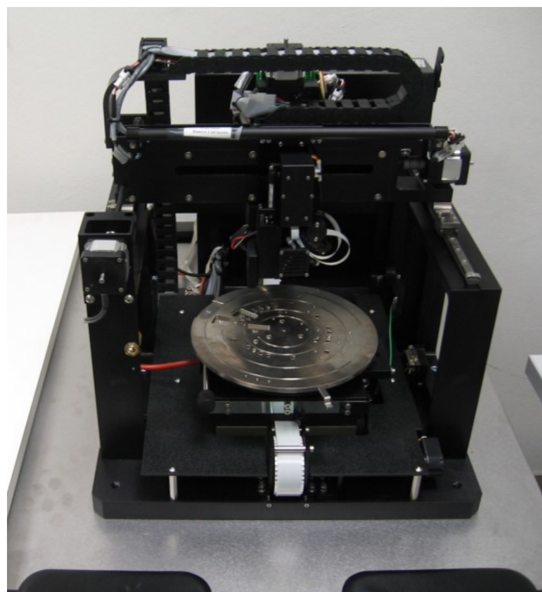

Figure 6.2 Veeco Dektakt 8 profilometer.

The samples are prepared as following. A 10x10 mm sapphire is used as substrate in order to have a very flat surface as a starting point. Half part of the substrate is screened during the deposition process (on paragraph 7.3.5 the procedure will be describe more in detail). The sample is then characterized on the profilometer, with a scan along the step created between the nude sapphire surface and the Nb film. The typical profile curve is visible in Figure 6.3.

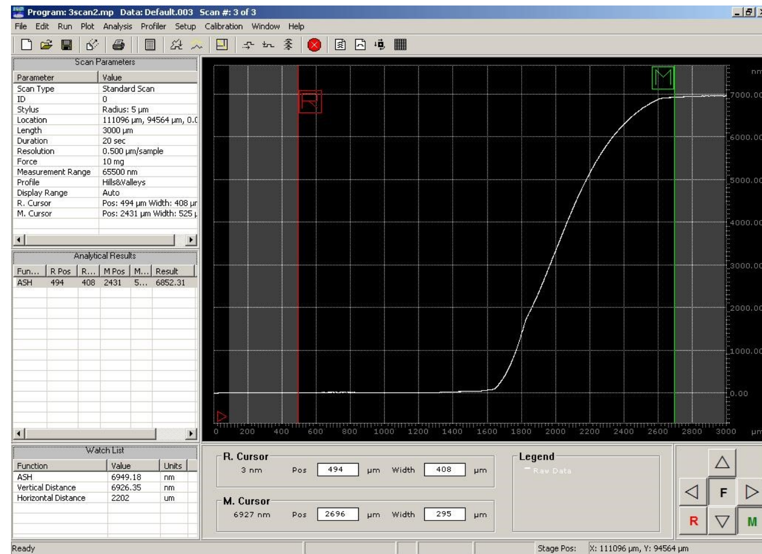

Figure 6.3 Typical profile curve for the samples thickness of this work.

6.3 Optical inspection

The optical inspection is performed to check an eventual defect evolution. The inspection is done before and after each polishing treatment, without any risk to touch the internal surface of the small cavity. The system was developed at LNL few years ago and automatized in 2013 [80]. It is made up of three main parts: miniature camera, mechanical support and a PC. The acquired images magnification is around 60x. Positioning the mobile tool near the point of interest, focusing and eventually correcting the lightening are the only necessary operations to obtain the desired image. The camera and the cavity can both move forward and backward along the guide, in which a graduated ruler helps to know the camera position inside the cavities. Four small wheels, on the cavity supports, allow the cavity rotation. The rotation angle can be measured by a goniometer.

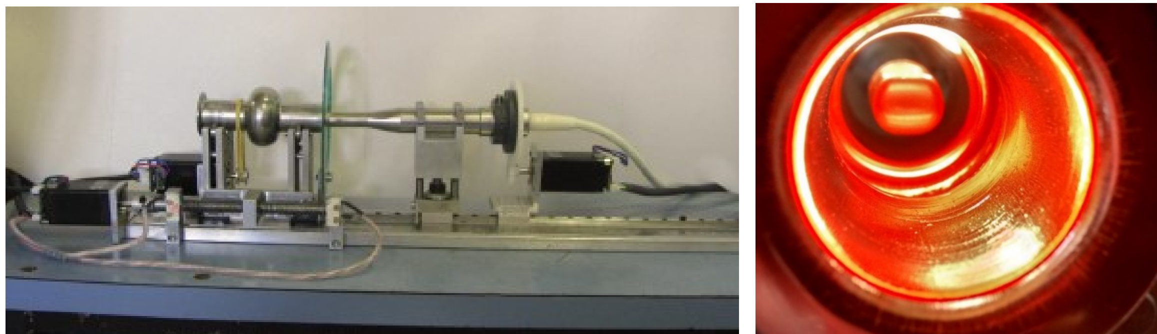

Figure 6.4 Picture of the optical inspection system on the left. Picture of the camera, inside the cavity, during an optical inspection on the right.

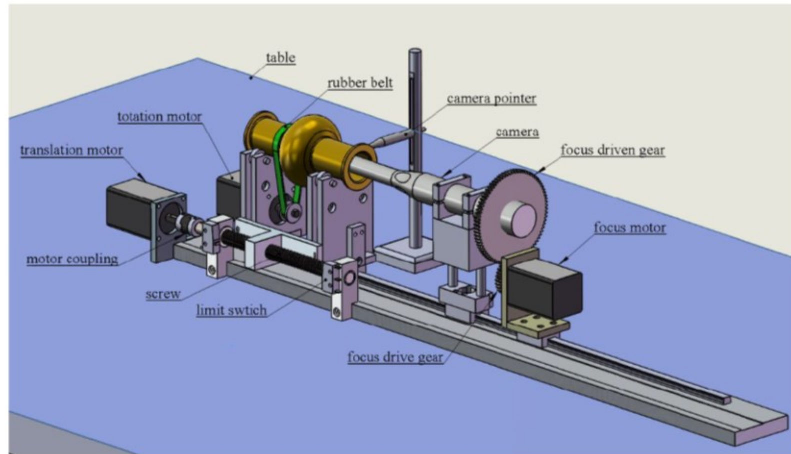

Figure 6.5 schematic diagram of the optical inspection system [80].

6.4 XRD

X-ray diffraction (XRD) is a powerful non-destructive method used to characterize structural properties, such as crystal structure, chemical composition, residual stress, grain size, amount of crystallographic defects. The technique is based on detecting the intensity of a monochromatic x-ray beam scattered hitting a sample surface, as a function of the incident and scattered angle. Because x-rays wavelengths has the same order of magnitude of the typical interatomic distances in crystalline solids, x-rays scattered from a crystalline solid can constructively interfere, producing a diffracted beam (see Figure 6.6). The Bragg's law gives the condition for constructive interference:

$$n\lambda = 2d \sin\theta \qquad \text{Equation 6.3}$$

where n is an integer, λ is the wavelength, d is the interatomic spacing, and Φ is the diffraction angle. The diffracted beam intensity will depend on several factors such as the chemical composition of the film and the local arrangement of the atoms. The x-rays are scattered by the electrons and the resulting angular dependent intensity distribution is measured with a detector. The x-ray diffraction pattern is representative of the crystal structure of the given sample. The scattered beam intensity can be mapped in angular space or reciprocal space (often also referred to as K-space or Q-space). Thus, it is not possible to take a direct image of the real space sample structure with this method. For body-centered cubic crystal, as niobium is, once the interatomic distance d is measured, the reticular parameter *a* can be calculated (for each hkl plane) with:

$$a = \sqrt{h^2 + k^2 + l^2} \cdot d \qquad \text{Equation 6.4}$$

X-rays penetrate several hundred nanometers into the sample, so with XRD we have detailed information about the internal structure. For the characterization of coated films, a x-ray glancing incident angle is used in order to suppress peaks interfering from the substrate. In this configuration, the incident angle is fixed at grazing angles of 1 to 10 ° and the diffraction profile is recorded by detector angle scan only.

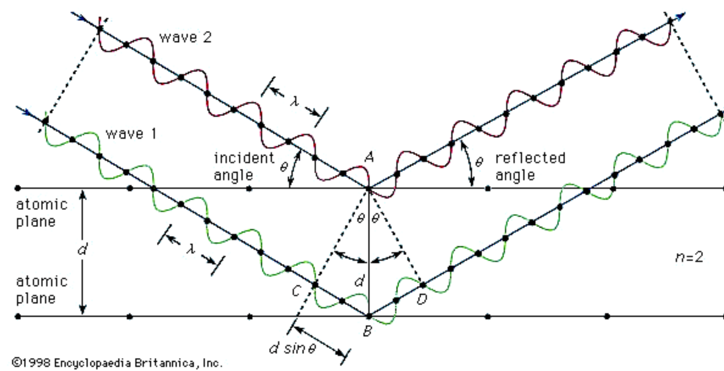

Figure 6.6 Bragg diffraction [109].

Theoretically, in a single crystal free of defects, reflections from the planes would approach a delta function. In a real crystal, the reflection that occurs would be broadened over a range of angles. In polycrystalline materials (the case of sputtered films), the presence of crystallites and grain boundaries reduces the periodicity of the crystal lattice thus broadening the reflection peak. The Scherrer method uses an analysis of x-ray data from a Φ - 2Φ scan to calculate the average crystallite size in a polycrystalline material [110]. For a polycrystalline film, the crystallite size D is given as:

$$\mathrm{D} = \frac{K\lambda}{\Delta_{2\theta}\cos(\theta)}$$ **Equation 6.5**

λ is the x-ray wavelength (0.15418 nm) for Cu Kα, 2θ is the location of the peak, $\Delta_{2\theta}$ is the full width at half the maximum of the peak (FWHM) and K is the appropriate shape factor (0.94 for cubic crystals) [111]. The Sherrer equation gives a lower limit for the grain size, because it does not take into account the other cause of peak broadening, such as strain, defects, or instrumental effects. Another important aspect to keep in mind is that the calculated grain size represents an average of all grains within the probed region.

The crystal structure of Nb films of this work was characterized at LNL by monochromatic Cu-Kα radiation on a Philips X'Pert X-ray diffractometer operated at 40 kV and 40 mA.

Figure 6.7 LNL-INFN Philips/PANalytical X'Pert X-ray diffractometer.

6.5 SEM

Scanning Electron Microscopy (SEM) is a versatile and widely used tool wich allows high magnification observation of samples, with great resolution and easy sample preparation, in order to have surface morphology information. Combined with energy dispersive X-ray spectroscopy (EDS or EDX), it is capable of fast elemental analysis at high resolution.

The area to be examined is irradiated with a finely focused electron beam, which performs a raster scan across the sample surface. The types of signals, which are produced when the focused beam impinges on a specimen surface, include secondary electrons, backscattered electrons, characteristic x-rays, Auger electrons, and photons of various energies. The primary signal of interest is the variation in secondary electron emission that takes place as the electron beam is swept in a raster across the sample surface, due to differences in surface topography. The secondary electrons yield is confined near the beam impact, which permits images to be obtained at a relatively high resolution. The 3D appearance of the images is due to the large depth focus of the SEM. The analysis of the characteristic x-ray radiation emitted from the region at which the electron bombardment occurs, with a combined EDS, yields compositional information of both a qualitative and quantitative nature [112].

In this work a Philips XL 30 as SEM and a Bruker X-Lash Detector 410-M for the EDS analysis it have been used (Figure 6.8).

Figure 6.8 LNL-INFN Philips XL 30 SEM.

7 Deposition system and procedure

On this chapter the vacuum system and the magnetron source used in this work are described, along with the deposition parameters explored in this work and the entire tests done in order to optimize the deposition process.

My contribution was the design of the vacuum system and the magnetron source while the entire SRF group did the assembling. I also directly realized all the tests for the deposition parameters choice and wrote the Labview program used in the multilayer deposition.

7.1 Vacuum system

The vacuum system used for the deposition is a refurbishing of the vacuum system used in a previous master degree thesis [113]. The system was totally dismounted, cleaned and remounted in a different way, in order to improve the vacuum performance. In the previous version, the 6 GHz vacuum system was part of a complex vacuum system, composed by four chambers. We decided to separate it in a single vacuum system for practical and technical reasons. To do that, part of the instrumentation has been changed. Moreover, during this work several upgrades have been done. For the sake of simplicity the present version of the vacuum system is hereby described.

The description of the vacuum system follows the scheme of Figure 7.2, starting from the exit pipe. The primary pump is a Pfeiffer DUO 20 rotary pump (RP) that reaches a vacuum in the order of 10^{-3} mbar. The rotary pump is closed by an electropneumatic valve (V1) that opens when the pump is switched-on and closes with the switching off. The system is provided with an absorption trap (ZT) to avoid the backstreaming problems, placed between V1 and RP. Another VAT angle valve (V2) is used to isolate the rotary pump during leak tests. Beyond the turbo pump, the UHV part of the vacuum system begin. The turbo pump is a Pfeiffer TMU071 P 60l/s. During the sputtering process (pressure of the order of 10^{-2} mbar) the standby option on turbo pump is activated in order to reduce the rotation speed and avoid waste of argon gas and turbo pump motor fatigue. A gate valve (GV) separates the turbo pump from the sputtering chamber. The sputtering chamber is composed by three long pipes, connected together, and flanged with standard CF100. The lower part of the sputtering chamber is inserted into a big coil that gives the magnetic field for the magnetron confinement during the deposition process. The 6 GHz cavity (and obviously the

cathode too) is housed in this zone of the sputtering chamber. The upper part of the pipe is flanged to the turbo pump and presents several CF flanges necessary for vacuum gauge, gas lines, safety valve and thermocouple. On the top of the sputtering chamber there is a CF100 flange used to insert the cathode and the 6GHz cavity to deposit. Two pressure gauges are connected to the sputtering chamber: full range Pfeiffer (10^{3}-10^{-10} mbar) BAG and a capacitive CMR264 Pfeiffer (1 - 10^{-4} mbar) CG. Three gas lines arrive to the chamber: nitrogen for the venting, pure argon for the sputtering and pure nitrogen for the high temperature venting (see paragraph 7.3.6.2). Pure argon and pure nitrogen are N60 (purity 99.9999%) and are provided by two 5l bottles fixed in the system.

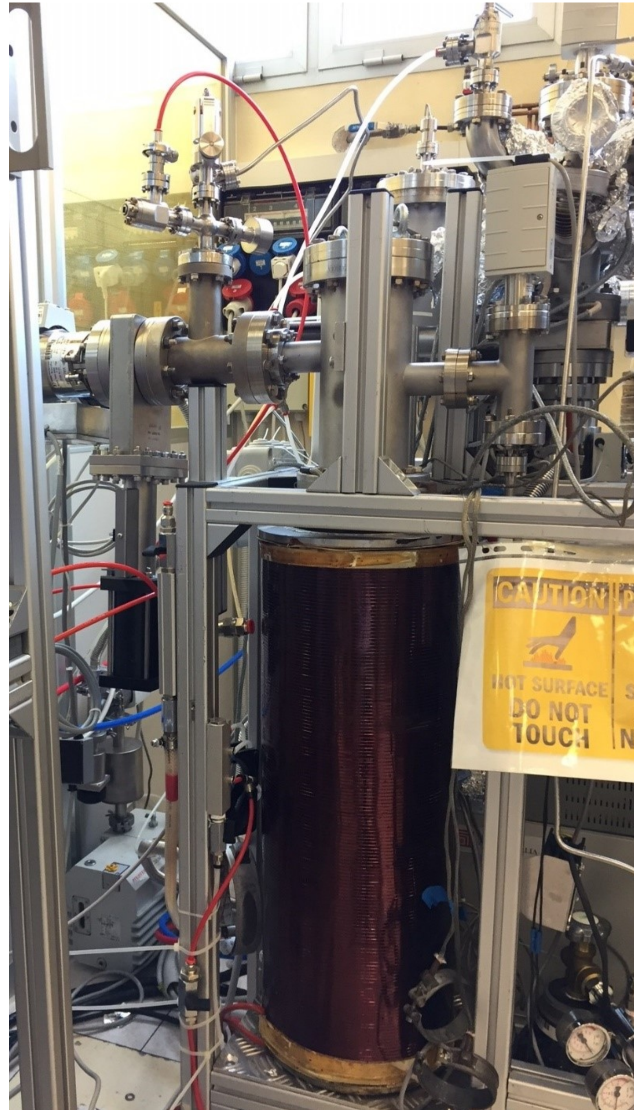

Figure 7.1 Picture of the deposition system used in this work for the deposition of the 6 GHz cavities

The base pressure of this system is about 1-2 ▪ 10^{-9} mbar (sometimes 8▪10^{-10} mbar) after 2 days of baking at 200 °C. For the baking of the system, we use resistive collars on each CF flange.

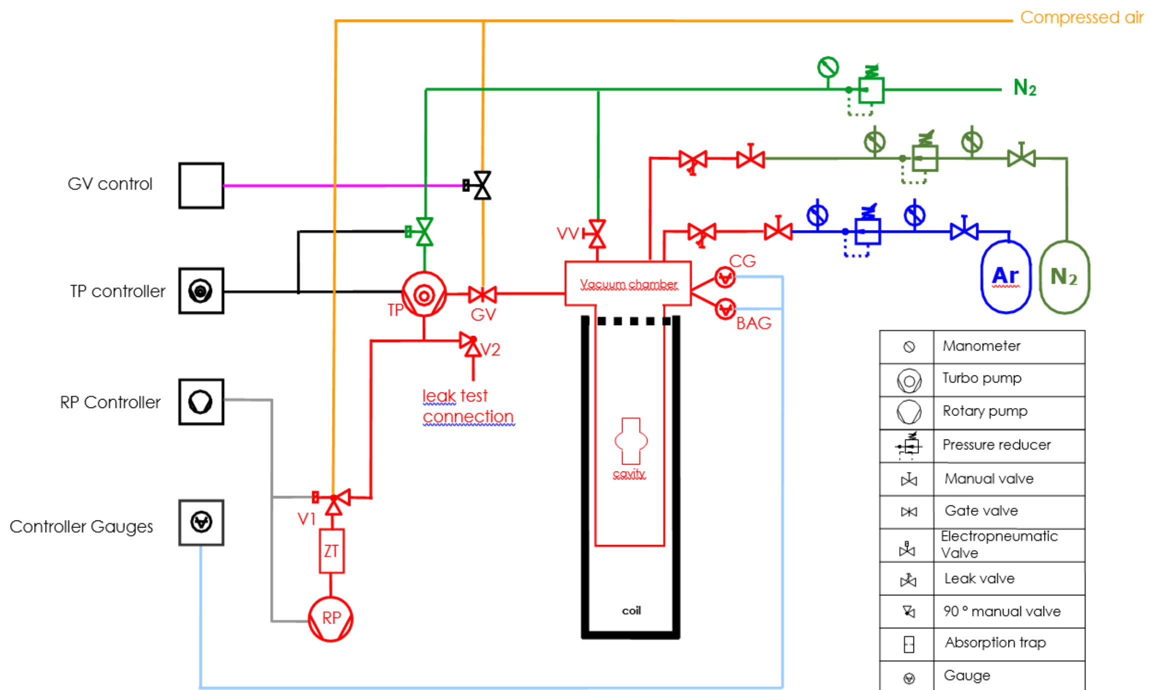

Figure 7.2 Scheme of the vacuum system

7.2 The cathode

The dimensional constrain of the 6 GHz cavities imposed the design of a compact sputtering source, where Nb cathode, 6 GHz cavity and IR lamp, are mounted together (with the appropriate electrical insulation) on a CF100 flange. The result is visible in Figure 7.3 and Figure 7.4.

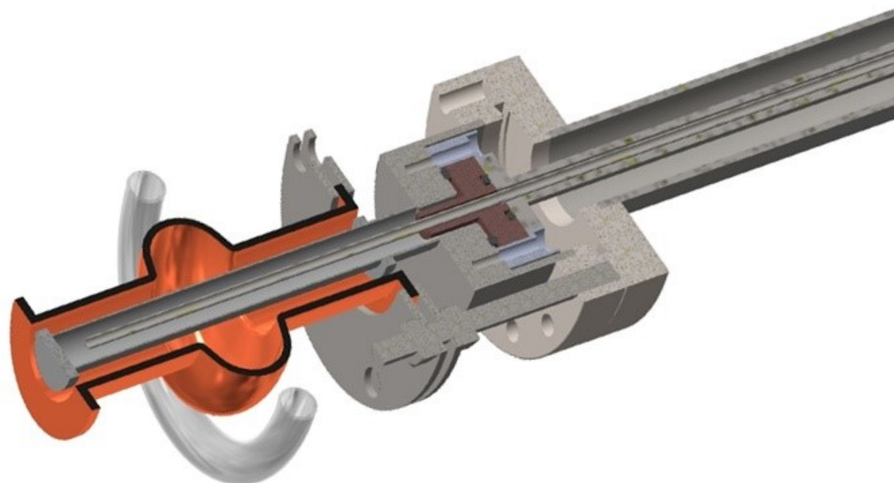

Figure 7.3 3D section of the "compact magnetron sputtering source" used in this work.

We chose the post magnetron configuration, since in the cylindrical symmetry it allows a high plasma confinement, fundamental for the low mean free path of electrons inside the cavity: in the cut off, distance between cathode and cavity is less than 5 mm. The cathode is a Nb RRR300 rod of 11 mm of diameter, 160 mm long, but with an active length of 100mm (the length of a 6 GHz from

flange to flange). The two wings have a diameter of 15.5 mm. On the upper part of the cathode a screw is machined in order to connect the cathode to a copper baseplate. The vacuum sealing is done with a viton o-ring. The cathode active part must be exclusively the one inside the cavity; an alumina tube prevents the sputtering of the non-active upper part. To water-cool the cathode during the deposition, 7.5mm hole is done on the Nb rod. An external coil is used to produce a magnetic field of 800 Gauss necessary for the magnetic confinement of the plasma (see Figure 7.1).

Two stainless steel rings are used to sustain and center the 6 GHz cavity and the IR lamp used to heat the cavity copper surface. Around the IR lamp a copper sheet screen is placed in order to increase the heating efficiency. A thermocouple is fixed on the cavity cell in order to measure the temperature.

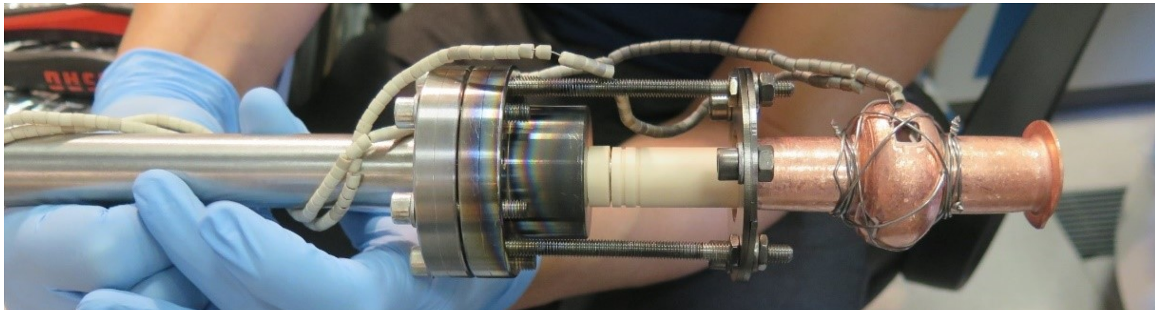

Figure 7.4 Side view of the "compact magnetron sputtering source" used in this work. A cavity test with quartz sample is mounted.

Figure 7.5 Bottom view of the "compact magnetron sputtering source". Centering the cathode with respect to the cavity is very important in order to have a symmetrical deposition process.

7.3 Coating parameters

As we saw in chapter 2, the principal magnetron sputtering critical parameters are pressure, temperature, current and magnetic field. In the following paragraphs the tests done to evaluate the influence of each parameter in the Nb thick film growth are shown and the reasons behind the choice of each single critical parameter are exposed. The different values used in the 6 GHz cavity

depositions are also highlighted for each parameter. Two different deposition processes are investigated: the standard one shot mode in which a single thick layer is grown, and a multilayer mode in which the thick film is composed by hundreds of thin films. Last, we explore the possibility to adapt the doping process of bulk cavities [114] [115], to the Nb on Cu cavities. We call this procedure “High temperature venting”. Resuming, in this work the cavity depositions are carried out with the following set of parameters:

- cavity temperature: 550 °C (600 °C during the preliminary baking process);
- argon pressure: from $7\cdot10^{-3}$ to $5\cdot10^{-2}$ mbar;
- cathode current: 1 A (0,017 A/cm^2);
- standard thickness: from 20 µm to 70 µm (on the cell);
- deposition time: 4-9 hours;
- deposition mode: one shot or multilayer;
- venting mode: standard or high temperature.

Heat treatments, as post treatments, are also investigated. We study the effect of annealing at 600°C and the baking at 120°C on thick film cavities.

7.3.1 Nomenclature

To identify the coating process, we use two numbers: a process number and a cavity number.

Cavity number

The cavity number, identifies the cavity substrate and the coating at the same time. Each 6 GHz copper cavity has a different number marked on the external surface. Each coating is defined by a set of numbers composed in these way: X.Y. Where X is the substrate number (1,2,3,…) marked on the cavity, and Y defines the coating process (0,1,2,…). The Y number is necessary because after the characterization, the coating can be stripped and the substrate reused again for a new coating process.

Process number

The process number helps us to identify immediately the single treatment performed in one cavity. It is a univocal number, referred to a single treatment characterized by a Q VS E_{acc} curve (at 4.2K and 1.8K). Every post treatment, like for example a BCP on the Nb film or a baking process, has a different coating number. For a single cavity number we can have one or more coating numbers. Coating numbers and cavity numbers are not necessarily chronologically ordered.

The cavity number plus a letter compose the coating number. The letters from A to E, identify the following treatments:

A: coating treatment

B: BCP treatment

C,D,E: heat treatment

For example, the process number 3.0.A, identifies the rf test of the first coating on cavity 3, as sputtered. The process number 7.1.B, identifies the rf test of the second coating on cavity 7, after the BCP.

7.3.2 Magnetic field and current

In this work two different external coils are used. The first one comes from the old sputtering system (see paragraph 7.1) and is visible in Figure 7.6. Because of its small length, it did not guarantee the magnetic field uniformity, as is reported on Figure 7.7. The plasma confinement is strongly influenced by this non-uniformity, and at low pressure the plasma is present only in the upper part of the cathode. To obtain a uniform plasma along the cathode, at pressure above $4{\cdot}10^{-2}$ mbar is required. Only one cavity (cav 1.0) was sputtered with this magnetic configuration.

Figure 7.6 Deposition system with the small coil.

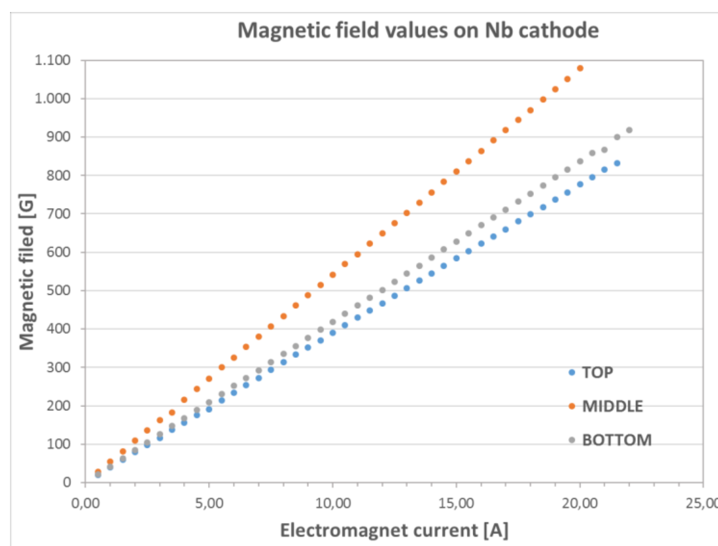

Figure 7.7 Magnetic field in function of the position in the cell. The magnetic field is maximum in the middle of the cathode. Top and bottom values are very similar, but at 800 Gauss on the cell, the magnetic field on the cut offs is in the order of 600 Gauss.

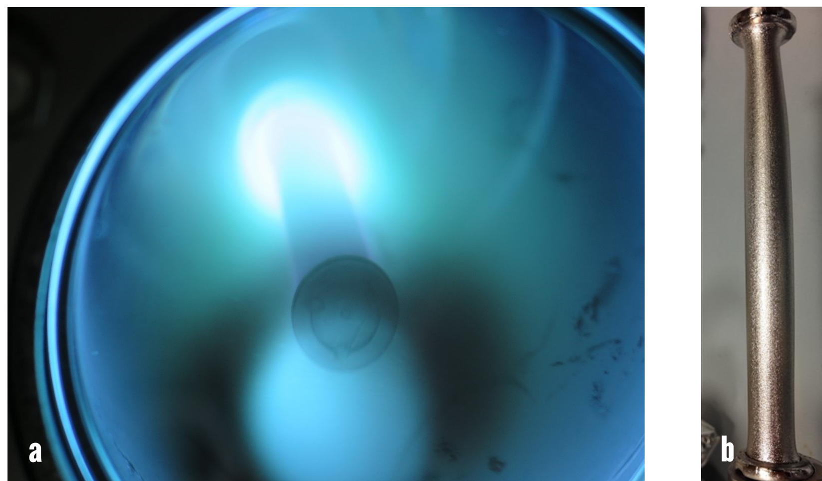

Figure 7.8 The non uniform plasma confinement at pressure below $4 \cdot 10^{-2}$ mbar. The upper part maximized target erosion is visible in b.

After the first bad rf test and the impossibility to explore sputtering pressures below $5 \cdot 10^{-2}$ mbar, we decided to substitute the original coil with a new longer one (Figure 7.1), that guarantees perfect uniformity along the cathode length. In all the pressure range, in which the glow discharge is sustained, the plasma covers all the cathode length.

All the deposition, except Cav1.0, are carried out with these magnetic configuration. A magnetic field of 830 Gauss and a Magnetron current of 1 A. The choice of this two parameters was driven by the maximization of the deposition rate in order to reduce the deposition time, critical parameter in thick film deposition, that can reached the 9 hours in our case. 830 Gauss is the magnetic field value for 10 A of current circulating in the coil. This is the maximum current maintainable by the coil during 9 hours of sputtering. At higher current the coil warm-up saturates the power supply. The magnetron current of 1 A, instead, is the maximum value in which the glow discharge is sustainable at pressure below $1 \cdot 10^{-2}$ mbar.

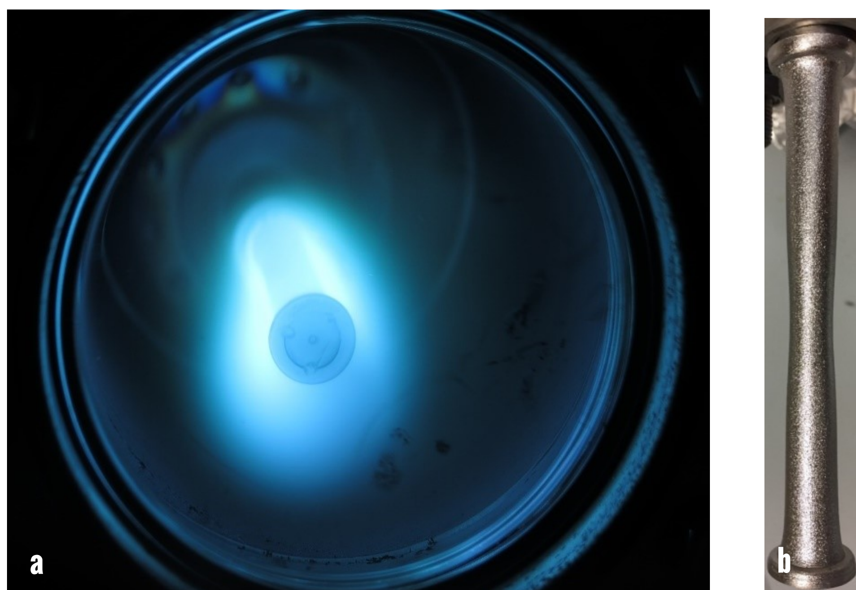

Figure 7.9 A uniform confinement along the cathode length is obtained with the long coil.

7.3.3 Temperature

Temperature plays a fundamental role in the morphology of sputtered film (see paragraph 2.4 and 2.5) and in the case of Nb on Cu we need to choose a compromise between the high melting point of Nb (2469 °C) and the low melting point of Cu (1085 °C). The copper above 400-500 °C becomes softer and could loose his mechanical properties. On the other hand, for Nb, homologues temperature T_h in the order of 0.5 are desirable to enter the zone 2 and 3 of the Thornton or Anders structure zone diagram and obtain more dense and less stressed films. Temperature in the order of 400 °C was used in the coating of ALPI linac [5] and for ISOLDE too [49]. In this work we tried to increase the temperature, and we fixed it at 550 °C for all cavities. In order to prevent degassing from the surface during the sputtering process, the baking of the vacuum chamber is realized heating both the chamber with resistive collars at 200 °C and the cavity with the IR lamp at 600°C for two days. Over 600 °C the copper becomes too soft and the flange, in which the cavity is sustained during the deposition process, deforms (see Figure 7.10).

Figure 7.10 Flange deformation due to high temperature (650 °C). The copper becomes softer and lose his mechanical properties. A deformed flange is a very probable source of vacuum leaks, avoiding the possibility of the rf test.

7.3.4 Pressure

Pressure is the second critical parameter on the Thornton structure zone diagram [42] and is the main responsible of the intrinsic stress during the film growth (see paragraph 2.5). First, we take a look at the pressure range in which a glow discharge of 1A with a magnetic field of 830 Gauss is sustainable by our power supply (Figure 7.11)

The suitable pressure range starts from $7 \cdot 10^{-3}$ mbar to $8 \cdot 10^{-2}$ mbar. Higher pressures increase scattering, with consequently sputtered atoms with less energy. We did some cavities depositions at the lower possible sputtering pressure in order to have the higher kinetic energy on sputtered atoms, but at the same time, we investigated with a simple experiment the pressure stress curve (see Figure 2.9) in our configuration. The experiment consists of a deposition of a Nb thick film on a flexible kapton sample. The bending assumed by the kapton will show if the stress is tensile or compressive. Several depositions on kapton samples were done at different pressure values, in order to individuate the no stress point. Looking at Figure 7.12 it is clear that the zero stress point, for our configuration is at $5 \cdot 10^{-2}$ mbar.

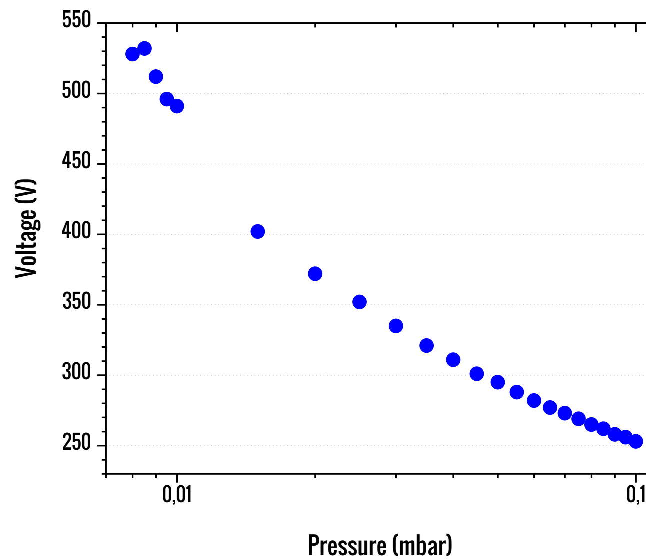

Figure 7.11 Glow discharge voltage as function of the pressure. Magnetron current is 1 A and magnetic field 830 Gauss. The lowest pressure at which the discharge is sustainable with our power supply is $7\cdot10^{-3}$ mbar.

Two principal pressure values were investigated in this work: $7\cdot10^{-3}$ mbar (5 cavities coated: cav 3.1, 4.0, 6.0, 7.0 and 9.0) and $5\cdot10^{-2}$ mbar (15 cavities coated). Two cavities were coated at $1\cdot10^{-2}$ mbar (cav 1.1 and cav 15.0).

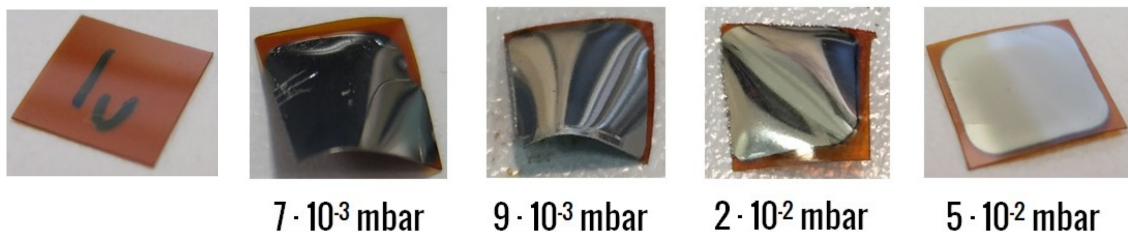

Figure 7.12 Thick films of Niobium (10 μm) sputtered on kapton substrates at different pressure values. We did also a test to prove that the kapton sample do not bends because of the high temperature (first sample from the left).

7.3.5 Deposition rate

We have measured the variation of the deposition rate along the cavity, at the three pressures in which the depositions were carried out. We used the cavity of Figure 7.13 where 6 quartz samples are placed in different points of the cavity. The quartz are masked in order to obtain a sharp step, to be easily measured at the profilometer (see paragraph 6.2). The ratio between measured step thickness and deposition time gives us the deposition rate value.

The deposition rates measured at different pressure and in different point of the cavity are visible in

Table 7.1. The shadow effect of the masking introduces a not negligible error in the measure. More tests were done at $5*10^{-2}$ mbar in order to increase the confidence in the deposition rate at the most common pressure of this work.

Table 7.1 Deposition rate along the cavity, at the different pressures of the deposition process.

Pressure (mbar)	Cell (nm/s)	Iris (nm/s)	Cut off (nm/s)
$7 \cdot 10^{-3}$	2.8 ± 0.5	2.8 ± 0.7	5.6 ± 1.2
$1 \cdot 10^{-2}$	2.6 ± 0.6	2.5± 0.8	5.5 ± 0.8
$5 \cdot 10^{-2}$	2.5 ± 0.2	2.8 ± 0.3	5.3 ± 0.9

The standard deposition process at $5 \cdot 10^{-2}$ mbar takes 7 hours. That means about 70 microns grown on the cavity cell and about 120 microns grown on the cavity cut off.

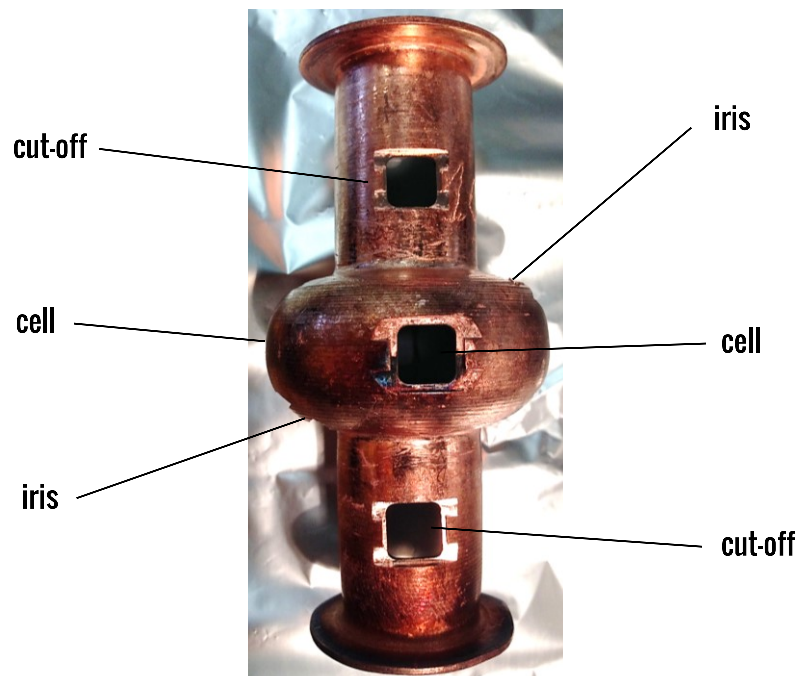

Figure 7.13 Cavity test with 6 sample holders for 10x10 quartz, sapphire or copper substrates.

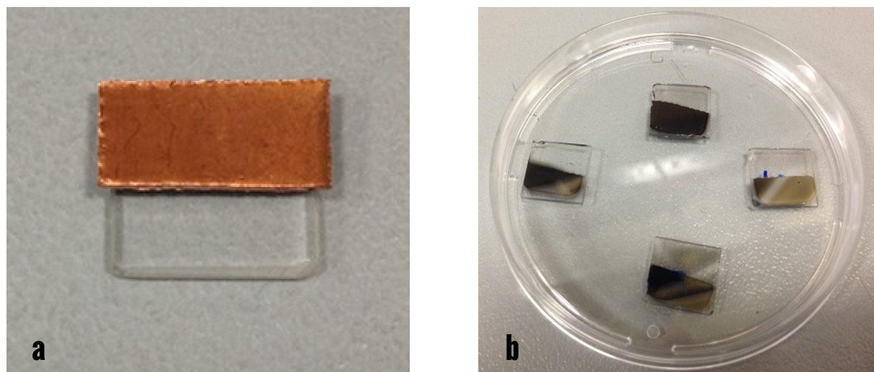

Figure 7.14 On the left masked sample and on the right sputtered masked samples ready for the characterizations.

7.3.6 Venting modes

Taking advantage from the opportunity offered by thick films, on several cavities (Cav 1.0, 1.1, 3.0, 3.1, 4.0, 5.0, 5.1, 6.0, 7.0 and 13.0) a variation of Nb doping protocol used for LCLS-II [115] was done and we called this process high temperature venting.

In order to distinguish the different procedures applied to the cavities after the coating processes applied, we can identify two different venting modes: standard venting and high temperature venting. The procedures are described below.

7.3.6.1 Standard venting mode

After the end of the sputtering process, the IR lamp is turned off and the argon gas valve is closed. The chamber is than vented, with the service nitrogen, after a night of cooling. Schematically, we can identify two times: t_0 and t_1.

Table 7.2 Standard venting mode description

time	action	P (mbar)	T (°C)
t_0 (after sputtering)	Turn off power supply and IR lamp. Close Ar gas valve.	$< 10^{-7}$	550
t_1 (after a night of cooling)	Venting the chamber with service nitrogen.	1000 (N_2)	≈ 30

7.3.6.2 High temperature venting mode

In LCLS-II Nb bulk cavities production, the doping process requires 2 minutes at 800 °C, with a pure N_2 pressure of $3{,}5 \cdot 10^{-2}$ mbar. Then, an annealing process, without nitrogen pressure, at 800 °C for 6 minutes is done. With copper, 800 °C is a temperature unachievable without losing mechanical properties of the cavity (see paragraph 7.3.3). To adapt this process at the sputtered cavities, we maintain the same pressure value, but we increase the treatment time, in order to have a comparable diffusion length. Doing some math on the second Fick law, we can write:

$$\frac{x}{2 \cdot \sqrt{D_T \cdot t}} = cost \qquad \textbf{Equation 7.1}$$

where D_T is the diffusion parameter at the temperature T and t is the diffusion time. Knowing the diffusion parameter at the two different temperatures of interest, we can calculate the diffusion parameter at 800 °C, and then extract the time value at 550 °C to obtain the same diffusion length, using:

$$x_T = 2 \cdot \sqrt{D_T \cdot t} \qquad \textbf{Equation 7.2}$$

On [116] we found the diffusion parameter at 550 °C and 800 °C ,respectively $D_{550} = 4{,}2 \cdot 10^{-11}$ cm^2/s and $D_{800} = 5{,}19 \cdot 10^{-10}$ cm^2/s. In order to have x_{550} of the same order of magnitude of x_{800}, we adopt the process described in Table 7.3 and below.

Table 7.3 High temperature venting mode description

time	action	P (mbar)	T (°C)
t_0 (after sputtering)	Turn off power supply. Close Ar gas valve. Open pure N_2 gas valve.	$3.5 \cdot 10^{-2}$ (pure N_2)	550
t_1 (10 min later t_0)	Close pure N_2 gas valve.	$< 10^{-7}$	550
t_2 (20 min later t_1)	Turn off IR lamp.	$< 10^{-7}$	550
t_3 (after a night of cooling)	Venting the chamber with service nitrogen.	1000 (N_2)	≈ 30

After the end of the sputtering process, the argon gas valve is closed and the IR lamp is maintained on. The pure nitrogen gas valve is then open at $3.5 \cdot 10^{-2}$ mbar for 10 minutes. Passing this time, the IR lamp is turned off and the pure nitrogen gas valve is closed. The chamber is then vented, with the service nitrogen, after a night of cooling. Schematically, we can identify four times: t_0, t_1, t_2 and t_3.

7.3.7 Multilayer mode

The depositions on cavities are carried out in two different ways, called respectively: one shot and multilayer deposition. Multilayer approach was applied to the last coated cavities: cav 8.1, 10.1, 12.0, 12.1, 16 and 17.

One shot mode

The one shot deposition is the standard way to approach the DC magnetron sputtering deposition. Knowing the deposition rate, the power supply is turned on for the calculated time necessary to grow the set film thickness. For 70 µm the time is 7 hours. Then the power supply is simply turned off and one of the venting procedure described in 7.3.6 can start.

Multilayer mode

In multilayer deposition, the power supply is switched on and off continuously, with a fixed duty-cycle of 0.7, as we can see in Figure 7.15. The idea is that the pause time is a sort of self-annealing, in which the adatoms have the time to rearrange on the surface and reduce the film stress.

The deposition is carried out with a software, developed at LNL, in Labview®, able to drive the power supply and to control all the sputtering parameters. We have explored the effect, on cavities performances, of different single layer thickness (100, 300, 400, 500 nm), keeping the total thickness fixed. The single layer thickness could be a compromise between SRF properties (that increase with thickness) and stress (that could be reduced decreasing the thickness).

In other works on semiconductors, it has been shown how this kind of multilayer approach can modify the morphology of the deposited film in function of the pause length [117]. At LNL the multilayer approach was also used to reduce the film stress in the radiopharmaceutical target production [46]. In this work, an effective influence in stress reduction, especially at low temperature of the substrate has been demonstrated.

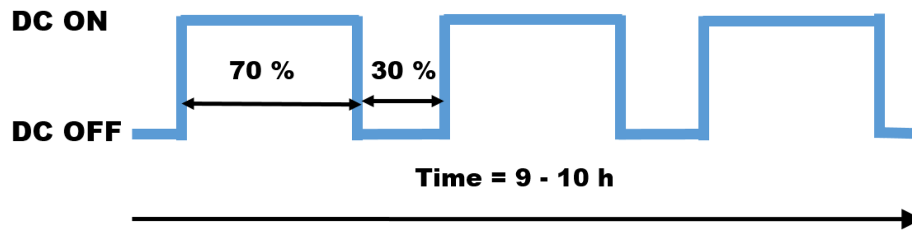

Figure 7.15 Scheme of the multilayer process. Duty cycle has been set to 0,7.

The multilayer approach in SRF was already used in ALPI Linac, but as a constriction due to the increase in cavity temperature during the deposition process. The process, in ALPI production, was done by turning off the power supply when the cavity temperature was close to the baking temperature, in order to avoid an increase in degassing and subsequent possible poisoning of the growing film during the deposition process. The deposition process was then restarted when the substrate temperature returned to the set value of 300 °C [5] [118].

Figure 7.16 Control panel of the Labview® software for the multilayer deposition developed in this thesis work

7.4 Post treatments

7.4.1 BCP

One of the big advantages of thick films is the possibility to use the post treatments normally exclusive of bulk Nb cavities. One of these is the buffer chemical polishing (BCP), used in bulk cavities to remove the surface defects due to mechanical machining [12]. In this work BCP has been used to remove few microns on the surface after the high temperature venting (cav 3.1, 6.0 and 7.0). In LCLS-II production 5 microns of surface material is removed in order to have the right doping level at the London penetration depth. Moreover, we have investigated if the film is poisoning during the night cooling process, removing few microns of the Nb surface in cav 9.0.

The BCP solution used in this work is composed by: hydrofluoric acid (HF), nitric acid (HNO_3) and phosphoric acid (H_3PO_4) in ratio 1:1:3. The function of the 3 acids is the following: nitric acid oxides the niobium surface, hydrofluoric acid dissolves the oxide and phosphoric acid has the role of reaction moderator. To reduce the etching rate of the chemical process, a BCP 1:1:3 is used, rather than the 1:1:2 normally used for bulk niobium.

To measure the etching rate of 1:1:3 BCP solution on Nb sputtered films, we realized the following test. A deposition of 40 microns of niobium onto copper samples was done. Then the sample was etched on the BCP solution until all the niobium was dissolved. From the time of the process, it is easy to obtain the etching rate.

We calculate an etching rate of 1,4 μm/min. In order to remove about 5 microns from the top of the Nb film, 2-3 minutes is the BCP time length used in this work.

Figure 7.17 Two of the samples used for the BCP test. The etching rate on the sputtered films is 1,4 μm/min

The exact etched thickness in a cavity post treatment is defined by the difference in weight before and after the BCP treatment. Anyhow, this measure gives us only an estimation, because the BCP is able also to etch the copper. For that reason, the cavity during the treatment is fully covered with Teflon tape in order to prevent the etching of the external surface. From Figure 7.18 it can be seen how part of the copper flange remains exposed to the chemical solution and contributes to the weight loss altering the measure of film eroded thickness.

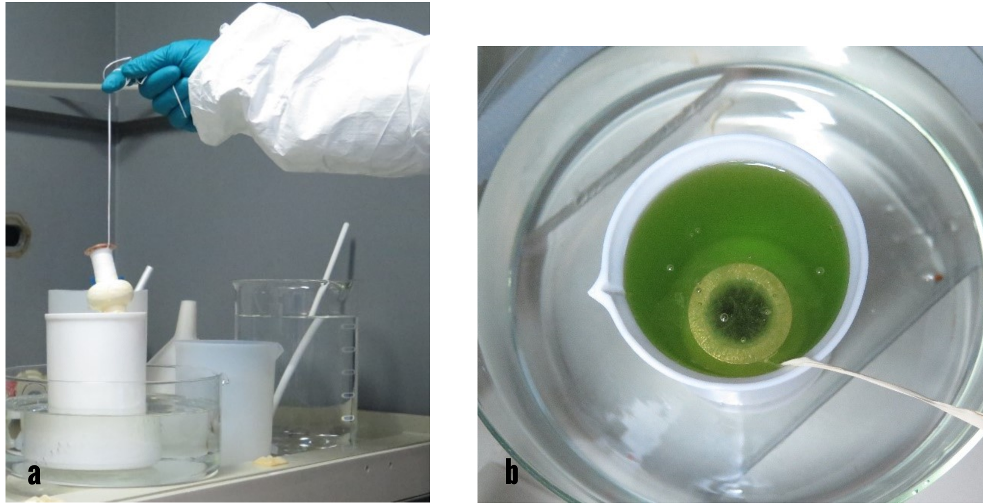

Figure 7.18 BCP of a sputtered cavity. In the pictures is visible the post treatment done on Cav 3.1.

7.4.2 Heat treatments

Heat treatments, as the high-temperature (600-800 °C) annealing for a few hours and the low-temperature (100-120 °C) baking for 24 h, are a fundamental step in Nb bulk cavities preparation, capable to increase the quality factor Q, the breakdown field and also eliminate the high-field *Q*-slope [14] [119] [120]. Heat treatments reduce hydrogen concentration [28], but there is no general agreement in the literature on the mechanisms of this effect and this issue remains an area of active investigation [14].

In this work, it is investigated if in thick film cavities the heat treatments can play a role as in Nb bulk cavities. Both annealing at 600 °C and low-temperature baking at 120 °C are tested in some cavities (cav 3-1, 7.0, 9.0, 13.0 and 16.0). The heat treatments were carried out in the vacuum chamber of Figure 7.19, with a base pressure of 10^{-7} mbar. An infrared lamp identical to the one used in the deposition process is used as heating source.

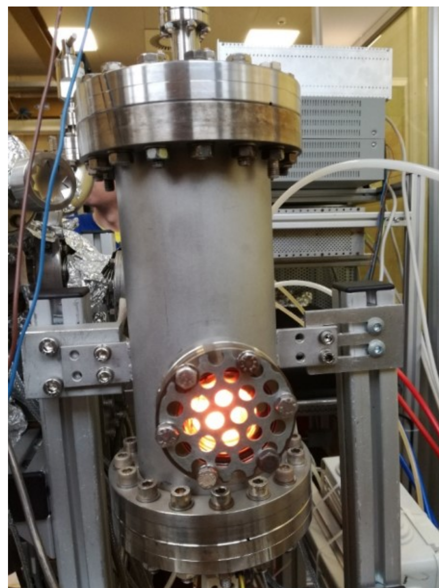

Figure 7.19 Vacuum chamber used for the heat treatments. The heating is realized with an infrared lamp.

8 Results and discussion

On this chapter all the results obtained from the characterization on planar samples and 6 GHz cavities are reported. For each cavity, the process parameters used and the curve of rf test done, are reported. A complete discussion of the role of each deposition parameter on rf performance is presented.

8.1 Planar sample test

Before proceeding to 6 GHz cavities deposition, some tests were carried out on sapphire and copper planar samples (9x9 mm), in order to check the quality of the sputtered film. A measure of T_c and RRR was done on sapphire substrates, while the XRD, SEM and EDS characterizations were done on the films sputtered on copper substrates. All the samples were sputtered in the following conditions:

Table 8.1 Coating parameters used in the planar samples depositions

Substrate Temperature T (°C)	*Argon Pressure* P (mbar)	*Cathode current* I (A)	*Magnetic field* B (G)	*Deposition Mode*	*Venting mode*
550 (600 °C during the preliminary baking process)	$5 \cdot 10^{-2}$	1 (0,017 A/cm^2)	830	One shot	standard

8.1.1 Superconductive properties

The RRR, T_c and ΔT_c of the samples coated are reported on Table 8.2. We can note how the RRR increases with thickness, confirming a well known behavior of sputtered films [9] [121]. The RRR values at 4.5 microns are also comparable with the ones obtained at CERN, at the same deposition temperatures and thickness. These results, in line with the best values in literature, confirm the quality and the cleanness of our system deposition and configuration, pushing us to explore the effect of Nb thick films in resonant cavities.

Table 8.2 Superconductive properties of Nb on sapphire samples

Thickness (µm)	RRR	T_c (K)	ΔT_c (K)
4,5	34,9	9,33	0,0484
7,5	43,7	9,32	0,1081
15	66,4	9,28	0,0090
18	50,0	9,30	0,0387
22	63,0	9,26	0,0196

8.1.2 XRD

The XRD was done on samples coated on copper substrate, in order to take into account also the substrate contribution. The high temperature produces a very sharp peaks on XRD spectra, index of big crystal grains and a crystal structure with few defects. Nb thick film grows with a preferential (110) orientation. Reticular parameter is 3,313 Å, very close to the reported Nb bulk value of 3,306 Å. The estimated grain size is about 40 nm. The values are underestimated, because the FWHW of XRD is affected not only by grain size, but also by crystal defect. For a comparison, with the same method, grain size of samples coated with a CERN standard procedure shows dimension around 10 nm [122].

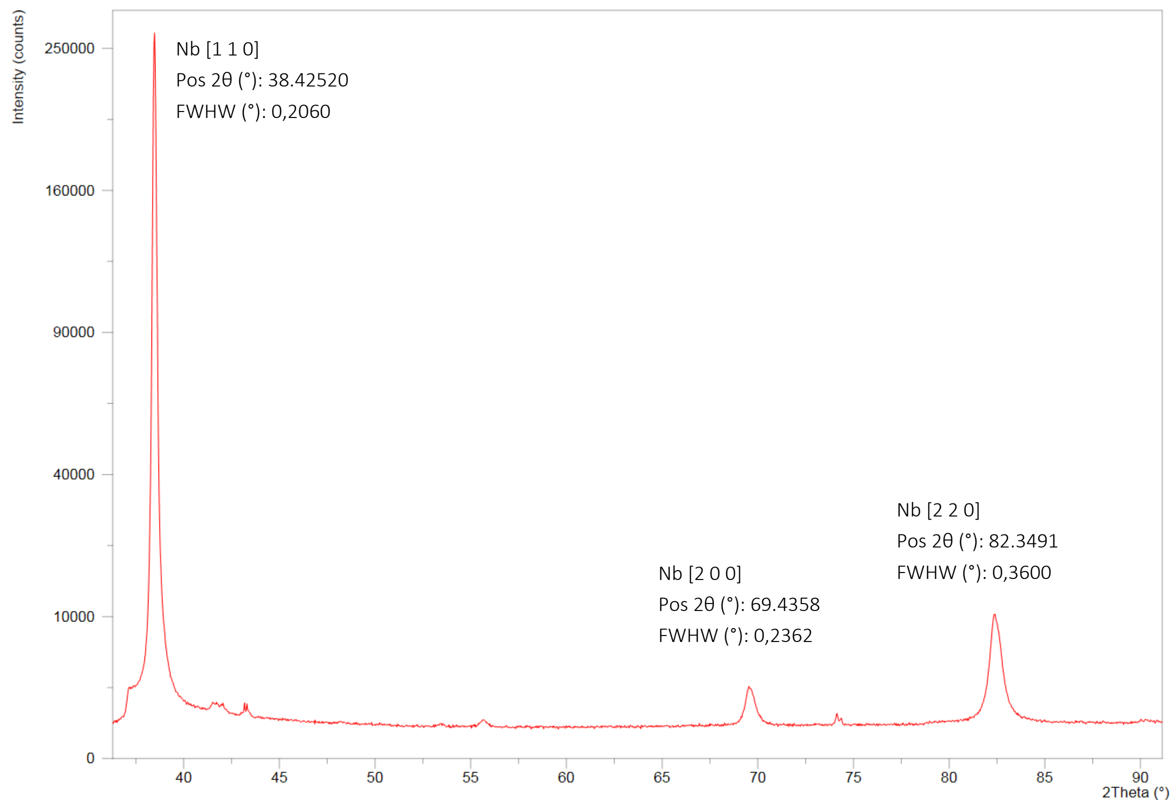

Figure 8.1 XRD spectra of 10 µm thick film coated with the parameters of Table 8.1.

8.1.3 SEM and EDS

Niobium thick film on copper shows a needle-shaped grain structure with an average longitudinal dimension of about 0,5 µm (Figure 8.2). The EDS analysis on surface confirms the presence of a very pure Nb: no traces of any other element except Nb is present. The cross section of the samples were done cooling the sample in liquid nitrogen and breaking the sample by fatigue method in order to preserve the film-substrate interface. This simple cutting method is unworkable on 6 GHz cavity. The 6 GHz cavities film microstructure will be characterized at Daresbury laboratories of Science & Technology Facilities Council (STFC) with more sophisticated technologies. Planar sample cross section (Figure 8.4) shows very dense microstructure: no columnar growth is visible. The EDS cross section map confirms the immiscibility of Nb and copper even at 550 °C.

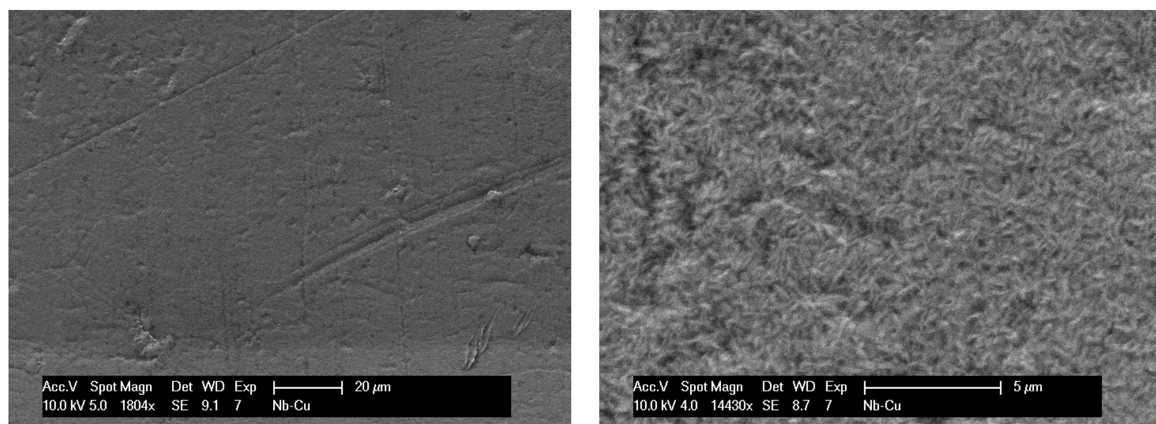

Figure 8.2 SEM Micrographs of the Nb film surface at two different magnifications.

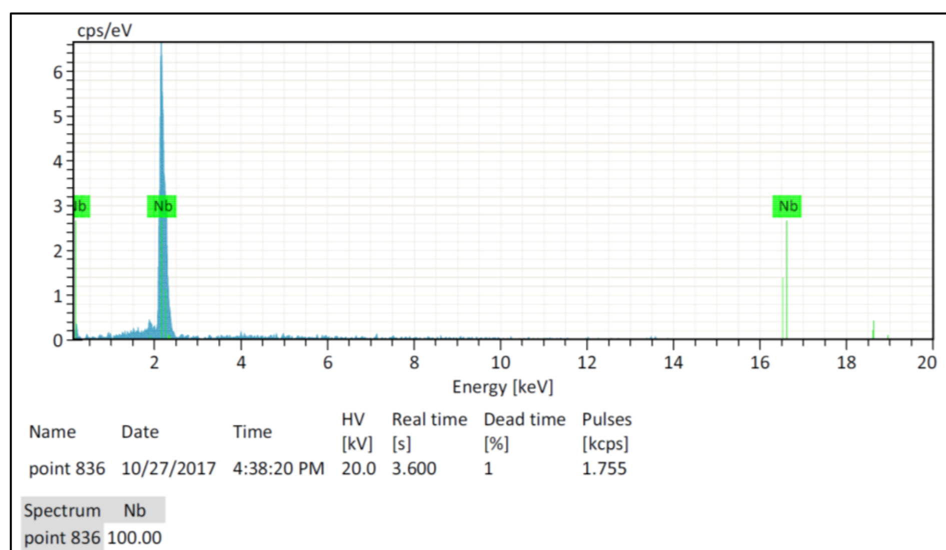

Figure 8.3 EDS spectra of a portion of the surface of Figure 8.2.

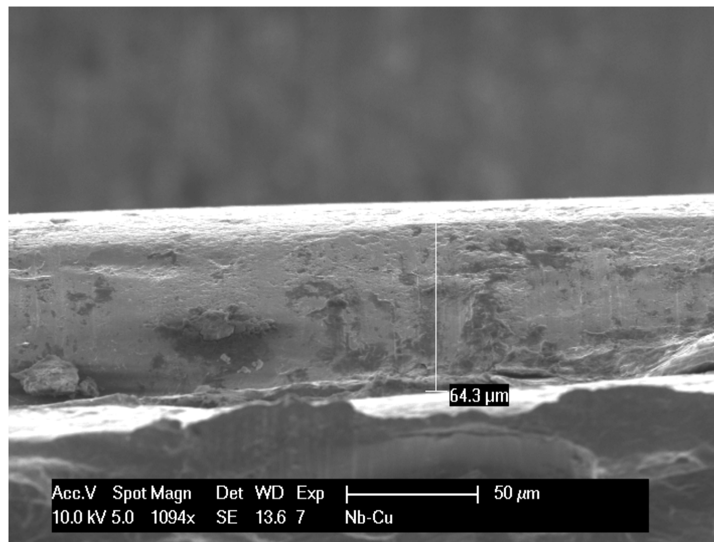

Figure 8.4 SEM micrograph of the film cross section.

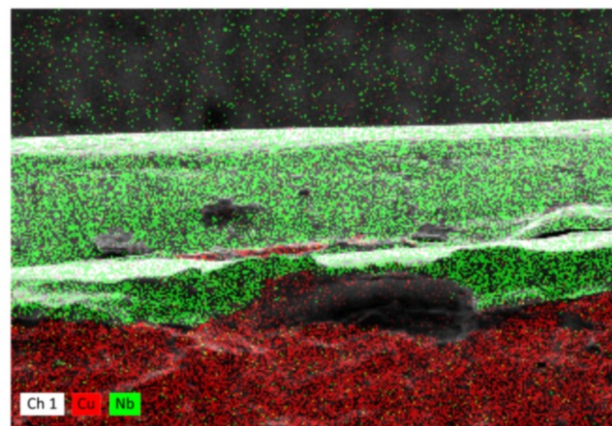

Figure 8.5 EDS map of the film cross section.

8.2 Cavity rf test

All the new spun cavities (identifiable by the number x.0) depositions of this work are carried out following this protocol:

1. lapping of the flanges;
2. degreasing with soap in ultrasonic bath;
3. 1 hour electropolishing;
4. 5 minutes chemical etching SUBU5;
5. 3 minutes passivation;
6. high pressure water rinsing (HPWR) at 100 bar;
7. baking at 600 °C for 48 hours;
8. coating;
9. HPWR at 100 bar;
10. rf test;
11. post treatment (eventual);
12. rf test.

At the end of the process, the cavity is stripped and reused again for another coating process (identifiable by the number x.1, x.2, etc.).

In the following pages a report of all the deposition conditions, post treatments, optical inspection of cell and iris, and rf tests done for each cavity coating is presented. All the conditions parameters and post treatments are already described in the previous chapter. Some notes are reported to show and explain particular choices or parameters that are different from the standard procedure described before. The discussion on the rf tests are presented in paragraph 8.3, in order to offer a more comprehensive view of all the obtained results. The resume table, where maximum Q and maximum gradient are reported, helps to have a picture of all the depositions done, but only the rf test gives the exact prospective on the rf cavity performances.

In this work, through the rf tests, we explore the role on the SRF performances of the following deposition parameters: pressure, venting mode, deposition mode and the effect of the following post treatments: BCP and thermal treatments.

Table 8.3 Resuming table of the depositions parameters and rf test. All the reported test was done at 1.8K.
* cavity coated with small coil.
On deposition mode column, M.100nm means multilayer mode with a single layer of 100nm.

Cav#	Sputtering parameters				rf test as sputtered		rf test after BCP		rf test after baking	
	thickness (μm)	P (mbar)	Deposition mode	Venting	Q_0 max	E_{acc} max	Q_0 max	E_{acc} max	Q_0 max	E_{acc} max
1.0*	100	$5\cdot10^{-2}$	one shot	High T.	4,0E+07	0,7				
1.1	70	$7\cdot10^{-3}$	one shot	standard	4,2 K rf test only					
2.0	frequency of 6.1 GHz: not measurable									
3.0	70	$5\cdot10^{-2}$	one shot	High T.	delaminated					
3.1	70	$7\cdot10^{-3}$	one shot	High T.	5,9E+08	6,9	1,2E+08	1,6	4,2 K rf test only	
4.0	40	$7\cdot10^{-3}$	one shot	High T.	4,2 K rf test only					
5.0	40	$5\cdot10^{-2}$	one shot	High T.	4,4E+08	4,2				
5.1	70	$5\cdot10^{-2}$	one shot	High T.	2,0E+09	3,1				
6.0	40	$7\cdot10^{-3}$	one shot	High T.	4,9E+08	4,4				
7.0	70	$7\cdot10^{-3}$	one shot	High T.	1,7E+07	0,3	1,9E+08	5,7	4,2 K rf test only	
8.0	2	$5\cdot10^{-2}$	one shot	standard	delaminated					
8.1	56	$5\cdot10^{-2}$	M.100nm	standard	3,0E+08	5,9				
9.0	70	$7\cdot10^{-3}$	one shot	standard	2,3E+09	4,2	3,8E+08	7,6	1,6E+09	7,4
10.0	2	$5\cdot10^{-2}$	one shot	standard	Delaminated					
10.1	40	$5\cdot10^{-2}$	M.500nm	standard	6,7E+06	0,4				
11.0	60	$5\cdot10^{-2}$	one shot	standard	2,0E+08	6.5				
11.1	70	$5\cdot10^{-2}$	M.300nm	standard	4,2 K rf test only					
12.0	40	$5\cdot10^{-2}$	M.400nm	standard	7.4E+08	13.2				
13.0	70	$5\cdot10^{-2}$	one shot	High T.	5,6E+08	9,3			1,8E+08	1,4
14.0	70	$5\cdot10^{-2}$	one shot	standard	delaminated					
15.0	70	$1\cdot10^{-2}$	one shot	standard	1,1E+07	0,8				
16.0	70	$5\cdot10^{-2}$	M.500nm	standard	9,5E+08	9,2			2,7E+08	9,9
17.0	70	$5\cdot10^{-2}$	M.400nm	standard	4,2 K rf test only					

Cav 1.0

Chronologically Cav 1.0 is the first cavity coated, and the only one sputtered with the small external coil. In this configuration the deposition rate was higher in the cell than in the cut-offs. The rf performances are very low. No post treatments were done.

Table 8.4 Deposition parameters for Cav1.0. PROCESS 1.0.A.
I=magnetron current, V=magnetron voltage, P=sputtering Ar pressure, B=magnetron magnetic field, T=substrate temperature, d=total thickness on the cell, t=total deposition time.

I (A)	V (V)	P (mbar)	B (G)	T (°C)	d (μm)	t (h)	deposition mode	venting mode
1	≈330	$5\cdot10^{-2}$	810	550	≈100	5	one-shot	High temp.

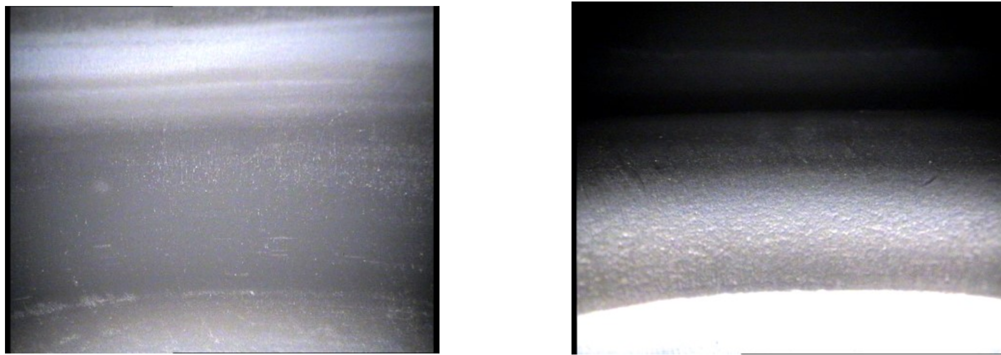

Figure 8.6 Internal inspection of the cell (on the left) and iris (on the right) for Cav1.0.

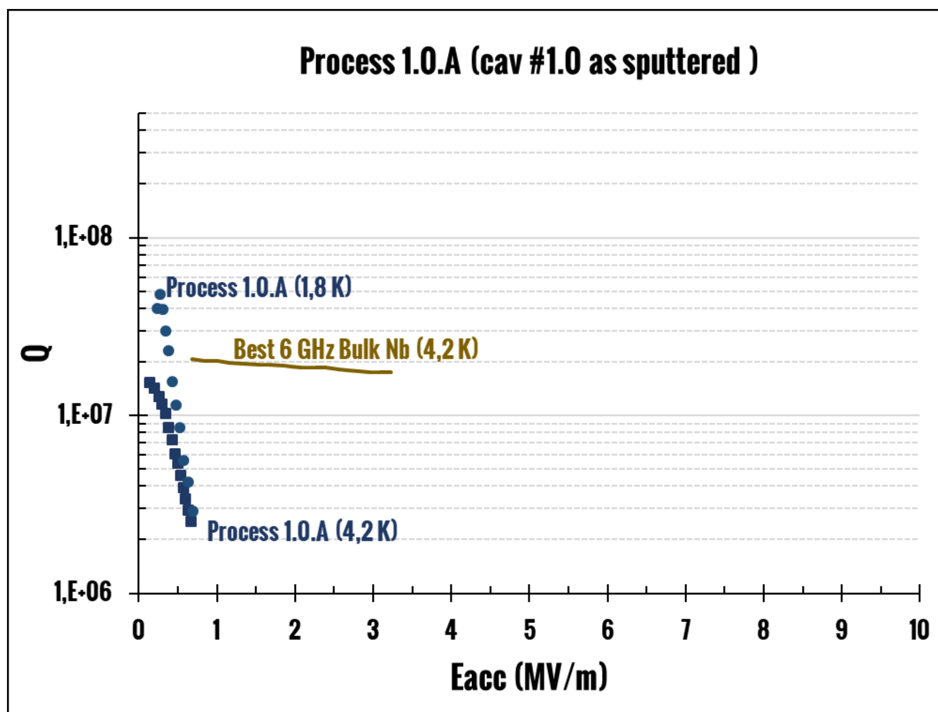

Figure 8.7 Rf test at 4.2K and 1.8K for Cav1.0.

Cav 1.1

Cav 1 was stripped from Nb film and re-coated in the new configuration with the big coil, which guarantees a better magnetic field uniformity. Rf test was done only at 4.2 K, because a vacuum leak appeared at helium λ point during the cool down at 1.8 K. No post treatments were done.

Table 8.5 Deposition parameters for Cav1.1. PROCESS 1.1.A.
I=magnetron current, V=magnetron voltage, P=sputtering Ar pressure, B=magnetron magnetic field, T=substrate temperature, d=total thickness on the cell, t=total deposition time.

I (A)	V (V)	P (mbar)	B (G)	T (°C)	d (μm)	t (h)	deposition mode	venting mode
1	≈530	$1 \cdot 10^{-2}$	830	550	≈70	7	one-shot	standard

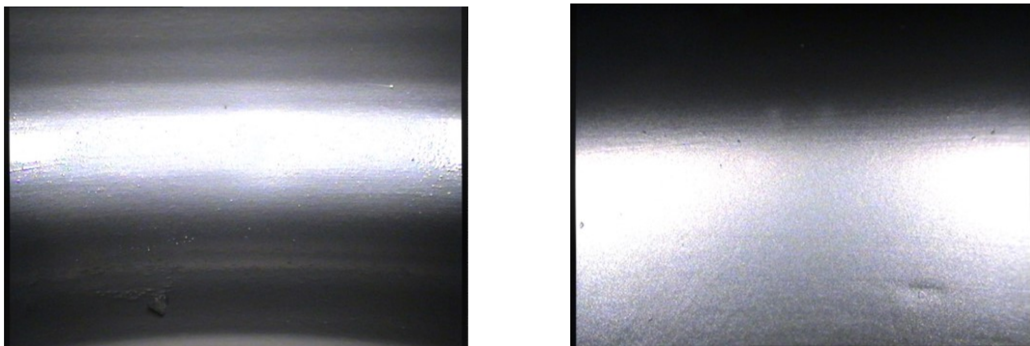

Figure 8.8 Internal inspection of the cell (on the left) and iris (on the right) for Cav1.1.

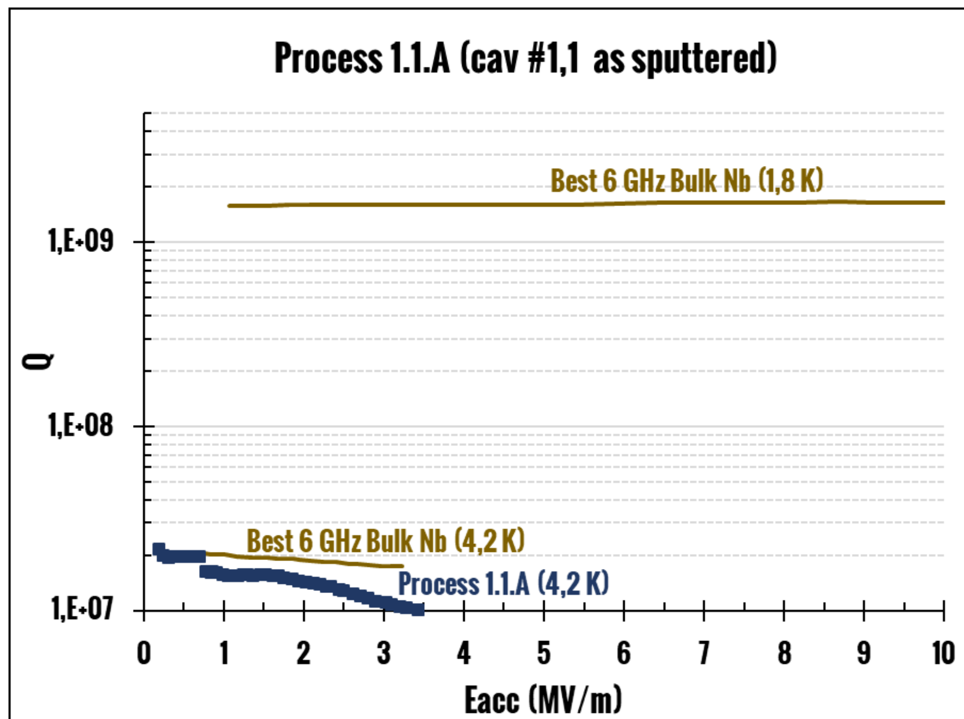

Figure 8.9 Rf test at 4.2K for Cav1.1.

Cav 3.1

Cav 3 was stripped from Nb after two failed depositions in which peeling occurred. On Cav 3.1 a high temperature venting was done. This is the first cavity that presents a flat Q. On Cav 3.1 a BCP was also done, in order to remove 5 µm and see the rf performance on a surface with a less concentration of nitrogen. A baking process was also done, in order to remove the hydrogen coming from the BCP process. The rf curve at 1.8K was not collected after the baking process, because a vacuum leak appeared at helium λ point during the cool down at 1.8 K. Rf performance decreased after the post treatments.

Table 8.6 Deposition parameters for Cav3.1. PROCESS 3.1.A.
I=magnetron current, V=magnetron voltage, P=sputtering Ar pressure, B=magnetron magnetic field, T=substrate temperature, d=total thickness on the cell, t=total deposition time.

I (A)	V (V)	P (mbar)	B (G)	T (°C)	d (µm)	t (h)	deposition mode	venting mode
1	≈350	$7 \cdot 10^{-3}$	830	550	≈70	7	one-shot	High temp.

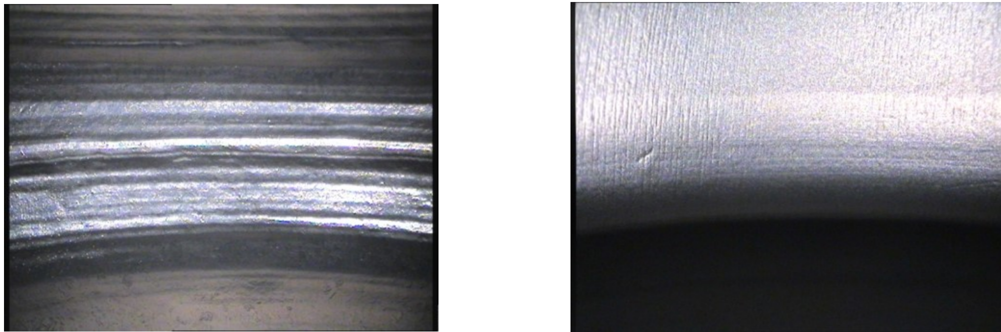

Figure 8.10 Internal inspection of the cell (on the left) and iris (on the right) for Cav1.1.

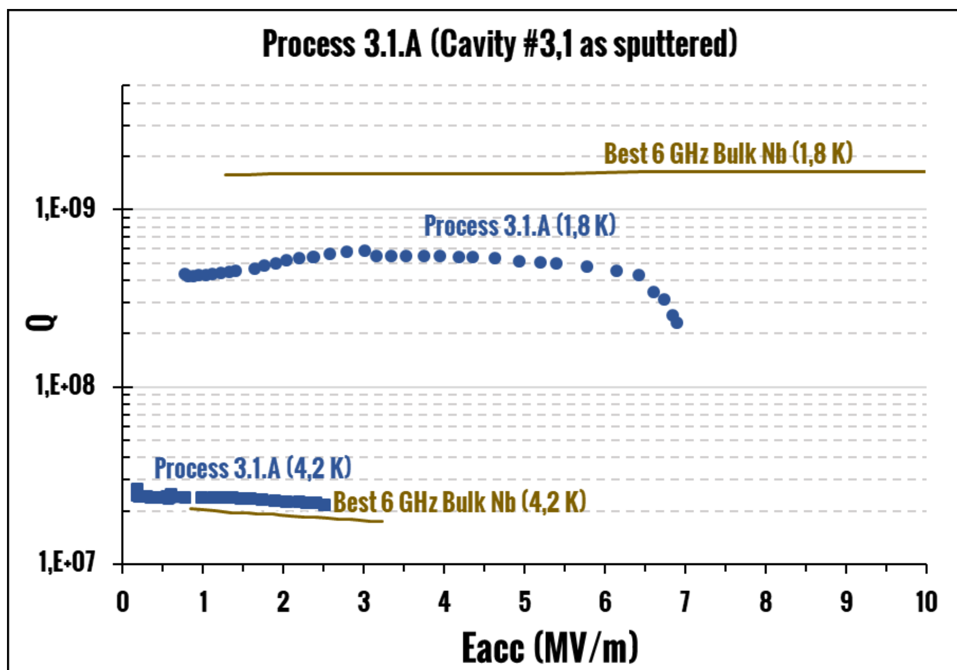

Figure 8.11 Rf test at 4.2K and 1.8K for Cav3.1.

Table 8.7 BCP parameters for Cav3.1. PROCESS 3.1.B.

Solution	concentration (ratio)	time (s)	Etching thickness (μm)
$HF:HNO_3:H_3PO_4$	1:1:3	120	5,5

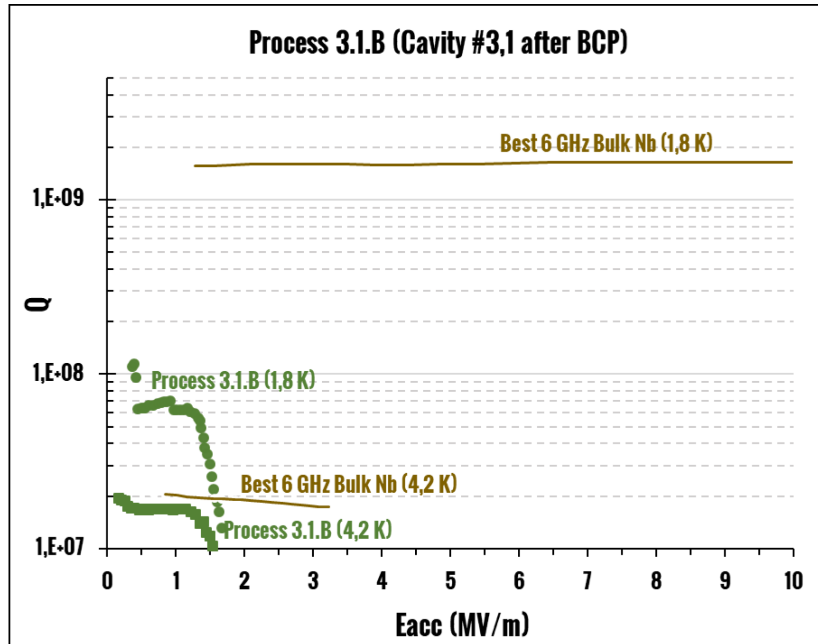

Figure 8.12 Rf test at 4.2K and 1.8K for Cav3.1 after BCP.

Table 8.8 Baking parameters for Cav3.1. PROCESS 3.1.C.

Temperature (°C)	Time (hours)
120	24

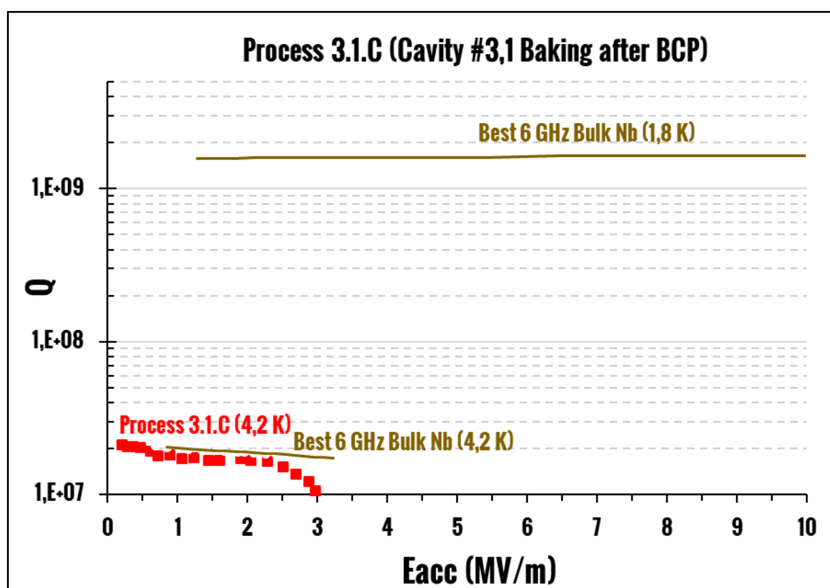

Figure 8.13 Rf test at 4.2K for Cav3.1 after baking.

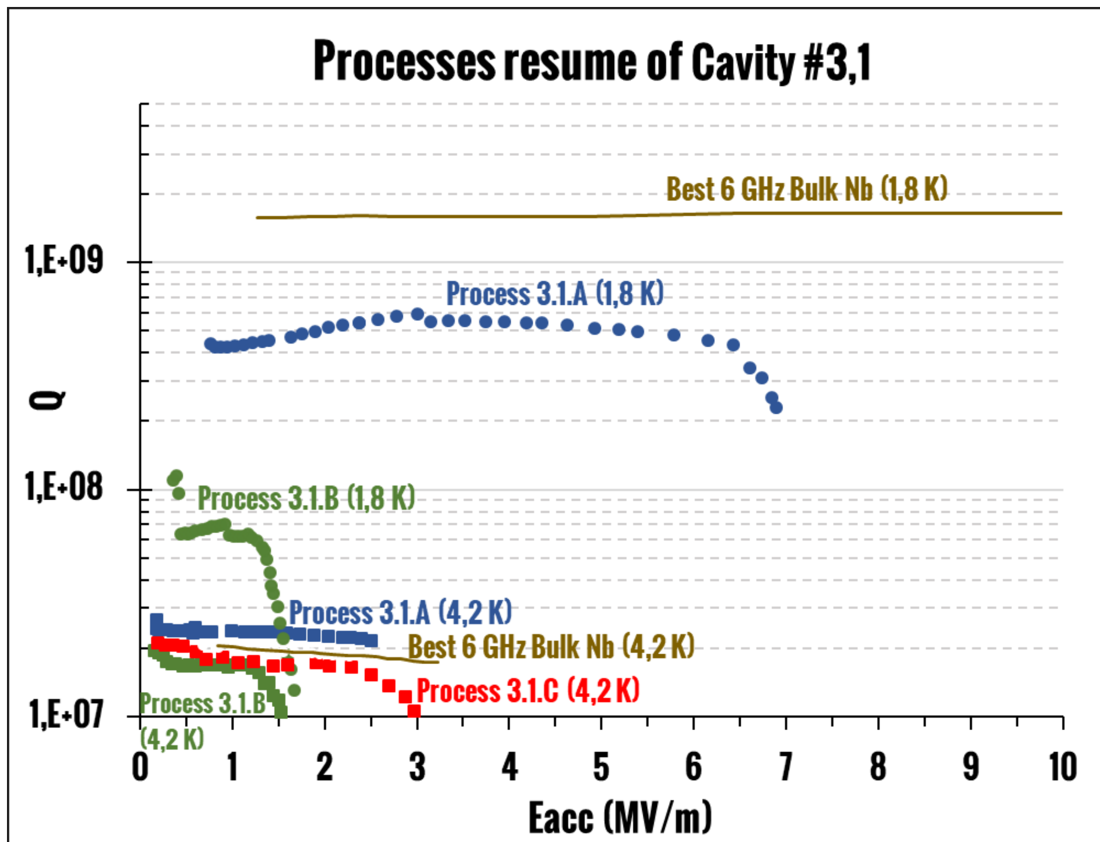

Figure 8.14 Rf test at 4.2K and 1.8K for all the processes Cav3.1

Cav 4.0

On Cav 4.0 a high temperature venting was done. The rf test at 1.8K was not done after the baking process, because a vacuum leak appeared at helium λ point during the cool down at 1.8 K. No post treatments were done.

Table 8.9 Deposition parameters for Cav4.0. PROCESS 4.0.A.
I=magnetron current, V=magnetron voltage, P=sputtering Ar pressure, B=magnetron magnetic field, T=substrate temperature, d=total thickness on the cell, t=total deposition time.

I (A)	V (V)	P (mbar)	B (G)	T (°C)	d (μm)	t (h)	deposition mode	venting mode
1	≈330	$7 \cdot 10^{-3}$	830	550	≈40	3	one-shot	High temp.

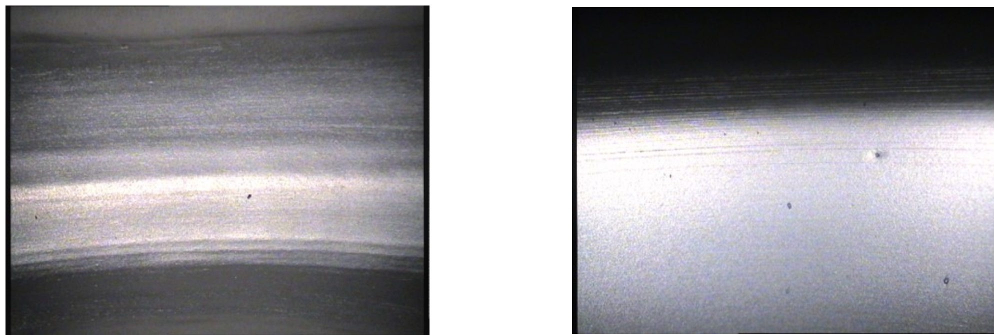

Figure 8.15 Internal inspection of the cell (on the left) and iris (on the right) for Cav4.0.

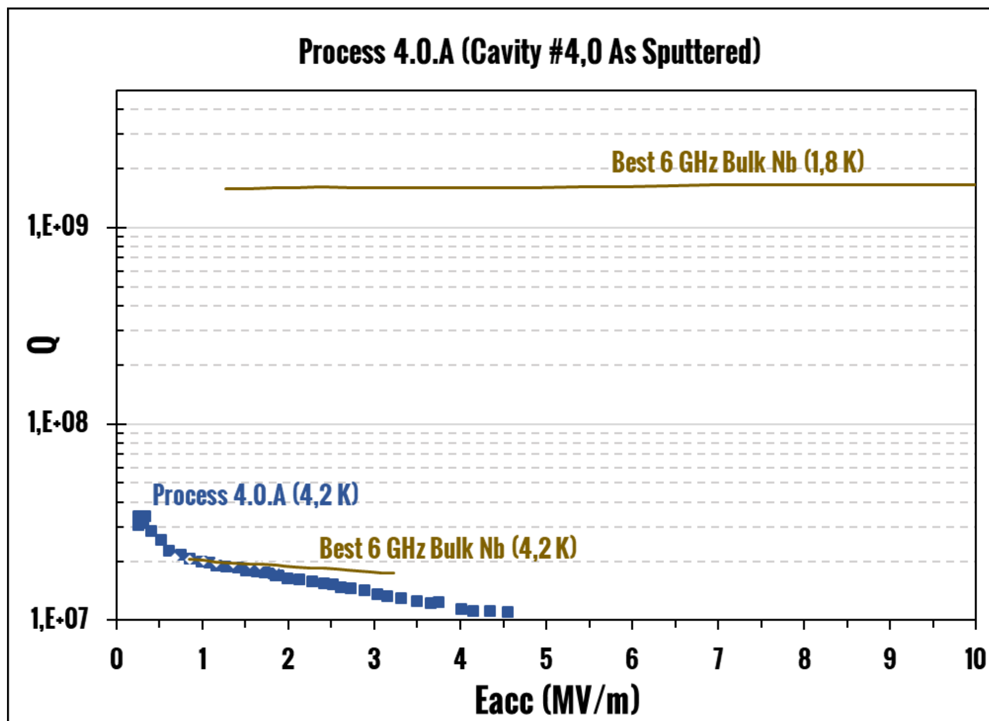

Figure 8.16 Rf test at 4.2K for Cav4.0.

Cav 5.0

On Cav 5.0 a high temperature venting was done. No post treatments were done.

Table 8.10 Deposition parameters for Cav5.0. PROCESS 5.0.A.
I=magnetron current, V=magnetron voltage, P=sputtering Ar pressure, B=magnetron magnetic field, T=substrate temperature, d=total thickness on the cell, t=total deposition time.

I (A)	V (V)	P (mbar)	B (G)	T (°C)	d (μm)	t (h)	deposition mode	venting mode
1	≈330	$5 \cdot 10^{-2}$	830	550	≈40	3	one-shot	High temp.

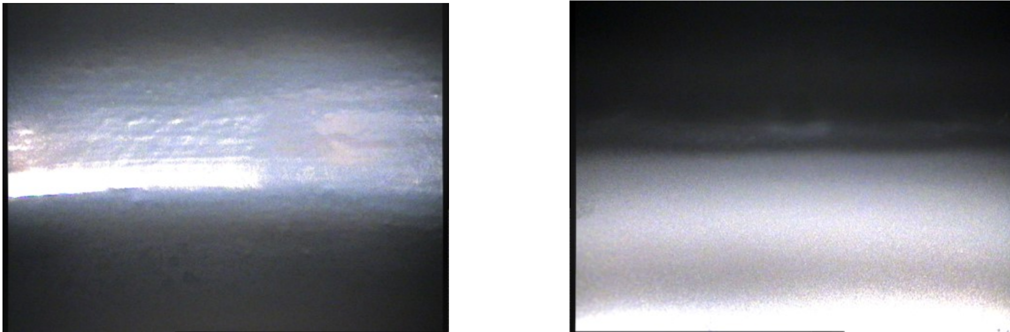

Figure 8.17 Internal inspection of the cell (on the left) and iris (on the right) for Cav5.0.

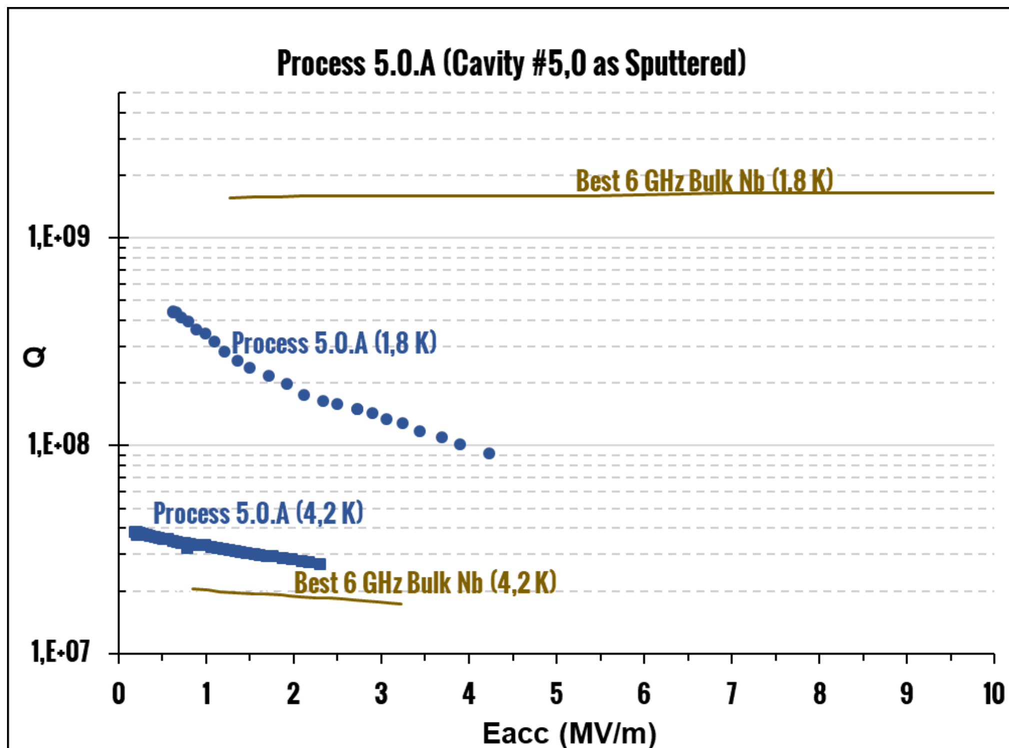

Figure 8.18 Rf test at 4.2K and 1.8K for Cav5.0.

Cav 5.1

Cav 5 was stripped from Nb of process 5.0.A. On Cav 5.1 a high temperature venting was done. No post treatments were done. The film looks very stressed at the optical inspection.

Table 8.11 Deposition parameters for Cav5.1. PROCESS 5.1.A.
I=magnetron current, V=magnetron voltage, P=sputtering Ar pressure, B=magnetron magnetic field, T=substrate temperature, d=total thickness on the cell, t=total deposition time.

I (A)	V (V)	P (mbar)	B (G)	T (°C)	d (μm)	t (h)	deposition mode	venting mode
1	≈530	$5{\cdot}10^{-2}$	830	550	≈70	3	one-shot	High temp.

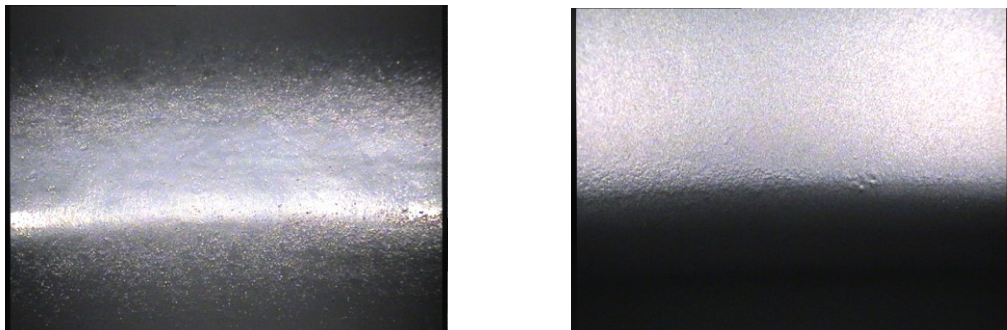

Figure 8.19 Internal inspection of the cell (on the left) and iris (on the right) for Cav5.1.

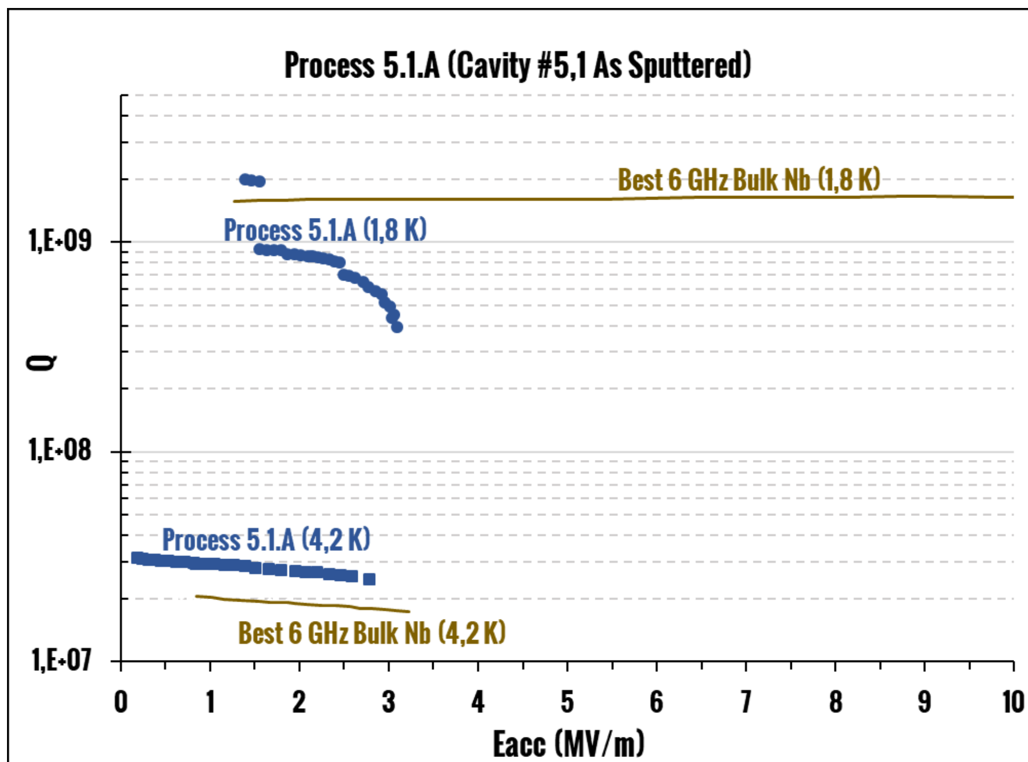

Figure 8.20 Rf test at 4.2K and 1.8K for Cav5.1.

Cav 6.0

On Cav 6.0 a high temperature venting was done. No post treatments were done. The crystallographic grain in the cell optical inspection is visible

Table 8.12 Deposition parameters for Cav6.0. PROCESS 6.0.A.
I=magnetron current, V=magnetron voltage, P=sputtering Ar pressure, B=magnetron magnetic field, T=substrate temperature, d=total thickness on the cell, t=total deposition time.

I (A)	V (V)	P (mbar)	B (G)	T (°C)	d (μm)	t (h)	deposition mode	venting mode
1	≈330	$7 \cdot 10^{-3}$	830	550	≈40	3	one-shot	High temp.

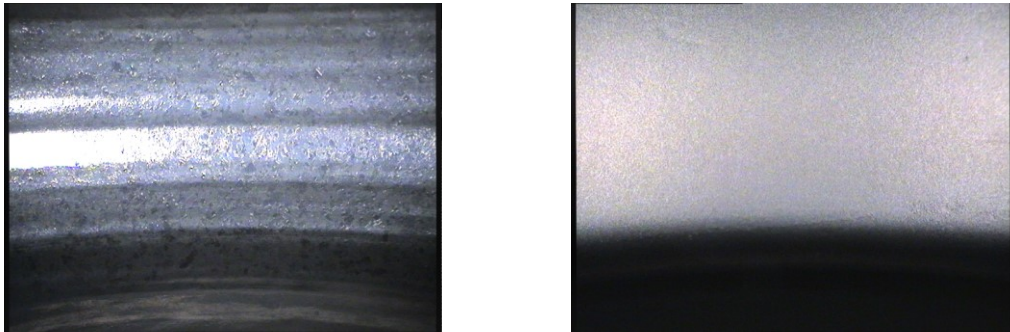

Figure 8.21 Internal inspection of the cell (on the left) and iris (on the right) for Cav6.0.

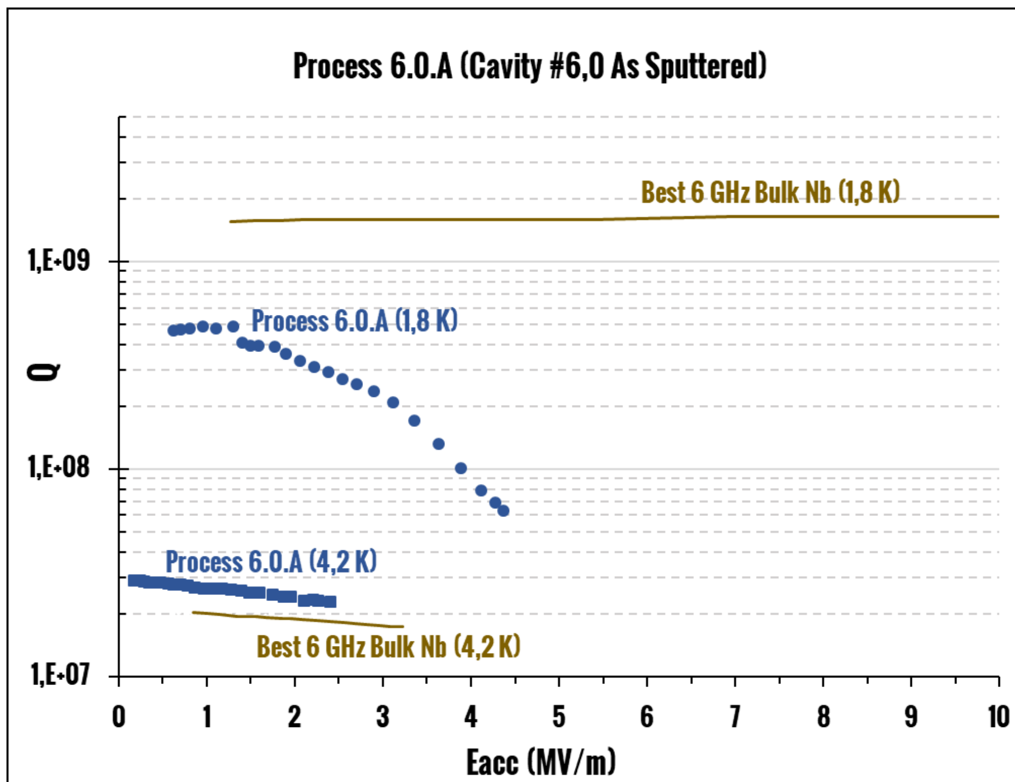

Figure 8.22 Rf test at 4.2K and 1.8K for Cav6.0.

Cav 7.0

On Cav 7.0 a high temperature venting was done. The rf test at 1.8K was not done after the baking process, because a vacuum leak appeared at helium λ point during the cool down at 1.8 K, probably due to a defect on the flange. A BCP was also done, in order to remove 5 µm and see the rf performance on a surface with a less concentration of nitrogen. The BCP etched also the flange and removed the defect, allowing the srf properties at 1.8 K to be measured. A baking process was also done, in order to remove the hydrogen coming from the BCP process. The rf test at 1.8K was not done after the baking process, because a vacuum leak appeared at the helium λ point during the cool down at 1.8 K. Rf performance decreased after the post treatments.

Table 8.13 Deposition parameters for Cav7.0. PROCESS 7.0.A.
I=magnetron current, V=magnetron voltage, P=sputtering Ar pressure, B=magnetron magnetic field, T=substrate temperature, d=total thickness on the cell, t=total deposition time.

I (A)	V (V)	P (mbar)	B (G)	T (°C)	d (µm)	t (h)	deposition mode	venting mode
1	≈480	$7 \cdot 10^{-3}$	830	550	≈70	7	one-shot	High temp.

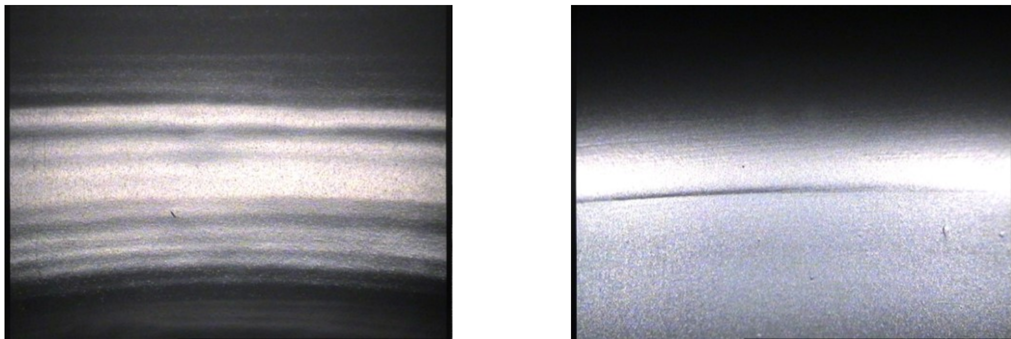

Figure 8.23 Internal inspection of the cell (on the left) and iris (on the right) for Cav7.0.

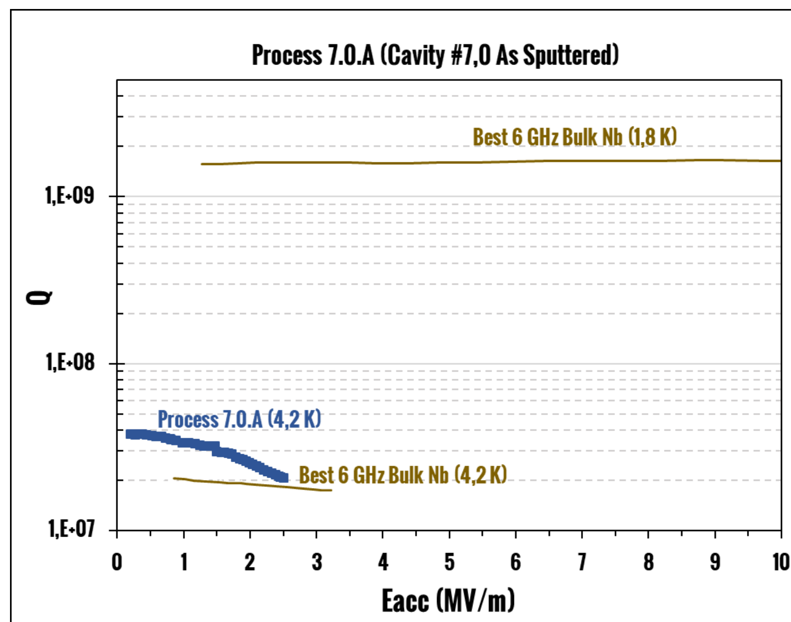

Figure 8.24 Rf test at 4.2K for Cav7.0.

Table 8.14 BCP parameters for Cav7.0 PROCESS 7.0.B

Solution	concentration (ratio)	time (s)	Etching thickness (μm)
$HF:HNO_3:H_3PO_4$	1:1:3	120	5,5

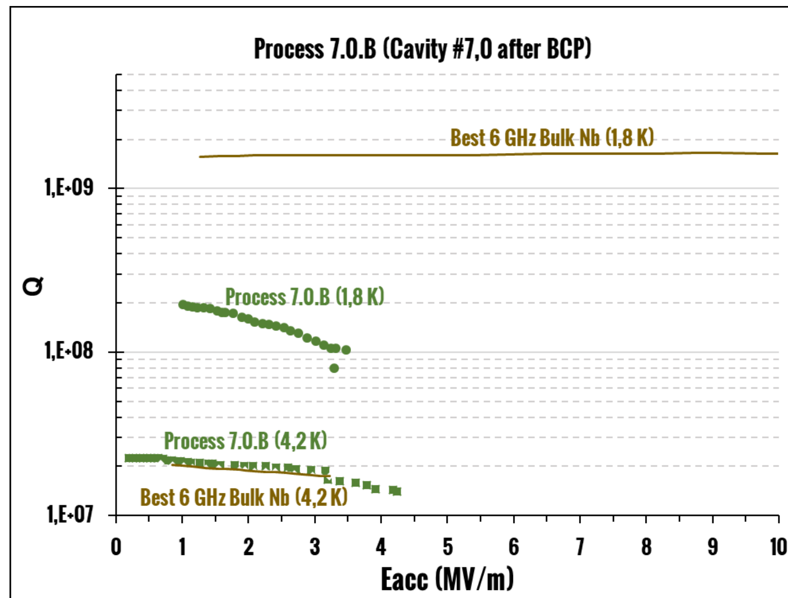

Figure 8.25 Rf test at 4.2K and 1.8K for Cav7.0 after BCP.

Table 8.15 Baking parameters for Cav7.0. PROCESS 7.0.C.

Temperature (°C)	Time (hours)
120	24

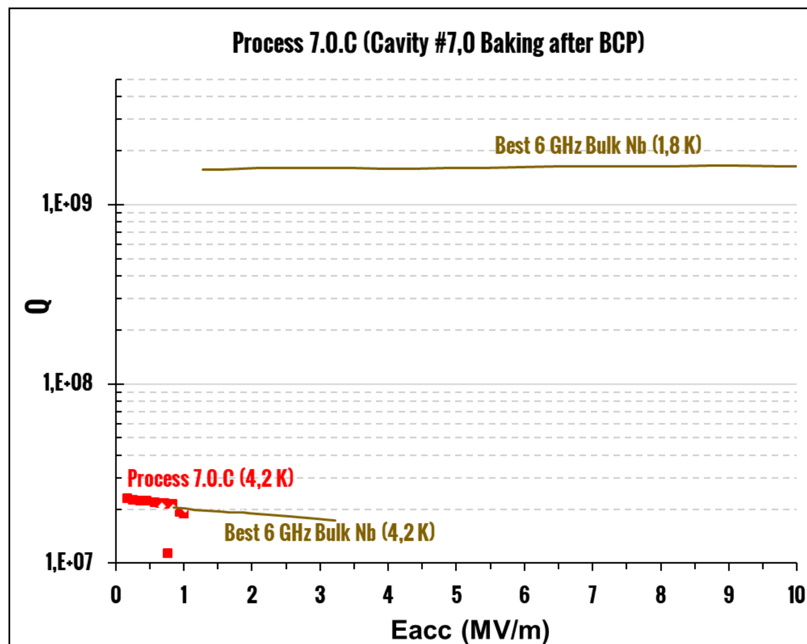

Figure 8.26 Rf test at 4.2K for Cav7.0 after baking.

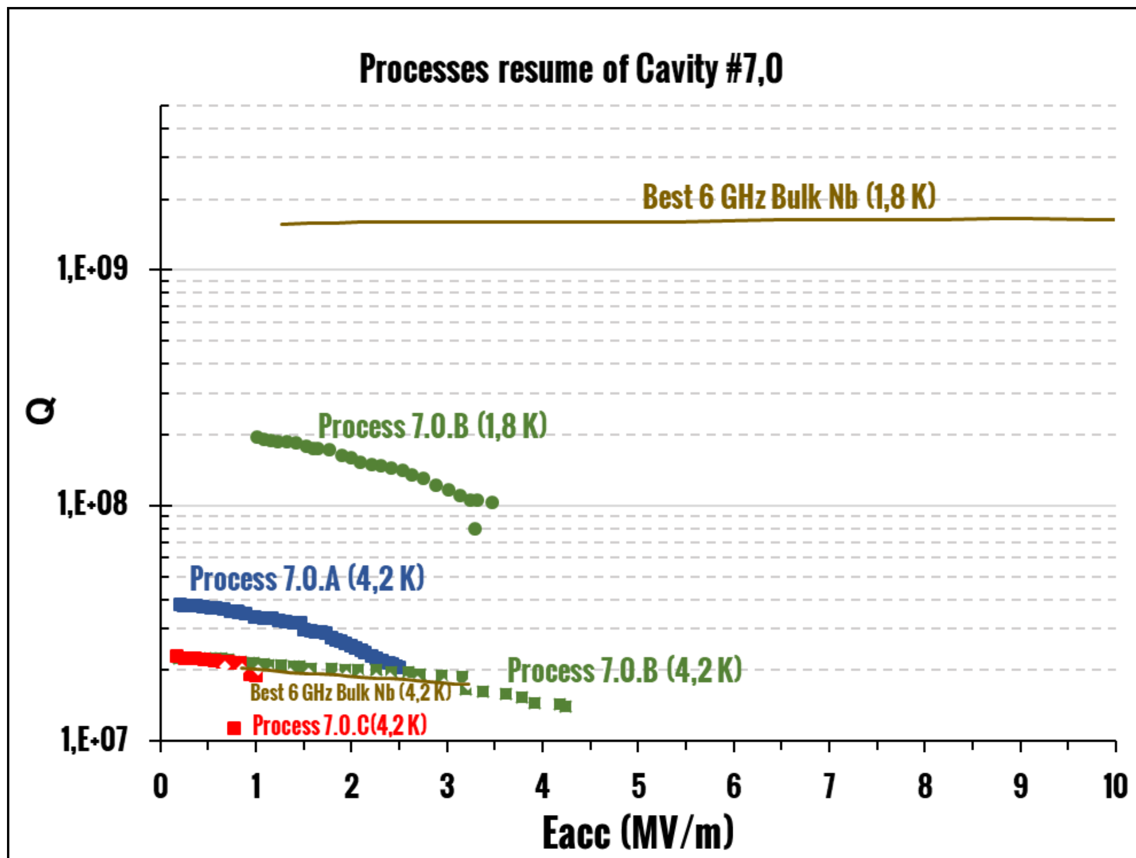

Figure 8.27 Rf test at 4.2K and 1.8K for all the processes Cav7.0

Cav 8.1

Cav 8 was stripped from Nb after one failed deposition in which peeling occurred. On Cav 8.1 a multilayer deposition and a standard venting were done. No post treatments were done. A deformation on the cell surface appeared at the thermocouple contact point.

Table 8.16 Deposition parameters for Cav8.1. PROCESS 8.1.A.
I=magnetron current, V=magnetron voltage, P=sputtering Ar pressure, B=magnetron magnetic field, T=substrate temperature, d=total thickness on the cell, d_{sl}=single layer thickness, n_{sl}=total numbers of single layers, D=sputtering duty cycle.

I (A)	V (V)	P (mbar)	B (G)	T (°C)	d (μm)	dep. mode	d_{sl} (nm)	n_{sl}	D	venting mode
1	≈335	$5\cdot10^{-2}$	830	550	≈56	multilayer	100	560	0.7	standard

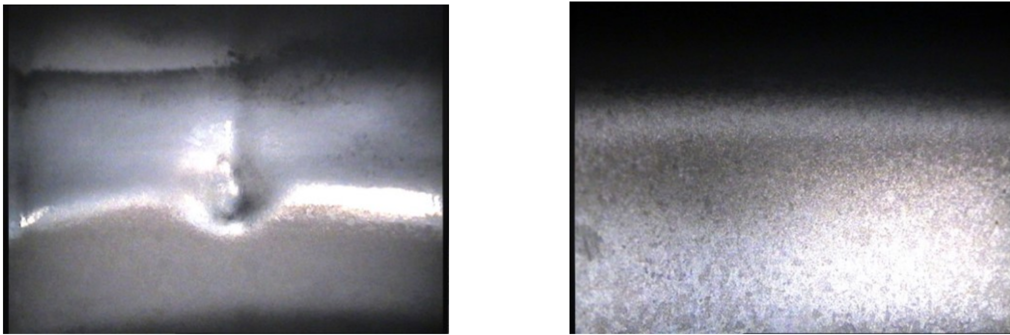

Figure 8.28 Internal inspection of the cell (on the left) and iris (on the right) for Cav8.1. A deformation of the cell surface appears at the thermocouple contact point.

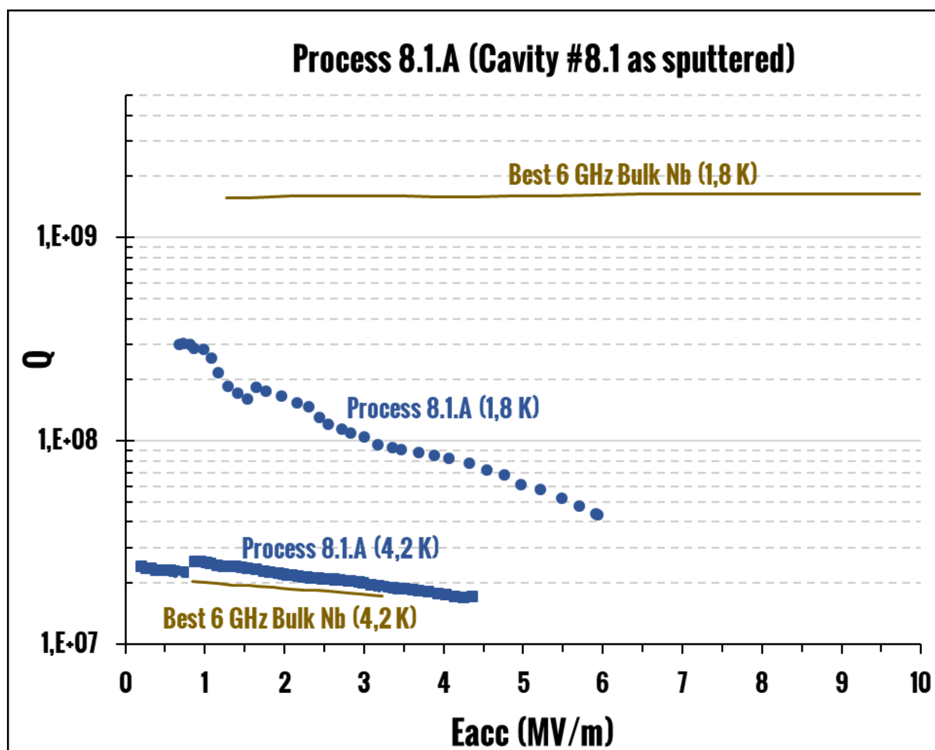

Figure 8.29 Rf test at 4.2K and 1.8K for Cav8.1.

Cav 9.0

On Cav 9.0 a standard venting was done. The cavity shows a very high and flat Q, but quench at 4 MV/m. A BCP was also done, in order to remove 5 μm and see if the rf performances are limited by an accidental poisoning occurring during the cool down process. Three different baking process were also done, in order to remove the hydrogen coming from the BCP process.

Table 8.17 Deposition parameters for Cav9.0. PROCESS 9.0.A.
I=magnetron current, V=magnetron voltage, P=sputtering Ar pressure, B=magnetron magnetic field, T=substrate temperature, d=total thickness on the cell, t=total deposition time.

I (A)	V (V)	P (mbar)	B (G)	T (°C)	d (μm)	t (h)	deposition mode	venting mode
1	≈400	$7 \cdot 10^{-3}$	830	550	≈70	7	one-shot	standard

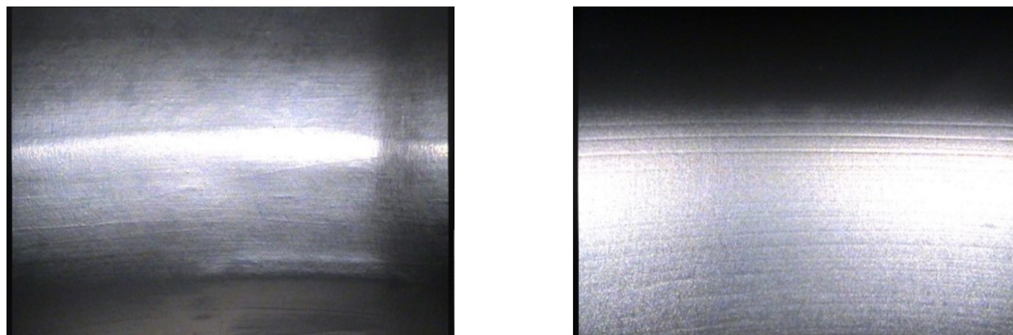

Figure 8.30 Internal inspection of the cell (on the left) and iris (on the right) for Cav9.0.

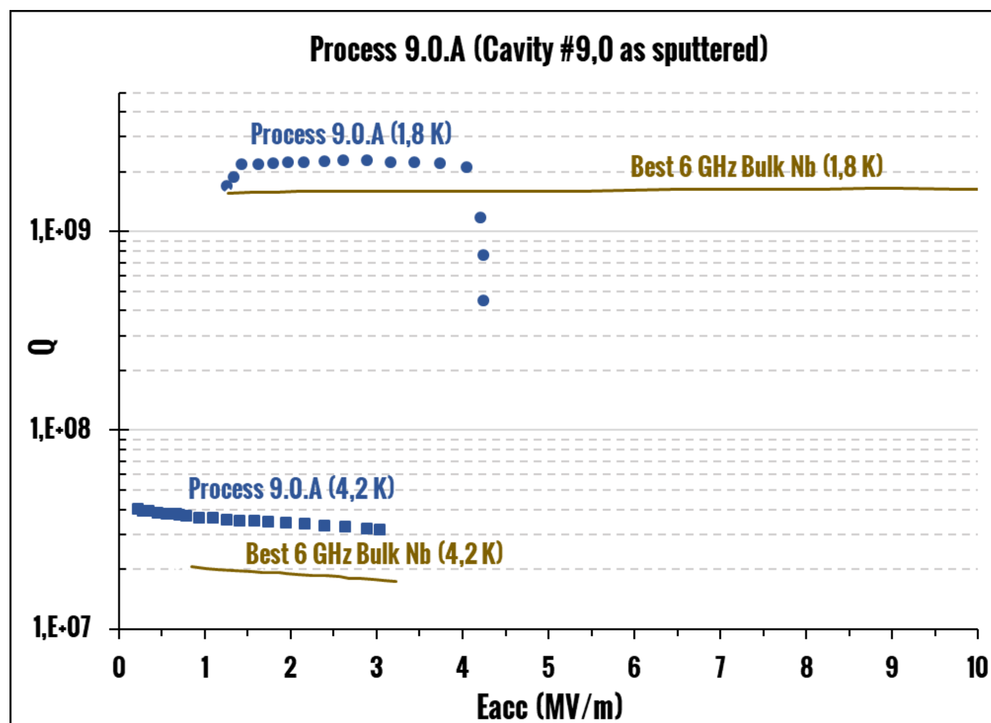

Figure 8.31 Rf test at 1.8K and 4.2K for Cav9.0.

Table 8.18 BCP parameters for Cav9.0 PROCESS 9.0.B

Solution	concentration (ratio)	time (s)	Etching thickness (μm)
$HF:HNO_3:H_3PO_4$	1:1:3	300	6

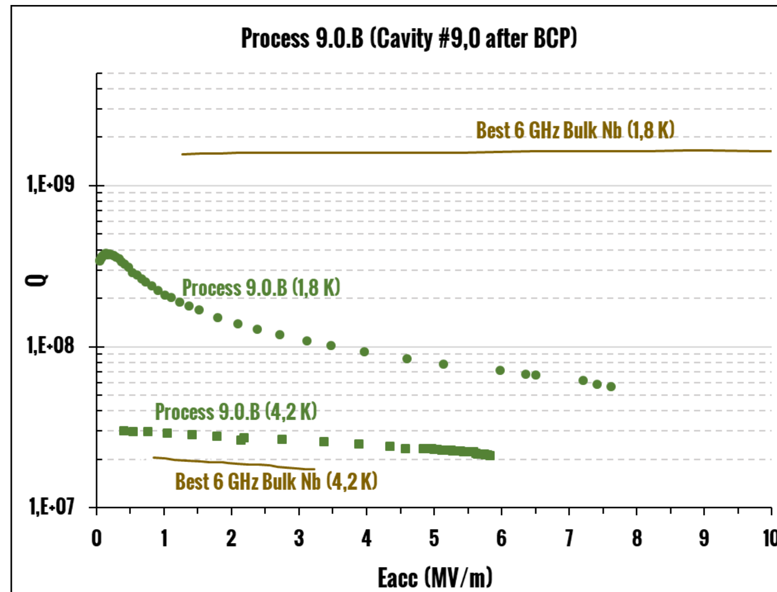

Figure 8.32 Rf test at 4.2K and 1.8K for Cav9.0 after BCP.

Table 8.19 Baking parameters for Cav9.0. PROCESS 9.0.C.

Temperature (°C)	Time (hours)
100	48

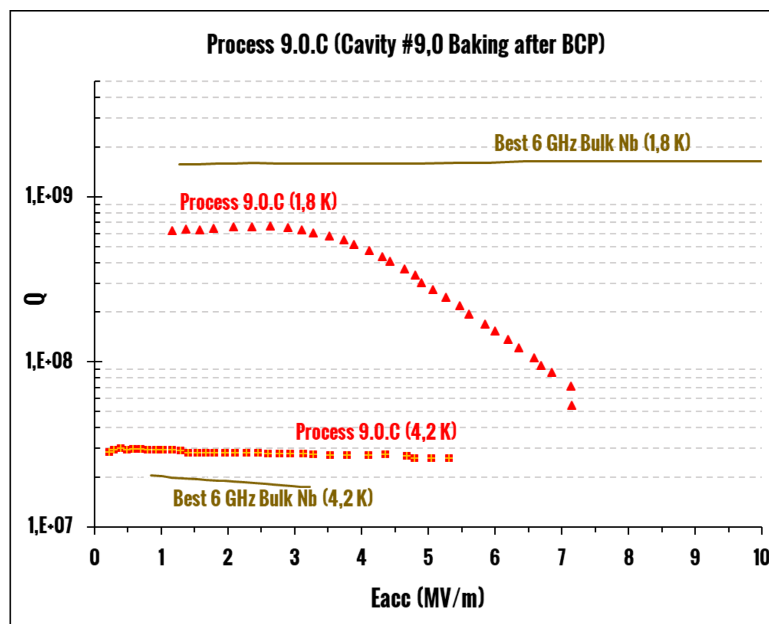

Figure 8.33 Rf test at 1.8 K and 4.2K for Cav9.0 after the first baking process.

Table 8.20 Baking parameters for Cav9.0. PROCESS 9.0.D.

Temperature (°C)	Time (hours)
100	120

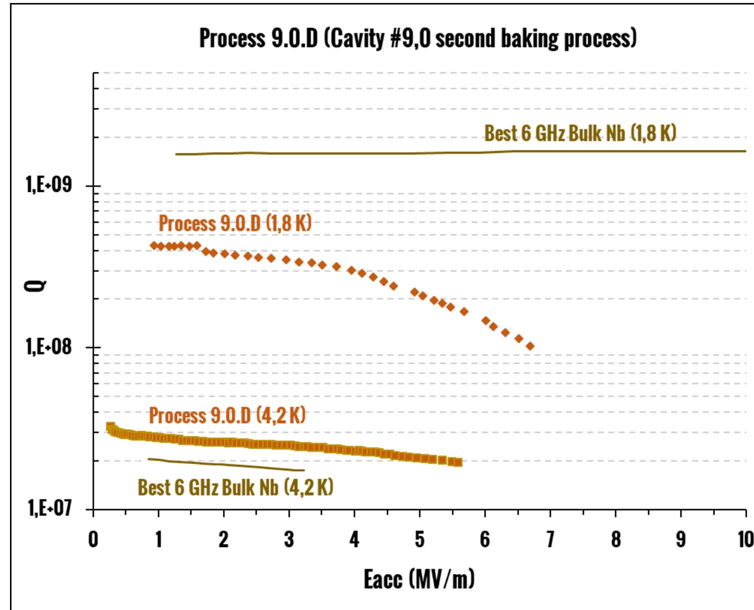

Figure 8.34 Rf test at 1.8 K and 4.2K for Cav9.0 after the second baking process.

Table 8.21 Baking parameters for Cav9.0. PROCESS 9.0.C.

Temperature (°C)	Time (hours)
120	24

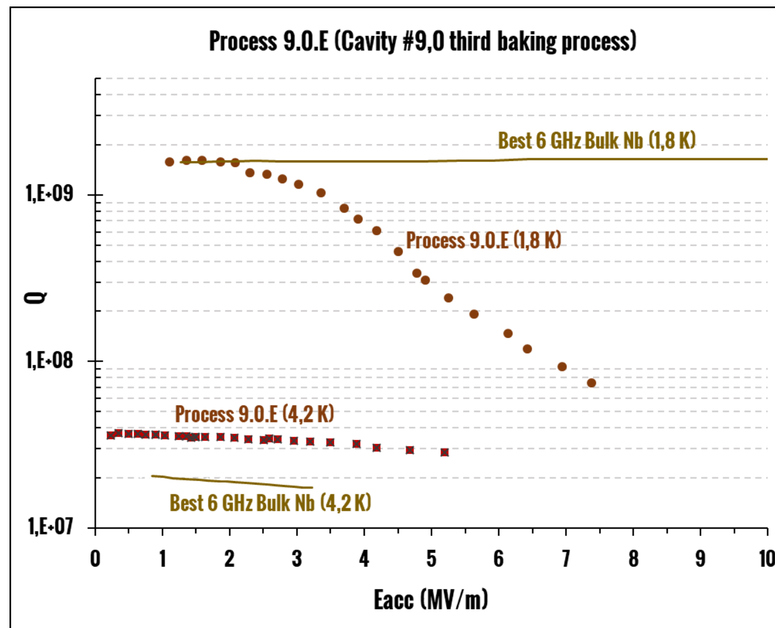

Figure 8.35 Rf test at 1.8 K and 4.2K for Cav9.0 after the third and last baking process.

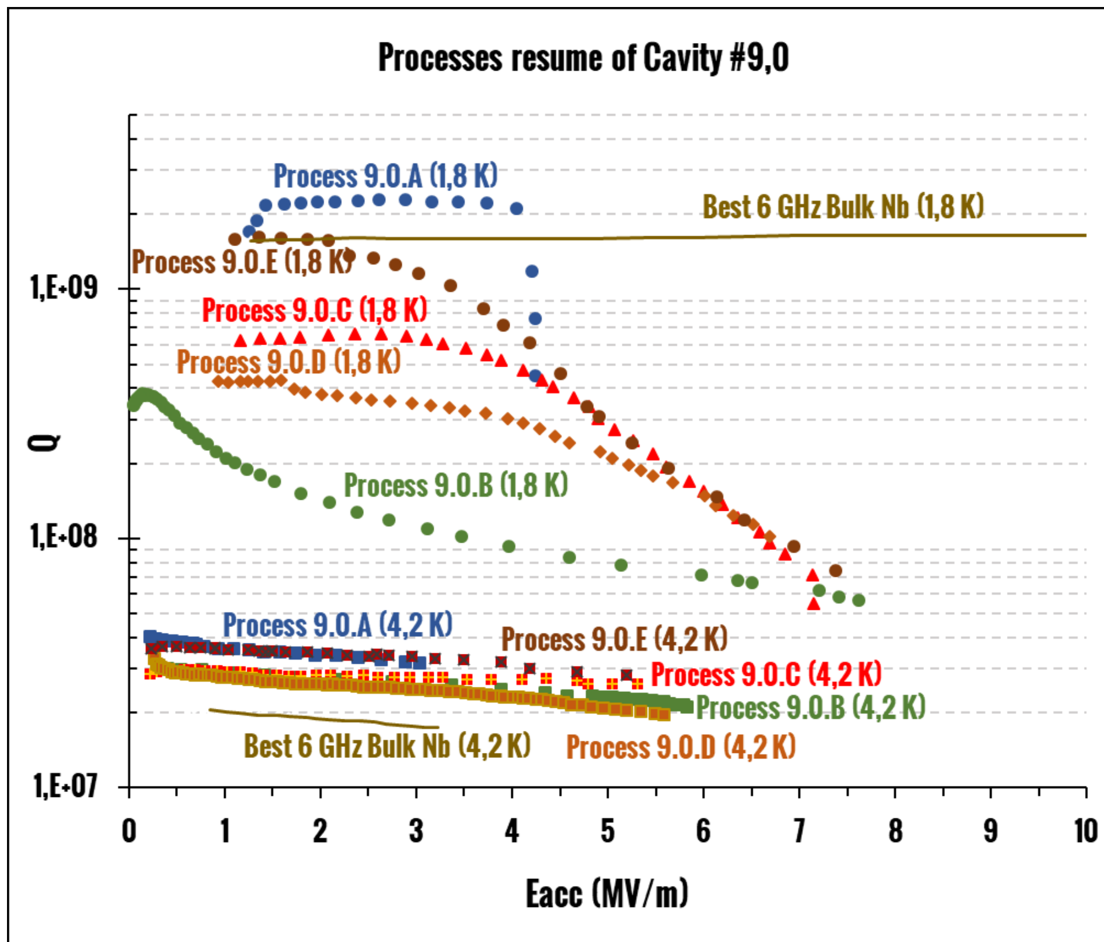

Figure 8.36 Rf test at 4.2K and 1.8K for all the processes Cav9.0

Cav 10.1

Cav 10 was stripped from Nb after one failed deposition in which peeling occurred. On Cav 10.1 a multilayer deposition and a standard venting were done. The cavity shows a very poor performance, probably due to the flakes present in vacuum chamber and incorporated during the deposition process. No post treatments were done.

Table 8.22 Deposition parameters for Cav10.1. PROCESS 10.1.A.
I=magnetron current, V=magnetron voltage, P=sputtering Ar pressure, B=magnetron magnetic field, T=substrate temperature, d=total thickness on the cell, d_{sl}=single layer thickness, n_{sl}=total numbers of single layers, D=sputtering duty cycle.

I (A)	V (V)	P (mbar)	B (G)	T (°C)	d (μm)	dep. mode	d_{sl} (nm)	n_{sl}	D	venting mode
1	≈400	$5\cdot10^{-2}$	830	550	≈ 40	multilayer	≈ 500	108	0.7	standard

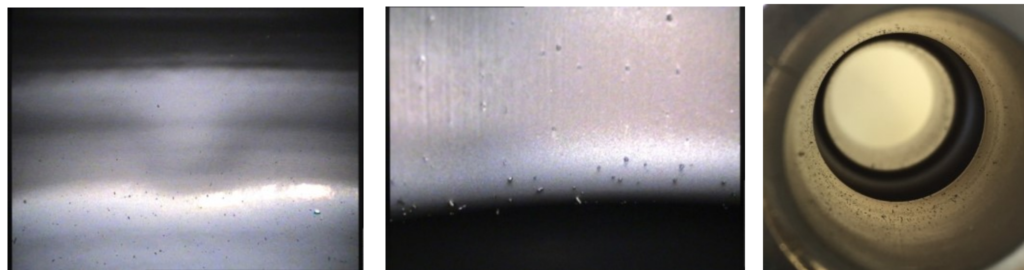

Figure 8.37 Internal inspection of the cell (on the left) and iris (on the center) and of the cut off (on the right) for Cav10.1. Flakes on the surface are visible and probably are the explanation for the bad rf performances.

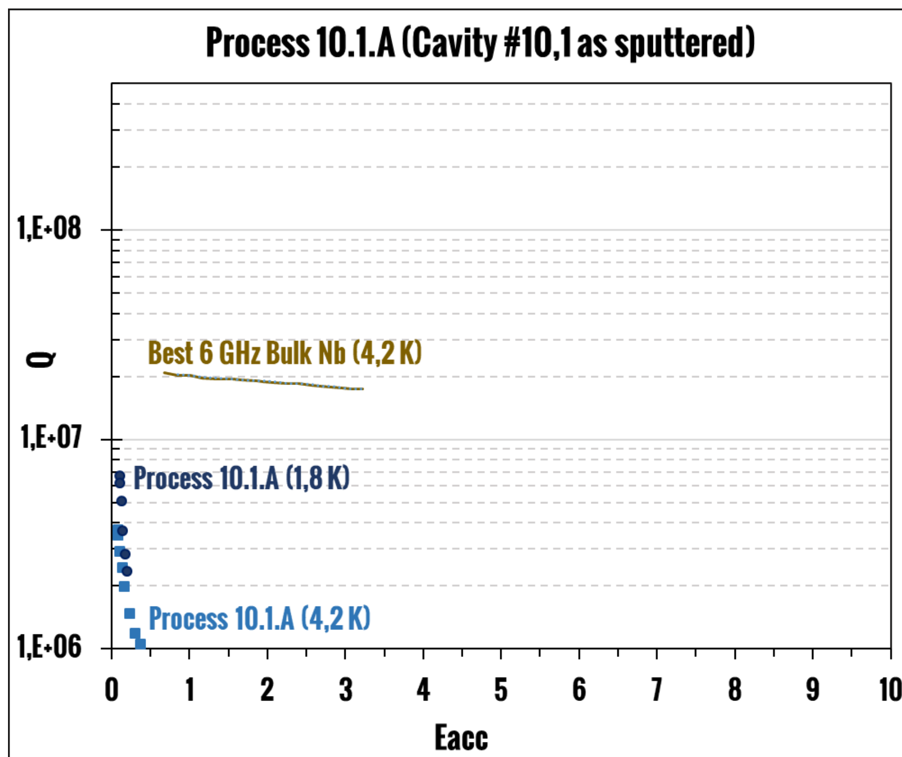

Figure 8.38 Rf test at 1.8K and 4.2K for Cav10.1.

Cav 11.0

On Cav 11.0 a one-shot deposition and a standard venting was done. The rf test at 1.8K was not done after the baking process, because a vacuum leak appeared at the helium λ point during the cooling down at 1.8 K. No post treatments were done.

Table 8.23 Deposition parameters for Cav11.0. PROCESS 11.0.A.
I=magnetron current, V=magnetron voltage, P=sputtering Ar pressure, B=magnetron magnetic field, T=substrate temperature, d=total thickness on the cell, t=total deposition time.

I (A)	V (V)	P (mbar)	B (G)	T (°C)	d (μm)	t (h)	deposition mode	venting mode
1	≈300	$5\cdot10^{-2}$	830	550	≈60	6	one-shot	standard

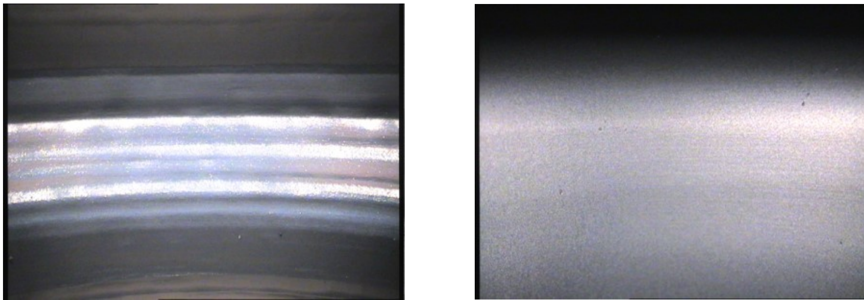

Figure 8.39 Internal inspection of the cell (on the left) and iris (on the right) for Cav11.0.

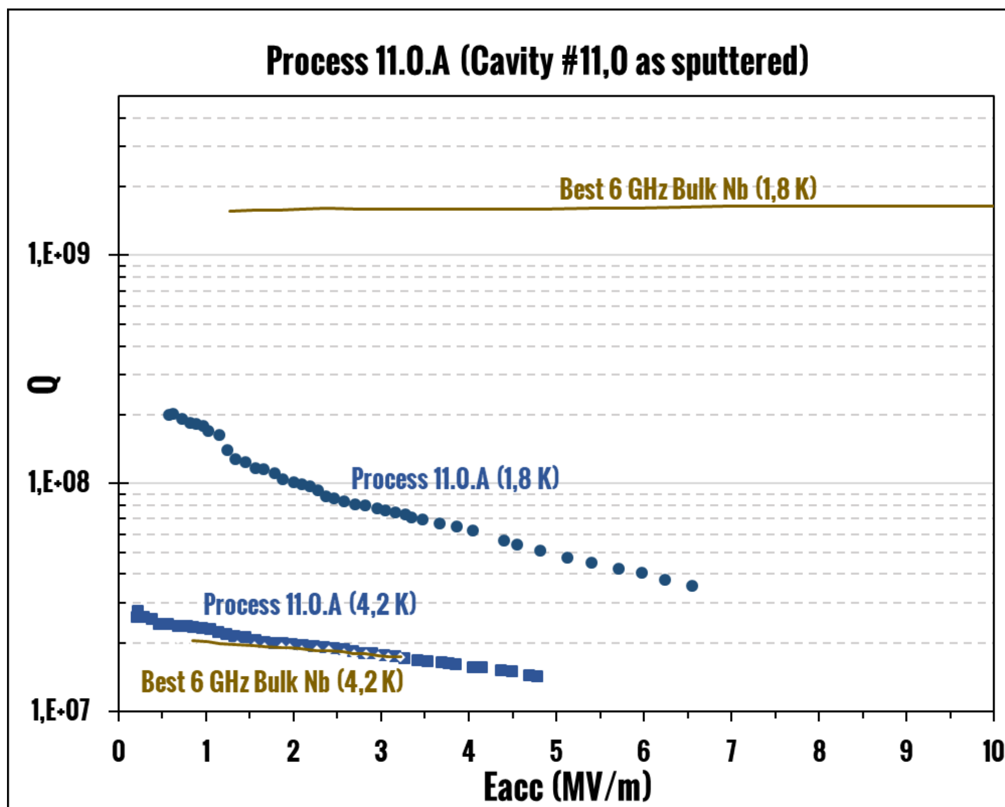

Figure 8.40 Rf test at 1.8 K and 4.2K for Cav11.0.

Cav 11.1

Cav 11 was stripped from Nb of process 11.0.A. On Cav 11.1 a multilayer deposition and a standard venting were done. A final 5 µm thickness layer was deposited in order to avoid SRF performance deterioration due to the incidental oxide layer formation during the pause time. The rf test at 1.8K was not done after the baking process, because a vacuum leak appeared at helium λ point during the cooling down at 1.8 K. No post treatments were done.

Table 8.24 Deposition parameters for Cav11.1. PROCESS 11.1.A.
I=magnetron current, V=magnetron voltage, P=sputtering Ar pressure, B=magnetron magnetic field, T=substrate temperature, d=total thickness on the cell, d_{sl}=single layer thickness, d_{fl}= final layer thickness ,n_{sl}=total numbers of single layers, D=sputtering duty cycle.

I (A)	V (V)	P (mbar)	B (G)	T (°C)	d (µm)	dep. mode	d_{sl} (nm)	d_{fl} (µm)	n_{sl}	D	venting mode
1	≈300	$5\cdot10^{-2}$	830	550	≈70	multilayer	300	5	216	0.7	standard

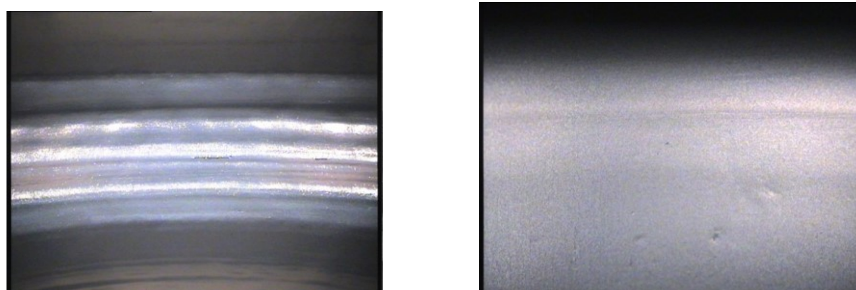

Figure 8.41 Internal inspection of the cell (on the left) and iris (on the right) for Cav11.1.

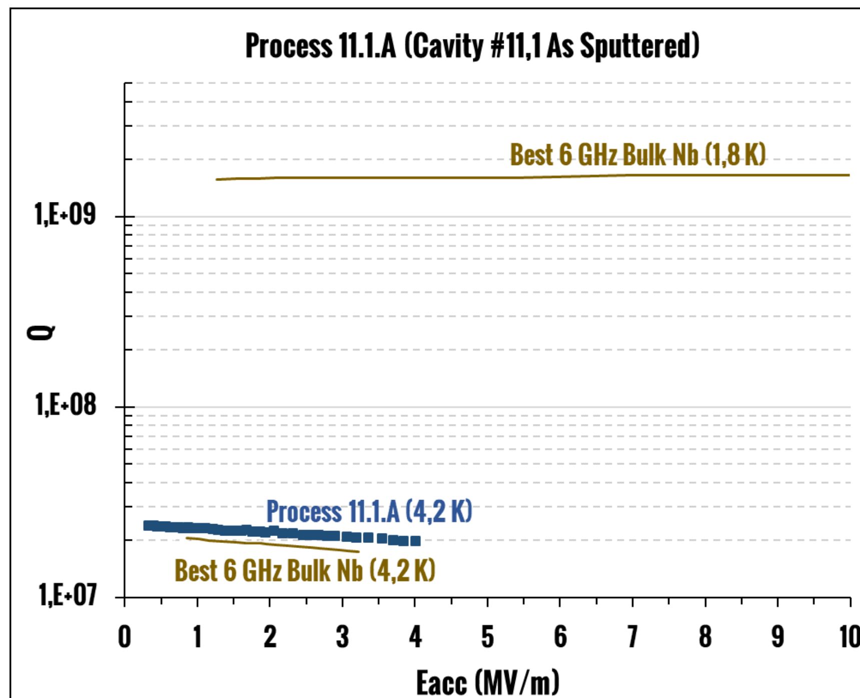

Figure 8.42 Rf test at 4.2K for Cav11.1.

Cav 12.0

On Cav 12.0 a multilayer deposition and a standard venting was done. No post treatments were done. A final 5 µm thickness layer was deposited in order to avoid SRF performance deterioration due to the incidental oxide layer formation during the pause time.

Table 8.25 Deposition parameters for Cav12.0. PROCESS 12.0.A.
I=magnetron current, V=magnetron voltage, P=sputtering Ar pressure, B=magnetron magnetic field, T=substrate temperature, d=total thickness on the cell, d_{sl}=single layer thickness, , d_{fl}= final layer thickness n_{sl}=total numbers of single layers, D=sputtering duty cycle.

I (A)	V (V)	P (mbar)	B (G)	T (°C)	d (µm)	dep. mode	d_{sl} (nm)	d_{fl} (µm)	n_{sl}	D	venting mode
1	≈300	$5\cdot10^{-2}$	830	550	≈40	multilayer	400	5	87	0.7	standard

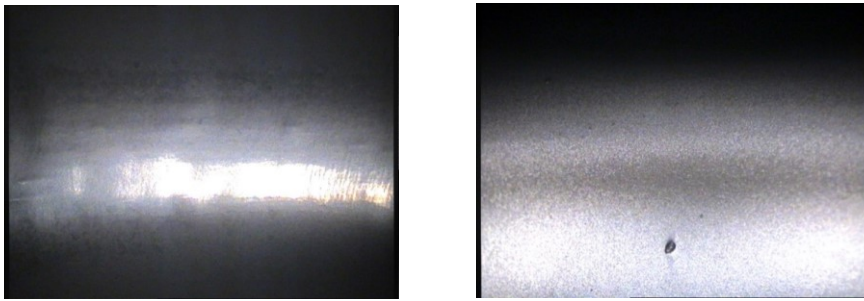

Figure 8.43 Internal inspection of the cell (on the left) and iris (on the right) for Cav12.0.

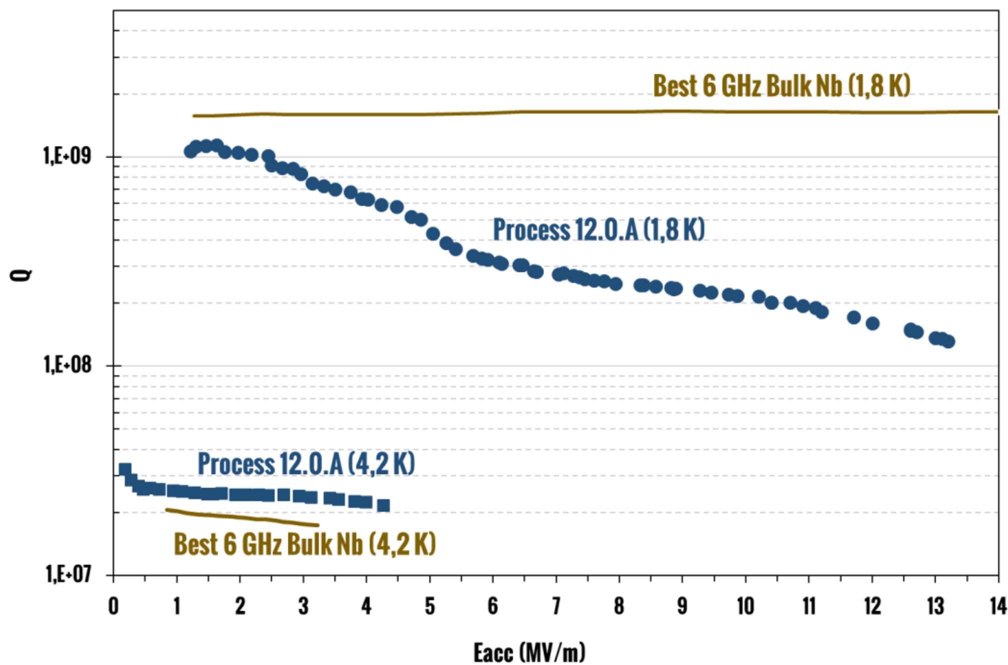

Figure 8.44 Rf test at 1.8K and 4.2K for Cav12.0.

Cav 13.0

On Cav 13.0 a high temperature venting was done. In this cavity we tested the high temperature venting with different conditions (see Table 8.27). The pure nitrogen pressure has been increased from $3.5 \cdot 10^{-2}$ to $1 \cdot 10^{-2}$ mbar and the time has been reduced from 10 to 3 minutes. A baking process was also done in order to test the effect of a thermal treatment on a sputtered thick film. Rf performance decreased after the post treatments.

Table 8.26 Deposition parameters for Cav13.0. PROCESS 13.0.A.
I=magnetron current, V=magnetron voltage, P=sputtering Ar pressure, B=magnetron magnetic field, T=substrate temperature, d=total thickness on the cell, t=total deposition time.

I (A)	V (V)	P (mbar)	B (G)	T (°C)	d (μm)	t (h)	deposition mode	venting mode
1	≈350	$5 \cdot 10^{-2}$	830	550	≈70	7	one-shot	High temp mod. Table 8.27

Table 8.27 High temperature venting mode modify for PROCESS 13.0.A

time	action	P (mbar)	T (°C)
t_0 (after sputtering)	Turn off power supply. Close Ar gas valve. Open pure N_2 gas valve.	$1 \cdot 10^{-2}$ (pure N_2)	550
t_1 (3 min later t_0)	Close pure N_2 gas valve.	$< 10^{-7}$	550
t_2 (20 min later t_1)	Turn off IR lamp.	$< 10^{-7}$	550
t_3 (after a night of cooling)	Venting the chamber with service nitrogen.	1000 (N_2)	≈ 30

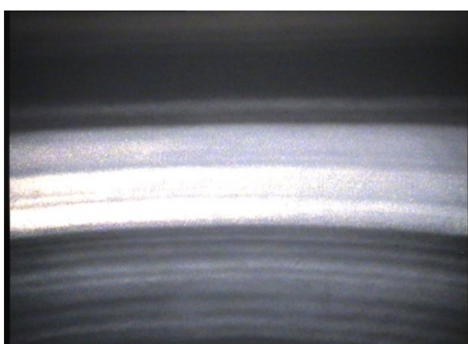
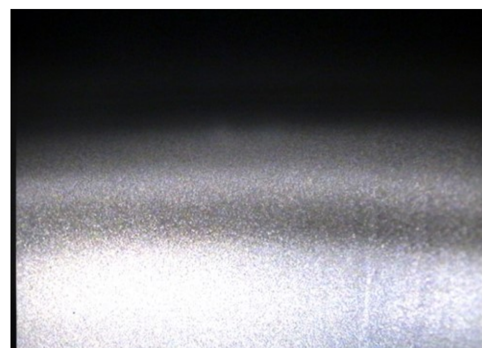

Figure 8.45 Internal inspection of the cell (on the left) and iris (on the right) for Cav13.0.

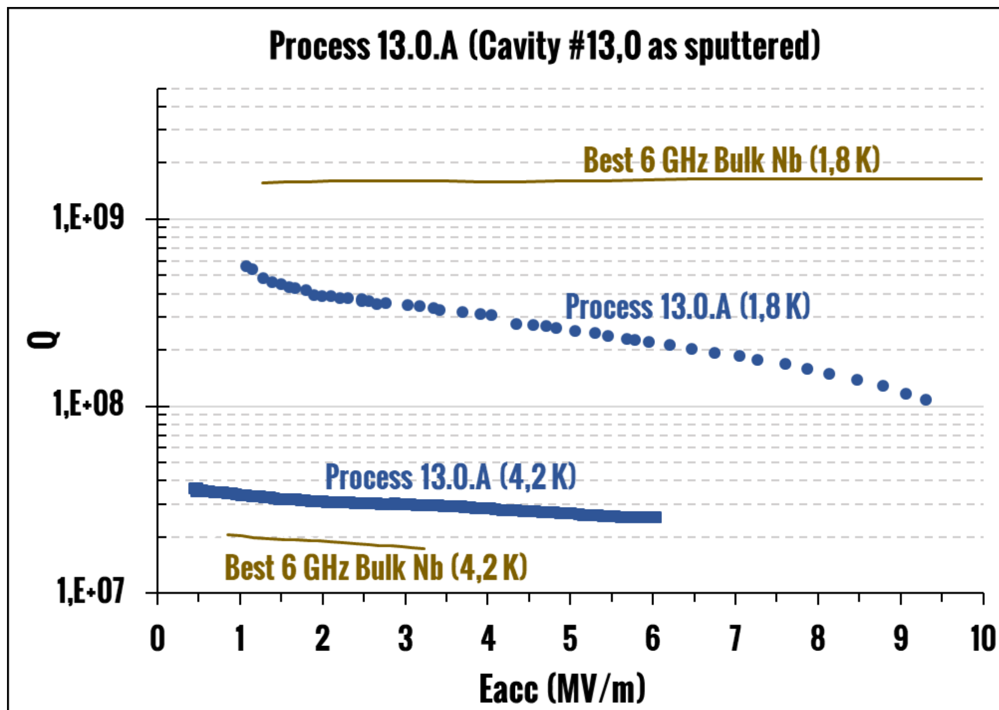

Figure 8.46 Rf test at 1.8K and 4.2K for Cav13.0.

Table 8.28 Baking parameters for Cav13.0. PROCESS 13.0.C.

Temperature (°C)	Time (hours)
100	48

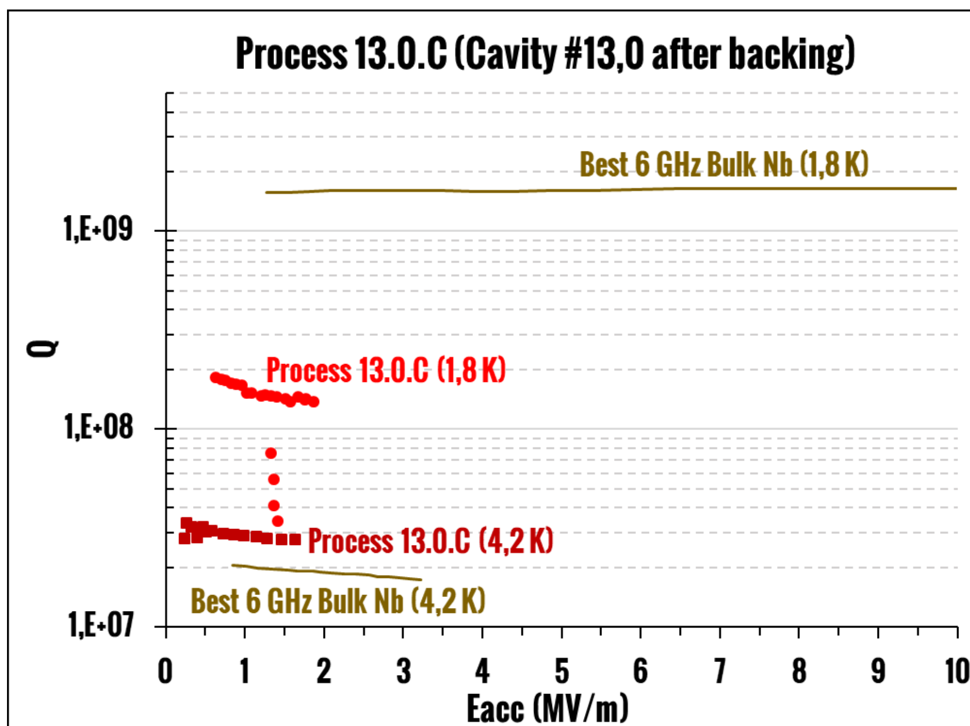

Figure 8.47 Rf test at 1.8K and 4.2K for Cav13.0 after baking.

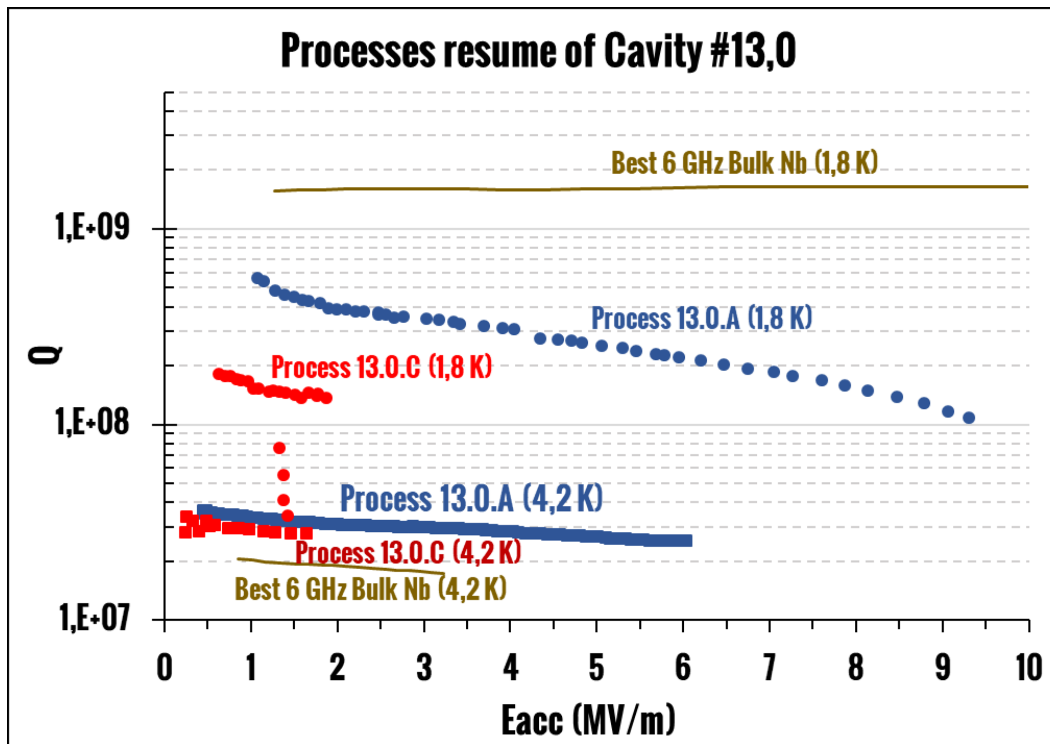

Figure 8.48 Rf test at 4.2K and 1.8K for all the processes Cav9.0

Cav 15.0

On Cav 15.0 a one-shot deposition and a standard venting was done. Some peeling occurred near one of the flanges. The cavity shows very poor performance. No post treatments were done.

Table 8.29 Deposition parameters for Cav11.0. PROCESS 15.0.A.
I=magnetron current, V=magnetron voltage, P=sputtering Ar pressure, B=magnetron magnetic field, T=substrate temperature, d=total thickness on the cell, t=total deposition time.

I (A)	V (V)	P (mbar)	B (G)	T (°C)	d (μm)	t (h)	deposition mode	venting mode
1	≈650	$1{\cdot}10^{-2}$	830	550	≈70	7	one-shot	standard

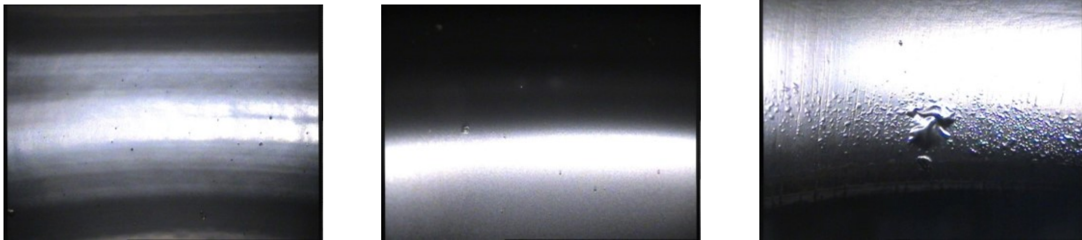

Figure 8.49 Internal inspection of the cell (on the left), iris (on the center) and near the flange (on the right, where peeling occurs) for Cav15.0.

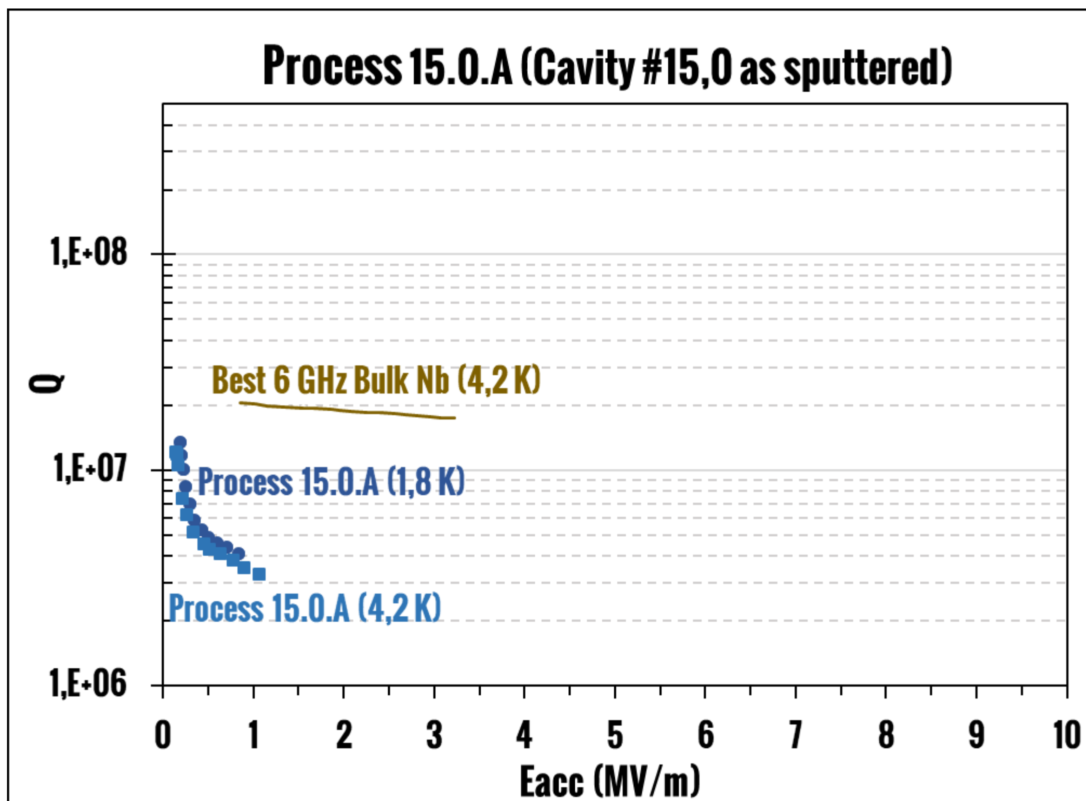

Figure 8.50 Rf test at 1.8 K and 4.2K for Cav15.0.

Cav 16.0

On Cav 16.0 a multilayer deposition and a standard venting was done. The rf test shows a tricky behavior. At low field the Q is very flat, but two Q switches occur at 3 and 4 MV/m. After the second Q switch the curve shows a slope. We did three different thermal treatments that eliminate the Q switch, reduce the Q value, but elongate the flat part of the curve almost to 9 MV/m.

Table 8.30 Deposition parameters for Cav16.0. PROCESS 16.0.A.
I=magnetron current, V=magnetron voltage, P=sputtering Ar pressure, B=magnetron magnetic field, T=substrate temperature, d=total thickness on the cell, d_{sl}=single layer thickness, n_{sl}=total numbers of single layers, D=sputtering duty cycle.

I (A)	V (V)	P (mbar)	B (G)	T (°C)	d (μm)	dep. mode	d_{sl} (nm)	n_{sl}	D	venting mode
1	≈320	$5 \cdot 10^{-2}$	830	550	≈70	multilayer	500	140	0.7	standard

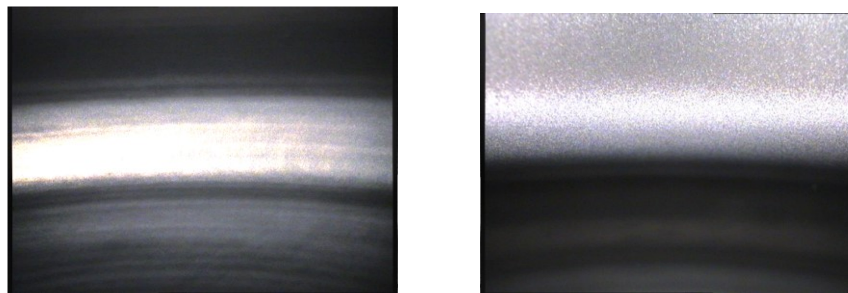

Figure 8.51 Internal inspection of the cell (on the left) and iris (on the right) for Cav16.0.

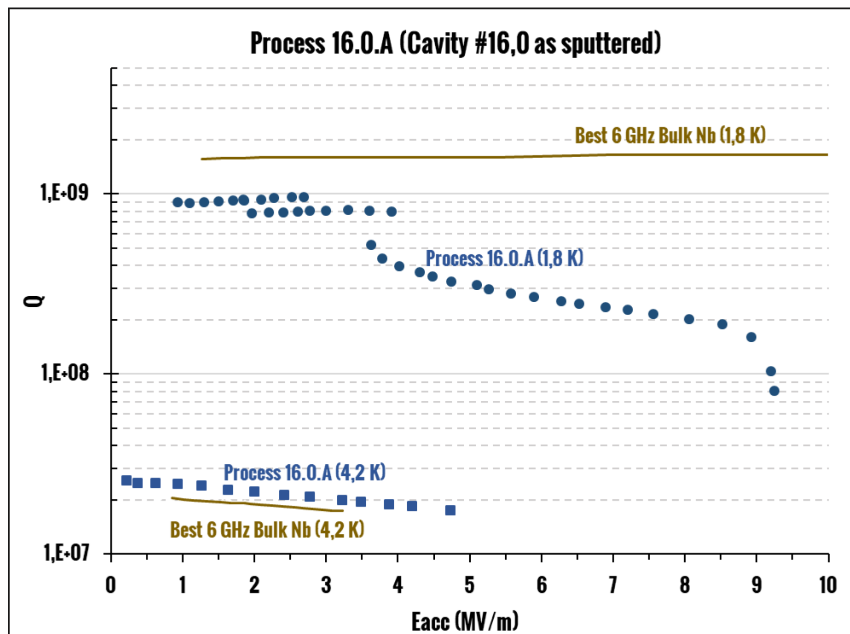

Figure 8.52 Rf test at 1.8K and 4.2K for Cav16.0.

Table 8.31 Baking parameters for Cav16.0. PROCESS 16.0.C.

Temperature (°C)	Time (hours)
120	24

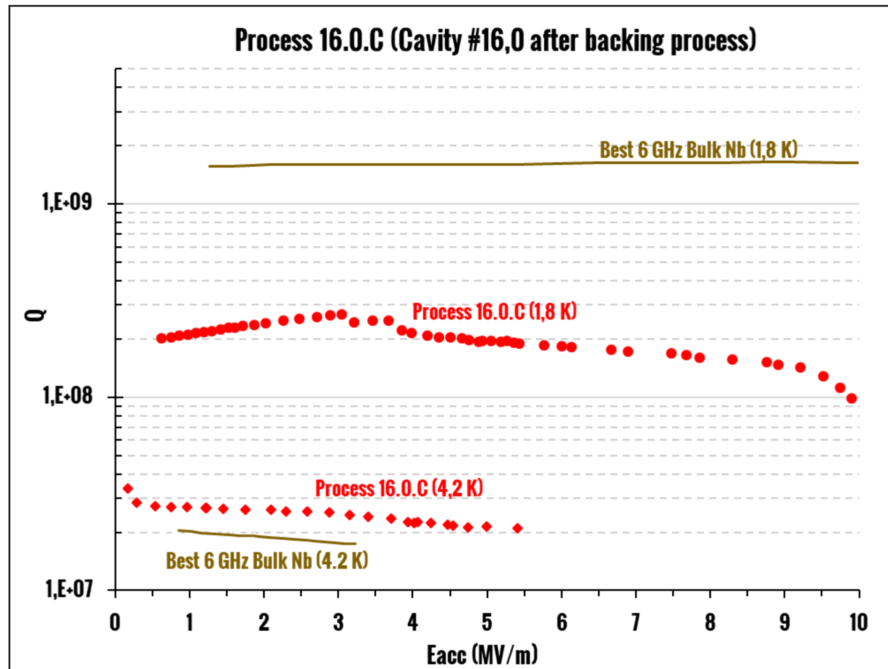

Figure 8.53 Rf test at 1.8 K and 4.2K for Cav16.0 after the baking process.

Table 8.32 Annealing parameters for Cav16.0. PROCESS 16.0.D.

Temperature (°C)	Time (hours)
600	10

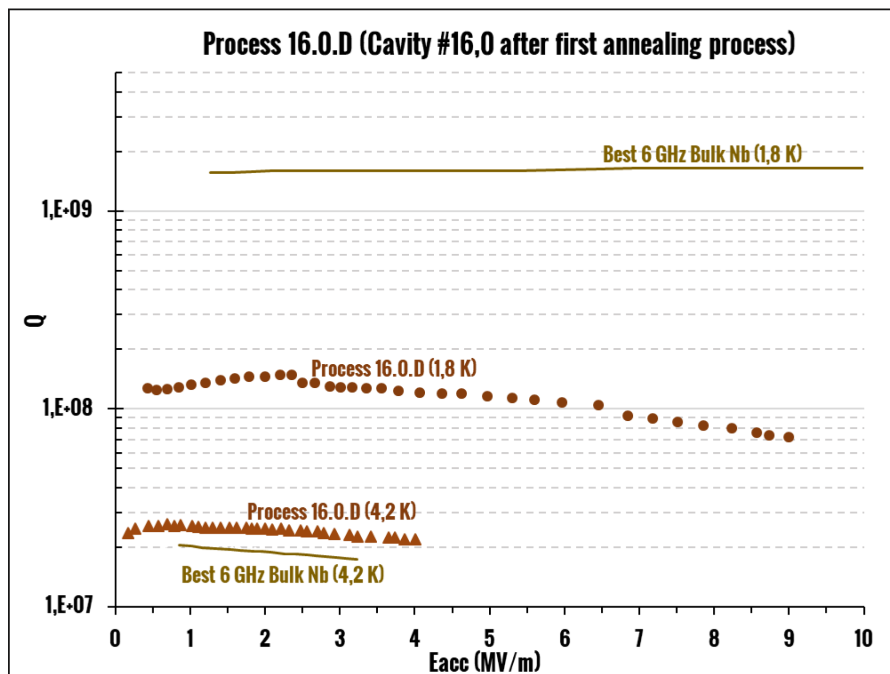

Figure 8.54 Rf test at 1.8 K and 4.2K for Cav16.0 after the first annealing process.

Table 8.33 Second annealing parameters for Cav16.0. PROCESS 16.0.E.

Temperature (°C)	Time (min)
730	40

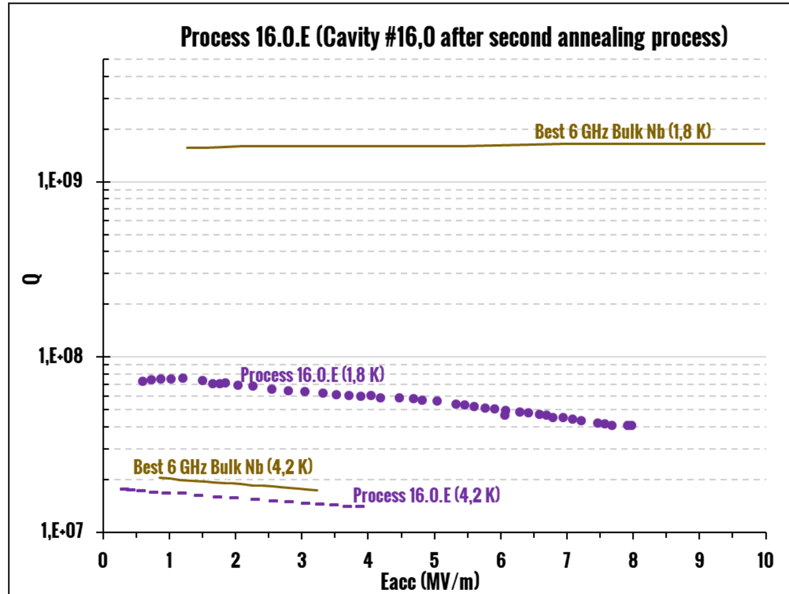

Figure 8.55 Rf test at 1.8 K and 4.2K for Cav16.0 after the first annealing process.

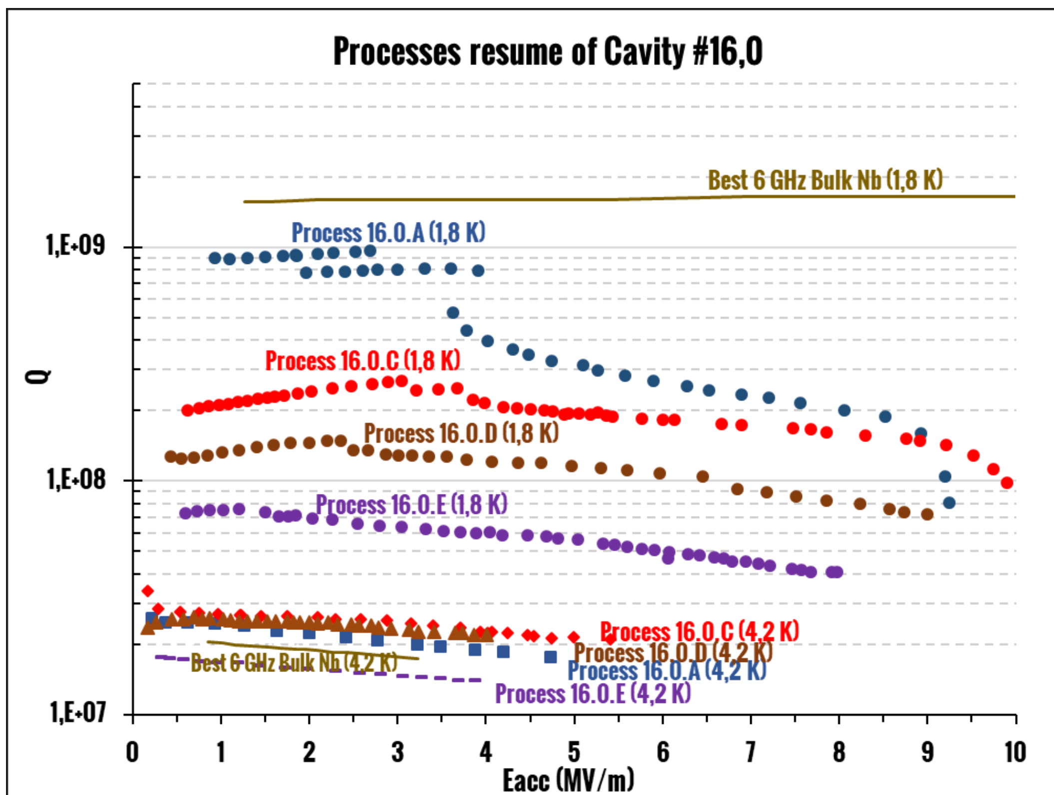

Figure 8.56 Rf test at 4.2K and 1.8K for all the processes Cav16.0

Cav 17.0

On Cav 17.0 a multilayer deposition and a standard venting was done. A final 5 μm thickness layer was deposited in order to avoid SRF performance deterioration due to the incidental oxide layer formation during the pause time. The rf test at 1.8K was not done after the baking process, because a vacuum leak appeared at the helium λ point during the cooling down at 1.8 K. No post treatments were done.

Table 8.34 Deposition parameters for Cav17.0. PROCESS 17.0A.
I=magnetron current, V=magnetron voltage, P=sputtering Ar pressure, B=magnetron magnetic field, T=substrate temperature, d=total thickness on the cell, d_{sl}=single layer thickness, d_{fl}= final layer thickness, n_{sl}=total numbers of single layers, D=sputtering duty cycle.

I (A)	V (V)	P (mbar)	B (G)	T (°C)	d (μm)	dep. mode	d_{sl} (nm)	d_{fl} (μm)	n_{sl}	D	venting mode
1	≈315	$5\cdot10^{-2}$	830	550	≈70	multilayer	400	5	162	0.7	standard

Figure 8.57 Internal inspection of the cell (on the left) and iris (on the right) for Cav17.0.

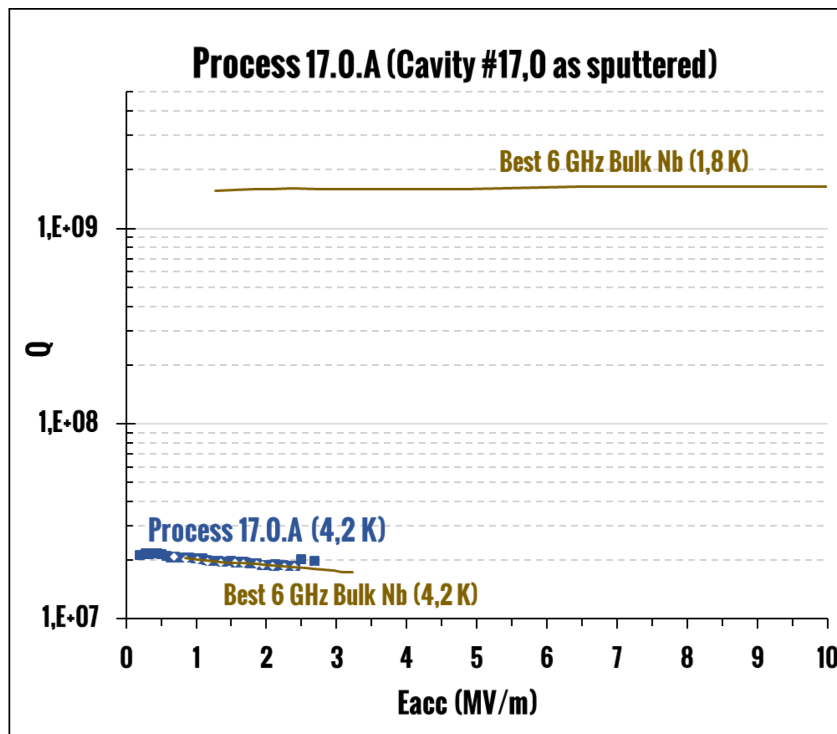

Figure 8.58 Rf test at 4.2K for Cav17.0.

8.3 Results discussion

The rf tests have been treated in order to find out any correlation between the critical deposition parameters and the cavity performances. For each parameter the rf test are replotted in order to put in evidence the different values used and see, at a glance, if a direct correlation between parameters and SRF performances exists or not. We analyzed the effect of the pressure, venting mode, multilayer deposition and the influence of post treatments: chemical polishing and heat treatments.

8.3.1 Flat Q and Q slope on thick film cavities

Three thick film cavities have shown a quite flat Q-value versus the accelerating field and are undoubtedly the 6GHz Nb/Cu cavities with the best performances ever obtained (Figure 8.59). For the first time, a Nb/Cu sputtered cavity does not suffer the Q-slope problem. Furthermore, if we compare the curves with the rf test of the best 6 GHz thin film cavities ever done at LNL, we see a dramatic increase of the SRF performances. One cavity also presents a Q_0 at low field higher than the best 6 GHz bulk cavity used as reference.

Two cavities were sputtered in one shot mode and one with the multilayer approach. For this last cavity, a 24 hours baking at 120 ° was done with an improvement of the maximum accelerating field, a flatter Q-curve, but a sensible decrease of the Q-value at low fields. In Cav 3.1 a high temperature venting was done. All the other cavities present the characteristic Q-slope of sputtered cavities.

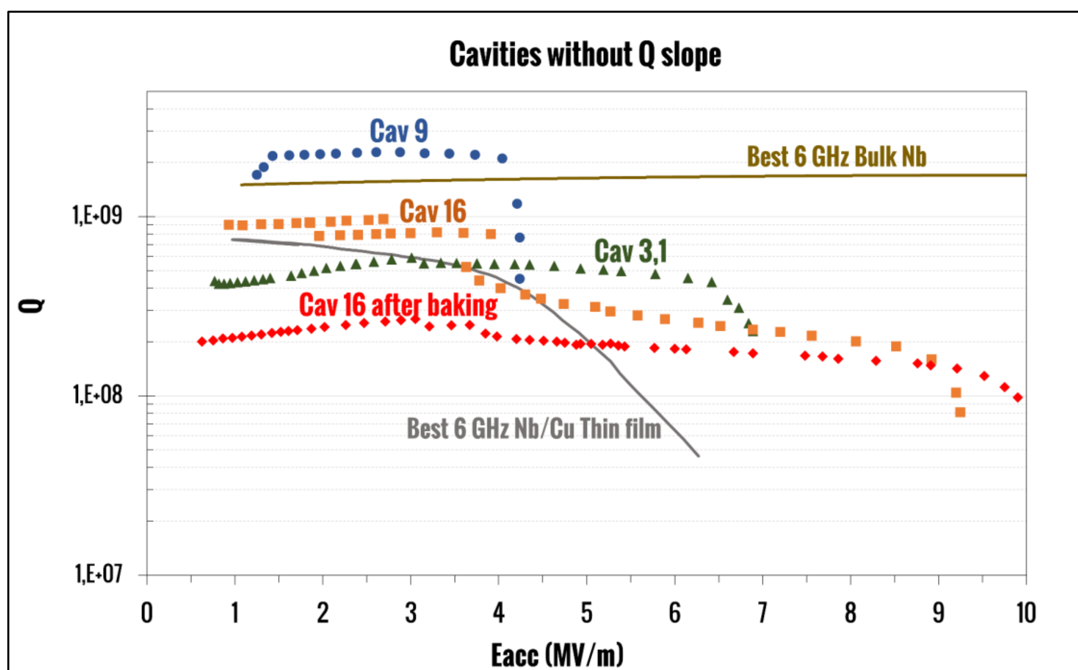

Figure 8.59 Q vs E_{curve} at 1.8K of the 3 best thick Nb/Cu 6 GHz cavities. Cav 3.1 and Cav 9 are sputtered in one shot mode, Cav 16 are sputtered with the multilayer approach. On Cav 16 a 120°C baking was done for 24 hours. On the graph is reported the best 6 GHz Nb bulk cavity curve and the best 6 GHz Nb/Cu thin film ever measured.

The fact that a flat Q has been obtained with different deposition conditions, pushes the idea that Q-slope is an intrinsically characteristic of thin films and that can be solved with higher sputtering thickness. On the other hand, in our configuration we are missing the parameter that plays the fundamental role for the SRF performances. As we will see in the next paragraphs, pressure and multilayer approach have an important effect on the rf curve, but we suppose that the rf performances are strongly influenced by the initial substrate preparation. In chapter 4 we saw as some surface defects, coming from spinning process, remain after the chemistry as well. All these defects are possible points of enhanced thermal boundary resistance. This theory, of a central role on rf performances by the initial copper substrate conditions, is confirmed by another project at CERN on HIPIMS deposition [51] [63]. Hence, the sputtering of an optimum Nb film is a necessary condition, but not sufficient for a flat high Q curve. If we really want to understand the mechanism behind the Q slope and develop the thick film technique in order to obtain an industrialized process for the Nb/Cu cavities of the future, an improvement of the spinning process and of the cavity preparation is mandatory.

8.3.2 Role of pressure

We divided the rf test curves in two main groups: low pressure deposition ($7 \cdot 10^{-3}$ and $1 \cdot 10^{-2}$ mbar) in red and high pressure deposition ($5 \cdot 10^{-2}$ mbar) in blue. Looking at Figure 8.60, we note that the Q value does not show any correlation with pressure, both at 1.8K and 4.2K curves. The highest Q was obtained at $7 \cdot 10^{-3}$ mbar (Cav 9.0), but the other cavities sputtered at the same pressure present Q values similar or lower to the Q values of cavities coated at $5 \cdot 10^{-2}$ mbar. A trend is visible in the maximum gradient value. Al the curves that pass 8 MV/m at 1,8 K are coated at $5 \cdot 10^{-2}$ mbar. Also, at 4,2 K the trend is respected. On a total of 14 cavities measured as sputtered, 8 are coated at high pressure and 6 at low pressure. 5 of the 8 cavities coated at $5 \cdot 10^{-2}$ mbar overpass the gradient of 4 MV/m, instead, on the cavities coated at low pressure, only one overpasses the 4 MV/m and is the one with the lowest Q value (Cav 4.0).

A possible explanation of these results comes from the kapton stress test reported in paragraph 7.3.4. At $5 \cdot 10^{-2}$ mbar we have the minimum stress for the coated film. In first approximation, it is reasonable to think that the pressure deposition and film stress play a role in the superconducting properties, but at the same order of other contributions, as for example the initial substrate morphology, RRR, multilayers depositions, venting mode, etc. On the other hand, in the interface scenario proposed by Vaglio and Palmieri ([10] and 1.4.5), a stressed film produces forces at the Nb-Cu interface, that tend to separate the film from the substrate, increasing the dimension of the existing voids and then producing an enhancement of the thermal defects. The thermal defects, due to film stress, produce a thermal quench of the superconductive film at lower accelerating field values compared to the non-stressed ones.

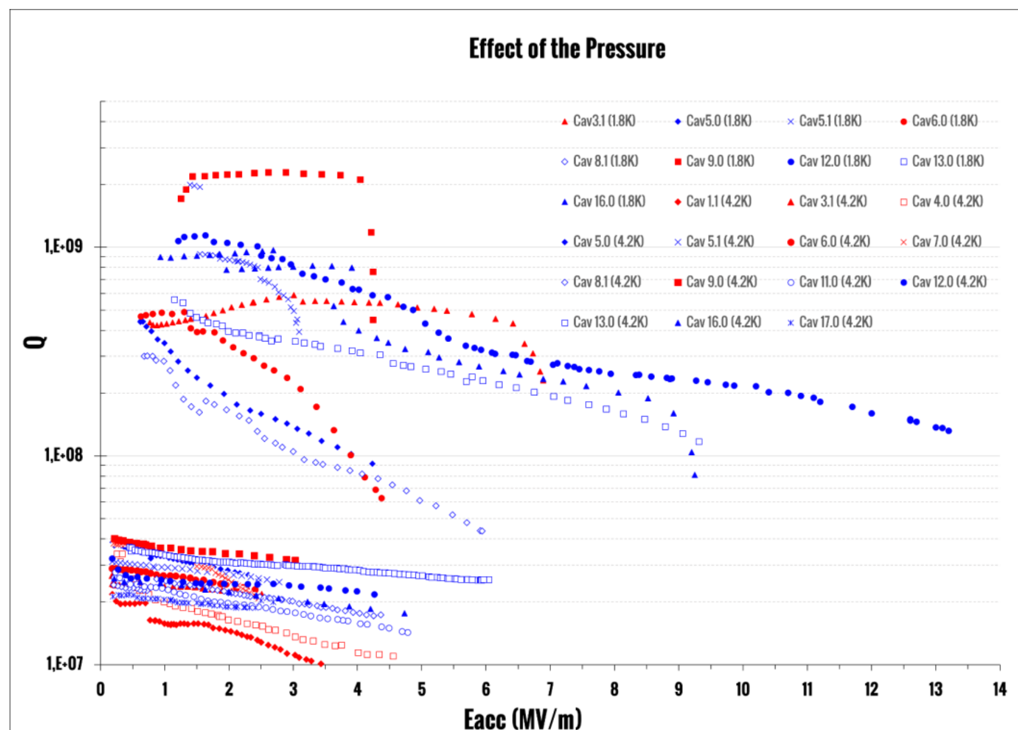

Figure 8.60 On the graph the rf test curves at 4.2 K and 1.8 K are plotted in blue or red in function of their deposition pressure. In red low pressure deposition (7×10^{-3} and 1×10^{-2} mbar) and in blue high pressure deposition (5×10^{-2} mbar).

8.3.3 Role of venting

High temperature venting (in red on Figure 8.61) does not seem to enhance the rf performances. At 1,8 K, the best curves are obtained with the standard venting procedure. At 4,2 K, on the other hand, all the red curves are in the upper part of the Q values.

However, the evaluation of the high temperature effect is more complex than that. We need to take into account the BCP process, since, also in the Nb bulk cavities doping process, the initial nitriding process reduce the rf performances [114]. The high Q values are obtained after the chemical process necessary to remove the high-doped superficial 5 µm, in order to have the right nitrogen doping value on Niobium London penetration depth. On Cav 3.1 and Cav 7.0 the complete process was done (BCP and post thermal treatment), but rf performances have decreased compared to the un-chemical treated ones. There are two possible explanations: the doping process applied is not optimized for sputtered cavities, or the doping process does not increase the rf performance in sputtered cavities as it does in bulk cavities. The second possibility can be taken into account, why one of the main theory to explain the doping effect [81], implies a reduction of the mean free path in the bulk niobium after the doping process. In sputtered cavities, mean free path is already small compared to the bulk ones. The first possibility, instead, is definitely possible. We have adapted the bulk cavities process to the sputtered cavities with theoretical considerations, but we need an experimental confirmation that the nitrogen concentration on the surface is comparable to the one of Nb bulk doped cavities. The characterization will be done at the Daresbury laboratories of Science & Technology Facilities Council (STFC), partner of LNL and CERN in this project. From the cross section of the cavity we can obtain information about the nitrogen concentration profile and modify the procedure in order to arrive at the bulk situation.

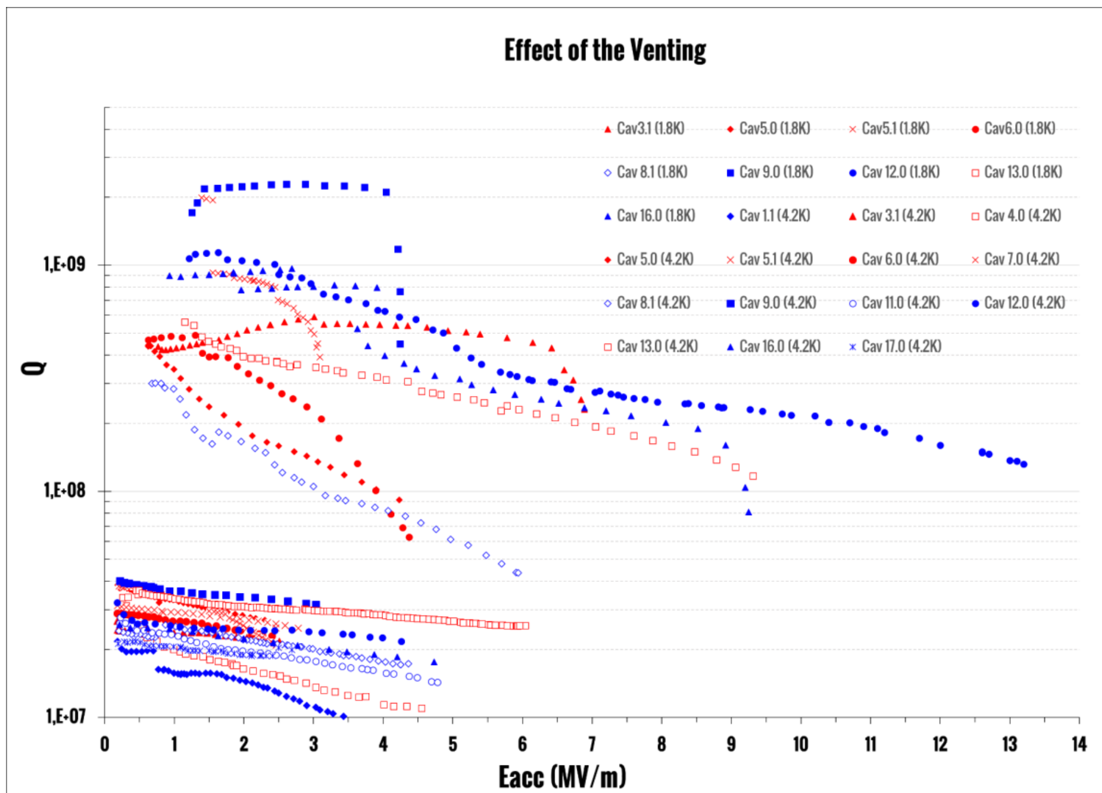

Figure 8.61 On the graph the rf test curves at 4.2 K and 1.8 K are plotted in blue or red in function of venting procedure adopted. In blue standard venting, in red high temperature venting.

8.3.4 Role of multilayer deposition

Unfortunately, only two of the four multilayer cavities have been tested at 1,8 K, and it is very difficult to extrapolate the contribution of multilayer deposition from the rf tests. We immediately note that the maximum accelerating field was obtained in multilayer mode (Cav 12.0). At 4,2 K all the multilayer curves overpass 4 MV/m and they have Q values on the average of 4,2 K Q values of this work. It is a bit dazed, but a similar contribution to that given by the high pressure can be identified in the multilayer deposition. Both are able to reduce the film stress and both increase the maximum accelerating field.

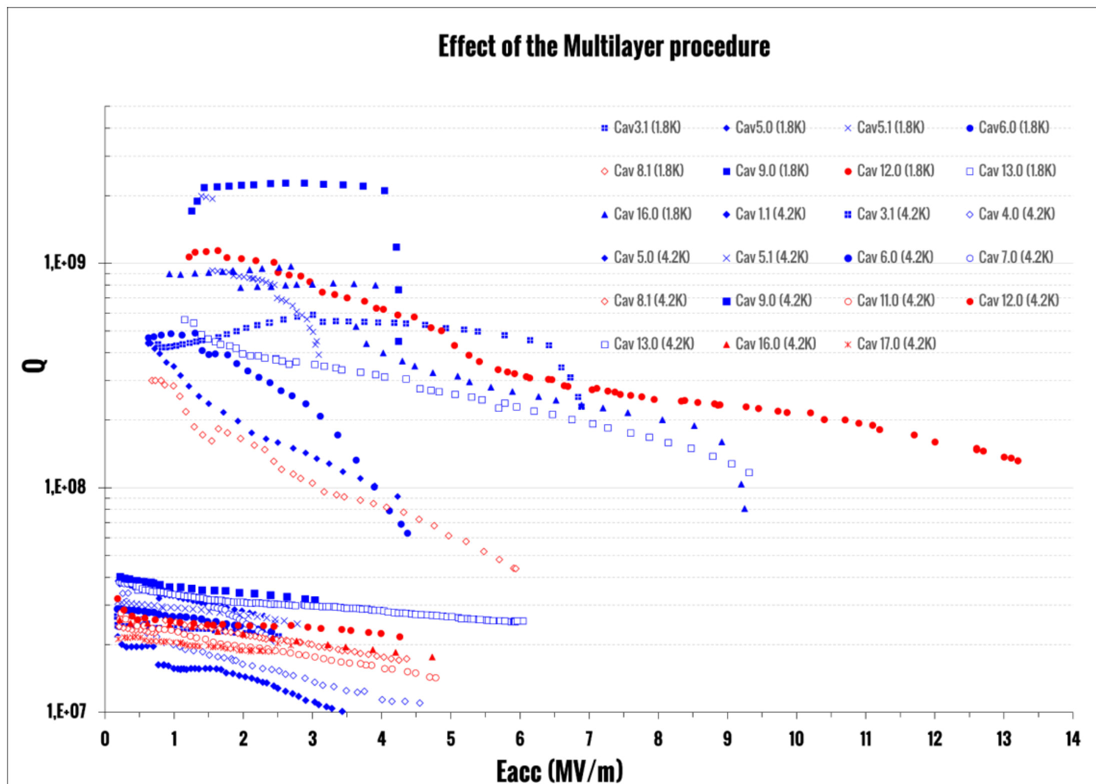

Figure 8.62 On the graph the rf test curves at 4.2 K and 1.8 K are plotted in blue or red in function of sputtering mode adopted. In blue one shot mode, in red multilayer mode.

A remarkable aspect involves the Q-slope of the multilayer films. Figure 8.63 shows the Q vs E_{acc} curves at 4.2 K of 5 different cavities coated with the multilayer approach, but with different single layer thickness. If we plot the slope values as a function of the single layer thickness, we obtain the interesting behavior visible in Figure 8.64. Further investigation is needed, but, from our preliminary results, the Q-slope can be modulated simply varying the single layer thickness.

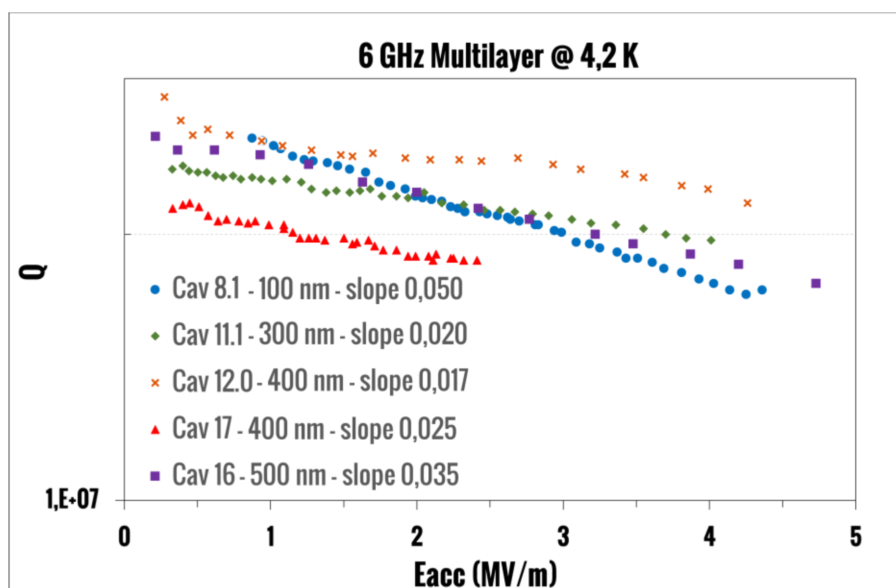

Figure 8.63 Q vs E_{curve} measured at 4.2 K and 6 GHz for different single layer thickness.

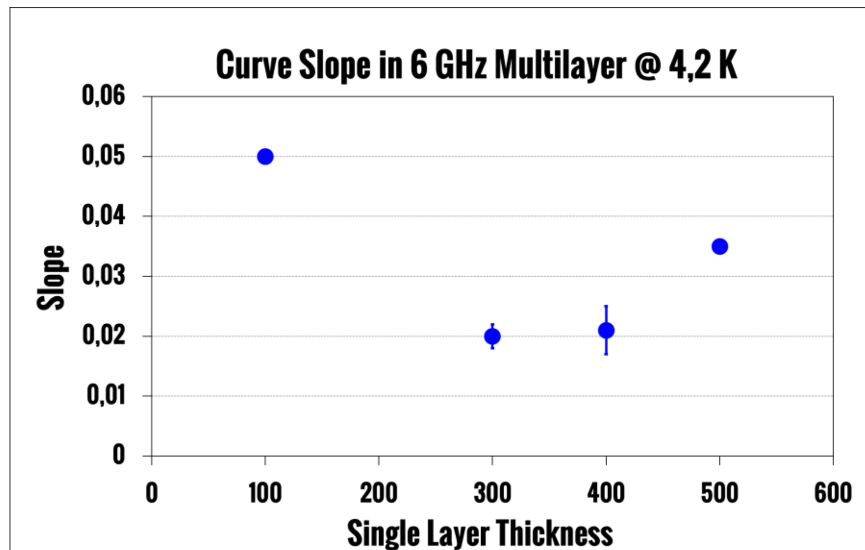

Figure 8.64 Curve slope at 4.2 K for different single layer thickness.

8.3.5 Role of BCP

BCP was applied on Cav 3.1, 7.0 ad 9.0. On the first two cavities, BCP was applied after a high temperature venting process, and the results have already been discussed on 8.3.3. Cav 9.0, coated in a standard venting mode, shows the highest Q ever obtained in a 6 GHz cavities. The Q curve is also flat (no typical Q slope of sputtered cavities), but quenches at very low fields: 4,5 MV/m. We suppose a possible contamination of the niobium surface during the cooling down process, because Nb is a powerful getter and at 550 °C the surface is very active.

BCP was applied to Cav 9.0 in order to remove the first 5 microns. The chemical treatment produces an increment of the accelerating field (that passes from 4.5 to 8 MV/m), but also a dramatically decreasing of the quality factor and the appearance of the Q slope. The subsequent heat treatments mitigate the fall of Q_0, returning it to the initial values, but keeping the Q slope.

A possible explanation is that the BCP, due to the porosity of sputtered layer, also act at the Nb/Cu interface, increasing the interface defects, and causing the Q slope. To confirm this theory, we are awaiting for a cross section characterization from STFC.

8.3.6 Role of thermal treatments

Thermal treatments were applied on Cav 3.1, 7.0, 9.0, 13.0 and 16.0. On cavities 3.1, 7.0 and 9,0 heat treatment was applied after a BCP process, on Cav 13.0 and 16.0 heat treatment was applied on the cavity as sputtered. In Cav 3.1, 7.0 and 13.0 a high temperature venting was also done.

The results are different, and it is better to discuss them case by case.

In Cav 3.1, a baking of 24 hours at 120°C was done. The characterization was done only at 4,2 K and shows a gradient increase compared to the measured value after the BCP.

In Cav 7.0, the same process of Cav 3.1 were done, but with a diametrically opposite result.

In Cav 9.0, two heat treatments at 100 °C (short of 48 hours and long one of 100 hours) and one at 120 °C for 24 hours was done. Both heat treatments increase the Q after the BCP process, as we expected, but the best result was obtained at 120 °C.
In Cav 13.0, a baking of 100 °C for 48 hours produces a dramatically decrease both in quality factor and maximum accelerating field.
In Cav 16.0 the baking process of 24 hours at 120 °C decreases almost an order of magnitude the Q at low fields, but at the same time removes the Q slope at high fields. On this cavity, also two annealing processes at 600 °C and 730 °C were done, but the rf performance decreases after both processes.

In conclusion, baking at 120 °C shows the ability, as in bulk cavities, to reduce Q slope at high fields, and increase the Q slope values after a chemical process. The baking process, on the other hand, need to be validated by more statistics. Baking at 100 °C seems, however, not to be sufficiently efficient, and post annealing at 600 °C and 700 °C produces a reduction of the cavity rf performances.

9 Conclusions

The main purpose of the present work has been to explore the possibility to grow thick films of the order of tens of microns in order to solve the problem of Q-slope in Nb/Cu sputtered cavities. The deposition of 70 µm thick film of Nb onto 6 GHz copper cavities, for the first time, demonstrates the possibility to obtain flat curve of Q-factor versus accelerating field in sputtered cavities.

To arrive at this important result, an optimized magnetron sputtering configuration for the deposition of thick films onto 6 GHz cavities at high temperature was designed, built and tested. RRR values of 35 for 4.5 µm thick film (similar to the best MS films reported in literature) and over 60 for 15 µm thick film are reported. High RRR values, reticular parameter close to the bulk Nb and dense film structure, demonstrate the high quality of the Nb coated films.

During this work, 17 different Copper Cavities substrates have been used, 18 different magnetron sputtering depositions have been carried out, 30 different processes have been characterized at 4.2 K and 24 processes at 1,8 K; only 3 coatings have shown peeling.

Of the 24 curves, measured at 1.8 K after the sputtering, four show flat Q, while the others present the characteristic Q slope of sputtered cavities. The reason has been ascribed to the initial substrate preparation. In chapter 4 we saw how some surface defects due to spinning process remain after the chemistry. All these defects are possible points of enhanced thermal boundary resistance. Hence, the sputtering of an optimum Nb film is a necessary condition, but not sufficient for a flat high Q curve. An improvement of the 6 GHz spinning process and of the cavity preparation is mandatory, in order to understand the mechanism behind the Q slope, and develop the thick film technique capable to become an industrialized process for the Nb/Cu cavities of the future.

Through the rf tests done, important information have been obtained on the thick film dependence. The role of the deposition parameters on the SRF performances has been explored. In detail, the explored parameters are: pressure, venting mode, deposition mode, and the effect of the following post treatments: BCP and thermal treatments. From the analysis of the different Q VS E_{acc} curves several considerations can be done. The principal ones are reported below.

The deposition pressure plays a role in the maximum gradient achievable, but it does not seems to have any influence on the Q value. The best results have been obtained at $5 \cdot 10^{-2}$ mbar, the pressure at which there is no stress on the coated film.

A multilayer process, instead of the standard one shot deposition, was done, in order to mitigate the film stress. The rf test shows an effect on the final gradient enhancement comparable to the one obtained varying the pressure, and, in first approximation, confirm a possible film stress

reduction. The role of the single film thickness has been also investigated, showing a possible correlation between Q slope and single layer thickness.

Two different venting procedures have been tested: a standard one and a high temperature one, in which pure nitrogen is inserted in the vacuum chamber immediately after the end of the sputtering process. For this second venting process, an adaptation of the parameters used in LCLS-II was done and a cavity with a flat curve was obtained. However, a deep characterization on film structure and composition is necessary in order to optimize the parameters used in the high temperature venting process.

BCP on thick films produced a dramatically reduction of the SRF performances. It is very likely that the process etched also the niobium-copper interface, causing the appearance of a lot of defects.

Baking process at 120 °C for 24 hours shows the ability to reduce Q slope at high fields, and increase the Q value after a chemical process. Nevertheless, more statistics is necessary to validate this conclusion. Post annealing at 600 °C and 700 °C seems to be not suitable in sputtered cavities, because a reduction of the cavity rf performances has been shown on the test done.

This work is a first approach to the thick film for SRF applications. We are just at the beginning: further work needs to be done in order to optimize the deposition procedure and understand the mechanism that explains the flat Q in thick films. At the moment, however, the guiding lights are the very promising results obtained after decades of several attempts. They prospect a possible way toward the solution of the Q-slope problem in sputtered cavities.

9.1 Future developments

In the framework of the collaboration with the Daresbury laboratories of Science & Technology Facilities Council (STFC), partner of LNL and CERN in this project, a fully characterization of several cavities will be done in order to correlate film and interface microstructure to the deposition parameters and rf performances. The characterization will be done in a feedback mode, in order to try to improve the quality of the film coating using the information extrapolated from the film analysis. We have planned to cut the coated cavities in different points and characterize the cross sections with SEM, EDS, XRD, AFM, XPS, AFM and RRR measure.

In order to improve the internal surface quality of the 6 GHz spun cavities, a new die is under developing. Future plans provide the R&D of all the substrate preparation test. It is mandatory to continue the developing of the thick films coating in a copper substrate without any scratch and defect.

After the optimization of the substrate preparation, the future strategy consists in optimizing the results already got for 70 micron thick film cavities, in order to achieve the highest possible Q and accelerating field. Once obtained that, the next step is to determine the minimum thickness required for having flat Q-curves versus E_{acc}.

Bibliography

[1] H. Padamsee, “SRF Accelerators Flourish In a Golden Age,” presented at the 6th International Particle Accelerator Conference, Richmond, VA, USA, 2015.

[2] C. Benvenuti, N. Circelli, and M. Hauer, “Niobium films for superconducting accelerating cavities,” *Appl. Phys. Lett.*, vol. 45, no. 5, pp. 583–584, 1984.

[3] W. Weingarten, “Progress in thin film techniques,” *Part Accel*, vol. 53, no. CERN-SL-95-122-RF-8, pp. 199–215, 1995.

[4] S. Bauer *et al.*, “Production of Nb/Cu sputtered superconducting cavities for LHC,” in *Proceedings of the 9th Workshop on RF Superconductivity, Santa Fe, New Mexico, USA*, 1999.

[5] S. Stark *et al.*, “Niobium sputter-coated QWRs,” in *Proceedings of 8th International Conference on RF Superconductivity (SRF1997), Abano Terme (Padova), Italy*, 1997.

[6] W. Venturini Delsolaro *et al.*, “Nb Sputtered Quarter Wave Resonators for the HIE-ISOLDE,” in *Proceedings of 16th International Conference on RF Superconductivity (SRF2013), Paris, France*, 2013.

[7] V. Palmieri *et al.*, “The way of thick films toward a flat Q-curve in sputtered cavities,” in *Proceedings of 18th International Conference on RF Superconductivity (SRF2017), Lanzhou, China*, 2017.

[8] T. Fujino *et al.*, “Promising Performance of the Nb/Cu Clad Seamless Superconducting RF Cavities,” in *9th International Conference on RF Superconductivity (SRF2009),Santa Fe, New Mexico, USA*, 2009.

[9] C. Benvenuti, S. Calatroni, and G. Orlandi, “Superconducting cavities for particle accelerators,” *Phys. B Condens. Matter*, vol. 197, no. 1, pp. 72–83, Mar. 1994.

[10] V. Palmieri and R. Vaglio, “Thermal contact resistance at the Nb/Cu interface as a limiting factor for sputtered thin film RF superconducting cavities,” *Supercond. Sci. Technol.*, vol. 29, no. 1, p. 015004, Jan. 2016.

[11] T. Junginger, “Basic Principles of RF superconductivity,” presented at the Tutorials of 18th International Conference on RF Superconductivity (SRF2017), Lanzhou, China, 2017.

[12] H. Padamsee, J. Knobloch, and T. Hays, *RF Superconductivity for Accelerators*. Wiley-VCH, 1998.

[13] A. P. Banford and G. H. Stafford, “The feasibility of a superconducting proton linear accelerator,” *J. Nucl. Energy Part C Plasma Phys. Accel. Thermonucl. Res.*, vol. 3, no. 4, p. 287, 1961.

[14] A. Gurevich, “Superconducting Radio-Frequency Fundamentals for Particle Accelerators,” *Rev. Accel. Sci. Technol.*, vol. 05, pp. 119–146, Jan. 2012.

[15] H. K. Onnes, “Further experiments with liquid helium. C. On the change of electric resistance of pure metals at very low temperatures etc. IV. The resistance of pure mercury at helium temperatures,” in *Through Measurement to Knowledge: The Selected Papers of Heike Kamerlingh Onnes 1853–1926*, K. Gavroglu and Y. Goudaroulis, Eds. Dordrecht: Springer Netherlands, 1991, pp. 261–263.

[16] M. Tinkham, *Introduction to Superconductivity*, 2nd ed. McGraw-Hill, Inc., 1996.

[17] J. File and R. G. Mills, “Observation of Persistent Current in a Superconducting Solenoid,” *Phys. Rev. Lett.*, vol. 10, no. 3, pp. 93–96, Feb. 1963.

[18] K. Fossheim, *Superconductivity: Discoveries and Discoverers*. Berlin, Heidelberg: Springer Berlin Heidelberg, 2013.

[19] W. Meissner and R. Ochsenfeld, “Ein neuer Effekt bei Eintritt der Supraleitfähigkeit,” *Naturwissenschaften*, vol. 21, no. 44, pp. 787–788, Nov. 1933.

[20] F. London and H. London, “The Electromagnetic Equations of the Supraconductor,” *Proc. R. Soc. Lond. Ser. Math. Phys. Sci.*, vol. 149, no. 866, pp. 71–88, 1935.

[21] V. L. Ginzburg and L. D. Landau, “On the Theory of superconductivity (In Russian),” *Zh Eksperim Teor Fiz*, vol. 20, pp. 1064–1082, 1950.

[22] J. Bardeen, L. N. Cooper, and J. R. Schrieffer, “Microscopic theory of superconductivity,” *Phys. Rev.*, vol. 106, no. 1, p. 162, 1957.

[23] J. Bardeen, L. N. Cooper, and J. R. Schrieffer, “Theory of superconductivity,” *Phys. Rev.*, vol. 108, no. 5, p. 1175, 1957.
[24] G. Ciovati, “Basic Principles of RF superconductivity,” presented at the Tutorials of 17th International Conference on RF Superconductivity (SRF2015), Whistler, BC, Canada, 2015.
[25] A. B. Pippard and W. L. Bragg, “An experimental and theoretical study of the relation between magnetic field and current in a superconductor,” *Proc. R. Soc. Lond. Ser. Math. Phys. Sci.*, vol. 216, no. 1127, p. 547, Feb. 1953.
[26] A. Gurevich and G. Ciovati, “Dynamics of vortex penetration, jumpwise instabilities, and nonlinear surface resistance of type-II superconductors in strong rf fields,” *Phys Rev B*, vol. 77, no. 10, p. 104501, Mar. 2008.
[27] C. Benvenuti *et al.*, “Study of the surface resistance of superconducting niobium films at 1.5 GHz,” *Phys. C Supercond.*, vol. 316, no. 3, pp. 153–188, May 1999.
[28] H. Padamsee, *RF superconductivity: science, technology, and applications*. Weinheim: Wiley-VCH, 2009.
[29] S. De Ambrosis, “A method to test A15 intermatallic compounds rf properties.,” PhD dissertation, Università degli studi di Padova (Italy), 2008.
[30] B. Visentin, “3.8 Low, Medium, High Field Q-Slopes Change with Surface Treatments,” *Beam Dyn. Newsl.*, p. 94, 2006.
[31] T. Higuchi, K. Saito, Y. Yamazaki, T. Ikeda, S. Ohgushi, and others, “Hydrogen Q disease and electropolishing,” in *Proceedings of 10th Workshop on RF Superconductivity (SRF2001), Tsukuba, Ibaraki, Japan*, 2001.
[32] A.-M. Valente-Feliciano, “Superconducting RF materials other than bulk niobium: a review,” *Supercond. Sci. Technol.*, vol. 29, no. 11, p. 113002, Nov. 2016.
[33] W. Singer, A. Ermakov, and X. Singer, “RRR-measurement techniques on high purity niobium,” *TTC Rep.*, vol. 2, 2010.
[34] S. Aull *et al.*, “On the understanding of Q-Slope of niobium thin films,” in *17th International Conference on RF Superconductivity (SRF2015), Whistler, BC, Canada*, 2015, pp. 494–500.
[35] C. Benvenuti, S. Calatroni, P. Darriulat, M. A. Peck, A.-M. Valente, and C. A. V. Hof, “Study of the residual surface resistance of niobium films at 1.5 GHz,” *Phys. C Supercond.*, vol. 351, no. 4, pp. 421–428, Apr. 2001.
[36] R. Vaglio and V. Palmieri, “Thermal boundary resistance model and defect statistical distribution in Nb/Cu cavities,” in *Proceedings of 18th International Conference on RF Superconductivity (SRF2017), Lanzhou, China*, 2017.
[37] C. Benvenuti, S. Calatroni, M. Hakovirta, H. Neupert, M. Prada, and A. M. Valente, “CERN studies on niobium-coated 1.5 GHz copper cavities,” in *Proc. of the 10th Workshop on Superconductivity, Tsukuba, Japan, Sep*, 2001, pp. 6–11.
[38] D. M. Mattox, *Handbook of physical vapor deposition (PVD) processing*, 2. ed. Amsterdam: Elsevier, 2010.
[39] D. M. Mattox, *The foundation of vacuum coating technology*. Norwich: Noyes Pubblications / William Andrew Publishing, 2003.
[40] A. Anders, “Tutorial: Reactive high power impulse magnetron sputtering (R-HiPIMS),” *J. Appl. Phys.*, vol. 121, no. 17, p. 171101, May 2017.
[41] M. Ohring, *Materials science of thin films*. Academic press, 2001.
[42] J. A. Thornton and D. W. Hoffman, “Stress-related effects in thin films,” *Thin Solid Films*, vol. 171, no. 1, pp. 5–31, 1989.
[43] D. Tonini *et al.*, “Morphology of niobium films sputtered at different target–substrate Angle,” in *Proceeding of 11th Workshop on RF Superconductivity (SRF2003), Lubek (Germany)*, 2003.
[44] B. A. Movchan and A. V. Demchishin, *Fiz Met Met.*, vol. 28, p. 653, 1969.
[45] A. Anders, “A structure zone diagram including plasma-based deposition and ion etching,” *Thin Solid Films*, vol. 518, no. 15, pp. 4087–4090, May 2010.
[46] H. Skliarova, “Development of novel cyclotron target for 99mTc production,” PhD dissertation, Università degli studi di Ferrara (Italy), 2017.
[47] N. Sharma, M. Hooda, and S. K. Sharma, “Synthesis and Characterization of LPCVD Polysilicon and Silicon Nitride Thin Films for MEMS Applications,” *J. Mater.*, vol. 2014, pp. 1–8, 2014.
[48] V. Palmieri, R. Preciso, V. L. Ruzinov, S. Y. Stark, L. Badan, and A. M. Porcellato, “Sputtering of Niobium Thin Films onto Copper Quarter Wave Resonators,” in *Proceedings of 5th Workshop on RF Superconductivity (SRF1991), DESY, Hamburg, Germany*, 1991.

[49] A. Sublet *et al.*, “Thin Film Coating Optimization for HIE-ISOLDE SRF Cavities: Coating Parameters Study and Film Characterization,” in *Proceedings of 16th International Conference on RF Superconductivity (SRF2013), Paris, France*, 2013.

[50] V. Palmieri, R. Preciso, and S. Y. Stark, “Seamless 1.5 GHz cavities obtained by spinning a circular blank of copper or niobium,” in *Proceedings of 6th International Conference on RF Superconductivity (SRF1993), CEBAF, Newport News, Virginia, USA*, 1993.

[51] G. J. Rosaz, S. Aull, E. A. Ilyina, A. Sublet, and W. Venturini Delsolaro, “SRF Cavity Coatings: Review of Alternative Materials and Coating Techniques,” in *Proceedings of 18th International Conference on RF Superconductivity (SRF2017), Lanzhou, China*, 2017.

[52] N. Hosokawa, T. Tsukada, and T. Misumi, “Self-sputtering phenomena in high-rate coaxial cylindrical magnetron sputtering,” *J. Vac. Sci. Technol.*, vol. 14, no. 1, pp. 143–146, 1977.

[53] V. Kouznetsov, K. Macák, J. M. Schneider, U. Helmersson, and I. Petrov, “A novel pulsed magnetron sputter technique utilizing very high target power densities,” *Surf. Coat. Technol.*, vol. 122, no. 2, pp. 290–293, Dec. 1999.

[54] A. Hecimovic and J. T. Gudmundsson, “Preface to Special Topic: Reactive high power impulse magnetron sputtering,” *J. Appl. Phys.*, vol. 121, no. 17, p. 171801, May 2017.

[55] A.-M. Valente-Feliciano, “Development of SRF thin film materials for monolayer/multilayer approach to increase the performance of SRF accelerating structures beyond bulk Nb,” PhD dissertation, Université Paris XI (France), 2014.

[56] A. Anders *et al.*, “Deposition of niobium and other superconducting materials with high power impulse magnetron sputtering: concept and first results,” in *Proceedings of 15th International Conference on RF Superconductivity (SRF2011), Chicago, IL, USA,* 2011.

[57] G. Terenziani, S. Calatroni, T. Junginger, and I. A. Santillana, “Nb coating developments with HIPIMS for SRF applications,” in *Proceedings of 16th International Conference on RF Superconductivity (SRF2013), Paris, France*, 2013.

[58] M. Burton, R. Beebe, R. A. Lukaszew, A. Palczewski, H. L. Phillips, and C. E. Reece, “RF results of Nb coated SRF accelerator cavities via HiPIMS,” in *Proceedings of 18th International Conference on RF Superconductivity (SRF2017), Lanzhou, China*, 2017.

[59] S. Wilde, R. Valizadeh, and O. B. Malyshev, “DC magnetism of Niobium thin films,” in *Proceedings of 18th International Conference on RF Superconductivity (SRF2017), Lanzhou, China*, 2017.

[60] A. Anders, “Discharge physics of high power impulse magnetron sputtering,” *PSE 2010 Spec. Issue*, vol. 205, no. Supplement 2, pp. S1–S9, Jul. 2011.

[61] D. Horwat and A. Anders, “Compression and strong rarefaction in high power impulse magnetron sputtering discharges,” *J. Appl. Phys.*, vol. 108, no. 12, p. 123306, Dec. 2010.

[62] J. Andersson and A. Anders, “Self-Sputtering Far above the Runaway Threshold: An Extraordinary Metal-Ion Generator,” *Phys. Rev. Lett.*, vol. 102, no. 4, p. 045003, Jan. 2009.

[63] G. J. Rosaz, “Private communication,” 2017.

[64] R. L. Boxman, D. M. Sanders, and P. J. Martin, *Handbook of Vacuum Arc Science and Technology*. William Andrew, 1996.

[65] R. Russo *et al.*, “Niobium Coating of Cavities Using Cathodic Arc,” *IEEE Trans. Appl. Supercond.*, vol. 19, no. 3, pp. 1394–1398, Jun. 2009.

[66] L. Catani *et al.*, “Nb coating of copper cavities by UHV cathodic arc,” in *Proceedings of 13th International Conference on RF Superconductivity (SRF2007), Peking Univ., Beijing, China*, 2007.

[67] K. Velas, S. Chapman, I. Irfan, and M. Krishnan, “Energetic Condensation Growth of Nb on Cu SRF Cavities,” in *17th International Conference on RF Superconductivity (SRF2015), Whistler, BC, Canada, Sept. 13-18, 2015*, 2015, pp. 629–632.

[68] G. Wu *et al.*, “Studies of niobium thin film produced by energetic vacuum deposition,” *Thin Solid Films*, vol. 489, no. 1, pp. 56–62, Oct. 2005.

[69] K. Saito *et al.*, “R&D of Nb/Cu clad seamless cavities at KEK,” in *Proceedings of 10th International Conference on RF Superconductivity (SRF2001), Tsukuba, Japan*, 2001.

[70] I. Itoh, K. Saito, H. Inoue, and W. Singer, “Hot roll bonding method for Nb/Cu clad seamless SC cavity,” in *Proceedings of 11th International Conference on RF Superconductivity (SRF2003), Lübeck/Travemünder, Germany*, 2003.

[71] W. Singer, “Seamless/bonded niobium cavities,” *Phys. C Supercond.*, vol. 441, no. 1–2, pp. 89–94, Jul. 2006.

[72] W. Singer *et al.*, “Hydroforming of NbCu clad cavities at DESY,” in *Proceedings of 10th International Conference on RF Superconductivity (SRF2001), Tsukuba, Japan*, 2001.

[73] J. Lin, W. D. Sproul, J. J. Moore, S. Lee, and S. Myers, “High rate deposition of thick CrN and Cr2N coatings using modulated pulse power (MPP) magnetron sputtering,” *Surf. Coat. Technol.*, vol. 205, no. 10, pp. 3226–3234, Feb. 2011.

[74] W.-Y. Ho, Y.-S. Chang, B.-Y. Chou, and C.-L. Lin, “Evaluation of Cathodic Arc Deposited Thick CrAlSiN Coatings by Erosion Test,” *J. Mater. Sci. Chem. Eng.*, vol. 03, no. 01, pp. 66–71, 2015.

[75] O. Zimmer and F. Kaulfuß, “PO4046-Hard Coatings with High Film Thickness Prepared by PVD,” *Plasma Process. Polym.*, vol. 6, no. S1, pp. S152–S156, Jun. 2009.

[76] J. Vetter, G. Barbezat, J. Crummenauer, and J. Avissar, “Surface treatment selections for automotive applications,” *ICMCTF 2005*, vol. 200, no. 5, pp. 1962–1968, Nov. 2005.

[77] V. Palmieri, H. Skliarova, S. Cisternino, M. Marengo, and G. Cicoria, “Metodo per l’ottenimento di un target solido per la produzione di radiofarmaci,” 102017000102990.

[78] K. Kab-Seog and K. Yong-Mo, “Fabbrication process for a thick film by magnetron sputtering,” US 2011/0017588 Al.

[79] K. Kab-Seog, K. Yong-Mo, and H. Jeon Geon, “Apparatus and methods for manufacturing stress-free flexible printed circuit board,” US 8,354,009 B2.

[80] G. Yu, “Development of a new mechanical surface treatment for the internal finishing of 6 GHz superconducting cavities,” Master dissertation, Università degli studi di Padova (Italy), 2013.

[81] J. T. Maniscalco, D. Gonnella, and M. Liepe, “The importance of the electron mean free path for superconducting radio-frequency cavities,” *J. Appl. Phys.*, vol. 121, no. 4, p. 043910, Jan. 2017.

[82] A. Andreone *et al.*, “Surface impedance measurements of superconducting (NbTi)N films by a ring microstrip resonator technique,” *J. Appl. Phys.*, vol. 73, no. 9, pp. 4500–4506, May 1993.

[83] I. Petrov, P. B. Barna, L. Hultman, and J. E. Greene, “Microstructural evolution during film growth,” *J. Vac. Sci. Technol. Vac. Surf. Films*, vol. 21, no. 5, pp. S117–S128, Sep. 2003.

[84] H. Padamsee, “Calculations for breakdown iduced by ‘large defects’ in superconducting niobium cavities,” *IEEE Trans. Magn.*, vol. Mag-17, p. 947, 1981.

[85] P. Kneisel, K. Saito, and R. Parodi, “Performance of 1300 MHz KEK-Type Single Cell Niobium Cavities,” in *Proceedings of 8th International Workshop on RF Superconductivity (SRF1997), Abano Terme (Padova), Italy*, 1997.

[86] K. Saito, “Surface Smoothness for High Gradient Niobium SC RF Cavities,” in *Proceeding of 11th Workshop on RF Superconductivity (SRF2003), Lubek (Germany)*, 2003.

[87] “ARIES WP15, https://aries.web.cern.ch/content/wp15.” .

[88] V. Palmieri, “Seamless cavities: the most creative topic in RF Superconductivity,” in *Proceedings of 8th International Workshop on RF Superconductivity (SRF1997), Abano Terme (Padova), Italy*, 1997, vol. 3.

[89] V. Palmieri, “Advancements on spinning of seamless multicell reentrant cavities,” in *Proceedings of 11th International Conference on RF Superconductivity (SRF2003), Lübeck/Travemünder, Germany*, 2003, pp. 357–361.

[90] D. Williams, *Guide to Cleaner Technologies: Cleaning and Degreasing Process Changes*. United States Enviromental Protection Agency, 1994.

[91] D. M. Turley and L. E. Samuels, “The nature of mechanically polished surfaces of copper,” *Metallography*, vol. 14, no. 4, pp. 275–294, Dec. 1981.

[92] V. Palmieri, “Fundamentals of Electrochemistry - The Electrolytic Polishing of Metals: Application to Copper and Niobium,” in *Proceedings of 11th International Conference on RF Superconductivity (SRF2003), Lübeck/Travemünder, Germany, 2003*, 2003.

[93] V. Palmieri, F. Stivanello, S. Y. Stark, C. Roncolato, and M. Valentino, “Besides the standard niobium bath chemical polishing,” in *Proceedings of 10th International Workshop on RF Superconductivity (SRF2001), Tsukuba, Japan*, 2001.

[94] S. Calatroni, “Niobium coating techniques,” *J. Phys. Conf. Ser.*, vol. 114, p. 012006, May 2008.

[95] J.-P. Birabeau and J. M. A. Guerin, “Patent No 88 09820, Institut National de la Propriété Industrielle, 1993.”

[96] J. D. Adams, J.-P. Birabeau, J. M. A. Guerin, and S. Pousse, “Procedes de preparation de surface de cuivre compatibles avec un depot de niobium realize par pulverisation cathodique. Presentation d’un bain de polissage chimique repondant a ce critere,” CERN Technical Note 85/SB/AC/B/3199/gp, 1985.

[97] P. Kneisel and B. Lewis, “Advanced surface cleaning methods: three years of experience with high pressure ultrapure water rinsing of superconducting cavities,” in *Proceedings of 7th Workshop on RF Superconductivity (SRF1995), Gif-sur-Yvette, France*, 1995.

[98] R.-K. Takur, A. Rossi, and S. Stark, “SRF measurement procedure of tesla type 6 GHz cavities,” LNL internal procedure, 2012.

[99] G. Lanza, "New Magnetron Configurations for sputtering niobium thin films into copper tesla-type superconducting cavities," PhD dissertation, Università degli studi di Padova (Italy), 2008.

[100] A. Rossi, "A miniaturized 6 GHz infrastructure for cutting down the cost of RF superconducting research Supervisor: Prof. V. Palmieri Academic Year," Master dissertation, Università degli studi di Padova (Italy), 2008.

[101] E. Mahner, S. Calatroni, E. Chiaveri, E. Haebel, and J. M. Tessier, "A new instrument to measure the surface resistance of superconducting samples at 400 MHz," *Rev. Sci. Instrum.*, vol. 74, no. 7, pp. 3390–3394, Jun. 2003.

[102] G. Eremeev, B. Xiao, C. Reece, and A.-M. Valente-Feliciano, "Characterization of superconducting samples with SIC system for thin film developments: Status and recent results," in *Proceedings of 16th International Conference on RF Superconductivity (SRF2013), Paris, France*, 2013.

[103] L. Badan *et al.*, "RF characterization of small scale cavities," in *Proceedings of 8th International Workshop on RF Superconductivity (SRF1997), Abano Terme (Padova), Italy*, 1997, vol. 62, pp. 117–123.

[104] T. Powers, "Theory and practice of cavity RF test systems," presented at the Proceedings of 12th In. Workshop on RF Superconductivity (SRF2005), Cornell University, Ithaca, New York, USA, 2005.

[105] S. Stark, V. Palmieri, A. M. Porcellato, and A. Rossi, "Recent Upgrade of Ultra-Broadband RF System for Cavity Characterization," in *Proceedings of 16th International Conference on RF Superconductivity (SRF2013), Paris, France*, 2013.

[106] M. Checchin, "Innovative High Temperature Treatments for High Quality Factor Superconducting Niobium Elliptical Cavities," Master dissertation, Università degli studi di Padova (Italy), 2014.

[107] A. Rossi *et al.*, "An Innovative Purification Technique of 6 GHz Tesla Type Nb Cavities in UHV System," presented at the 16th International Conference on RF Superconductivity (SRF2013), Paris, France, 2013.

[108] *Veeco Dektak 8 Advanced Development Profiler Manual*. 2005.

[109] The Editors of Encyclopædia Britannica, "Bragg law," *Encyclopaedia Britannica*. Encyclopædia Britannica, inc., 2016.

[110] A. Taylor and H. Sinclair, "On the determination of lattice parameters by the debye-scherrer method," *Proc. Phys. Soc.*, vol. 57, no. 2, p. 126, 1945.

[111] V. Pankov, M. Evstigneev, and R. H. Prince, "Enhanced stability of rocksalt-type AIN phase in AIN/TiN superlattices synthesized by room-temperature pulsed laser deposition," *J. Appl. Phys.*, vol. 92, no. 8, pp. 4255–4260, 2002.

[112] J. I. Goldstein, D. E. Newbury, J. W. Colby, H. Yakowitz, E. Lifshin, and J. R. Coleman, *Pratical scanning electron microscopy*. New York: Plenum Press, 1975.

[113] M. Martinello, "Study of Niobium sputtered copper accelerating cavities as a possible alternative to the bulk technology," Master dissertation, Università degli studi di Padova (Italy), 2014.

[114] A Grassellino and A Romanenko and D Sergatskov and O Melnychuk and Y Trenikhina and A Crawford and A Rowe and M Wong and T Khabiboulline and F Barkov, "Nitrogen and argon doping of niobium for superconducting radio frequency cavities: a pathway to highly efficient accelerating structures," *Supercond. Sci. Technol.*, vol. 26, no. 10, p. 102001, 2013.

[115] F. Marhauser, "Technical Challenge of Cavity Mass Production in LCLS-II," presented at the Tesla Technology Collaboration Meeting at SLAC, 01-Dec-2015.

[116] J. T. Clenny and C. J. Rosa, "Nitridation kinetics of niobium in the temperature range of 873 to 1273 K," *Metall. Trans. A*, vol. 11, no. 9, pp. 1575–1580, Settembre 1980.

[117] S. Sengupta, N. Halder, S. Chakrabarti, M. Herrera, M. Bonds, and N. D. Browning, "Investigation of the effect of varying growth pauses on the structural and optical properties of InAs/GaAs quantum dot heterostructures," *Superlattices Microstruct.*, vol. 46, no. 4, pp. 611–617, Oct. 2009.

[118] V. Palmieri, "Private communication," 2016.

[119] G. Ciovati, "Effect of low-temperature baking on the radio-frequency properties of niobium superconducting cavities for particle accelerators," *J. Appl. Phys.*, vol. 96, no. 3, pp. 1591–1600, 2004.

[120] G. Ciovati, G. Myneni, F. Stevie, P. Maheshwari, and D. Griffis, "High field Q slope and the baking effect: Review of recent experimental results and new data on Nb heat treatments," *Phys. Rev. Spec. Top. - Accel. Beams*, vol. 13, no. 2, Feb. 2010.

[121] A. Andreone, A. Cassinese, M. Iavarone, R. Vaglio, I. I. Kulik, and V. Palmieri, "Relation between normal-state and superconductive properties of niobium sputtered films," *Phys. Rev. B*, vol. 52, no. 6, p. 4473, 1995.

[122] C. Pira, "Nuove configurazioni da sputtering ad enhanced ionization dischrarge per film sottili di niobio in cavità acceleratrici per collider lineari di nuova generazione," Master dissertation, Università degli studi di Padova (Italy), 2006.

List of figures

Figure 1.1 Only the electrons that are traveling almost parallel to the surface participate to the conduction. 4
Figure 1.2 Different behavior of type I and type II superconductors in a magnetic field..9
Figure 1.3 the Meissner state can remain metastable at higher fields, H > H_{c1} up to the superheating field H_{sh}................9
Figure 1.4 Electric and magnetic electric fields in a pill box cavity during the acceleration process […]...........................10
Figure 1.5 Elliptical cavity description [28]...11
Figure 1.6 Principal limitation in a superconducting resonant cavity [1] 12
Figure 1.7 The BCS surface resistance at 1.5 GHz as a function of Nb purity […]..16
Figure 1.8 Q-factor versus the accelerating field for Nb film sputtered cavities compared to bulk niobium cavities. […].18
Figure 1.9 Best RF performance at 1.7 K for several 1.5 GHz Nb/Cu cavities sputtered coated with Kr at CERN […] 18
Figure 1.10 Model for an isolated thermal defect at the Nb/Cu interface, and relative local temperature profile [35]. ..19
Figure 2.1 Schematic illustration of the sputtering process: A collision cascade is triggered inside the target, […]..........22
Figure 2.2 Paschen curve for a number of gases.(CIT A. Von Engel, Ionized Gases, Oxford university press 1965) 23
Figure 2.3 Characteristic I-V curve of an electrical discharge in vacuum. 24
Figure 2.4 Structure zone diagram (SZD) proposed by Thornton. […]...25
Figure 2.5 Structure zone diagram (SZD) proposed by Anders in 2010 [44]. 26
Figure 2.6Tensile (a) and compressive (b) thermal stress in thin film [45]...27
Figure 2.7 Schematic representation of thermal and intrinsic stress contribution [41]. 28
Figure 2.8 Typical evolution of average film stress σ as a function of film thickness t_f during the deposition […]...........28
Figure 2.9 Force per unit width produced at coating-substrate interface by internal stress […] 29
Figure 2.10 Diode Bias Sputtering configuration for the ALPI QWR (a) [5] and HIE Isolde (b) [50]. 31
Figure 2.11 Sputtering target configuration [38]...32
Figure 2.12 Schematic drawing of the CERN elliptical single cell resonator coating system [26]. 33
Figure 2.13 schematic of the LBNL dual magnetron HIPIMS deposition system for 1.3 GHz cavities coating [55]. 35
Figure 2.14 HIPIMS results at CERN. Different BIAS voltage was applied [50]. 36
Figure 2.15 The best result achieved in a single-cell NbCu clad cavity produced at DESY […]..38
Figure 3.1 Defect growth during deposition: […]...40
Figure 3.2 Stress-free thick film composed by a multilayer of alternative compressive Cu and tensile Cu […] 41
Figure 3.3 Variation of RRR as a function of the Nb film thickness. […] 42
Figure 3.4 The heat flow in thin film will be transmitted only unidimensionally and cannot by-pass the thermal defect.43
Figure 3.5 The heat flow in thick film could be transmitted more tridimensionally […] 43
Figure 4.1 Schematic representation of a spinning process for an elliptical single cell cavity […].....................................47
Figure 4.2 Lapping of the flanges (a). The flange surface appearance after the lapping process (b). 47
Figure 4.3 a) Scotch Brite™ cross shaped abrasive. b) Mechanical grinding of the 6 GHz monocell. […]..........................48
Figure 4.4 Internal surface of the 6 GHz cavities (cell zone) as appear after the spinning production process. 48
Figure 4.5 Internal surface of the 6 GHz cavities (cell zone) as appear after the mechanical polishing treatment. […] 49
Figure 4.6 Schematic sketch of the structure observed for an abraded OFHC Copper surface [91]. 50
Figure 4.7 Current density vs. voltage for Copper electropolishing in phosphoric acid [91]. 51
Figure 4.8 *Time evolution of the I-V characteristic plateau* [92]. 51
Figure 4.9 Figure 4: I-V characteristic for a standard electropolishing process (circles); […]...52
Figure 4.10 EP software used at LNL..52
Figure 4.11 In this picture the mini-chemical system set up for 6 GHz cavities EP is visible. […] 53

Figure 4.12 The SUBU 6 GHz cavities configuration. […]. 54
Figure 4.13 After all the polishing process, the internal cavity surface looks very glossy (a). […]. 54
Figure 4.14 High Pressure Rinsing (HPR) of a 6 GHz cavity at LNL. On the right the water jet used is visible. 55
Figure 5.1 Principal dimension of a 6 GHz elliptical resonant cavity (expressed in mm). 58
Figure 5.2 Measuring System layout [104]. 62
Figure 5.3 Five steps of the calibration procedure [104]. 64
Figure 5.4 LNL rf software main panel 67
Figure 5.5 Simplified scheme of the INFN-LNL 6 GHz cryostat and the pumping system [105]. 68
Figure 5.6 Helium tank (A) and helium tank cross section (B). In the figures the 3 cavity stands, […]. 69
Figure 5.7 6 GHz cryostat, with two stands mounted, during a helium transfer. 69
Figure 5.8 Phase diagram of Helium. At the temperature of the lambda point 2,168 K […]. 70
Figure 5.9 New flange design for the stand flange. This composed by two pieces, machined together. […] 71
Figure 6.1 Picture of all the instrumentation used for RRR and T_C characterization 74
Figure 6.2 Veeco Dektakt 8 profilometer. 74
Figure 6.3 Typical profile curve for the samples thickness of this work. 75
Figure 6.4 Picture of the optical inspection system on the left. Picture of the camera, […] 75
Figure 6.5 schematic diagram of the optical inspection system [79]. 76
Figure 6.6 Bragg diffraction [108]. 77
Figure 6.7 LNL-INFN Philips/PANalytical X'Pert X-ray diffractometer. 77
Figure 6.8 LNL-INFN Philips XL 30 SEM. 78
Figure 7.1 Picture of the deposition system used in this work for the deposition of the 6 GHz cavities 80
Figure 7.2 Scheme of the vacuum system 81
Figure 7.3 3D section of the "compact magnetron sputtering source" used in this work. 81
Figure 7.4 Side view of the "compact magnetron sputtering source" used in this work. […] 82
Figure 7.5 Bottom view of the "compact magnetron sputtering source". […] 82
Figure 7.6 Deposition system with the small coil. 84
Figure 7.7 Magnetic field in function of the position in the cell. The magnetic fied is maximum in […] 84
Figure 7.8 The non uniform plasma confinement at pressure below $4 \cdot 10^{-2}$ mbar. […] 85
Figure 7.9 A uniform confinement along the cathode length is obtained with the long coil. 85
Figure 7.10 Flange deformation due to high temperature (650 °C). […] 86
Figure 7.11 Glow discharge voltage as function of the pressure. […] 87
Figure 7.12 Thick films of Niobium (10 μm) sputtered on kapton substrates at different pressure values. […]. 87
Figure 7.13 Cavity test with 6 sample holders for 10x10 quartz, sapphire or copper substrates. 88
Figure 7.14 On the left masked sample and on the right sputtered masked samples ready for the characterizations. 88
Figure 7.15 Scheme of the multilayer process. Duty cycle has been set to 0,7. 91
Figure 7.16 Control panel of the Labview® software for the multilayer deposition developed in this thesis work 91
Figure 7.17 Two of the samples used for the BCP test. The etching rate on the sputtered films is 1,4 μm/min 92
Figure 7.18 BCP of a sputtered cavity. In the pictures is visible the post treatment done on Cav 3.1. 93
Figure 7.19 Vacuum chamber used for the heat treatments. The heating is realized with an infrared lamp. 93
Figure 8.1 XRD spectra of 10 μm thick film coated with the parameters of Table 8.1. 96
Figure 8.2 SEM Micrographs of the Nb film surface at two different magnifications. 97
Figure 8.3 EDS spectra of a portion of the surface of Figure 8.2. 97
Figure 8.4 SEM micrograph of the film cross section. 98
Figure 8.5 EDS map of the film cross section. 98
Figure 8.6 Internal inspection of the cell (on the left) and iris (on the right) for Cav1.0. 100
Figure 8.7 Rf test at 4.2K and 1.8K for Cav1.0. 100
Figure 8.8 Internal inspection of the cell (on the left) and iris (on the right) for Cav1.1. 101
Figure 8.9 Rf test at 4.2K for Cav1.1. 101
Figure 8.10 Internal inspection of the cell (on the left) and iris (on the right) for Cav1.1. 102
Figure 8.11 Rf test at 4.2K and 1.8K for Cav3.1. 102
Figure 8.12 Rf test at 4.2K and 1.8K for Cav3.1 after BCP. 103
Figure 8.13 Rf test at 4.2K for Cav3.1 after baking. 103
Figure 8.14 Rf test at 4.2K and 1.8K for all the processes Cav3.1. 104

Figure 8.15 Internal inspection of the cell (on the left) and iris (on the right) for Cav4.0. 105
Figure 8.16 Rf test at 4.2K for Cav4.0....105
Figure 8.17 Internal inspection of the cell (on the left) and iris (on the right) for Cav5.0. 106
Figure 8.18 Rf test at 4.2K and 1.8K for Cav5.0....106
Figure 8.19 Internal inspection of the cell (on the left) and iris (on the right) for Cav5.1. 107
Figure 8.20 Rf test at 4.2K and 1.8K for Cav5.1....107
Figure 8.21 Internal inspection of the cell (on the left) and iris (on the right) for Cav6.0. 108
Figure 8.22 Rf test at 4.2K and 1.8K for Cav6.0....108
Figure 8.23 Internal inspection of the cell (on the left) and iris (on the right) for Cav7.0. 109
Figure 8.24 Rf test at 4.2K for Cav7.0....109
Figure 8.25 Rf test at 4.2K and 1.8K for Cav7.0 after BCP....110
Figure 8.26 Rf test at 4.2K for Cav7.0 after baking. 110
Figure 8.27 Rf test at 4.2K and 1.8K for all the processes Cav7.0....111
Figure 8.28 Internal inspection of the cell (on the left) and iris (on the right) for Cav8.1. […] 112
Figure 8.29 Rf test at 4.2K and 1.8K for Cav8.1....112
Figure 8.30 Internal inspection of the cell (on the left) and iris (on the right) for Cav9.0. 113
Figure 8.31 Rf test at 1.8K and 4.2K for Cav9.0....113
Figure 8.32 Rf test at 4.2K and 1.8K for Cav9.0 after BCP....114
Figure 8.33 Rf test at 1.8 K and 4.2K for Cav9.0 after the first baking process. 114
Figure 8.34 Rf test at 1.8 K and 4.2K for Cav9.0 after the second baking process. 115
Figure 8.35 Rf test at 1.8 K and 4.2K for Cav9.0 after the third and last baking process. 115
Figure 8.36 Rf test at 4.2K and 1.8K for all the processes Cav9.0....116
Figure 8.37 Internal inspection of the cell (on the left) and iris (on the center) and of the cut off (on the right) […]. 117
Figure 8.38 Rf test at 1.8K and 4.2K for Cav10.1....117
Figure 8.39 Internal inspection of the cell (on the left) and iris (on the right) for Cav11.0. 118
Figure 8.40 Rf test at 1.8 K and 4.2K for Cav11.0....118
Figure 8.41 Internal inspection of the cell (on the left) and iris (on the right) for Cav11.0. 119
Figure 8.42 Rf test at 4.2K for Cav11.1....119
Figure 8.43 Internal inspection of the cell (on the left) and iris (on the right) for Cav12.0. 120
Figure 8.44 Rf test at 1.8K and 4.2K for Cav12.0....120
Figure 8.45 Internal inspection of the cell (on the left) and iris (on the right) for Cav13.0. 121
Figure 8.46 Rf test at 1.8K and 4.2K for Cav13.0....122
Figure 8.47 Rf test at 1.8K and 4.2K for Cav13.0 after baking. 122
Figure 8.48 Rf test at 4.2K and 1.8K for all the processes Cav9.0....123
Figure 8.49 Internal inspection of the cell (on the left), iris (on the center) and near the flange […] 124
Figure 8.50 Rf test at 1.8 K and 4.2K for Cav15.0....124
Figure 8.51 Internal inspection of the cell (on the left) and iris (on the right) for Cav16.0. 125
Figure 8.52 Rf test at 1.8K and 4.2K for Cav16.0....125
Figure 8.53 Rf test at 1.8 K and 4.2K for Cav16.0 after the baking process. 126
Figure 8.54 Rf test at 1.8 K and 4.2K for Cav16.0 after the first annealing process. 126
Figure 8.55 Rf test at 1.8 K and 4.2K for Cav16.0 after the first annealing process. 127
Figure 8.56 Rf test at 4.2K and 1.8K for all the processes Cav16.0....127
Figure 8.57 Internal inspection of the cell (on the left) and iris (on the right) for Cav17.0. 128
Figure 8.58 Rf test at 4.2K for Cav17.0....128
Figure 8.59 Q vs E_{curve} at 1.8K of the 3 best thick Nb/Cu 6 GHz cavities. […]....129
Figure 8.60 On the graph the rf test curves at 4.2 K and 1.8 K […]....131
Figure 8.61 On the graph the rf test curves at 4.2 K and 1.8 K […]....132
Figure 8.62 On the graph the rf test curves at 4.2 K and 1.8 K […]....133
Figure 8.63 Q vs E_{curve} measured at 4.2 K and 6 GHz for different single layer thickness. 133
Figure 8.64 Curve slope at 4.2 K for different single layer thickness....134

List of tables

Table 1.1 Physical and superconducting parameters for niobium ... 14
Table 5.1 Important parameters when calculating the cavity excitation curve [29]. ... 58
Table 7.1 Deposition rate along the cavity, at the different pressures of the deposition process. ... 88
Table 7.2 Standard venting mode description ... 89
Table 7.3 High temperature venting mode description ... 90
Table 8.1 Coating parameters used in the planar samples depositions ... 95
Table 8.2 Superconductive properties of Nb on sapphire samples ... 96
Table 8.3 Resuming table of the depositions parameters and rf test. All the reported test was done at 1.8K. […]. ... 99
Table 8.4 Deposition parameters for Cav1.0. PROCESS 1.0.A. […]. ... 100
Table 8.5 Deposition parameters for Cav1.1. PROCESS 1.1.A. […] ... 101
Table 8.6 Deposition parameters for Cav3.1. PROCESS 3.1.A. […] ... 102
Table 8.7 BCP parameters for Cav3.1. PROCESS 3.1.B. ... 103
Table 8.8 Baking parameters for Cav3.1. PROCESS 3.1.C. ... 103
Table 8.9 Deposition parameters for Cav4.0. PROCESS 4.0.A. […] ... 105
Table 8.10 Deposition parameters for Cav5.0. PROCESS 5.0.A. […]. ... 106
Table 8.11 Deposition parameters for Cav5.1. PROCESS 5.1.A. […] ... 107
Table 8.12 Deposition parameters for Cav6.0. PROCESS 6.0.A. […]. ... 108
Table 8.13 Deposition parameters for Cav7.0. PROCESS 7.0.A. […] ... 109
Table 8.14 BCP parameters for Cav7.0 PROCESS 7.0.B ... 110
Table 8.15 Baking parameters for Cav7.0. PROCESS 7.0.C. ... 110
Table 8.16 Deposition parameters for Cav8.1. PROCESS 8.1.A. […]. ... 112
Table 8.17 Deposition parameters for Cav9.0. PROCESS 9.0.A. […] ... 113
Table 8.18 BCP parameters for Cav9.0 PROCESS 9.0.B ... 114
Table 8.19 Baking parameters for Cav9.0. PROCESS 9.0.C. ... 114
Table 8.20 Baking parameters for Cav9.0. PROCESS 9.0.D. ... 115
Table 8.21 Baking parameters for Cav9.0. PROCESS 9.0.C. ... 115
Table 8.22 Deposition parameters for Cav10.1. PROCESS 10.1.A. […]. ... 117
Table 8.23 Deposition parameters for Cav11.0. PROCESS 11.0.A. […] ... 118
Table 8.24 Deposition parameters for Cav11.1. PROCESS 11.1.A. […]. ... 119
Table 8.25 Deposition parameters for Cav12.0. PROCESS 12.0.A. […]. ... 120
Table 8.26 Deposition parameters for Cav13.0. PROCESS 13.0.A. […] ... 121
Table 8.27 High temperature venting mode modify for PROCESS 13.0.A ... 121
Table 8.28 Baking parameters for Cav13.0. PROCESS 13.0.C. ... 122
Table 8.29 Deposition parameters for Cav11.0. PROCESS 15.0.A. […] ... 124
Table 8.30 Deposition parameters for Cav16.0. PROCESS 16.0.A. […] ... 125
Table 8.31 Baking parameters for Cav16.0. PROCESS 16.0.C. ... 126
Table 8.32 Annealing parameters for Cav16.0. PROCESS 16.0.D. ... 126
Table 8.33 Second annealing parameters for Cav16.0. PROCESS 16.0.E. ... 127
Table 8.34 Deposition parameters for Cav17.0. PROCESS 17.0A. […]. ... 128

List of abbreviations

AC	Alternating Current
BCP	Buffer Chemical Polish
BCC	body center cubic
BCS	Bardeen, Cooper and Schrieffer
DC	Direct Current
EDS	Energy Dispersive Spectroscopy
EP	Electro-polishing
HPR	High-Pressure Rinse
LCLS	Linac Coherent Light Source
LINAC	Linear Accelerator
RF	Radio Frequency
RRR	Residual Resistivity Ratio
SEM	Scanning Electron Microscope
SRF	Superconducting Radio Frequency
UHV	Ultra-High Vacuum